

Politecnico di Bari

Repository Istituzionale dei Prodotti della Ricerca del Politecnico di Bari

Instabilities and receptivities of turbulent aerospace flows

This is a PhD Thesis

Original Citation:
Instabilities and receptivities of turbulent aerospace flows / Variale, D.. - ELETTRONICO. - (2026).

Availability:
This version is available at http://hdl.handle.net/11589/307620 since: 2026-11-18

Published version
DOI:

Publisher: Politecnico di Bari

Terms of use:

(Article begins on next page)

20 November 2026

Arts et Métiers Sciences et Technologies

ÉCOLE DOCTORALE SCIENCES ET MÉTIERS DE L'INGÉNIEUR
Laboratoire de Dynamique des Fluides (DynFluid) - Campus de Paris

THÈSE

Présentée par : **Donato VARIALE**
Soutenue le : **30 September 2026**

pour obtenir le diplôme de **Doctorat** *délivré par* :

L'École Nationale Supérieure d'Arts et Métiers

Spécialité : **Mécanique, génie mécanique, génie civil**

Instabilities and receptivities of turbulent aerospace flows

THÈSE dirigée par :
Jean-Christophe ROBINET & Stefania CHERUBINI

et co-encadrée par :
Nicolas ALFEREZ

Jury

M. E. GONCALVES	Prof., Pprime, ISAE-ENSMA	Examinateur
M. L. LESSHAFFT	Dir. Rech., LadHyX/CNRS, Ecole Polytechnique	Rapporteur
M. E. MARTELLI	Prof., DIMEAS, Politecnico di Torino	Rapporteur
M. V. JAUNET	Dr., Pprime, ISAE-ENSMA	Examinateur
M. J. CROUCH	Dr., Flight Sciences, The Boeing Company	Examinateur
M. J.-C. ROBINET	Prof., DynFluid Lab., ENSAM	Directeur
M. N. ALFEREZ	Dr., DynFluid Lab., CNAM	Encadrant
Mme. S. CHERUBINI	Prof., DMMM, Politecnico di Bari - Italy	co-Directrice
M. S. BLANCHARD	Dr., CNES, DTN/STS/EPM	Invité

THÈSE

Résumé

Les écoulements turbulents dans les applications aérospatiales présentent souvent une dynamique instationnaire qui peut être étudiée de manière adéquate à l'aide d'une analyse de stabilité globale basée sur un ensemble d'équations URANS. L'un des objectifs de ce travail est de développer un framework unifié permettant de résoudre des problèmes de stabilité linéaire pour les écoulements turbulents en utilisant à la fois des méthodes par pas de temps et des méthodes de formation de matrices. À l'issue d'une phase de validation à l'aide de tests canoniques, deux configurations présentant un intérêt technique sont examinées. Tout d'abord, l'écoulement transsonique à travers un diffuseur (modèle G de Sajben) est étudié dans des configurations à choc fort (avec décollement) et à choc faible (sans décollement). L'analyse de stabilité globale en 2D révèle que la non-stationnarité observée expérimentalement n'est pas due à une instabilité globale. L'analyse par résolvant met en évidence un pic à la même fréquence, indiquant qu'il s'agit d'un mécanisme de réceptivité. L'extension de l'étude à la direction transversale, par superposition d'une perturbation 3D sur l'écoulement de base 2D, révèle l'émergence d'un mode instable de fréquence nulle dans le cas du choc fort ; il s'agit d'une instabilité centrifuge qui, toutefois, n'apparaît pas dans le cas du choc faible.
Ensuite, on analyse le jet 3D à écoulement à contre-courant, qui reproduit la phase d'atterrissage des lanceurs réutilisables. En l'absence d'angle d'attaque, l'écoulement est globalement stable ; avec un angle d'attaque de $\theta = 10°$, le spectre présente plusieurs modes instables à la même fréquence que la PSD d'URANS. On distingue deux familles de modes : des modes à basse fréquence dont l'activité maximale se situe dans la couche de mélange et des modes à haute fréquence dont l'activité maximale se situe dans la région du sillage.

Keywords : Écoulements turbulents, dynamique à basse fréquence, stabilité globale, matrix-forming, time-stepper, jet à contre-courant, diffuseur sur-détendue.

Abstract

Turbulent flows in aerospace applications often exhibit unsteady dynamics that can be adequately studied using a global stability analysis based on a set of URANS equations. One of the objectives of this work is to develop a unified framework for solving linear stability problems for turbulent flows using both time-stepping and matrix-forming methods. Following a validation phase using canonical tests, two configurations of engineering interest are examined. Firstly, the transonic flow through a diffuser (Sajben model G) is investigated in both a strong shock (with flow separation) and a weak shock (without separation) configurations. The 2D global stability analysis reveals that the unsteadiness observed experimentally is not driven by a global instability. Through the resolvent analysis, a peak is observed at the same frequency, indicating that this is a receptivity mechanism. Extending the study to the spanwise direction by superimposing a 3D perturbation onto the 2D base flow reveals the emergence of a zero-frequency unstable mode for the strong-shock case; this is a centrifugal instability which, however, does not emerge in the weak-shock case.
Secondly, the 3D jet with counter-current flow is analysed, which mimics the landing phase of reusable launch vehicles. Without an angle of attack, the flow is globally stable; with an angle of attack of $\theta = 10°$, the spectrum exhibits several unstable modes at the same frequency as the URANS PSD. Two families of modes can be distinguished: A lower-frequency modes whose peak activity lies in mixing layer and a higher-frequency modes whose peak activity lies in the wake region .

Keywords : Turbulent flows, low-frequency dynamics, global stability, matrix forming, time-stepper, counter-current jet, overxpanded diffuser.

Contents

Résumé **3**

Abstract **5**

List of Tables **11**

List of Figures **20**

Introduction **21**

1 Theoretical formulation **29**

1.1 Governing equations 30

1.1.1 Navier-Stokes equations 30

1.1.2 Curvilinear Navier-Stokes equations 32

1.2 Turbulence Modelling 35

1.2.1 Features of turbulence 35

1.2.2 Scales of turbulence 38

1.2.3 Reynolds Average Navier-Stokes equations. 40

1.2.4 Spalart-Allmaras one-equation model 44

1.2.5 k-ω SST two-equation model 46

1.3 Stability analysis 49

1.3.1 Modal stability analysis 49

1.3.2 Non modal stability analysis . . . 52
1.3.2.1 Resolvent analysis . . . 52
1.3.3 On the choice of the base flow . . . 54

2 Numerical framework **57**

2.1 dNami . . . 58
2.1.1 Finite difference method . . . 61
2.1.2 Runge Kutta methods . . . 63
2.1.3 Shock capturing scheme . . . 64
2.1.4 Boundary conditions . . . 66
2.1.4.1 No-slip adiabatic wall . . . 66
2.1.4.2 Slip adiabatic wall . . . 66
2.1.4.3 Inflow/Outflow . . . 68
2.1.4.4 Riemann invariant inflow/outflow . . . 72
2.2 liNami . . . 73
2.2.1 Automatic differentiation . . . 73
2.2.2 Matrix-free methods for stability analysis . . . 77
2.2.2.1 Fixed point . . . 78
2.2.2.2 Eigenvalue problem . . . 83
2.2.3 Matrix-forming method . . . 84
2.2.3.1 Jacobian extraction . . . 84
2.2.3.2 Eigenvalue problem . . . 94

3 Validation test cases **97**

3.1 Turbulent boundary layer . . . 98
3.2 Flow around a cylinder . . . 100
3.3 Lid driven cavity . . . 107

3.3.1 LDC 2D . . . 111
3.3.2 LDC 3-D . . . 114
3.4 Buffet over OAT15 profile . . . 115

4 Sajben Diffuser **123**
4.1 Geometric configuration . . . 124
4.2 2D Global stability and resolvent analysis . . . 128
4.3 Parametric study on Sajben diffuser . . . 140
4.3.1 Diffuser length variation . . . 140
4.3.2 Pressure ratio variation . . . 145
4.4 Physical discussion . . . 148

5 3-D Counter current jet **151**
5.1 Geometric configuration . . . 152
5.2 No incidence angle . . . 158
5.3 Incidence angle $\theta = 10°$ . . . 160
5.3.1 URANS simulation . . . 160
5.3.2 Global stability analysis . . . 162
5.4 Physical discussion . . . 168

Conclusion and perspectives **179**

Bibliography **185**

Appendices **204**

A More on Sajben diffuser **205**
A.1 Strong shock case: acoustic mode . . . 207

B Wall Law in dNami **211**

List of Tables

2.1 Stencil coefficients for 1D Burgers equation 87

4.1 Constant for convergent and divergent profile computation. 126

4.2 Summary of computational cases and parameters. 127

4.3 Comparison between frequency of least stable mode , 1D acoustic model **A-A** and 1D convective-acoustic model **C-A**. 143

5.1 Summary of thermodynamic and kinematic parameters 156

List of Figures

1.1 Simplified 2D representation of the physical domain (x, y, z) and the computational domain (ξ, η, ζ). 33

1.2 Sketch of Reynolds' dye experiment from [1]. 37

1.3 Effect of Reynolds number on mixing layers. Figure taken from [2]. 39

1.4 Time averaged velocity field $U_i(\boldsymbol{x}, t)$ for unsteady turbulent flow. Figure taken from [3]. 41

2.1 Definition of the problem in *dNami* for Burgers 1D equation. 59

2.2 Code generation using *dNami* for the 1D Burgers equation. 60

2.3 Varshift dictionary in *dNami*. 61

2.4 1D representation of finite difference with different approaches. 62

2.5 Source transformation performed by TAPENADE and subsequent post-treatment performed by *liNami*. 75

2.6 Source transformation performed by TAPENADE + *liNami* for 1D Burgers convective term. 76

2.7 Matrix coloring at two different iterations. 87

2.8 Test vector construction st first iteration. 89

2.9 Full Jacobian matrix structure. 90

2.10 $\underline{dudu}$ matrix extraction at iteration k=1,l=1. 91

2.11 $\underline{dudu}$ matrix extraction at iteration k=2,l=1 (left) and k=1,l=2 (right). 91

3.1 Sketch of 2D zero pressure gradient flat plate with sponge zones. 98

3.2 Friction coefficient C_f (left), and inner streamwise velocity u^+ (right) at $x = 0.97$. . . 99

3.3 Turbulent viscosity μ_t/μ_∞. Profile at $x = 0.97$ (left) and contours (right). 99

3.4 Comparison of friction coefficient (left) and inner velocity (right) profiles for different Δy values 101

3.5 Comparison of friction coefficient (left) and inner velocity (right) profiles for different spatial discretisation order 101

3.6 Sketch of 2D flow past circular cylinder 103

3.7 Fixed point streamwise velocity contours u_0 for $Re = 50$. 104

3.8 Streamlines for the case $Re = 40$ (left) and $Re = 50$ (right) 104

3.9 Evolution of growth rate σ (left) and St (right) in function of Re. 105

3.10 Real part of streamwise velocity perturbation $\mathcal{R}(u')$ and cross-stream velocity perturbation $\mathcal{R}(v')$for $Re = 40$ 106

3.11 Direct and adjoint eigenspectra comparison for $Re = 40$ 106

3.12 Real part of adjoint streamwise velocity $\mathcal{R}(u^\dagger)$ and adjoint cross-stream velocity $\mathcal{R}(v^\dagger)$ for $Re = 40$ 107

3.13 Structural sensitivity for $Re = 40$. 108

3.14 Evolution of the gain σ_ω in function of St at $Re = 40$ 108

3.15 Optimal forcing (left) and optimal response (right) of the streamwise velocity component for $Re = 40$ and $St = 0.114$ 109

3.16 Optimal forcing (left) and optimal response (right) of the cross stream velocity component for $Re = 40$ and $St = 0.114$ 109

3.17 Schematic representation of the 2D lid-driven cavity. 112

3.18 Fixed points comparisons between *dNami* computed (left) and Fortin computed [4] (right).112

3.19 Streamwise velocity u_0 and wall-normal velocity v_0 contours of the fixed point for $Re = 8050$. 113

3.20 Eigenspectra comparison between time stepper and Jacobian extraction methods. . . . 113

3.21 Real part of streamwise velocity perturbation (left) and wall-normal perturbation (right) 114

3.22 Schematic representation of th 2.5D lid-driven cavity. 114

3.23 Evolution of growth rate (left) and frequency (right) in function of β for modes S1, T1, T2, T3 at $Re = 1000$. 116

3.24 Real part of spanwise velocity perturbation $\mathcal{R}(w')$ and 3-D reconstruction of the mode $\mathcal{R}\left(\hat{w}(x,y)e^{i\beta z}\right)$ 116

3.25 Geometry and computational mesh for the buffet on OAT15 profile. 118

3.26 Pressure coefficient distribution compared with [5] 119

3.27 Streamwise velocity contours (left) and turbulent viscosity contours (right) of the fixed point 119

3.28 Eigenspectrum for buffet configuration at $\theta = 4.5°$ 120

3.29 Real part of density ρ' (left) and modified viscosity ν'_{SA} (right) of the unstable mode at $St = 0.0725$ 120

3.30 Eigenspectrum computed with $\tau = 0.0625$ (left) and real part of streamwise component of the mode at higher frequency ($St > 1$) (right). 121

4.1 Compu. 127

4.2 Fixed point contours. Density ρ_0 and turbulent viscosity μ_{t0} (left), streamwise velocity u_0 and wall normal velocity v_0 (right). 129

4.3 Wall pressure distribution. Bottom wall (left) , top wall (right) 129

4.4 Streamwise velocity profile at two different sections. $x/h_{in} = 2.8$ (left) , $x/h_{in} = 4.6$ (right). 130

4.5 Eigenspectra compared with experimental frequency and numerical frequency of reference. 130

4.6 Real part of the mode at $St = 0.11$ (270 Hz). Streamwise and wall-normal velocity (left), density and turbulent eddy viscosity (right). 131

4.7 Spectrum and pseudospectrum. 132

4.8 Direct and adjoint eigenspectra comparison (left) and real part of streamwise $u^\dagger$ and wall-normal $v^\dagger$ adjoint mode at St = 0.11. 133

4.9 Structural sensitivity or wavemaker for the mode at $St = 0.11$. Streamwise velocity component $\|(\hat{u})\| \, \|(u^\dagger)\| / < u^\dagger, \hat{u} >$. 133

4.10 Optimal gain in function of St (left) and optimal response and forcing of the streamwise velocity component at $St = 0.11$ (right). 134

4.11 Eigenspectra comparison at $\beta = 0$ and $\beta = 0.8$ (left) and real part of streamwise velocity and wall normal velocity perturbation at low β (right). 134

4.12 Evolution of growth rate σ and pulsation ω at different β values for 2D mode. 135

4.13 Eigenspectrum at $\beta = 8$ (left) and evolution of growth rate σ at different β values for 3D mode (right). 135

4.14 Real part of streamwise velocity u' of the stationary mode at $\beta = 8$. 2D contours (left) and 3D contours reconstruction $\hat{u}e^{(i\beta z)}$ (right). 136

4.15 Real part of wall-normal velocity v' of the stationary mode at $\beta = 8$. 2D contours (left) and 3D contours reconstruction $\hat{v}e^{(i\beta z)}$ (right). 136

4.16 Real part of spanwise velocity w' of the stationary mode at $\beta = 8$. 2D contours (left) and 3D contours reconstruction $\hat{w}e^{(i\beta z)}$ (right). 137

4.17 Evolution of growth rate σ at different β values and different pressure ratios (left); 2D eigenspectrum for the case at $R_p = 0.813$ (right). 137

4.18 Gr number evolution in divergent part of the diffuser for $R_p = 0.813$ (weak shock) and $R_p = 0.72$ (strong shock). The are shown in shaded gray is the instability trigger region. 139

4.19 Contours of optimal gain for $R_p = 0.813$ for different ω and β values. 139

4.20 Streamwise velocity optimal response (top) and forcing (bottom) at $(St, \beta) = (0.023, 0)$ (left) and $(St, \beta) = (0, 2)$ (right) for $R_p = 0.813$. 140

4.21 Streamwise velocity contours of the fixed point at different diffuser length. From top to bottom: $L/h_{in} = 6.1$, $L_1/h_{in} = 6.8$, $L_2/h_{in} = 7.5$, $L_3/h_{in} = 8.2$ 141

4.22 Pressure wall distribution for different lengths. Bottom wall (left) and top wall (right). 142

4.23 Streamwise velocity profile at two different sections for different lengths. $x/h_{in} = 2.8$ (left) and $x/h_{in} = 4.6$ (right). 142

4.24 Eigenspectra comparison for different diffuser length. 144

4.25 Real part of the mode at $St = 0.09$ for the case at $L = L_3$. Streamwise and wall-normal velocity (left), density and modified viscosity (right) 144

4.26 Streamwise velocity contours of the fixed point at different pressure ratios. From top to the bottom: $R_p = 0.72$, $R_{p1} = 0.68$, $R_{p2} = 0.64$, $R_{p3} = 0.60$. 146

4.27 Pressure wall distribution for different pressure ratios. Bottom wall (left) and top wall (right). 146

4.28 Streamwise velocity profile at two different sections for different pressure ratios. $x/h_{in} = 2.8$ (left) and $x/h_{in} = 4.6$ (right). 147

4.29 Eigenspectra comparison for different pressure ratios. 147

4.30 Real part of the mode at $St = 0.17$ for the case at $R_p = R_{p3}$. Streamwise and wall-normal velocity (left), density and modified viscosity (right) 147

5.1 Academic simplified vehicle geometry. 154

5.2 2D representation of the computational grid in $x - y$ plane with a close-up on the 3D nozzle. 155

5.3 A simplified overview of the case under investigation with boundary conditions 156

5.4 A simplified overview of the case under investigation with boundary conditions (close up on the nozzle) 157

5.5 Pressure sensors at three different location. 158

5.6 Contours of streamwise velocity $\tilde{u}$ with streamlines in 3-D (left) and $x - y$ plane (right). 159

5.7 Contours of streamwise velocity $\tilde{u}$ with streamlines in $z - y$ plane at $x = 15D$ (left) and $x - z$ plane (right). 159

5.8 Contours of turbulent kinetic energy k_t (left) and logarithm of turbulent dissipation rate $\tilde{\omega}$ (right) in $x - y$ plane. 160

5.9 Pressure sensors at three different location. 161

5.10 Contours of streamwise velocity $\tilde{u}$ at three different time instances in $x - y$ plane. . . 161

5.11 Contours of turbulent kinetic energy k_t at three different time instances in $x - y$ plane. 161

5.12 Contours of streamwise velocity u_0 of the base flow at $\theta = 10°$ in $x-y$ plane (left) and $z-y$ plane at $x = 15D$ (right). 163

5.13 Contours of the transversal velocity v_0 of the base flow at $\theta = 10°$ (left) and turbulent kinetic energy k_{t0} (right) in $x-y$ plane 163

5.14 Contours of the vorticity component Ω_z of the base flow at $\theta = 10°$ (left) and Mach number M (right)in $x-y$ plane. 164

5.15 Contours of streamwise velocity with streamlines superposed in plane $(x-y)$ 3-D of the base flow at $\theta = 10°$ 165

5.16 Eigenspectrum compared with main URANS frequencies. 166

5.17 Contours of the real part of streamwise velocity $\mathcal{R}(u')$ of the mode at $St = 0.03$ in $x-y$ plane (left) and $z-y$ plane at $x = 15D$ (right). 167

5.18 Contours of the real part of density $\mathcal{R}(\rho')$ of the mode at $St = 0.03$ in $x-y$ plane (left) and $z-y$ plane (right). 167

5.19 Contours of the real part of transversal velocity mode $\mathcal{R}(v')$ at $St = 0.03$ in $x-y$ plane (left) and real part of spanwise velocity $\mathcal{R}(w')$ in $x-z$ plane (right). 168

5.20 Contours of the real part of turbulent kinetic energy $\mathcal{R}(k_t')$ (left) and $z-$ component of vorticity vector $\mathcal{R}(\Omega_z')$ (right) of the mode at $St = 0.03$ in $x-y$ plane 168

5.21 Contours of the real part of streamwise velocity $\mathcal{R}(u')$ of the mode at $St = 0.014$ in $x-y$ plane (left) and $z-y$ plane (right). 169

5.22 Contours of the real part of density $\mathcal{R}(\rho')$ of the mode at $St = 0.014$ in $x-y$ plane (left) and $z-y$ plane (right). 169

5.23 Contours of the real part of transversal velocity mode $\mathcal{R}(v')$ at $St = 0.014$ in $x-y$ plane (left) and real part of spanwise velocity $\mathcal{R}(w')$ in $x-z$ plane (right). 170

5.24 Contours of the real part of turbulent kinetic energy $\mathcal{R}(k_t')$ (left) and $z-$ component of vorticity vector $\mathcal{R}(\Omega_z')$ (right) of the mode at $St = 0.014$ in $x-y$ plane 170

5.25 A streamline of length L_s originating at $(0,0,0)$ with its respective normal planes. The opaque contours in the planes represent the distance from the streamline. 171

5.26 In the left frame tangential velocity contours u_t on the plane at $s/L_s = 0.16$. The portion of the curve n that is perpendicular to the current line is shown in white with a dotted line. In the frame on the right, a plot of the tangential velocity relative to this curve is shown. 172

5.27 In the left frame tangential velocity contours u_t on the plane at $s/L_s = 0.50$. The portion of the curve n that is perpendicular to the current line is shown in white with a dotted line. In the frame on the right, a plot of the tangential velocity relative to this curve is shown. 172

5.28 In the left frame tangential velocity contours u_t on the plane at $s/L_s = 0.83$. The portion of the curve n that is perpendicular to the current line is shown in white with a dotted line. In the frame on the right, a plot of the tangential velocity relative to this curve is shown. 173

5.29 Profile of second derivative $D_2(u_t)$ and module of pressure perturbation $|p'|$ for the mode at $St = 0.03$ in planes $s/L_s = 0.16$ (left), $s/L_s = 0.5$ (center) and $s/L_s = 0.83$ (right). 173

5.30 Profile of second derivative $D_2(u_t)$ and module of pressure perturbation $|p'|$ for the mode at $St = 0.014$ in planes $s/L_s = 0.16$ (left), $s/L_s = 0.5$ (center) and $s/L_s = 0.83$ (right). 173

5.31 Profile of real part of tangential velocity perturbation $\mathcal{R}(u'_t)$ for the mode ad $St = 0.03$ in planes $s/L_s = 0.16$ (left), $s/L_s = 0.5$ (center) and $s/L_s = 0.83$ (right). 174

5.32 Profile of real part of tangential velocity perturbation $\mathcal{R}(u'_t)$ for the mode ad $St = 0.014$ in planes $s/L_s = 0.16$ (left), $s/L_s = 0.5$ (center) and $s/L_s = 0.83$ (right). 174

5.33 A streamline originating at $(0, 0, 0)$ with multiple normal planes superposed. Each plane depicts the contours of the tangential component of vorticity of the fixed point. 175

5.34 A streamline originating at $(0, 0, 0)$ with multiple normal planes superposed. Each plane depicts the contours of the tangential component of vorticity of the perturbation. Mode at $St = 0.03$ (left), mode at $St = 0.014$ (right). 175

5.35 Contours of the real part of streamwise velocity $\mathcal{R}(u')$ (left) and of the divergence $\nabla \cdot \mathcal{R}(u')$ of the mode at $St = 0.03$ in $x - y$ plane with streamlines superimposed . . . 176

5.36 Left: Mach number contours with isolines of the real part of the streamwise velocity for the mode at $St = 0.03$ (green for positive and yellow for negative), with the streamline passing through the perturbation superimposed and the normal axis n shown as a dashed line . Right: Profile of the tangential velocity u_t relative to the dashed axis in the figure on the left 176

5.37 Different planes normal to the central streamline (left) and Görtler number computed for each plane. 177

5.38 Representation of the self-sustaining mechanism. 178

A.1 Comparison of wall pressure distribution. Bottom wall (left) , top wall (right) 206

A.2 Comparison of Streamwise velocity profile at two different sections. $x/h_{in} = 2.8$ (left) , $x/h_{in} = 4.6$ (right) 206

A.3 Turbulence model comparison of wall pressure distribution. Bottom wall (left) , top wall (right) 207

A.4 Turbulence model comparison of streamwise velocity profile at two different sections. $x/h_{in} = 2.8$ (left) , $x/h_{in} = 4.6$ (right) 208

A.5 Eigenspectrum compared with experimental frequency and numerical frequency of reference 208

A.6 Real part of the mode at $St = 0.86$ for the case at $R_p = 0.72$. Streamwise and wall-normal velocity (left), density and modified viscosity (right) 208

A.7 Real part of the mode at $St = 1.7$ for the case at $R_p = 0.72$. Streamwise and wall-normal velocity (left), density and turbulent eddy viscosity (right) 209

B.1 Comparison between reference solution and wall law results (test 1) of friction coefficient (left), turbulent viscosity (center) and inner velocity (right) profiles. 213

B.2 Comparison between reference solution and wall law results (test 2) of friction coefficient (left), turbulent viscosity (center) and inner velocity (right) profiles. 214

B.3 Comparison between reference solution and wall law results (test 3) of friction coefficient (left), turbulent viscosity (center) and inner velocity (right) profiles. 214

Introduction

The design of modern aerospace vehicles and propulsion systems requires a thorough understanding of turbulent and compressible flows. Due to the high speeds and characteristic dimensions involved, flows in the aeronautical and space sectors are typically characterized by high Reynolds numbers and transonic or supersonic Mach numbers. Under these conditions, the interaction between turbulence and compressibility effects, such as the presence of shock waves, gives rise to highly complex fluid dynamic phenomena. From an engineering perspective, significant difficulties arise during the design phase, as these issues must be taken into account, particularly when they involve the onset of non-stationary behaviour.

Several canonical and industrial flow configurations exhibit this complex interplay of high Reynolds number, compressibility, and unsteadiness. Among the most investigated cases are the flow patterns within the nozzles . The main operating parameter is the ratio between the combustion chamber total pressure and the ambient static pressure ($p_{c,0}/p_a$), commonly known as Nozzle Pressure Ratio (NPR). Nozzles operate in distinct regimes defined by the ratio of exit pressure (at the nozzle lip) to ambient pressure p_e/p_a. If the exit pressure is higher than the ambient pressure, the gas continues to expand violently outside the nozzle in supersonic exhaust plumes, the nozzle is under-expanded. On the contrary, when the ambient pressure exceeds the nozzle exit pressure, an internal adverse pressure gradient triggers oblique shock waves inside divergent sections often accompanied by a separation of the turbulent boundary layer. This operating state is referred to as "over-expanded." Under certain conditions, this separation can be highly unsteady, subjecting the divergent to fluctuating and asymmetrical pressure forces commonly referred to as side loads [6]-[7]. Two regimes of separated over-expanded flow can be distinguished: Free Shock Separation (FSS) and Restricted Shock Separation (RSS), depending on the nozzle pressure ratio or the geometry under consideration . In the FSS regime, the flow does not reattach, and at the separation point the pressure rises abruptly to a plateau value p_p and then increases slowly up to the external pressure p_e. In the RSS regime, however, the flow reattaches, causing an irregular pressure trend that can even reach values higher than the external pressure before stabilising [8]. In the FSS regime, side loads are caused by an oscillation of the shock wave within the nozzle; furthermore, a peak in these loads has been observed during the transition from FSS to RSS [9]. These forces can cause deformation of the divergent or significant stress on the engine positioning system and are therefore one of the limiting factors in the design of high expansion ratio engines[10].

Whilst rocket nozzles are responsible for expanding the flow to generate thrust, another non-steady and undesirable phenomenon affects supersonic air intakes. When operating under subcritical conditions (i.e. the engine requires less flow rate than is entering), the shock wave present in the divergent section of the air intake is expelled due to the back pressure that builds up. The interaction of the shock wave with the boundary layer causes flow separation, which chokes the diffuser. The engine continues to draw in air, the pressure drops again and the shock is drawn back into the duct. This low-frequency cycle is commonly known as 'buzz' [11]-[12] and results in both a loss of efficiency and the formation of cyclic stress that can damage the structure. In this context, the experimental [13]-[14]-[15]-[16]-[17]-[18] and numerical [19]-[20]-[21]-[22]-[23] campaign carried out by Sajben and colleagues, in which the interaction between shock waves and the boundary layer within diffusers is isolated, is particularly well known and will be detailed in the dedicated chapter.

Among other phenomena involving supersonic turbulent flows is the jet noise. In the case of supersonic, turbulent jets, large turbulent structures are the main source of noise; furthermore, in the case of 'imperfectly' expanded jets, in which the classic shock cell structure forms, two additional noise components are introduced: the screech tone and broadband shock-associated noise [24]. Powell [25] was the first to identify the screech phenomenon: a disturbance triggers Kelvin-Helmholtz instability ; the vortices propagating downstream interact with the shock cell structure; this interaction is the source of acoustic waves that travel upstream to the nozzle lips, once again disturbing the mixing layer and closing the feedback loop . When the jet emits a strong screech tone, the flow undergoes significant oscillations that depend on the jet's Mach number [26]; consequently, the occurrence of the screech not only causes sonic fatigue problems but also results in thermal loads that place stress on the structure.

One does not need to reach supersonic Mach numbers to encounter dangerous non-stationary phenomena; in fact, the evolution of a transonic flow around an airfoil is just as interesting. Due to the shape of the airfoil, the flow accelerates, leading to the formation of shock waves. The interaction between the shock and the boundary layer on the suction side causes flow separation; the shock takes on the classic lambda pattern and a recirculation bubble is observed at the foot of the shock. When the angle of attack then exceeds the critical value, the shock wave oscillates periodically at a low frequency and high amplitude; this mechanism is commonly known as 'buffet' and, when coupled with the structural mode, causes the buffeting of the structure [27]. This phenomenon, which has been

studied experimentally since the 1950s [28], is very dangerous as it does not require external energy to be sustained, but is maintained through a feedback loop.

The scenario described above is but a glimpse of a very rich and complex panorama involving compressible turbulent flows in aerospace applications. However, despite the different geometries and engineering applications involved, all the phenomena described share a defining physical characteristic: the emergence of low-frequency dynamics dominated by large-scale structures. When studying these applications, the high Reynolds number makes the use of LES approaches very complex and renders the use of DNS computationally prohibitive; however, precisely because of the low-frequency dynamics, a URANS approach remains an excellent compromise between reduced computational costs and the achievable physical insights. Furthermore, if the difference between the turbulence timescale T_1 and the unsteadiness timescale T_2 is of a few orders of magnitude, and if the time horizon T over which the Reynolds average is defined is such that $T_1 << T << T_2$, then the URANS approach allows us to observe part of the non-stationary dynamics.

In order to study the mechanisms underlying these non-stationary phenomena driven by coherent structures, the fluid dynamics community has, in recent years, turned its attention increasingly to the tools of linear stability theory. Historically, however, this theory was employed for a different purpose: to predict the transition from laminar to turbulent flow [29]. Stability analysis involves studying the asymptotic behaviour over time of a perturbation; in practical terms, this comes down to studying the signs of the eigenvalues of the Jacobian operator of the linearised system under consideration. To solve for the eigenvalues numerically, researchers in the past had to adapt to the computational resources available at the time. Indeed, the earliest stability studies were based on the Orr–Sommerfeld equations [30]-[31], which are simplified one-dimensional equations obtained by considering a single inhomogeneous direction of flow; Orszag's work [32] on channel flow was pioneering in this regard, having calculated a critical Reynolds number $Re = 5772.23$ at which the flow ceases to be linearly asymptotically stable. Over time, computational resources have increased. This has made it possible to relax the assumption of parallel flows and consider two-dimensional cases such as the flow around a cylinder [33]-[34], the flow in a lid-driven cavity [35] or backward facing step [36]. The aforementioned work therefore falls within what is known as *global* stability analysis [37]. In this case, the flow can behave in two ways: either as an oscillator – that is, it has at least one unstable eigenvalue and imposes its intrinsic dynamics – or as a selective noise amplifier, in which case it has no unstable eigen-

values and merely filters and amplifies external noise. Although systems of this second type exhibit asymptotically stable behaviour, due to the non-normal nature of the operator they may experience pseudo-resonance, that is, manifest a strong response to a certain excitation [38]. In this context, it is far more interesting to carry out the resolvent analysis, which allows us to evaluate the optimal forcing that enables maximum energy amplification of the system and the corresponding response.
As mentioned earlier, in recent years linear stability analysis has also been used to analyse the mechanisms driving unsteady phenomena, and this also applies to flows that are already turbulent. In this case, however, identifying a base flow around which to linearise the equations becomes more challenging.
The approach adopted in this thesis is based on a triple decomposition, as described in [39]. A periodic signal $f(x,t)$ in a turbulent flow field can in fact be divided into three components as follows:

$$f(x,t) = \overline{f}(x) + f'(x,t) + f''(x,t) \tag{1}$$

where $\overline{f}(x)$ represents the infinite-time average , $f'(x,t)$ the coherent motion term, and $f''(x,t)$ the incoherent turbulent term. When we apply a URANS approach, we use the Boussinesq approximation to model only the term related to turbulence; and when we move on to the linear stability analysis, we superimpose a coherent perturbation $\epsilon f'(x,t)$ – the dynamics of which we wish to study – onto the time-independent solution $\overline{f}(x)$. Two things are clear: firstly, this approach is suitable for scenarios where the timescales involved differ significantly, meaning that the low-frequency dynamics do not depend on turbulence; secondly, within the range of applicability of this approach, the base flow to be used coincides with the RANS solution.
Crouch was the first to propose this global stability framework for turbulent and compressible flows [40]-[41]. In his seminal work, he predicted the onset of buffet on a NACA0012 airfoil for $Re = 10^7$ with the Spalart-Allmaras model. For a Mach number $M = 0.76$, he found a critical angle of attack $\theta = 3.03°$; the results were then compared with McDevitt's [42] experimental data, demonstrating the ability of stability analysis to accurately predict the onset of unsteadiness for different values of M. Following on from the previous work, a series of further studies on buffet were carried out. Iorio *et al.* [43] continued Crouch's work on the same airfoil profile and using the same turbulence model, but employing a finite-volume approach. In addition to the global stability analysis, they also calculated the structural sensitivity, showing that the most sensitive region of the flow is the area at the base of the shock where it interacts with the boundary layer. Furthermore, they performed a 3D

study of the same extruded profile in the spanwise direction, noting that the phenomenon remains largely two-dimensional. The following year, Sartor *et al* [5] presented a global stability study on the supercritical OAT15 profile, again using the Spalart-Allmaras model. For this profile, the onset of instability occurs at an angle of attack $\theta = 3.5°$, in agreement with Deck's previous ZDES [44] and with the critical value of $\theta = 3.25°$ found experimentally by Jacquin [45]. Furthermore, a resolvent analysis was also conducted, revealing a second peak in energy gain at higher frequencies associated with a Kelvin–Helmholtz-type instability. The first attempt to create a fully 3D wing was carried out by Timme & Thormann [46], but no globally unstable mode was observed due to a lack of convergence in the base flow; however, this was merely a testing ground for the 2018 work [47], in which an unstable mode was identified, the spatial structure of which resembled high-frequency buffet cells.

Later, Crouch [48] also analysed the case of unswept and swept 3D wings, but using a different approach known as *quasi-3D* (i.e. the z-direction gradients of the base flow are set to zero). He noted that, in the unswept case compared with classical 2D buffet, two new zero-frequency modes emerge: one at medium wavelength and one at short wavelength. When the wing is swept, the 2D buffet mode retains its low frequency and propagates inboard, whilst the medium-wavelength mode begins to oscillate at a very high frequency—comparable to that observed in experiments—and propagates outboard along the wing. Similar results were obtained by Paladini *et al.* [49], who also carried out a structural sensitivity analysis, pointing out that the centre of the instability shifts from the shock foot in the 2D case to the recirculation zone in the 3-D case.

Although the buffet problem dominates the field of global stability of turbulent and compressible flows, it is not the only one addressed. In 2014, Mettot [50] investigated flow over an open cavity, using not only the Spalart-Allmaras model but also Wilcox's k-ω model; several unstable modes were identified relating to Kelvin–Helmholtz instabilities and acoustic resonance modes. The next year, Sartor [51] studied the interaction between a shock and the boundary layer in a transonic flow over a bump. In this case, no global instability was identified, but through a resolvent analysis he was able to determine that the flow amplifies the medium and low frequencies associated, respectively, with the motion of the shock and the mixing-layer instability. More lately, again in the context of shock-turbulent boundary layer interaction – though this time concerning flow over a ramp – Hao [52], using a global stability analysis approach, determined the critical angle of the ramp at which a global instability occurs at zero frequency. Also recently, Franchini's PhD thesis [53] was published,

in which he examined the phenomenon of screech in turbulent jets using a full 3-D global stability analysis (GSA) with a time-stepper approach.

Over the last two decades, therefore, global stability analysis has established itself as an invaluable tool for the prediction and study of complex unsteady phenomena in compressible turbulent flows. This thesis follows in the footsteps of recent literature, with a twofold objective. Firstly, it aims to develop a dedicated numerical tool (in-house tool) for stability analysis, capable of adapting efficiently to both computationally light configurations (2-D or quasi-3-D) and industrial geometries with high computational costs (full 3-D). Secondly, this numerical framework will be used to investigate the dynamics of two case studies of primary interest for modern aerospace applications.

The tool is called *dNami* [54] and was developed by Nicolas Alferez. Through a DSL (Domain-Specific Language), it enables the solution of systems of balance equations in an HPC environment. The numerical framework is detailed in Chapter 2; what is important to emphasise here is its dual functionality: namely, dNami, when coupled with TAPENADE [55]—an automatic differentiation tool—provides easy access to a linearised source code (*liNami*). At this stage, time-stepper methodologies have been implemented, which are necessary for problems with a high number of degrees of freedom, for global stability analysis: fixed-point calculation using Newton-Krylov method and eigenvalue calculation using Krylov-Schur method. In parallel, it is also possible to perform direct extraction of the Jacobian matrix for problems with a limited number of degrees of freedom using a colouring technique [56] similar to that presented in [57]. From a code development perspective, I was responsible for implementing and validating the turbulence modelling component and for incorporating the algorithms required for Jacobian matrix extraction. Various validation tests and comparisons between the two methods – time-stepping and matrix-forming – were carried out wherever possible. The first case considered is the Sajben diffuser mentioned at the beginning. Following the experimental and numerical study, some questions remained unanswered regarding the non-stationary nature of the interaction between the shock and the boundary layer within the diffuser; for this reason, it is of interest to analyse this geometry using an approach different from that employed in the past, namely a linear stability approach. Given that, experimentally, suction slots were inserted inside the diffuser to render the flow field two-dimensional, this case has always been treated numerically as 2-D in the literature and is therefore well suited to a matrix-forming approach involving the extraction of the Jacobian. The second flow configuration considered, on the other hand, is a turbulent jet impacted by a counterflow

at a variable angle of attack. Unlike the previous case, this is a fully three-dimensional scenario and allows for the reproduction of the final landing phase of reusable vehicles, during which the engines are re-ignited. Previous numerical simulations have shown that in this configuration, for a counterflow at Mach $M = 0.8$, low-frequency oscillations of the jet occur above a certain angle of attack; it is therefore very interesting to attempt to predict these using a global stability approach.

The manuscript is structured as follows: Chapter one describes the theoretical section, focusing first on turbulence modelling and then on global stability analysis and resolvent analysis. The topic of base flow is also revisited, presenting other approaches found in the literature. Chapter two, on the other hand, describes the numerical framework, discussing the methods implemented for both the non-linear and linear aspects, and demonstrates how to extract the matrix in dNami using the Burger equation as an example. Chapter three presents the validation tests. Flow around a cylinder and a lid-driven cavity are discussed as validation test cases for stability analysis using both the time-stepper and matrix-forming methods; next, the case of the turbulent boundary layer is examined, which enabled the validation of the turbulence modelling; finally, the case of buffet on an OAT15 airfoil is presented to validate the stability analysis on a turbulent case. Chapter Four discusses the first case, namely the Sajben diffuser, analysed using both the time-stepper and matrix methods. A global stability and resolvent analysis are carried out on this geometry, solved in $2D$ and $2.5D$, followed by a parametric study involving variations in the nozzle length and the ratio between the static outlet pressure and the isentropic stagnation pressure at the inlet. Chapter five, on the other hand, deals with the counter-current jet case The results of the URANS simulations are presented for the case with no angle of incidence and for the case with an angle of incidence of $\theta = 10°$; subsequently, the results of the global stability analysis for the case with $\theta = 10°$ are shown, and the main unstable modes identified are discussed. Finally, the conclusions and perspectives for future work are presented.

Chapter 1

Theoretical formulation

Contenu

1.1 Governing equations 30
1.1.1 Navier-Stokes equations 30
1.1.2 Curvilinear Navier-Stokes equations 32
1.2 Turbulence Modelling 35
1.2.1 Features of turbulence 35
1.2.2 Scales of turbulence 38
1.2.3 Reynolds Average Navier-Stokes equations. 40
1.2.4 Spalart-Allmaras one-equation model 44
1.2.5 k-ω SST two-equation model 46
1.3 Stability analysis 49
1.3.1 Modal stability analysis 49
1.3.2 Non modal stability analysis 52
1.3.3 On the choice of the base flow 54

1.1 Governing equations

1.1.1 Navier-Stokes equations

The equations describing the behaviour of a Newtonian fluid, i.e. a fluid in which the deformation velocity and stress tensor are linked by a linear relationship, are commonly known as the Navier-Stokes equations. In the general case of a compressible fluid, they consist of one mass conservation equation, three momentum balance equations, and one energy conservation equation. In a Cartesian reference system and in differential form, the equations read:

$$\begin{cases} \dfrac{\partial \rho^*}{\partial t^*} + \boldsymbol{\nabla} \cdot (\rho^* \boldsymbol{u}^*) = 0, \\ \dfrac{\partial \rho^* \boldsymbol{u}^*}{\partial t^*} + \boldsymbol{\nabla} \cdot (\rho^* \boldsymbol{u}^* \boldsymbol{u}^*) = -\boldsymbol{\nabla} p^* + \rho^* \boldsymbol{f}^* + \boldsymbol{\nabla} \cdot \boldsymbol{\tau}^*, \\ \dfrac{\partial \rho^* E^*}{\partial t^*} + \boldsymbol{\nabla} \cdot (\rho^* E^* \boldsymbol{u}^* + p \boldsymbol{u}^*) = \rho^* \boldsymbol{f}^* \cdot \boldsymbol{u}^* + \boldsymbol{\nabla} \cdot (\boldsymbol{\tau}^* \cdot \boldsymbol{u}^*) - \boldsymbol{\nabla} \cdot \boldsymbol{Q}^*, \end{cases} \tag{1.1}$$

where the superscript ' * ' denotes dimensional quantities, namely: density ρ^*, velocity vector $\boldsymbol{u}^* = (u^*, v^*, w^*)^T$, pressure p^*, volume forces $\boldsymbol{f}^*$, stress tensor $\boldsymbol{\tau}^*$, total energy $E^* = e^* + 1/2(u^*u^* + v^*v^* + w^*w^*)$, heat flux $\boldsymbol{Q}^*$ and time t^*. As it stands, the system cannot be resolved due to too many unknowns and must therefore be closed using several hypotheses.

In this thesis, air at a temperature that is not too high will be considered, therefore the assumptions of a thermally and calorically perfect gas can be made. For a thermally perfect gas:

$$p^* = \rho^* R^* T^*, \tag{1.2}$$

where T^* is the temperature and $R^* = 287.05\ J/(kgK)$ is the specific gas constant for the air, while for a calorically perfect:

$$e^* = C_v^* T^*, \qquad\qquad h^* = C_p^* T^*, \tag{1.3}$$

where C_v^* and C_p^* are respectively the specific heat at constant volume and constant pressure and they are constants ($C_v^* = 717.85\ J/(kgK)$, $C_p^* = 1005\ J/(kgK)$ for air) while e^* is the internal energy and h^* is the enthalpy. For a Newtonian fluid such as air, Stokes' relation can be used to determine the stress tensor, which reads

$$\boldsymbol{\tau}^* = 2\mu^* \left(\boldsymbol{S}^* - \frac{1}{3} (\boldsymbol{\nabla} \cdot \boldsymbol{u}^*) \boldsymbol{I} \right), \qquad\qquad \boldsymbol{S}^* = \frac{1}{2} \left(\boldsymbol{\nabla} \boldsymbol{u}^* + \boldsymbol{\nabla} \boldsymbol{u}^{T*} \right), \tag{1.4}$$

where μ^* is the molecular viscosity, and $\boldsymbol{S}^*$ is the symmetric part of the velocity gradient. In order to compute the molecular viscosity, the Sutherland law can be applied for a wide range of temperature [58]:

$$\mu^*(T^*) = \mu_{ref} \left(\frac{T^*}{T_{ref}} \right)^{\frac{3}{2}} \frac{(T_{ref} + S)}{(T^* + S)}, \tag{1.5}$$

with $\mu_{ref} = 1.716 \times 10^{-5}\ kg/(ms)$, $T_{ref} = 273.15\ K$, $S = 110.4\ K$. Finally, to describe heat flux, Fourier's law is used, which links heat to the temperature gradient as follows:

$$\boldsymbol{Q}^* = -\lambda \boldsymbol{\nabla} T^*, \tag{1.6}$$

where λ is the thermal conductivity, which can be computed using the Prandtl number. $Pr = C_p \mu / \lambda = 0.72$ for air at a low temperature [59].

At this point, the system is closed and can be solved numerically, but it is generally preferable to rewrite it in dimensionless form. This improves the numerical stability (there are no values that are excessively high or low) and allows the physics under consideration to be described using characteristic dimensionless parameters. There are several possible choices for dimensionless equations. The important aspect to keep in mind is that the thermodynamic state of the system depends on two quantities, and the subsequent ones will be automatically determined based on the assumptions made previously. If the following reference values are set:

$$\boldsymbol{u} = \frac{\boldsymbol{u}^*}{U_{ref}}, \qquad \rho = \frac{\rho^*}{\rho_{ref}}, \qquad T = \frac{T^*}{T_{ref}}, \qquad x = \frac{x^*}{L_{ref}}, \qquad p = \frac{p^*}{\rho_{ref} U_{ref}^2}, \qquad t = \frac{t^* U_{ref}}{L_{ref}}, \tag{1.7}$$

the system becomes :

$$\begin{cases} \dfrac{\partial \rho}{\partial t} + \boldsymbol{\nabla} \cdot (\rho \boldsymbol{u}) = 0, \\ \dfrac{\partial \rho \boldsymbol{u}}{\partial t} + \boldsymbol{\nabla} \cdot (\rho \boldsymbol{u}\boldsymbol{u}) = -\boldsymbol{\nabla} p + \rho \boldsymbol{f} + \boldsymbol{\nabla} \cdot \boldsymbol{\tau}, \\ \dfrac{\partial \rho E}{\partial t} + \boldsymbol{\nabla} \cdot (\rho E \boldsymbol{u} + p \boldsymbol{u}) = \rho \boldsymbol{f} \cdot \boldsymbol{u} + \boldsymbol{\nabla} \cdot (\boldsymbol{\tau} \cdot \boldsymbol{u}) - \boldsymbol{\nabla} \cdot \boldsymbol{Q}, \end{cases} \tag{1.8}$$

Although the system retains the same form, dimensionless parameters appear within the various terms:

$$\boldsymbol{\tau} = 2 \frac{\mu}{Re} \left(\boldsymbol{S} - \frac{1}{3} (\boldsymbol{\nabla} \cdot \boldsymbol{u}) \boldsymbol{I} \right), \tag{1.9}$$

where μ is computed through the dimensionless form of Sutherland law:

$$\mu = (T)^{\frac{3}{2}} \frac{(1 + S)}{(T + S)}, \tag{1.10}$$

and Re is the Reynolds number based on reference parameter:

$$Re = \frac{\rho_{ref} U_{ref} L_{ref}}{\mu_{ref}}, \tag{1.11}$$

while dimensionless specific heats can be written as:

$$C_v = \frac{1}{M^2 \gamma(\gamma - 1)}, \qquad C_p = \frac{1}{M^2(\gamma - 1)}, \tag{1.12}$$

where $\gamma = C_p/C_v$, M is the Mach number defined as:

$$M = U_{ref}/c_{ref}, \tag{1.13}$$

and c_{ref} is the sound of speed computed with respect to reference values:

$$c_{ref} = \sqrt{\frac{\gamma p_{ref}}{\rho_{ref}}}. \tag{1.14}$$

Finally the dimensionless heat flux becomes:

$$\boldsymbol{Q} = \frac{C_p \mu}{PrRe} \boldsymbol{\nabla} T = \frac{\mu}{PrReM^2(\gamma - 1)} \boldsymbol{\nabla} T. \tag{1.15}$$

1.1.2 Curvilinear Navier-Stokes equations

The system of equations (1.8) can be rewritten in strong conservative form [60] by explicitly showing the convective and viscous flows as follows in a Cartesian coordinate system (x, y, z)

$$\frac{\partial \mathbf{q}}{\partial t} + \frac{\partial \mathbf{f}}{\partial x} + \frac{\partial \mathbf{g}}{\partial y} + \frac{\partial \mathbf{h}}{\partial z} = \frac{\partial \mathbf{f_v}}{\partial x} + \frac{\partial \mathbf{g_v}}{\partial y} + \frac{\partial \mathbf{h_v}}{\partial z}, \tag{1.16}$$

$$\mathbf{q} = \begin{bmatrix} \rho \\ \rho u \\ \rho v \\ \rho w \\ \rho E \end{bmatrix}, \qquad \mathbf{f} = \begin{bmatrix} \rho u \\ \rho uu + p \\ \rho uv \\ \rho uw \\ (\rho E + p)u \end{bmatrix}, \qquad \mathbf{g} = \begin{bmatrix} \rho v \\ \rho vu \\ \rho vv + p \\ \rho vw \\ (\rho E + p)v \end{bmatrix}, \qquad \mathbf{h} = \begin{bmatrix} \rho w \\ \rho wu \\ \rho wv \\ \rho ww + p \\ (\rho E + p)w \end{bmatrix}, \tag{1.17}$$

$$\mathbf{f_v} = \begin{bmatrix} 0 \\ \tau_{xx} \\ \tau_{yx} \\ \tau_{zx} \\ \beta_x \end{bmatrix}, \qquad \mathbf{g_v} = \begin{bmatrix} 0 \\ \tau_{xy} \\ \tau_{yy} \\ \tau_{zy} \\ \beta_y \end{bmatrix}, \qquad \mathbf{h_v} = \begin{bmatrix} 0 \\ \tau_{xz} \\ \tau_{yz} \\ \tau_{zz} \\ \beta_z \end{bmatrix}. \tag{1.18}$$

In this formulation, all terms related to volume forces have been omitted, as they will not be taken into consideration in the rest of this work, and $\boldsymbol{\beta}$ is the total heat flux, moreover the subscript 'v'

stands for *viscous*. The system expressed in this form can only be solved numerically in the case of uniform Cartesian grids. In order to consider flow configurations with complex geometries, boundary layers, etc., it is necessary to introduce a curvilinear coordinate transformation $(x, y, z) \Rightarrow (\xi, \eta, \zeta)$.

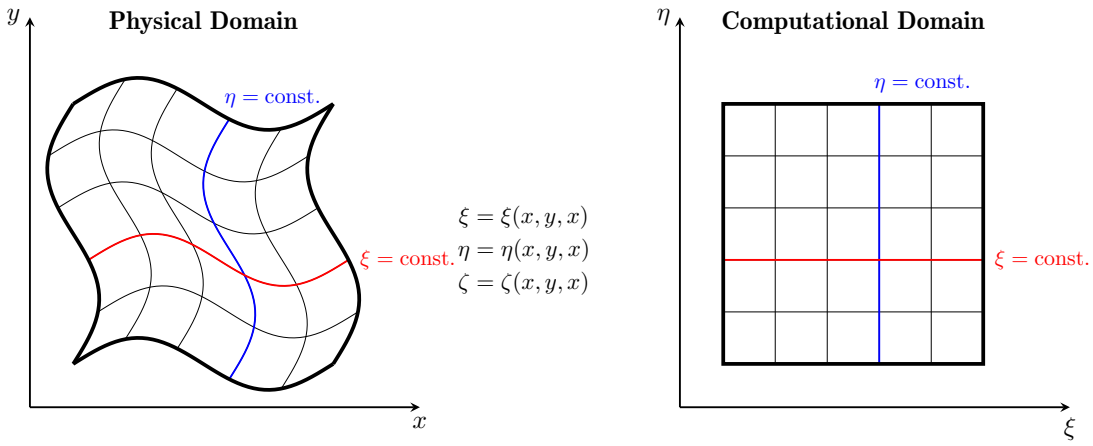


Figure 1.1: Simplified 2D representation of the physical domain (x, y, z) and the computational domain (ξ, η, ζ).

Figure (1.1) shows a complex geometry mesh both within the physical domain and in the computational domain, where $\Delta\xi = \Delta\eta = \Delta\zeta = 1$. Relations (1.19) and (1.20) describe the transformation into curvilinear coordinates and its inverse, respectively:

$$\begin{bmatrix} dx \\ dy \\ dz \end{bmatrix} = \underbrace{\begin{bmatrix} x_\xi & x_\eta & x_\zeta \\ y_\xi & y_\eta & y_\zeta \\ z_\xi & z_\eta & z_\zeta \end{bmatrix}}_{A} \begin{bmatrix} d\xi \\ d\eta \\ d\zeta \end{bmatrix}, \tag{1.19}$$

$$\begin{bmatrix} d\xi \\ d\eta \\ d\zeta \end{bmatrix} = \underbrace{\begin{bmatrix} \xi_x & \xi_y & \xi_z \\ \eta_x & \eta_y & \eta_z \\ \zeta_x & \zeta_y & \zeta_z \end{bmatrix}}_{B} \begin{bmatrix} dx \\ dy \\ dz \end{bmatrix}, \tag{1.20}$$

where, in this case, the various subscripts indicate the partial derivatives.

If we consider the derivative of a generic variable f it is written using the chain rule as:

$$f_x = f_\xi \xi_x + f_\eta \eta_x + f_\zeta \zeta_x. \tag{1.21}$$

It is clear that it is necessary to define the terms $\xi_x, \eta_x, \zeta_x, \ldots$ commonly known as metrics, with respect to the computational domain; therefore, it is necessary to invert the transformation matrix A.

After a few algebraic steps , it can be proven that:

$$\begin{bmatrix} d\xi \\ d\eta \\ d\zeta \end{bmatrix} = J \underbrace{\begin{bmatrix} (y_\eta z_\zeta - y_\zeta z_\eta) & (x_\zeta z_\eta - x_\eta z_\zeta) & (x_\eta y_\zeta - x_\zeta y_\eta) \\ (y_\zeta z_\xi - y_\xi z_\zeta) & (x_\xi z_\zeta - x_\zeta z_\xi) & (x_\zeta y_\xi - x_\xi y_\zeta) \\ (y_\xi z_\eta - y_\eta z_\xi) & (x_\eta z_\xi - x_\xi z_\eta) & (x_\xi y_\eta - x_\eta y_\xi) \end{bmatrix}}_{A^{-1}} \begin{bmatrix} dx \\ dy \\ dz \end{bmatrix}, \tag{1.22}$$

where J is the inverse of the determinant of the transformation matrix:

$$J^{-1} = x_\xi(y_\eta z_\zeta - y_\zeta z_\eta) - x_\eta(y_\xi z_\zeta - y_\zeta z_\xi) + x_\zeta(y_\xi z_\eta - y_\eta z_\xi). \tag{1.23}$$

After equating matrix B with inverse matrix A^{-1}, it is therefore possible to obtain the relationships for all metrics as follows [61]:

$$\begin{aligned} \xi_x &= J(y_\eta z_\zeta - y_\zeta z_\eta), & \eta_x &= J(y_\zeta z_\xi - y_\xi z_\zeta), & \zeta_x &= J(y_\xi z_\eta - y_\eta z_\xi), \\ \xi_y &= J(z_\eta x_\zeta - z_\zeta x_\eta), & \eta_y &= J(y_\zeta x_\xi - z_\xi x_\zeta), & \zeta_y &= J(z_\xi x_\eta - z_\eta x_\xi), \\ \xi_z &= J(x_\eta y_\zeta - x_\zeta y_\eta), & \eta_z &= J(x_\zeta y_\xi - x_\xi y_\zeta), & \zeta_z &= J(x_\xi y_\eta - x_\eta y_\xi), \end{aligned} \tag{1.24}$$

Exploiting the metrics thus defined, it is possible to rewrite the system (1.25) with respect to the reference (ξ, η, ζ)

$$\frac{\partial \mathbf{q}}{\partial t} + \frac{\partial \mathbf{F}}{\partial \xi} + \frac{\partial \mathbf{G}}{\partial \eta} + \frac{\partial \mathbf{H}}{\partial \zeta} = \frac{\partial \mathbf{F_v}}{\partial \xi} + \frac{\partial \mathbf{G_v}}{\partial \eta} + \frac{\partial \mathbf{H_v}}{\partial \zeta}, \tag{1.25}$$

$$\mathbf{q} = J^{-1}\begin{bmatrix} \rho \\ \rho u \\ \rho v \\ \rho w \\ \rho E \end{bmatrix}, \qquad \mathbf{F} = J^{-1}\begin{bmatrix} \rho U \\ \rho U u + \xi_x p \\ \rho U v + \xi_y p \\ \rho U w + \xi_z p \\ (\rho E + p)U \end{bmatrix}, \qquad \mathbf{G} = J^{-1}\begin{bmatrix} \rho V \\ \rho V u + \eta_x p \\ \rho V v + \eta_y p \\ \rho V w + \eta_z p \\ (\rho E + p)V \end{bmatrix}, \tag{1.26}$$

$$\mathbf{H} = J^{-1}\begin{bmatrix} \rho W \\ \rho W u + \zeta_x p \\ \rho W v + \zeta_y p \\ \rho W w + \zeta_z p \\ (\rho E + p)W \end{bmatrix}, \qquad \mathbf{F_v} = J^{-1}\begin{bmatrix} 0 \\ \xi_x\tau_{xx} + \xi_y\tau_{xy} + \xi_z\tau_{xz} \\ \xi_x\tau_{yx} + \xi_y\tau_{yy} + \xi_z\tau_{yz} \\ \xi_x\tau_{zx} + \xi_y\tau_{zy} + \xi_z\tau_{zz} \\ \xi_x\beta_x + \xi_y\beta_y + \xi_z\beta_z \end{bmatrix},$$

$$\mathbf{G_v} = J^{-1}\begin{bmatrix} 0 \\ \eta_x\tau_{xx} + \eta_y\tau_{xy} + \eta_z\tau_{xz} \\ \eta_x\tau_{yx} + \eta_y\tau_{yy} + \eta_z\tau_{yz} \\ \eta_x\tau_{zx} + \eta_y\tau_{zy} + \eta_z\tau_{zz} \\ \eta_x\beta_x + \eta_y\beta_y + \eta_z\beta_z \end{bmatrix}, \qquad \mathbf{H_v} = J^{-1}\begin{bmatrix} 0 \\ \zeta_x\tau_{xx} + \zeta_y\tau_{xy} + \zeta_z\tau_{xz} \\ \zeta_x\tau_{yx} + \zeta_y\tau_{yy} + \zeta_z\tau_{yz} \\ \zeta_x\tau_{zx} + \zeta_y\tau_{zy} + \zeta_z\tau_{zz} \\ \zeta_x\beta_x + \zeta_y\beta_y + \zeta_z\beta_z \end{bmatrix}, \tag{1.27}$$

The relation (1.25) is written in strong conservative form; within the new convective fluxes, the

contravariant velocities U, V, W appear, defined as:

$$\begin{aligned} U &= \xi_x u + \xi_y v + \xi_z w, \\ V &= \eta_x u + \eta_y v + \eta_z w, \\ W &= \zeta_x u + \zeta_y v + \zeta_z w. \end{aligned} \tag{1.28}$$

As pointed out by Visbal & Gaitonde [62], the following identities are used in writing the relationship 1.25:

$$\begin{aligned} I_1 &= (J^{-1}\xi_x)_\xi + (J^{-1}\eta_x)_\eta + (J^{-1}\zeta_x)_\zeta = 0, \\ I_2 &= (J^{-1}\xi_y)_\xi + (J^{-1}\eta_y)_\eta + (J^{-1}\zeta_y)_\zeta = 0, \\ I_3 &= (J^{-1}\xi_z)_\xi + (J^{-1}\eta_z)_\eta + (J^{-1}\zeta_z)_\zeta = 0. \end{aligned} \tag{1.29}$$

From a physical and geometric point of view, these three identities constitute a differential statement of surface conservation for a closed cell. However, when moving into the discrete world, if centred finite differences are used (as will be shown to be the case with dNami in the next chapter), these identities are not respected in the case of non-trivial 3D geometries due to the failure of exact cancellation of metrics. To address this problem, Thomas & Lombard [63] proposed a new expression of the metrics in an equivalent conservative form:

$$\begin{aligned} \xi_x &= J(y_\eta z)_\zeta - (y_\zeta z)_\eta, & \eta_x &= J(y_\zeta z)_\xi - (y_\xi z)_\zeta, & \zeta_x &= J(y_\xi z)_\eta - (y_\eta z)_\xi, \\ \xi_y &= J(z_\eta x)_\zeta - (z_\zeta x)_\eta, & \eta_y &= J(z_\zeta x)_\xi - (z_\xi x)_\zeta, & \zeta_y &= J(z_\xi x)_\eta - (z_\eta x)_\xi, \\ \xi_z &= J(x_\eta y)_\zeta - (x_\zeta y)_\eta, & \eta_z &= J(x_\zeta y)_\xi - (x_\xi y)_\zeta, & \zeta_z &= J(x_\xi y)_\eta - (x_\eta y)_\xi. \end{aligned} \tag{1.30}$$

1.2 Turbulence Modelling

Although equations describing Newtonian fluids are available, even for complex geometries, they are not sufficient to numerically solve the main flows of engineering interest, such as those discussed in this work. Due to the high Reynolds number, it is not possible to perform a direct numerical simulation because the ratio between the largest and smallest scales that must be solved is extremely high. Therefore, further modelling based on knowledge of turbulent flows is necessary.

1.2.1 Features of turbulence

At first glance and in general terms the concept of turbulent flow can be understood by contrast, starting with a description of laminar flow. A laminar flow is a flow controlled mainly by viscous

diffusion. It is characterised by a low Reynolds number and regularity in its dynamics. The name laminar, in fact, derives from *laminae*, meaning layers, which is what laminar flow appears to consist of. Consequently, a turbulent flow will be a flow with: a high Reynolds number, where inertia prevails over viscous effects, three-dimensional, multi-scale and highly time-dependent.

Historically, the first written traces of the word turbulence can be found in one of Leonardo da Vinci's works. As early as 1510, in the Codex Leicester, he described the motion of water falling into a pool, noting how smaller vortices were present within larger ones. After Leonardo da Vinci, it was not until 1839 that real physical experiments were conducted, when Hagen carried out his studies on the flow of water through round tubes [64]. He observed that in laminar flow (at lower speeds) the water flowed out of the pipe perfectly and crystal clear, while at higher speeds the water flowed intermittently and was opaque, thus realising that it no longer responded linearly to the increase in pressure in the cylinder. The flow was transitioning in turbulent conditions. During the same period, Poiseuille, studying blood flow, made the identical observations [65].

Finally, in 1883, thanks to Reynolds' work [1], further progress was made in understanding turbulence. In his experiment on pipe flows, he considered pipes of different diameters and water at different temperatures, adding ink to the inlet to observe its behaviour. He noticed that the critical velocity was inversely proportional to the diameter of the pipe used and concluded that the transition to a turbulent flow regime depended not only on velocity but also on a characteristic length of the flow and viscosity combined in the aforementioned Reynolds number.

Afterwards, numerous other experiments were conducted to describe turbulence in configurations different from pipe flow. To mention just a few, there was the discovery of the boundary layer by Prandtl in 1904 [66] or the study of flow around a cylinder by Von Karman in 1911 [67] as well as the study of flow between cylinders with the inner one rotating by Taylor in 1923 [68]. However, as many years have passed, even today there is still no clear definition of turbulence , and it remains one of the unsolved problems of physics. What can be done, however, following in Wilcox's footsteps [3], is to describe the main features of turbulence through the words of leading scientists.

In a lecture Von Karman described turbulence as *an irregular motion which in general makes its appearance in fluids, gaseous or liquid* to point out that a turbulent and non-periodic flow will always be a function of the three coordinates of space and time. Obviously, this definition is not sufficient, and Hinze [69] clarifies in his book that *Turbulent fluid motion is an irregular condition of flow in which*

various quantities show a random variation with time and space coordinate, so that statistically distinct average values can be discerned to explain how, although the instantaneous quantities of a turbulent flow are extremely sensitive to initial conditions, the statistical averages are not, so turbulence can be studied through the laws of probability. The fact that a deterministic system of equations such as

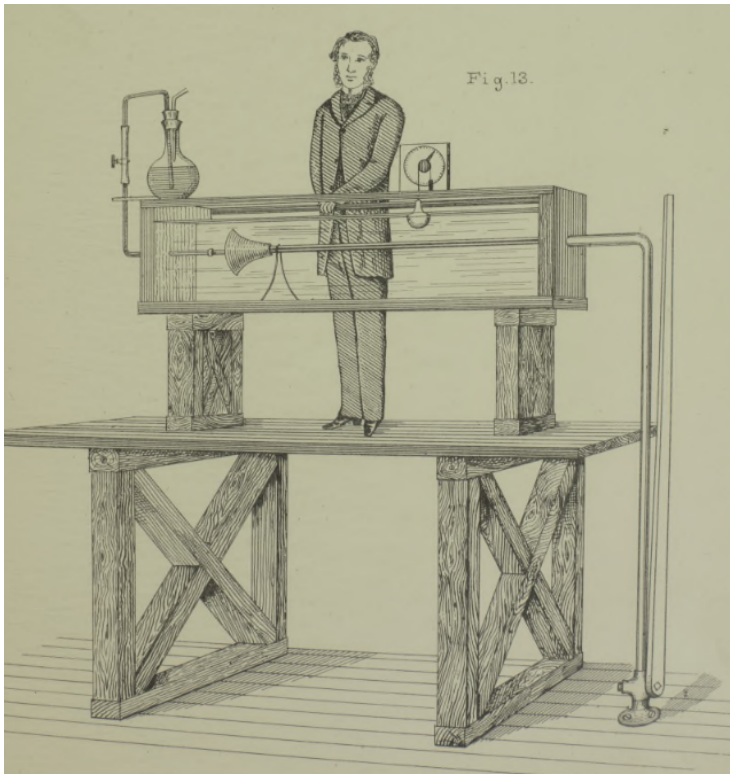


Figure 1.2: Sketch of Reynolds' dye experiment from [1].

Navier-Stokes can give rise to different solutions for fixed initial and boundary conditions may seem paradoxical, however, Lorenz in [70] shows how a system of ordinary differential equations subject to a very small variation in the initial conditions, which can be represented by a truncation error in numerical simulations or the presence of impurities in experiments, can lead to completely different instantaneous solutions.

A further key piece of information for understanding turbulence was added by Richardson, who in 1922 [71] stated *Big whorls have little whorls, which feed on their velocity; and little whorls have lesser whorls and so on to viscosity.* These words encapsulate the concept of energy cascade, whereby kinetic energy is transferred from large vortices to small vortices until molecular viscosity prevails and the

smaller vortices dissipate into heat, meaning that turbulent flows are always dissipative. The concept of scales is also introduced. In fact, a turbulent flow consists of a continuous range of scales that can be seen as vortices of different sizes, starting from the largest scale, which is a characteristic scale of the flow (pipe diameter, boundary layer thickness, etc.), down to the last scale that resists molecular dissipation. Despite the presence of very small scales, Tennekes & Lumley in [72] state that turbulence is a continuum phenomenon, in accordance with the fact that the Navier-Stokes equations are able to capture it. In fact, the Knudsen number calculated with respect to the mean free path and the smallest scale of turbulence is $\ll 1$, ensuring that the continuum assumption is valid.

1.2.2 Scales of turbulence

We mentioned earlier that smaller eddies dissipate due to molecular viscosity, but how can we estimate their scale? Kolmogorov's theory of universal equilibrium [73] provides the answer to this question . Small-scale eddies are independent of the slow dynamics of large scales and the mean flow; therefore, small scales can be considered isotropic. Furthermore, smaller eddies gain kinetic energy at the same rate at which smallest eddies dissipate it, $\epsilon = dk/dt$, where ϵ is precisely the rate of dissipation of turbulent kinetic energy k. Starting from these premises, and using dimensional analysis, one can define velocity scales u_η, length scales l_η and time scales t_η solely in terms of ϵ and the kinematic viscosity ν.

$$u_\eta = (\nu\epsilon)^{\frac{1}{4}}, \qquad l_\eta = \left(\frac{\nu^3}{\epsilon}\right)^{\frac{1}{4}}, \qquad t_\eta = \left(\frac{\nu}{\epsilon}\right)^{\frac{1}{2}}, \tag{1.31}$$

where the subscript η denotes the Kolmogorov or dissipative scales. Since, under equilibrium conditions, the dissipation is equal to the rate at which energy is transferred from the large-scale structures, it is possible to define ϵ in terms of the latter:

$$\epsilon = \frac{U^3}{L}, \tag{1.32}$$

being U and L velocity and length of largest eddies respectively. Now, if we calculate the ratio of L to l_η by substituting the relation (1.32), we obtain:

$$\frac{L}{l_\eta} = \frac{L\epsilon^{\frac{1}{4}}}{\nu^{\frac{3}{4}}} = \frac{LU^{\frac{3}{4}}}{\nu^{\frac{3}{4}}L^{\frac{1}{4}}} = \left(\frac{LU}{\nu}\right)^{\frac{3}{4}} = (Re)^{\frac{3}{4}}. \tag{1.33}$$

This explains why, for high Reynolds numbers turbulent flows, there is a wide range of scales . One can clearly see this aspect in Figure (1.3), which shows a mixing layer at increasing Reynolds numbers

from bottom to top, taken from the work of Brown & Roshko [2]. It is evident that as Re increases, progressively smaller vortical structures can be identified within the larger ones. Understanding the

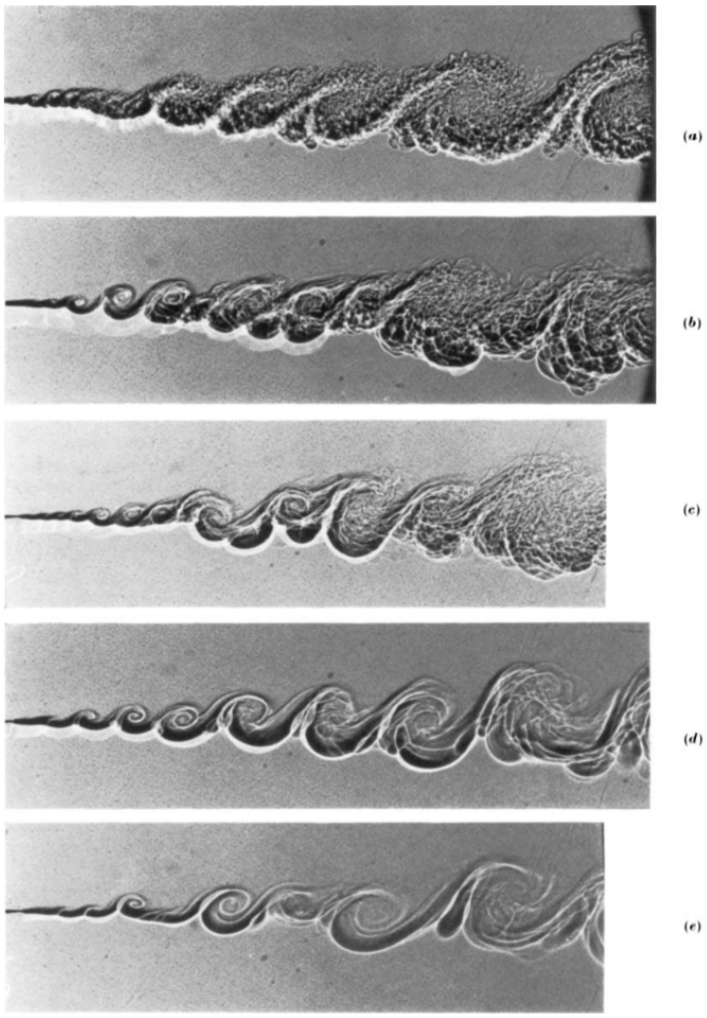


Figure 1.3: Effect of Reynolds number on mixing layers. Figure taken from [2].

scale relationship of turbulence is also of great importance from a numerical perspective. If one wants to carry out 3D simulations in order to capture both the largest and smallest scales, the spatial resolution required would be:

$$\left(\frac{L}{l_\eta}\right)^3 \approx (Re)^{\frac{9}{4}}. \tag{1.34}$$

For engineering flows with high Reynolds numbers, such as those to be discussed in this thesis, it remains impossible even today to perform a direct simulation using the computational resources cur-

rently available. It is therefore necessary to model the effect of the smaller scales without solving them directly; depending on the spatial wavenumber at which one chooses to cut off, different strategies are possible:

- **Direct Numerical Simulation (DNS)**. This method involves solving the equations (1.25) directly, without any cutoff wavenumber. As mentioned above, due to the large number of grid points required, its use is limited to fundamental research into turbulent flows rather than to flows of engineering interest

- **Large Eddy Simulation (LES)** . As the name suggests, only the largest-scale and therefore most energetic eddies are resolved, whilst the smaller ones are modelled. The grids used are therefore unable to capture the small-scale features, and so-called sub-grid models are employed. It remains, however, a rather computationally expensive technique, but it allows for the processing of more complex flows than a DNS.

- **Reynolds Averaged Navier-Stokes (RANS) equation**. There is no cutoff wavenumber, as the averaged Navier-Stokes equations are used. Following the averaging operation, equations similar to the original ones are obtained, with the addition of an extra stress term known as the Reynolds stress tensor, which is responsible for the energy exchange between the mean field and the turbulent scales. With this approach, only the macroscopic scales are resolved and the computational cost is significantly reduced. The procedure for deriving the averaged equations will be detailed below, together with the problems that arise from it.

1.2.3 Reynolds Average Navier-Stokes equations.

In 1895, Reynolds introduced in [74] the decomposition of instantaneous quantities into a mean plus a fluctuating part. Various types of averages are relevant: ensemble average, spatial average and temporal average, but we consider only the latter. Generally, for a variable $f(\boldsymbol{x}, t)$:

$$f(\boldsymbol{x}, t) = \overline{f}(\boldsymbol{x}) + f''(\boldsymbol{x}, t), \tag{1.35}$$

where $\bar{(\cdot)}$ denotes the average operation:

$$\overline{f}(\boldsymbol{x}) = \lim_{T\to\infty} \frac{1}{T} \int_t^{t+T} f(\boldsymbol{x}, t) dt. \tag{1.36}$$

This averaging operation, with T tending to infinity, is suitable for the statistically steady-state turbulent flows. Indeed, if one substitutes the Reynolds decomposition into the NS equations and takes the average, the time derivative term disappears. In this work, however, we consider that the mean flow varies with time, but in such a way that the averaging operation holds, i.e., using the same notation as [3], the turbulence scale T_1 and the unsteadiness scale of the mean field T_2 differ by several orders of magnitude. The decomposition then becomes:

$$f(\boldsymbol{x},t) = \overline{f}(\boldsymbol{x},t) + f''(\boldsymbol{x},t), \tag{1.37}$$

with:

$$\overline{f}(\boldsymbol{x},t) = \frac{1}{T}\int_t^{t+T} f(\boldsymbol{x},t)dt, \qquad T_1 \ll T \ll T_2. \tag{1.38}$$

However, many flow patterns do not adhere to this large difference in scale; therefore, *a priori* knowledge of the physics being simulated is required. Now the time derivative term in the averaged equations

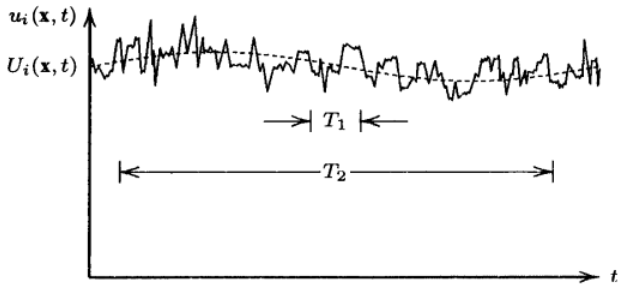


Figure 1.4: Time averaged velocity field $U_i(\boldsymbol{x},t)$ for unsteady turbulent flow. Figure taken from [3].

does not disappear; in fact, we can write that:

$$\overline{\frac{\partial f}{\partial t}} = \frac{1}{T}\int_t^{t+T} \frac{\partial}{\partial t}(\overline{f}(\boldsymbol{x},t) + f''(\boldsymbol{x},t))dt = \frac{\overline{f}(\boldsymbol{x},t+T) - \overline{f}(\boldsymbol{x},t)}{T} + \frac{f''(\boldsymbol{x},t+T) - f''(\boldsymbol{x},t)}{T}. \tag{1.39}$$

The second term in the equation can be omitted since $|\overline{f}| \gg |f''|$; furthermore, given that $T \ll T_2$, the first term is equivalent to the definition of the incremental ratio as $T \to 0$. It can be concluded that:

$$\overline{\frac{\partial f}{\partial t}} \approx \frac{\partial \overline{f}}{\partial t}. \tag{1.40}$$

Before injecting the decomposition (1.37) into (1.16), it is necessary to take compressibility effects into account. The average (1.38) is actually used as it is in the incompressible version of the Navier-Stokes equations; however, we are interested in high Mach number cases, and fluctuations in density and

temperature must be taken into account. Let us introduce the mass-average operation, also known as the Favre average [75]:

$$\tilde{f}(\boldsymbol{x}) = \frac{1}{\overline{\rho}} \lim_{T\to\infty} \frac{1}{T} \int_t^{t+T} \rho(\boldsymbol{x},t) f(\boldsymbol{x},t) dt = \frac{\overline{\rho f}}{\overline{\rho}}, \tag{1.41}$$

where indeed the superscript ($\tilde{\cdot}$) denotes the mass-average. A new decomposition can be employed as follows:

$$f(\boldsymbol{x},t) = \tilde{f}(\boldsymbol{x},t) + \check{f}(\boldsymbol{x},t). \tag{1.42}$$

The need to introduce this new decomposition is linked more to a mathematical aspect than a physical one. In fact, if one replaces (1.37) in continuity equation in Cartesian coordinates and performs time-average (1.38) , one obtains:

$$\frac{\partial \overline{\rho}}{\partial t} = \frac{\partial}{\partial x_i}(\overline{\rho u_i} + \overline{\rho'' u_i''}), \tag{1.43}$$

where the correlation $\overline{\rho'' u_i''}$ is unknown Instead, by using (1.42):

$$\frac{\partial \overline{\rho}}{\partial t} = \frac{\partial}{\partial x_i}(\overline{\rho}\tilde{u_i}). \tag{1.44}$$

Similarly to the continuity equation, using the Favre average allows us to reduce the number of unknown correlations in the other equations as well, without losing any physical information. Using the decomposition (1.42) into (1.16) and taking the time average, we get the following system, known as the Reynolds-Favre average Navier-Stokes equations, now written using Einstein notation to show all the additional terms related to correlations:

$$\begin{cases} \dfrac{\partial \overline{\rho}}{\partial t} + \dfrac{\partial}{\partial x_i}(\overline{\rho}\tilde{u_i}) = 0, \\ \dfrac{\partial}{\partial t}(\overline{\rho}\tilde{u_i}) + \dfrac{\partial}{\partial x_j}(\overline{\rho}\tilde{u_j}\tilde{u_i}) = -\dfrac{\partial \overline{p}}{\partial x_i} + \dfrac{\partial}{\partial x_j}\left(\overline{\tau}_{ij} - \overline{\rho \check{u}_j \check{u}_i}\right), \\ \dfrac{\partial}{\partial t}\left(\overline{\rho}\tilde{E}\right) + \dfrac{\partial}{\partial x_j}\left(\overline{\rho}\tilde{u_j}\tilde{H}\right) = \dfrac{\partial}{\partial x_j}\left(-\tilde{Q}_j - \overline{\rho \check{u}_j \check{h}} + \overline{\tau_{ij}\check{u}_i} - \dfrac{1}{2}\overline{\rho \check{u}_j \check{u}_i \check{u}_i}\right) + \dfrac{\partial}{\partial x_j}\left[\tilde{u}_i\left(\overline{\tau_{ij}} - \overline{\rho \check{u}_i \check{u}_j}\right)\right]. \end{cases} \tag{1.45}$$

The first new term appears in the momentum balance equation and corresponds to the Favre-averaged Reynolds stress tensor:

$$\overline{\rho}\tau_{ij}^R = -\overline{\rho \check{u}_i \check{u}_j}. \tag{1.46}$$

This represents the effect of fluctuations on the mean field and adds six new unknowns to the system, as it is a symmetric tensor. In the energy conservation equation, however, the total energy $\tilde{E}$ includes not only internal energy and kinetic energy but also turbulent kinetic energy:

$$\overline{\rho}\tilde{E} = \overline{\rho}\tilde{e} + \overline{\rho}\frac{\tilde{u}_i \tilde{u}_i}{2} + \overline{\rho}k. \tag{1.47}$$

with k turbulent kinetic energy defined as:

$$\overline{\rho}k = \frac{1}{2}\overline{\rho\check{u}_i\check{u}_i}, \tag{1.48}$$

while $\tilde{H}$ represents the total enthalpy, which also contains k. Always in equation of energy conservation further correlations can be found, proceeding in order, we have:

$$Q_{tj} = \overline{\rho\check{u}_j\check{h}}, \tag{1.49}$$

which is the turbulent counterpart of the laminar heat flux, then have two terms $\overline{\tau_{ij}\check{u}_i}$ and $\frac{1}{2}\overline{\rho\check{u}_j\check{u}_i\check{u}_i}$ corresponding to molecular diffusion and turbulent transport of turbulent kinetic energy respectively. It is therefore clear that the (1.45) system is underdetermined and that further relations are required to close it.

When attempting to derive analytical equations for the correlations mentioned above, one realises that new higher-order unknowns arise; consequently, it is not possible to proceed along this path – this is the well-known closure problem. Models are therefore necessary.

There are several models available, developed over the years; however, only two are used in this work: the single-equation Spalart-Allmaras model and the two-equations k-ω-SST model by Menter. For both models, as well as for all other zero-, one-, two- equations models, the Boussinesq approximation [76] is used to model the Reynolds stress tensor τ_{ij}^R; for compressible flows, this reads:

$$\overline{\rho}\tau_{ij}^R = 2\mu_t\left(\tilde{S_{ij}} - \frac{1}{3}\frac{\partial\tilde{u}_k}{\partial x_k}\delta_{ij}\right) - \frac{2}{3}\overline{\rho}k\delta_{ij}. \tag{1.50}$$

The relation (1.50) establishes a linear relationship between τ_{ij}^R and the strain rate tensor, by introducing a new variable: the turbulent viscosity μ_t. Essentially, the underlying idea is that the eddies in turbulent flows behave like fluid molecules, interacting with one another. This allows us to reduce the number of unknowns from six to just one—namely, the turbulent viscosity—which, however, is a property of the flow rather than of the fluid itself. Following the analogy between momentum and heat transfer, turbulent viscosity can also be used to derive a relationship for Q_{tj}, which is proportional to the temperature gradient:

$$Q_{tj} = \overline{\rho\check{u}_j\check{h}} = -\frac{\mu_t C_p}{Pr_t}\frac{\partial\tilde{T}}{\partial x_j}, \tag{1.51}$$

here a turbulent Prandtl number has been introduced. Commonly Pr_t is set as constant, in this work we fix $Pr_t = 0.9$. Finally, the molecular diffusion term $\overline{\tau_{ij}\check{u}_i}$ and the turbulent transport term

$\frac{1}{2}\overline{\rho\check{u}_j\check{u}_i\check{u}_i}$ are often neglected, particularly for low-Mach-number flows (up to the supersonic range), nevertheless, when these terms are taken into account, the most commonly used approximation is:

$$\overline{\tau_{ij}\check{u}_i} - \frac{1}{2}\overline{\rho\check{u}_j\check{u}_i\check{u}_i} = \left(\tilde{\mu} + \frac{\mu_t}{\sigma_k}\right)\frac{\partial k}{\partial x_j}. \tag{1.52}$$

The complete closure of the (1.45) therefore depends on the specific model used, as new quantities have been introduced; moreover we can still write them in compact form and in curvilinear coordinates exactly as (1.25). What changes is the physical meaning, as they do not solve instantaneous quantities but the Favre-averaged one, furthermore τ_{ij} is replaced by the total stress tensor $\tilde{\tau}_{ij}^{tot}$ and β_j is replaced by the total heat flux $\tilde{\beta}_j^{tot}$ to take into account the effect of turbulent fluctuations over the mean flow.

$$\tilde{\tau}_{ij}^{tot} = (\tilde{\mu} + \mu_t)\left(\tilde{S_{ij}} - \frac{1}{3}\frac{\partial \tilde{u}_k}{\partial x_k}\delta_{ij}\right) - \frac{2}{3}\overline{\rho}k\delta_{ij}, \tag{1.53}$$

$$\tilde{\beta}_j = \left(\frac{\tilde{\mu}C_p}{Pr} + \frac{\mu_t C_p}{Pr_t}\right)\frac{\partial \tilde{T}}{\partial x_j} + \tilde{u}_i\overline{\tau}_{ij} + \left(\tilde{\mu} + \frac{\mu_t}{\sigma_k}\right)\frac{\partial k}{\partial x_j}. \tag{1.54}$$

1.2.4 Spalart-Allmaras one-equation model

The Spalart-Allmaras model [77] is undoubtedly the most widely used one-equation model today, thanks to its versatility: it is local and does not require a finer grid than algebraic models; it is robust and does not require complex boundary conditions. The new variable introduced into the system is an intermediate variable known as modified viscosity, or Spalart-Allmaras viscosity, ν_{SA}, and its time-evolution equation in its general form is given by:

$$\frac{D\nu_{SA}}{Dt} = c_{b1}(1 - f_{t2})\hat{S}\nu_{SA} + \frac{1}{\sigma_{SA}}\left[\boldsymbol{\nabla}\cdot(\nu + \nu_{SA})\boldsymbol{\nabla}\nu_{SA} + c_{b2}\boldsymbol{\nabla}\nu_{SA}\cdot\boldsymbol{\nabla}\nu_{SA}\right] - \left(c_{w1}f_w - \frac{c_{b1}}{\kappa_{SA}^2}f_{t2}\right)\left(\frac{\nu_{SA}}{d_w}\right)^2, \tag{1.55}$$

where the terms production, diffusion and destruction can be distinguished on the right-hand side. Turbulent viscosity is then calculated from this according to the relationship $\mu_t = \overline{\rho}\nu_{SA}f_{v1}$, where f_{v1} is a damping function $f_{v1} = \chi^3/(\chi^3 + c_{v1}^3)$, being $\chi = \overline{\rho}\nu_{SA}/\tilde{\mu}$ and $c_{v1} = 7.1$. The intermediate variable is used because it behaves linearly at the wall, unlike ν_T, thus allowing for a simpler numerical solution. Other constants present in equation (1.55) are: $\sigma_{SA} = 2/3$, $\kappa_{SA} = 0.41$, $c_{b1} = 0.1355$, $c_{b2} = 0.622$,

$c_{w1} = c_{b1}/\kappa_{SA}^2 + (1 + cb_2)/\sigma_{SA}$, $c_{t3} = 1.2$, $c_{t4} = 0.5$, while the local variables read:

$$\begin{aligned} f_{t2} = c_{t3} e^{-c_{t4}\chi^2}, \qquad f_w = g\left(\frac{1+c_{w3}^6}{g^6+c_{w3}^6}\right)^{1/6}, \qquad g = r + c_{w2}(r^6 - r), \\ r = min\left(\frac{\nu_{SA}}{\hat{S}\kappa_{SA}^2 d_w^2}, 10\right), \qquad \hat{S} = \sqrt{2\tilde{\boldsymbol{\Omega}} : \tilde{\boldsymbol{\Omega}}} + \frac{\nu_{SA}}{\kappa_{SA}^2 d_w^2} f_{v2}, \\ \tilde{\boldsymbol{\Omega}} = \frac{1}{2}\left(\boldsymbol{\nabla}\tilde{\boldsymbol{u}} - \boldsymbol{\nabla}\tilde{\boldsymbol{u}}^T\right), \qquad f_{v2} = 1 - \frac{\chi}{1+\chi f_{v1}}. \end{aligned} \tag{1.56}$$

where d_w is the distance from the nearest wall.

The prescribed boundary conditions are:

$$\nu_{SA} = 0, \qquad \text{wall} \tag{1.57}$$

$$\nu_{SA} = 3\nu_\infty \; to \; 5\nu_\infty. \qquad \text{farfield} \tag{1.58}$$

It can be seen that there is no way to account for turbulent kinetic energy; therefore, when closing the equations, this term will not be included in the Boussinesq relation, and the terms for molecular diffusion and turbulent transport in the energy conservation equation are likewise omitted.

In [78] a few modifications to the original model have been proposed, and some of these have been adopted in this thesis. Although the original model is regarded as the standard for both incompressible and compressible flows, a conservative version is obtained by combining the mass conservation equation with the original model:

$$\overline{\rho}(SA) + \nu_{SA}(\text{continuity eq}) = 0. \tag{1.59}$$

To prevent the modified vorticity $\hat{S}$ from becoming numerically negative, a correction is applied based on the magnitude of the vorticity $\sqrt{2(\boldsymbol{\Omega} : \boldsymbol{\Omega})}$.

$$\hat{S} = \begin{cases} \sqrt{2\tilde{\boldsymbol{\Omega}} : \tilde{\boldsymbol{\Omega}}} + \dfrac{\nu_{SA}}{\kappa_{SA}^2 d_w^2} f_{v2}, & : \; \dfrac{\nu_{SA}}{\kappa_{SA}^2 d_w^2} f_{v2} \geq c_{v2}\sqrt{2\tilde{\boldsymbol{\Omega}} : \tilde{\boldsymbol{\Omega}}} \\ \sqrt{2\tilde{\boldsymbol{\Omega}} : \tilde{\boldsymbol{\Omega}}} + \dfrac{\sqrt{2\tilde{\boldsymbol{\Omega}} : \tilde{\boldsymbol{\Omega}}}\left(c_{v2}^2\sqrt{2\tilde{\boldsymbol{\Omega}} : \tilde{\boldsymbol{\Omega}}} + c_{v3}\frac{\nu_{SA}}{\kappa_{SA}^2 d_w^2} f_{v2}\right)}{(c_{v3} - 2c_{v2})\sqrt{2\tilde{\boldsymbol{\Omega}} : \tilde{\boldsymbol{\Omega}}} - \frac{\nu_{SA}}{\kappa_{SA}^2 d_w^2} f_{v2}} & : \; \dfrac{\nu_{SA}}{\kappa_{SA}^2 d_w^2} f_{v2} < c_{v2}\sqrt{2\tilde{\boldsymbol{\Omega}} : \tilde{\boldsymbol{\Omega}}} \end{cases} \tag{1.60}$$

with $c_{v2} = 0.7$ and $c_{v3} = 0.9$.

Furthermore, although analytically the equation does not allow for a negative value of ν_{SA}, numerically this can occur in certain regions of the flow (at the boundary layer edge); therefore, modifications to the standard model are required. To avoid negative values for turbulent viscosity, a limit is set:

$$\mu_t = \begin{cases} \overline{\rho}\nu_{SA} f_{v1}, & : \; \nu_{SA} \geq 0 \\ 0, & : \; \nu_{SA} < 0 \end{cases} \tag{1.61}$$

In addition, the entire equation changes, again depending on the sign of ν_{SA}, as follows (in conservative form):

$$\frac{D}{Dt}(\overline{\rho}\nu_{SA}) = \boldsymbol{\nabla}\cdot\left(\frac{1}{\sigma_{SA}}\overline{\rho}(\tilde{\nu}+(1-F1)\nu_{SA}+F1f_n\nu_{SA})\boldsymbol{\nabla}\nu_{SA}\right)+c_{b1}(1-(1-F1)f_{t2}-F1c_{t3})\hat{S}\overline{\rho}\nu_{SA}+ \\ +\frac{c_{b2}}{\sigma_{SA}}\boldsymbol{\nabla}\nu_{SA}\cdot\boldsymbol{\nabla}(\overline{\rho}\nu_{SA})-(1-F1)\overline{\rho}\left(c_{w1}f_w-\frac{c_{b1}}{\kappa_{SA}^2}f_{t2}\right)\left(\frac{\nu_{SA}}{d_w}\right)^2+F1\overline{\rho}c_{w1}f_w\left(\frac{\nu_{SA}}{d_w}\right)^2 \tag{1.62}$$

where the sign function $F1$ is introduced equal to 0 when ν_{SA} is negative and equal to one otherwise. For $\nu_{SA}\geq 0$ the conservative form of the standard model is retrieved and for $F=1$ one can notice that the classic destruction term changes sign. The new additional coefficients and local variables are the following:

$$c_{n1}=16, \qquad\qquad f_n=\frac{c_{n1}+\chi^3}{c_{n1}-\chi^3}. \tag{1.63}$$

1.2.5 k-ω SST two-equation model

The first k-ω model was proposed by Kolmogorov in [79], where he introduces ω as a rate of energy dissipation with dimension $1/time$. Over the years, numerous formulations of the model have been put forward; we have decided to use Menter's [80] - [81], already presented in a conservative formulation:

$$\begin{cases}\dfrac{D}{Dt}(\overline{\rho}k)=P-\beta^*\overline{\rho}\omega k+\boldsymbol{\nabla}\cdot[(\mu+\tilde{\sigma}_k\mu_t\boldsymbol{\nabla}k)], \\ \dfrac{D}{Dt}(\overline{\rho}\omega)=\dfrac{\gamma_t}{\nu_t}P-\beta\overline{\rho}\omega^2+\boldsymbol{\nabla}\cdot[(\mu+\tilde{\sigma}_\omega\mu_t\boldsymbol{\nabla}\omega)]+2(1-F_1)\dfrac{\rho\sigma_{\omega 2}}{\omega}\boldsymbol{\nabla}k\cdot\boldsymbol{\nabla}\omega,\end{cases} \tag{1.64}$$

with P the production term

$$P=min(\boldsymbol{\tau}^{tot}\cdot\boldsymbol{\nabla}\tilde{\boldsymbol{u}},10\beta^*\overline{\rho}\omega k), \tag{1.65}$$

and turbulent eddy viscosity computed as in [82]:

$$\mu_t=\frac{\overline{\rho}a_1k}{max(a_1\omega,\tilde{S}F_2)}, \qquad \tilde{S}=\sqrt{\tilde{\boldsymbol{S}}:\tilde{\boldsymbol{S}}}. \tag{1.66}$$

All constants are obtained by blending two values using the function F_1 as follows:

$$\phi=F_1\phi_1+(1-F_1)\phi_2. \tag{1.67}$$

In fact, the main advantage of the model is that it allows for a smooth transition from the k-ϵ model in the free shear regions and the outer region of the boundary layer to Wilcox's k-ω model [83] in

the inner region of the boundary layer, thereby eliminating the strong dependence of the classical k-ω model on free-stream values [84]. The blended constants are:

$$\begin{aligned}
&\gamma_1 = \frac{\beta_1}{\beta^*} - \frac{\sigma_{\omega 1}\kappa^2}{\sqrt{\beta^*}}, && \gamma_2 = \frac{\beta_2}{\beta^*} - \frac{\sigma_{\omega 2}\kappa^2}{\sqrt{\beta^*}}, \\
&\sigma_{k1} = 0.85, && \sigma_{\omega 1} = 0.5, && \beta_1 = 0.075, \\
&\sigma_{k2} = 1.0, && \sigma_{\omega 2} = 0.856, && \beta_2 = 0.0828, \\
&\beta^* = 0.09, && \kappa = 0.41, && a_1 = 0.31,
\end{aligned} \tag{1.68}$$

and the functions employed are:

$$\begin{aligned}
&F_1 = \tanh(arg_1^4), \\
&arg_1 = \min\left[\max\left(\frac{\sqrt{k}}{\beta^*\omega d_w}, \frac{500\nu}{d_w^2\omega}\right), \frac{4\rho\sigma_{\omega 2}k}{CD_{k\omega}d_w^2}\right], \\
&CD_{k\omega} = \max\left(2\rho\sigma_{\omega 2}\frac{1}{\omega}\boldsymbol{\nabla}k\cdot\boldsymbol{\nabla}\omega, 10^{-10}\right), \\
&F_2 = \tanh(arg_2^2), \\
&arg_2 = \max\left(2\frac{\sqrt{k}}{\beta^*\omega d_w}, \frac{500\nu}{d_w^2\omega}\right),
\end{aligned} \tag{1.69}$$

with d_w the distance from the nearest wall. The model formulation described above corresponds to the SST (Shear-Stress-Transport) version, which differs from the BSL version for the values of the constants ϕ_1 and for the introduction of a limit on turbulent viscosity. The prescribed boundary conditions are as follows:

$$\begin{aligned}
&\frac{U_\infty}{L} < \omega < 10\frac{U_\infty}{L}, && farfield \\
&\frac{10^{-5}U_\infty^2}{Re_L} < k < 10\frac{0.1U_\infty^2}{Re_L}, \\
&\omega = 10\frac{6\nu}{\beta_1(\Delta d_{w1})^2}, && wall \\
&k = 0,
\end{aligned} \tag{1.70}$$

where L is a domain length. The combination of k and ω should give a freestream turbulent viscosity such that: $10^{-5}\mu_\infty < \mu_t < 10^{-2}\mu_\infty$, while at wall $\mu_t = 0$ with $\omega \to 6\nu/(\beta_1(\Delta d_{w1})^2)$ and $d_w \to 0$ being

Δd_{w1} the wall distance of the first bulk mesh point .

One might observe that, for meshes with significant wall stretching, ω would tend towards very high values, causing numerical instability. For this reason, what is done in this work is to write an equation for $\tilde{\omega} = \log(\omega)$:

$$\frac{D}{Dt}(\overline{\rho}\tilde{\omega}) = \frac{\gamma_t}{\nu_t} P e^{-\tilde{\omega}} - \beta \overline{\rho} e^{\tilde{\omega}} + \boldsymbol{\nabla} \cdot [(\mu + \tilde{\sigma}_\omega \mu_t \boldsymbol{\nabla}\tilde{\omega})] + 2(1 - F_1)\frac{\rho\sigma_{\omega 2}}{e^{\tilde{\omega}}} \boldsymbol{\nabla} k \cdot \boldsymbol{\nabla}\tilde{\omega} + (\mu + \sigma_\omega \mu_t)\boldsymbol{\nabla}\tilde{\omega} \cdot \boldsymbol{\nabla}\tilde{\omega} \quad (1.71)$$

the updated functions are:

$$\begin{aligned} arg_1 &= \min\left[\max\left(\frac{\sqrt{k}}{\beta^* e^{\tilde{\omega}} d_w}, \frac{500\nu}{d_w^2 \omega}\right), \frac{4\rho\sigma_{\omega 2} k}{CD_{k\omega} d_w^2}\right], \\ CD_{k\omega} &= \max\left(2\rho\sigma_{\omega 2}\boldsymbol{\nabla} k \cdot \boldsymbol{\nabla}\tilde{\omega}, 10^{-10}\right), \\ arg_2 &= \max\left(2\frac{\sqrt{k}}{\beta^* e^{\tilde{\omega}} d_w}, \frac{500\nu}{d_w^2 e^{\tilde{\omega}}}\right) \end{aligned} \quad (1.72)$$

and boundary conditions:

$$\begin{aligned} log\left(\frac{U_\infty}{L}\right) < \omega < log\left(10\frac{U_\infty}{L}\right), \qquad & farfield \\ \omega = log\left(10\frac{6\nu}{\beta_1(\Delta d_{w1})^2}\right), \qquad & wall \end{aligned} \quad (1.73)$$

In compressible mixing layers, the model as it stands is unable to predict the reduction in the spreading rate; this is due to the effect of dilatational dissipation ϵ_d, which is a function of the turbulent Mach number $M_t^2 = 2k/c$, as postulated in [85]-[86]:

$$\epsilon_d = \xi^* F(M_t)\epsilon. \quad (1.74)$$

In [85], the following relations are used:

$$\xi^* = 1, \qquad F(M_t) = M_t^2. \quad (1.75)$$

This correction was subsequently adapted by Wilcox [87] for the ω equation in his model, via the correction of the coefficients βs as follows:

$$\begin{aligned} \beta^* &= \beta_0^*[1 + \xi^* F(M_t)], \\ \beta &= \beta_0 - \beta_0^* \xi^* F(M_t), \end{aligned} \quad (1.76)$$

where β_0 and β_0^* are the corresponding incompressible values. This compressibility correction is also adopted in this work.

1.3 Stability analysis

Linear stability analysis is a powerful tool for assessing the time evolution of non-linear dynamical systems, such as those described in the previous section, that can be written in general form as:

$$\frac{\partial \tilde{\boldsymbol{q}}}{\partial t} = \boldsymbol{F}(\tilde{\boldsymbol{q}}, t), \tag{1.77}$$

where $\tilde{\boldsymbol{q}} \in \mathbb{R}^n$ is the state vector of the system and $\boldsymbol{F}(\tilde{\boldsymbol{q}}, t)$ is the non-linear operator describing the right-hand side of the NS equations or the URANS system.
For a continuous time dynamical system described in (1.77) one can introduce the concept of fixed points. The fixed points, $\boldsymbol{q}_0$ are particular equilibrium solutions, such that:

$$\frac{\partial \boldsymbol{q}_0}{\partial t} = \boldsymbol{F}(\boldsymbol{q}_0) = 0. \tag{1.78}$$

It is important to notice that a dynamical system can have multiple fixed points, i.e. steady state solutions.
The goal of the stability analysis is to verify if a generic fixed point, $\boldsymbol{q}_0$, of a dynamical system is stable or not. The use of the fixed point as the base flow around which to linearise the equations is not the only possible choice; we will discuss the various options adopted in the literature later on, but for now we will continue to consider only the fixed point.

1.3.1 Modal stability analysis

In the case of modal stability, the asymptotic behaviour ($t \to \infty$) is studied when a fixed point is subjected to a perturbation. According to Lyapunov statement the system is referred to as *linearly stable* if after being perturbed it returns back to its equilibrium point [88].
To study the behaviour of the perturbation, the following decomposition is introduced:

$$\tilde{\boldsymbol{q}} = \boldsymbol{q}_0 + \epsilon \boldsymbol{q}', \tag{1.79}$$

then replacing (1.79) into (1.77), one gets:

$$\frac{\partial}{\partial t}(\boldsymbol{q}_0 + \epsilon \boldsymbol{q}') = \boldsymbol{F}(\boldsymbol{q_0} + \epsilon \boldsymbol{q}'), \tag{1.80}$$

finally considering that $\epsilon||\boldsymbol{q}'|| << ||\boldsymbol{q_0}||$, Taylor expansion can be employed truncated at first order as follows:

$$\boldsymbol{F}(\boldsymbol{q_0} + \epsilon\boldsymbol{q}') \approx \boldsymbol{F}(\boldsymbol{q_0}) + \frac{\partial \boldsymbol{F}(\boldsymbol{q}_0)}{\partial \boldsymbol{q}}\epsilon\boldsymbol{q}', \tag{1.81}$$

obtaining the linear equation which describes the time evolution of the perturbation:

$$\frac{\partial \boldsymbol{q}'}{\partial t} = \boldsymbol{\mathcal{L}}\boldsymbol{q}', \tag{1.82}$$

where:

$$\boldsymbol{\mathcal{L}} = \frac{\partial \boldsymbol{F}(\boldsymbol{q}_0)}{\partial \boldsymbol{q}}, \tag{1.83}$$

is the Jacobian operator.

Starting from (1.82), two types of approach are possible depending on the characteristics of the fixed point used. We talk about *local* stability when the fixed point considered has a single non-homogeneous direction (which we denote here by y), and the following ansatz can be applied:

$$\boldsymbol{q}'(x, y, t) = \hat{\boldsymbol{q}}(y)e^{i(\alpha x - \omega t)} + \text{ c.c.}, \tag{1.84}$$

where x is considered as homogeneous direction , α is the corresponding wavenumber, ω is the pulsation (note that to simplify z direction is not taken into account for the moment) and c.c. the complex conjugate. At this point, there are two types of local stability analysis. One is known as a temporal analysis, in which a real number α is fixed and a solution is found to a generalised eigenvalue problem for $\omega \in \mathbb{C}$ of type:

$$\boldsymbol{\mathcal{A}}\hat{\boldsymbol{q}} = \omega\boldsymbol{\mathcal{B}}\hat{\boldsymbol{q}}. \tag{1.85}$$

If there exists at least one eigenvalue for which $\omega_i > 0$, then the system is unstable and there exists a perturbation with wavelength $\lambda = 2\pi/\alpha$ that grows exponentially by extracting energy from the base flow. The other possible approach is known as spatial analysis and consists in setting a value for $\omega \in \mathbb{R}$ and solving the following eigenvalue problem for $\alpha \in \mathbb{C}$:

$$(\boldsymbol{\mathcal{A}}_0 + \alpha\boldsymbol{\mathcal{A}}_1 + \alpha^2\boldsymbol{\mathcal{A}}_2)\hat{\boldsymbol{q}} = 0. \tag{1.86}$$

If there exists at least one mode with $-\alpha_i > 0$, then we can say that if the system is perturbed at a fixed frequency ω, the perturbation grows exponentially as it travels downwards. Currently, it is important to distinguish between convective and absolute instability. If the instability is of the absolute type – that is, if the disturbance grows in place (i.e. the group velocity is zero) – the spatial

approach loses its meaning [37]. For the spatial instability identified to have physical significance, it must be of the convective type, i.e. it must grow as it propagates.

It is clear from the above that local stability is an approach constrained by very strict assumptions; however, its use was necessary in the past due to limited computational resources. The generic approach, which places no restrictions on the type of fixed point, is defined as *global* stability. The solution of the linearised system (1.82) at a time τ is given by:

$$\boldsymbol{q}'(\tau) = \boldsymbol{q}'(t=0)e^{\tau\boldsymbol{\mathcal{L}}} = \boldsymbol{q}'(t=0)\boldsymbol{M}_\tau, \tag{1.87}$$

where $\boldsymbol{M}_\tau$ is called *exponential operator* of the linearised system.

In order to perform the global stability a spectral composition of the Jacobian $\boldsymbol{\mathcal{L}}$ is required:

$$\boldsymbol{\mathcal{L}} = \boldsymbol{V}\boldsymbol{\Lambda}\boldsymbol{V}^{-1}, \tag{1.88}$$

where columns of the matrix $\boldsymbol{V}$ correspond to the eigenvectors $\boldsymbol{v}_i$ associated to eigenvalues $\lambda_i = \Lambda_{ii}$, with $\boldsymbol{\Lambda}$ diagonal matrix. Moreover through the Taylor expansion , we can also write:

$$e^{\tau\boldsymbol{\mathcal{L}}} = \boldsymbol{I} + \boldsymbol{L}\tau + \frac{1}{2!}(\boldsymbol{\mathcal{L}}\tau)^2 + \frac{1}{3!}(\boldsymbol{\mathcal{L}}\tau)^3 + ... = \boldsymbol{V}e^{\Lambda\tau}\boldsymbol{V}^{-1}. \tag{1.89}$$

Assuming that eigenvalues are sorted such that $\mathcal{R}(\lambda_i) > \mathcal{R}(\lambda_{i+1})$ one can easily show that:

$$\lim_{t\to\infty} \boldsymbol{q}'(t=0)e^{\tau\boldsymbol{\mathcal{L}}} = \lim_{t\to\infty} \boldsymbol{v}_1 e^{(\lambda_1 t)}. \tag{1.90}$$

So the asymptotic behaviour of the dynamical system is completely described by the eigenvalue with greatest real part. Through relation (1.90) a classification can be made:

- $\mathcal{R}(\lambda_1) > 0$: the perturbation grows exponentially in time, the fixed point is asymptotically linearly unstable;
- $\mathcal{R}(\lambda_1) < 0$: the perturbation decays exponentially in time, the fixed point is asymptotically linearly stable;
- $\mathcal{R}(\lambda_1) = 0$: the fixed point is elliptic, the study of eigenvalues is not enough. A weakly non linear analysis is required.

At this point, one naturally wonders what is the connection between local and global stability. It can be said that a system which is locally convectively unstable does not exhibit global instability but acts

merely as an amplifier of external noise. For the system to exhibit self-sustaining intrinsic dynamics (global instability), governed by its natural frequency, the presence of a region that is locally absolutely unstable is required. The reader may find a more complete and detailed description in [37]-[89].

1.3.2 Non modal stability analysis

The definition of Lyapunov stability given in previous section is not sufficient to describe the full behaviour of many dynamical systems, for example in wall bounded shear flows many dynamic processes occur on a finite time scale [90]. This happens when the matrix $\boldsymbol{\mathcal{L}}$ is said to be non-normal. The concept of non-normality can be expressed by introducing the adjoint-operator $\boldsymbol{\mathcal{L}}^\dagger$ which satisfies:

$$\langle \boldsymbol{y}, \boldsymbol{\mathcal{L}}\boldsymbol{x} \rangle = \left\langle \boldsymbol{\mathcal{L}}^\dagger \boldsymbol{y}, \boldsymbol{x} \right\rangle, \tag{1.91}$$

where $\langle \cdot, \cdot \rangle$ represents the inner product.
Then the non-normality of operator $\boldsymbol{\mathcal{L}}$ corresponds to:

$$\boldsymbol{\mathcal{L}}^\dagger \boldsymbol{\mathcal{L}} \neq \boldsymbol{\mathcal{L}} \boldsymbol{\mathcal{L}}^\dagger, \tag{1.92}$$

namely, the eigenvectors of $\boldsymbol{\mathcal{L}}$ do not form a set of orthonormal vectors [91].This often applies to the linearised operator for both NS and URANS, thus perturbations may experience a transient growth before decaying asymptotically. Furthermore, the non-orthogonality of the eigenvectors gives rise to the phenomenon of pseudo-resonance: the system becomes capable of greatly amplifying external disturbances across a wide frequency spectrum. The pseudo-spectrum $\boldsymbol{\Lambda}_\epsilon(\boldsymbol{\mathcal{L}})$ of the operator $\boldsymbol{\mathcal{L}}$ is defined as:

$$\boldsymbol{\Lambda}_\epsilon(\boldsymbol{\mathcal{L}}) = \{\lambda \in \mathbb{C} : ||(\lambda \boldsymbol{I} - \boldsymbol{\mathcal{L}})^{-1}|| > \epsilon^{-1}\}. \tag{1.93}$$

If the operator $\boldsymbol{\mathcal{L}}$ is normal, the pseudospectrum exactly represents the set of points $\in \mathbb{C}$ at a distance $< \epsilon$ from the eigenspectrum, while if $\boldsymbol{\mathcal{L}}$ is non normal, the distance can be much larger [38]. From this definition, it is clear that the calculation of the pseudo-spectrum is useful for assessing the sensitivity of the calculated spectrum to a disturbance of magnitude ϵ.

1.3.2.1 Resolvent analysis

When a system is globally stable, it may be interesting to inspect its response to a particular forcing. The complementary tool that allows us to do this is resolvent analysis. Let us consider our linear

system (1.82) subjected to a particular forcing $\boldsymbol{f}'$.

$$\frac{\partial \boldsymbol{q}'}{\partial t} = \boldsymbol{\mathcal{L}}\boldsymbol{q}' + \boldsymbol{f}', \tag{1.94}$$

expressing the response $\boldsymbol{q}'$ to the forcing $\boldsymbol{f}'$ using Fourier analysis yields the following relationship:

$$\hat{\boldsymbol{q}} = (i\omega \boldsymbol{I} - \boldsymbol{\mathcal{L}})^{-1}\hat{\boldsymbol{f}}, \tag{1.95}$$

where $\boldsymbol{\mathcal{R}}(\omega) = (\boldsymbol{I}\omega - \boldsymbol{\mathcal{L}})^{-1}$ is called resolvent operator and acts as a transfer function between forcing and response terms. The aim is to determine the optimal forcing that excites our system through the resolution of an optimization problem. In other words, by evaluating the pseudospectral properties of the linear operator, resolvent analysis uncovers both the harmonic input-output characteristics and the mechanisms driving transient energy growth [74]-[92]. At fixed ω , the optimization problem can be written as:

$$\sigma_\omega^2 = \max_{\hat{\mathbf{f}}} \frac{||\hat{\mathbf{q}}||_E^2}{||\hat{\mathbf{f}}||_f^2}, \tag{1.96}$$

where $||.||_E$ is a suitable energy norm and $||.||_f$ is a user-defined norm to compute forcing amplitude. A common choice to evaluate the forcing norm is to use the weight matrix $\boldsymbol{W}$:

$$||\hat{\mathbf{f}}||_f^2 = \mathbf{f}^\dagger \boldsymbol{W} \hat{\mathbf{f}}, \tag{1.97}$$

where $\boldsymbol{W}$ is a diagonal matrix containing cells volume (J_i for curvilinear equations). For energy norm, in compressible cases, a common approach is to use Chu's norm [93], which allows the various energy terms to be taken into account:

$$E_{chu} = \frac{1}{2}\int_V \left(\overline{\rho}_0 |\hat{\mathbf{u}}|^2 + \frac{\tilde{c}_0^2 \hat{\rho}^2}{\gamma \overline{\rho}} + \frac{\overline{\rho}_0 c_v \hat{T}^2}{\tilde{T}_0} \right) dV. \tag{1.98}$$

If we refer with $\boldsymbol{W}_{Chu}$ to the matrix related to the Chu energy, problem (1.96) can be rewritten as:

$$\sigma_\omega^2 = \max_{\hat{\mathbf{f}}} \frac{\mathbf{q}^\dagger \boldsymbol{W}_{Chu} \hat{\mathbf{q}}}{\mathbf{f}^\dagger \boldsymbol{W} \hat{\mathbf{f}}} = \max_{\hat{\mathbf{f}}} \frac{(\mathbf{f}^\dagger \boldsymbol{R}^\dagger) \boldsymbol{W}_{Chu} (\boldsymbol{R}\hat{\mathbf{f}})}{\mathbf{f}^\dagger \boldsymbol{W} \hat{\mathbf{f}}}. \tag{1.99}$$

Solving (1.99) is equivalent to solve the following generalized eigenvalue problem [57]:

$$\begin{cases} \boldsymbol{\mathcal{R}}^\dagger \boldsymbol{W}_{Chu} \boldsymbol{\mathcal{R}} = \sigma_\omega^2 \boldsymbol{W} \hat{\mathbf{f}}, \\ \hat{\boldsymbol{q}} = \dfrac{1}{\sigma_\omega} \boldsymbol{\mathcal{R}} \hat{\mathbf{f}} \end{cases} \tag{1.100}$$

Further details on the solution to the global stability problem and the resolvent analysis will be provided in the next chapter.

1.3.3 On the choice of the base flow

Choosing the base flow for laminar flows may seem straightforward, but this is not always the case. In fact, using the steady-state solution to the Navier-Stokes equations does not always lead to a correct prediction of the flow frequencies. In [94] , two approaches are compared in the global stability analysis around a cylinder for Re values exceeding the critical one: the use of base flow meant as a fixed point and the use of mean flow. In the steady-solution approach, the mode calculated via stability analysis does not have the same frequency as the vortex shedding observed in the non-linear calculation; whereas, when the mean flow is used, the results of the non-linear simulations can be reproduced. However, the system under consideration changes; in fact, the mean flow cannot be a solution to the Navier-Stokes equations due to the presence of the Reynolds stress tensor, which arises following the decomposition. Barkley therefore introduces an additional forcing term into the NS equations, which cancels out in the linearised version because it is considered stationary.
The reason why the fixed-point method fails is that we are too far from the Re critical value, and only the mean-flow method takes account of the deformations introduced by interactions with the non-linear terms. Sipp & Lebedev [95] subsequently sought a validity criterion for the mean-flow approach, using a weakly non-linear analysis. They showed that, for the mean-flow approach to be valid in the vicinity of the critical threshold, energy must be used to distort the mean flow rather than to generate second harmonics (i.e. zeroth harmonic of the mean flow being much stronger than the second harmonic).
Subsequently, Matič-Lugo *et al.* [96] introduced a self-consistent model – again for the case of flow around a cylinder – which overcomes the constraint of being close to the critical Reynolds number, yielding correct values for the vortex shedding frequency for $Re > Re_{cr}$. The method consists of iteratively solving the non-linear equation for the mean flow (including Reynolds stresses) and solving the eigenvalue problem for the perturbation. The most unstable mode is used in the non-linear equation to correct the mean flow, and so on. However, the application of this model remains limited to cases where the higher harmonics are negligible.
Extending these concepts to fully turbulent regimes is not, however, trivial; in turbulent flows, one cannot assume that energy transfer occurs exclusively between the fundamental mode and the mean flow, as the energy cascade mechanism plays a fundamental role. Nevertheless, there are some cases in the literature where a mean flow is used to carry out stability analyses. In [97], the authors perform

experimental tests on a fully turbulent, unforced jet and compare the results with the predictions of the linear stability analysis performed using the experimentally obtained mean field. Although the stability analysis correctly predicts the large-scale structures, the authors themselves state that theirs is a posteriori test, as they have made the assumption of disregarding non-linear interactions on the basis that non-linearities are partially taken into account through the mean flow. Another mean-flow-based approach, which however entails a change of paradigm, is the one introduced by McKeon & Sharma in [98]. Here, classical global stability is abandoned; the non-linear terms are not neglected by means of a hypothesis, but rather become the forcing in the resolvent analysis. The focus then shifts to studying the system's optimal response to a forcing that becomes an unknown variable. It should be noted, however, that the nature of the forcing term is something internal to the system under consideration, not external. The resolvent operator approach works in this case as long as the first singular value calculated via SVD is much larger than the subsequent ones. Whilst [98] presents only a local analysis, Beneddine *et al.* [99] extend the resolvent approach over the mean flow in order to obtain a global analysis. They demonstrated that the use of the mean flow is a valid strategy if the flow exhibits dominant convective instability and if the turbulent forcing does not exhibit a preferential direction towards sub-optimal forcings. Only under these conditions the flow dynamics is well represented by the optimal response.

For fully turbulent flows, it is nevertheless possible to return to a modal stability approach without using the mean flow. As anticipated in the introduction, we start with the triple decomposition of a periodic turbulent signal $f(x,t)$ [39]

$$f(x,t) = \tilde{f}(x) + f'(x,t) + \check{f}(x,t) \tag{1.101}$$

, where f represents both the velocity vector u_i and the pressure p, and this time the Favre average has been used for the triple decomposition. Substituting into the momentum balance equations and performing the time averaging operation, we obtain:

$$\overline{\frac{\partial \rho\tilde{u}_i}{\partial t} + \frac{\partial \rho u_i'}{\partial t} + \frac{\partial \rho\check{u}_i}{\partial t}} + \overline{\frac{\partial}{\partial x_j}[\rho(\tilde{u}_i + u_i' + \check{u}_i)(\tilde{u}_j + u_j' + \check{u}_j)]} = -\overline{\frac{\partial}{\partial x_i}(\tilde{p} + p' + \check{p})} + \overline{\frac{\partial}{\partial x_j}(\tilde{\tau_{ij}} + \tau_{ij}' + \check{\tau}_{ij})} \tag{1.102}$$

by exploiting the following properties: $\overline{\check{f}_i} = 0$, $\overline{f_i'} = 0$, $\overline{\rho\tilde{f}} = \overline{\rho}\tilde{f}$, $\overline{\rho f'} = 0$, $\partial/\partial t(\tilde{f}) = 0$, one gets:

$$\frac{\partial}{\partial x_j}(\overline{\rho}\tilde{u}_i\tilde{u}_j) + \frac{\partial \tilde{p}}{\partial x_i} - \frac{\partial \tilde{\tau_{ij}}}{\partial x_j} = -\frac{\partial}{\partial x_j}(\overline{\rho u_i' u_j'}) - \frac{\partial}{\partial x_j}(\overline{\rho\check{u}_i\check{u}_j}). \tag{1.103}$$

Finally by grouping the LHS in the operator $\mathcal{NS}$:

$$\mathcal{NS}(\tilde{u_i}, \tilde{p_i}) = -\frac{\partial}{\partial x_j}(\overline{\rho u_i' u_j'}) - \frac{\partial}{\partial x_j}(\overline{\rho \breve{u}_i \breve{u}_j}) \tag{1.104}$$

Where the first term corresponds to the Reynolds stress due to organised waves, whilst the second is the Reynolds stress of the turbulent motion. At this point, if we consider the URANS equations, these are decoupled from those for the coherent wave [100], the Boussinesq assumption models only the term related to turbulent motion. Therefore, by using the RANS solution as the base flow, a stability analysis can be carried out by superimposing the coherent perturbation. In a mean-flow approach, on the other hand, both terms on the right-hand side of 1.104 are taken into account. For this approach to be valid, it is important that the URANS framework is capable of capturing low-frequency unsteadiness, and this is only possible if the time scales differ by orders of magnitude. Furthermore, the assumption that we are close to the instability threshold must still hold; otherwise, the effects of non-linearities will alter the calculated frequencies.

Another approach to the stability analysis of turbulent flows is known in the literature as the *frozen eddy viscosity* method. It was introduced by Reynolds & Tiederman for modal analysis [101] and subsequently developed in other works on non-modal analysis [102]-[103]-[104], it consists of incorporating the effect of turbulence into the linearised equations via an effective viscosity $\nu_{eff} = \nu + \nu_t$ where ν_t is the unperturbed turbulent viscosity. In the specific case of these works, Cess's analytical relation [105] is used to determine the turbulent viscosity. Although it yields good results in some configurations, Crouch [40] has shown that, by not perturbing the turbulent viscosity in the case of buffet on the NACA0012 airfoil, the unstable mode disappears.

As mentioned in the introduction to this work, we follow Crouch's methodology, as it has proved to be optimal for various flow configurations in the aerospace sector; however, it was necessary to present a more comprehensive overview of the type of base flow adopted in turbulent flows for stability analysis.

Chapter 2

Numerical framework

Contenu

2.1 dNami 58
2.1.1 Finite difference method 61
2.1.2 Runge Kutta methods 63
2.1.3 Shock capturing scheme 64
2.1.4 Boundary conditions 66
2.2 liNami 73
2.2.1 Automatic differentiation 73
2.2.2 Matrix-free methods for stability analysis 77
2.2.3 Matrix-forming method 84

2.1 dNami

The systems of equations described in the previous chapter require appropriate numerical code both to be solved and to carry out the subsequent linear analyses. To fulfil these purposes efficiently and with minimal coding effort, we have chosen to use *dNami*.

dNami is a multi-language computational framework (Python, Fortran, C) that enables the solving of systems of balance equations, so it is not limited to the CFD domain but to any physical system that needs to be solved numerically [54].

dNami was born out of the need for researchers to reduce the time needed to implement codes in order to concentrate more on the physics of the problem of interest, with a framework that enables high performance thanks to an HPC environment.

It makes it possible to solve systems of equations of the type:

$$\frac{\partial \mathbf{q}}{\partial t} = \mathbf{F}(\mathbf{q}) + initial/boundary\ \ conditions \tag{2.1}$$

using explicit numerical schemes on structured mesh and MPI, loop-unrolling and cache blocking techniques to speed-up stencil-based operations.

The great advantage of *dNami* is that it allows the user to solve problems with large degrees of freedom (large scale problem) while retaining the versatility of Python language .

This is possible because it reconciles the advantages of a DSL (domain specific language) approach with all the advantages of precompiled Python modules in fact, *dNami* is based on the translation of symbolic expressions written at a high level in Python into equations discretised in low-level Fortran language.

The high-level layer of dNami is based on simple rules; the user only needs to specify symbols representing mathematical expressions, whether continuous or discrete, using Python strings. First, the user must define the vector **q** of the variables to be solved, plus the **LHS** and **RHS**. Figure (2.1) shows an example using the 1D Burgers equation; in this simplified case, the **LHS** corresponds to the vector **q**, but this is not always the rule. Within the **RHS**, the coefficient *nu* and the variable *dudx* appear. The coefficients are declared in a Python dictionary called *coefficients*, whilst to manage the auxiliary variables, the user has two options: the first option is to declare a new variable that will be stored; in this case, it will form part of a built-in dictionary called *varstored*, where the key will be linked to a symbolic expression and a 'group name' that allows the variable to be calculated at Python level

at run time. The second option, if only an alias is required, is to associate a new symbol with its expression; in this case, the dictionary used is *varloc*. Figure (2.1) also shows the symbolic expression

$$(u) \quad \xleftrightarrow{\mathbf{q}} \quad \texttt{\{"u" : 1\}}$$

$$(u) \quad \xleftrightarrow{\mathbf{LHS}} \quad \texttt{\{"u" : "u",\}}$$

$$\left(\frac{\partial}{\partial x}\left(\frac{u^2}{2}\right) - \frac{\partial}{\partial x}\left(\nu\frac{\partial u}{\partial x}\right)\right) \quad \xleftrightarrow{\mathbf{RHS}} \quad \texttt{\{"u" : "[0.5*u*u]_1x - [nu * dudx]_1x ", \}}$$

```
# Symbols for floating point
# coefficients
coefficients = {"nu" :  1}

# Preparing "dudx" value for varstored.
dudx = {"symb"        :  "[ u ]_1x",
        "group name"  :  "derivative"}
# The derivative is stored in the pyTree.
varstored = {"dudx" :  dudx}
```

Figure 2.1: Definition of the problem in *dNami* for Burgers 1D equation.

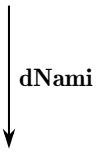
for the first-order spatial derivative; *dNami* automatically generates a Fortran backend that discretises the derivative using centered finite differences of arbitrary order, as shown in Figure (2.2). In this case, a simple second-order scheme is used. Since no ghost points are employed, the discretisation order is reduced down to a second order decentered scheme at the boundary.

Sometimes it can be useful for the user to have access to discrete mathematics, for example to impose extrapolation conditions, calculate y^+, or for other purposes. For this reason, *dNami* includes another built-in dictionary called *varshift*, where the user associates a discrete expression—shifted with respect to coordinates (i, j, k)—with a symbol. The figure shows the case where the variable *uend* has been defined to extrapolate the value of u from within the domain, i.e., at coordinate $(i-1, j, k)$.

To handle the temporal derivative , a low-storage third-order Runge-Kutta (RK) scheme is applied, although other explicit methods can be easily integrated. Parallelisation is ensured via classical domain decomposition techniques through point-to-point MPI communications using *mpi4py*.

Regarding post-processing, over the past year, dNami has been integrated into the CASSIOPEE (CFD Advanced Set of Services In an Open Python EnvironmEnt) framework developed at Onera

```
{"u"  :  "[ 0.5*u*u ]_1x - [ nu * dudx ]_1x "}
```




```
!************************************************************
!
!  building source terms in RHS for d(u)/dt ***************
!
!************************************************************

!
!
!  ([0.5_wp*u*u]_1x)
!
!

d1_conv_u_dx_0_im1jk = 0.5_wp*q(i-1,j,indvars(1))*q(i-1,j,indvars(1))

d1_conv_u_dx_0_ip1jk = 0.5_wp*q(i+1,j,indvars(1))*q(i+1,j,indvars(1))

d1_conv_u_dx_0_ijk = -0.5_wp*( d1_conv_u_dx_0_im1jk )
                     +0.5000000000000000000000_wp*( d1_conv_u_dx_0_ip1jk )

d1_conv_u_dx_0_ijk = d1_conv_u_dx_0_ijk*param_float(1)


!
!
!  -([nu*dudx]_1x)
!
!

d1_diss_u_dx_0_im1jk = param_float(1 + 5)*qst_dyn(i-1,j,indvarsst(1))

d1_diss_u_dx_0_ip1jk = param_float(1 + 5)*qst_dyn(i+1,j,indvarsst(1))

d1_diss_u_dx_0_ijk = -0.5_wp*( d1_diss_u_dx_0_im1jk )
                     +0.5000000000000000000000_wp*( d1_diss_u_dx_0_ip1jk )

d1_diss_u_dx_0_ijk = d1_diss_u_dx_0_ijk*param_float(1)
```

Figure 2.2: Code generation using *dNami* for the 1D Burgers equation.

[106], which is a set of Python modules providing advanced services for preparing CFD computations and post-processing CFD solutions.

```
# Preparing "uend" value for varshift.
uend = {"symb"   :  "u_im1jk",
        }
varshift= {"uend" :  uend}
```

Figure 2.3: Varshift dictionary in *dNami*.

2.1.1 Finite difference method

There are several approaches to handling spatial discretisation: finite elements, finite differences, finite volumes, etc. We will focus solely on finite differences. This is probably the simplest method for approximating spatial derivatives and is based on the Taylor series expansion; however, it is naturally applied to structured grids. A structured grid of dimension N is such that its points are given by the intersection of N families of lines, and each point of the mesh must lie on only one line per family [107]. In other words, each family of lines corresponds to a coordinate in computational space, generally ξ, η, ζ, and each point is uniquely defined by a triplet (i, j, k).

If we consider the general derivative of a function u with respect to the direction ξ, this is defined as:

$$\frac{\partial u}{\partial \xi} = \lim_{\Delta\xi \to 0} \frac{u(\xi + \Delta\xi) - u(\xi)}{\Delta\xi}. \tag{2.2}$$

If only the incremental ratio is considered, this provides an approximation of the derivative, the accuracy of which depends on the size of $\Delta\xi$. The smaller it is, the more accurate the approximation will be. To understand the magnitude of the error introduced, it is sufficient to expand $u(\xi + \Delta\xi)$ into a Taylor series:

$$u(\xi + \Delta\xi) = u(\xi) + \Delta\xi \frac{\partial u}{\partial \xi} + \frac{(\Delta\xi)^2}{2} \frac{\partial^2 u}{\partial \xi^2} + \frac{(\Delta\xi)^2}{3!} \frac{\partial^3 u}{\partial \xi^3} + ... \tag{2.3}$$

and by isolating the first order derivative:

$$\frac{\partial u}{\partial \xi} = \frac{u(\xi + \Delta\xi) - u(\xi)}{\Delta\xi} - \underbrace{\frac{(\Delta\xi)}{2} \frac{\partial^2 u}{\partial \xi^2} - \frac{(\Delta\xi)^2}{3!} \frac{\partial^3 u}{\partial \xi^3}}_{truncation\ error}, \tag{2.4}$$

The error introduced by using such an approximation is known as a truncation error, whilst the power of $\Delta\xi$ in the dominant term of the truncation error is referred to as the order of accuracy. In this case, we are talking about first-order accuracy.

To generalise the finite difference approximation, let us consider, for simplicity, a 1D mesh consisting of N points $\xi_i = i\Delta\xi$ (Figure 2.4). The function u at the mesh point ξ_i will be $u_i = u(\xi_i)$, using

relation 2.4, the finite difference expression of the first derivative in ξ_i can be written as:

$$\left(\frac{\partial u}{\partial \xi}\right)_i = \frac{u_{i+1} - u_i}{\Delta\xi} - \underbrace{\frac{(\Delta\xi)}{2}\left(\frac{\partial^2 u}{\partial \xi^2}\right)_i - \frac{(\Delta\xi)^2}{3!}\left(\frac{\partial^3 u}{\partial \xi^3}\right)_i + ...}_{truncation\ error} = \frac{u_{i+1} - u_i}{\Delta\xi} + O(\Delta\xi), \tag{2.5}$$

(2.5) represents the first order forward difference of the first derivative. Analogously, the backward

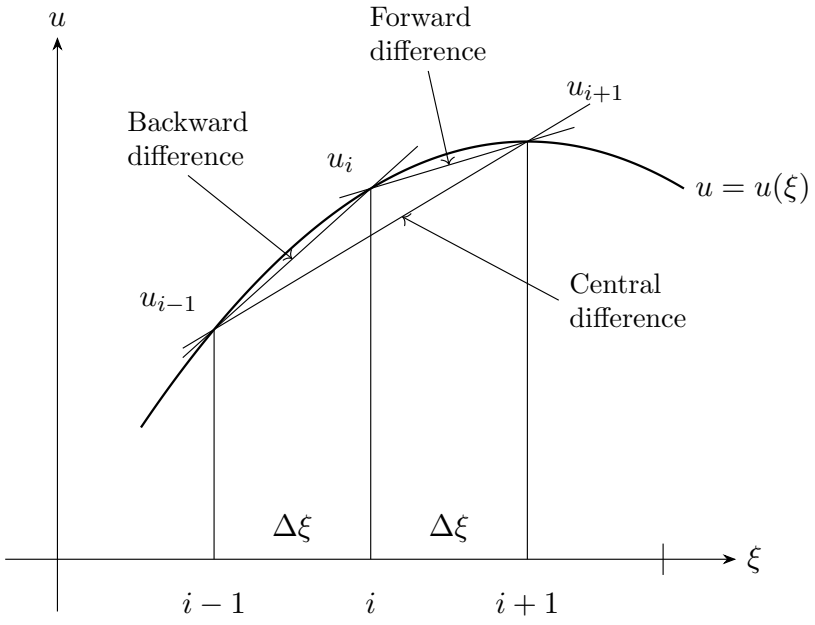


Figure 2.4: 1D representation of finite difference with different approaches.

formulation can be written for points i and $i-1$:

$$\left(\frac{\partial u}{\partial \xi}\right)_i = \frac{u_i - u_{i-1}}{\Delta\xi} + \underbrace{\frac{(\Delta\xi)}{2}\left(\frac{\partial^2 u}{\partial \xi^2}\right)_i - \frac{(\Delta\xi)^2}{3!}\left(\frac{\partial^3 u}{\partial \xi^3}\right)_i + ...}_{truncation\ error} = \frac{u_i - u_{i-1}}{\Delta\xi} + O(\Delta\xi), \tag{2.6}$$

Both approaches are referred to as one-sided, because they involve only points at one side of ξ_i. By combining (2.5) and (2.6) another finite difference approximation is obtained:

$$\left(\frac{\partial u}{\partial \xi}\right)_i = \frac{u_{i+1} - u_{i-1}}{2\Delta\xi} - \frac{(\Delta\xi)^2}{3!}\left(\frac{\partial^3 u}{\partial \xi^3}\right)_i + ... \tag{2.7}$$

This approach, on the other hand, is referred to as centered, and as can be seen, the order of accuracy is higher, namely $O(\Delta\xi^2)$. Increasing the number of points on which the discretisation is based – that is, the stencil – and by continuing to make use of the Taylor expansion, it is possible to obtain even higher orders, implicit formulations, expressions for higher-order derivatives, and so on [108] .

Even from low-order expressions, it is possible to assess the nature of the truncation error [109]. In a one-sided approach, the leading term of the truncation error has an even derivative; this results in additional numerical dissipation compared to the original equation under study. Whereas in the centred approach, the leading term of the truncation error has an odd derivative; this allows the solution to be preserved, whilst introducing a different type of error, namely a dispersion error.
In order to dissipate grid-to-grid oscillations introduced by central finite difference scheme, in *dNami* one option is to use the approach proposed in [110]. It consists in adding filter to state variables , without affecting physical long waves , as follows:

$$u^f(\xi_0) = u(\xi_0) - \sigma_d D_u(\xi_0), \qquad D_u(\xi_0) = \sum_{j=-N}^{N} d_j u(\xi_0 + j\Delta\xi), \tag{2.8}$$

where $0 < \sigma_d < 1$ and $d_j = d_{-j}$.

2.1.2 Runge Kutta methods

Let us consider the problem (2.1) in semi-discretised form, written as:

$$\frac{\partial q}{\partial t} = f(q, t), \tag{2.9}$$

where the subscripts relating to spatial discretisation have been dropped so as not to overcomplicate the subsequent notation. To handle the time integration in *dNami*, explicit Runge-Kutta (RK) methods are used. These are single-step, multi-stage methods whose general form is:

$$q^{n+1} = q_n + \Delta t \sum_{i=1}^{s} b_i K_i, \qquad n \geq 0 \tag{2.10}$$

where Δt is the time step such that $t^{n+1} = t^n + \Delta t$, s is the number of stages, b_i are the weight coefficients, and K_i is:

$$K_i = f\left(t^n + c_i \Delta t, q^n + \sum_{j=1}^{s} a_{ij} K_j\right) \tag{2.11}$$

with c_i coefficients that identify the fraction of time step at which f is computed, and a_{ij} coefficients that depend on each stage.
However, the general formulation leads to oscillations in the presence of steep gradients; for this reason, RK-TVD methods [111]-[112] have been implemented. These methods ensure that the total variation TV, defined as:

$$TV(q^n) = \sum_{p} |q^n_{p+1} - q^n_p|, \tag{2.12}$$

where the index p represents a point in the computational domain, does not increase over time:

$$TV(q^{n+1}) \leq TV(q^n). \tag{2.13}$$

The general formulation for RK-TVD is as follows:

$$\begin{aligned} q^0 &= q^n, \\ q^i &= \sum_{j=0}^{i-1} \left(\alpha_{ij} q^j + \Delta t \beta_{ij} f(q^j) \right), \qquad i = 1, 2, .., s \end{aligned} \tag{2.14}$$

In practical terms, it is a combination of Euler steps in which $\alpha_{ij} \geq 0$, $\beta_{ij} \geq 0$ and for each stage $\sum_{j=0}^{i-1} \alpha_{ij} = 1$ (convex combination).

Without going into the details of the stability analysis of numerical methods, it is worth spending a few words about the choice of time step. Indeed, for problems involving the Navier-Stokes equations, which contain both transport and diffusion terms, two conditions must be satisfied.

In the simple case of the 1D transport equation solved using explicit Euler methods, the condition imposed to ensure stability is known as the CFL condition and is defined as follows:

$$CFL = \frac{a \Delta t}{\Delta \xi} < 1, \tag{2.15}$$

with a transport velocity. Whereas in the case of the simple diffusion problem, the condition for ensuring stability is known as the Fourier condition and is defined as follows:

$$FOU = \frac{\nu \Delta t}{\Delta \xi^2} < 0.5. \tag{2.16}$$

The limit values imposed on CFL and FOU depend on the scheme adopted; furthermore, the expressions for the CFL and Fourier numbers also change for the full Navier-Stokes equations. In explicit schemes, this limitation necessitates the use of very small Δt values, particularly when using very fine meshes.

2.1.3 Shock capturing scheme

In addition to using filters as in [110], *dNami* offers the option of using a shock-capturing scheme which is better suited to situations where shocks are present, such as some of the cases discussed in this work. The shock capturing scheme adopted is based on the one initially proposed by Jameson [113]and then generalised by Sciacovelli *et al.* [114]. The scheme consists of adding a high-order

artificial dissipation term to the system of equations, but due to a pressure sensor, the numerical dissipation becomes low-order locally in order to resolve discontinuities. If we consider, for example, the semi-discrete equation in space for a generic variable q, in a single direction ξ, this becomes:

$$\frac{\partial q}{\partial t} = \mathcal{N}_i(q) - \mathcal{D}_i(q), \tag{2.17}$$

where $\mathcal{N}_i(q)$ is the spatial discretisation operator and $\mathcal{D}$ is the new dissipative operator:

$$\begin{aligned} \mathcal{D}_i(q) &= d_{i+\frac{1}{2}} - d_{i-\frac{1}{2}}, \\ d_{i+\frac{1}{2}} &= \rho(\mathcal{L})_{i+\frac{1}{2}} \left[\epsilon_2 \delta q - (-1)^{(P+1)} \epsilon_{2(P+2)} \delta^{(2P+3)} q\right]_{i+\frac{1}{2}}, \end{aligned} \tag{2.18}$$

with:

$$\epsilon_{2i+\frac{1}{2}} = k_2 max(\phi_i, \phi_{i+1}), \qquad \epsilon_{2(P+2)i+\frac{1}{2}} = max\left(0, k_{2(P+2)} - k_\epsilon \epsilon_{2i+\frac{1}{2}}\right). \tag{2.19}$$

$\rho(\mathcal{L})_{i+\frac{1}{2}}$ is the spectral radius of the Jacobian matrix in the $\xi-$direction, k_2 and $k_{2(P+2)}$ are adjustable dissipation coefficients, k_ϵ is a constant depending on the order used for the scheme. Finally, the shock sensor reads:

$$\phi_i = \frac{1}{2}\left[1 - tanh\left(2.5 + 10\frac{10\delta x}{c}\nabla \cdot \mathbf{u}\right)\right] \frac{(\nabla \cdot \mathbf{u})^2}{(\nabla \cdot \mathbf{u})^2 + |\nabla \times \mathbf{u}|^2 + \epsilon} \frac{|p_{i+1} - 2p_i + p_{i-1}|}{|p_{i+1} + 2p_i + p_{i-1}|}, \tag{2.20}$$

The ϕ_i sensor consists of three components. Starting from the right, we have the pressure sensor:

$$\frac{|p_{i+1} - 2p_i + p_{i-1}|}{|p_{i+1} + 2p_i + p_{i-1}|}, \tag{2.21}$$

which is the classic pressure sensor used by Jameson, then we have the Ducros sensor [115]:

$$\frac{(\nabla \cdot \mathbf{u})^2}{(\nabla \cdot \mathbf{u})^2 + |\nabla \times \mathbf{u}|^2 + \epsilon}, \tag{2.22}$$

which allows to limit numerical dissipation in the presence of vortices thanks to the presence of the vorticity in the denominator. Finally the term:

$$\frac{1}{2}\left[1 - tanh\left(2.5 + 10\frac{10\delta x}{c}\nabla \cdot \mathbf{u}\right)\right], \tag{2.23}$$

is a modification term proposed in [116], which enables dissipation to be activated only in areas of high compression, i.e. where the divergence is negative.

2.1.4 Boundary conditions

dNami includes several pre-defined boundary condition modules suitable for various scenarios for solving the NS equations; users also have the option of adding new ones. In general, in *dNami* we can distinguish between two types of conditions. The first ones are identified as q conditions, which modify the value of the primitive variable q_i following an assignment based on the physics of the problem (for example, the inlet velocity is specified). This category therefore includes all Dirichlet and Neumann conditions. The other possibility is to impose RHS-type conditions, i.e. conditions in which the right-hand side (RHS) of the equation to be solved is modified (for example, the solution of equations in characteristic form, which we shall see later).
In this subsection, we will detail the boundary conditions that have been used in this thesis. The boundary conditions used for the turbulent variables have already been specified in the section on turbulence models; therefore, here we focus on the classical NS variables.

2.1.4.1 No-slip adiabatic wall

This type of condition physically requires the velocity to be zero in all directions and the normal heat flux to the wall to be zero. This translates into imposing four q-type conditions: the three velocity components set to zero and the internal energy gradient at the wall set to zero, achieved by setting the discretisation of the derivative of e in the direction normal to the wall to zero via the *varshift*:

$$\frac{\partial e}{\partial \eta} \approx \frac{e_{ijp1k} - e_{ijk}}{\Delta \eta}, \qquad \Rightarrow \qquad e_{ijk} = E_{ijk} = e_{ijp1k}, \tag{2.24}$$

where the normal direction to wall $j\eta$, corresponding to j index, and a first-order approximation are taken as examples. As for the boundary condition on density, this depends on the specific case under consideration. In attached boundary layers, the pressure variation in the direction normal to the wall is negligible; therefore, a q-type condition can be formulated by combining a zero pressure gradient with the perfect gas law, or, more generally, the continuity equation can be solved suppressing tangential velocity gradients. In this case, the condition is of the RHS type.

2.1.4.2 Slip adiabatic wall

Unlike in the previous case, under slip-wall conditions, the tangential velocities are extrapolated whilst the normal velocity is set to zero to ensure that the wall is not penetrated. This makes it more complex

to express slip wall condition in curvilinear coordinates, because the velocity vector components along the curvilinear directions (u_ξ, u_η, u_ζ) do not correspond to the Cartesian components (u, v, w). In order to define (u_ξ, u_η, u_ζ), we must define the unit vectors of the curvilinear system, which we denote by $\boldsymbol{i}, \boldsymbol{j}, \boldsymbol{k}$. These can be calculated as:

$$\begin{aligned}
\boldsymbol{i} &= \left(\frac{dx}{d\xi}, \frac{dy}{d\xi}, \frac{dz}{d\xi}\right)\frac{1}{h_\xi}, \qquad & h_\xi &= \sqrt{\left(\frac{dx}{d\xi}\right)^2 + \left(\frac{dy}{d\xi}\right)^2 + \left(\frac{dz}{d\xi}\right)^2}, \\
\boldsymbol{j} &= \left(\frac{dx}{d\eta}, \frac{dy}{d\eta}, \frac{dz}{d\eta}\right)\frac{1}{h_\eta}, \qquad & h_\eta &= \sqrt{\left(\frac{dx}{d\eta}\right)^2 + \left(\frac{dy}{d\eta}\right)^2 + \left(\frac{dz}{d\eta}\right)^2}, \\
\boldsymbol{k} &= \left(\frac{dx}{d\zeta}, \frac{dy}{d\zeta}, \frac{dz}{d\zeta}\right)\frac{1}{h_\zeta}, \qquad & h_\zeta &= \sqrt{\left(\frac{dx}{d\zeta}\right)^2 + \left(\frac{dy}{d\zeta}\right)^2 + \left(\frac{dz}{d\zeta}\right)^2},
\end{aligned} \tag{2.25}$$

where h_i are the scale factors. To calculate the velocity components in the curvilinear system, we simply multiply the velocity vector $\boldsymbol{u} = (u, v, w)$ scalarly by the unit vectors:

$$\begin{aligned}
u_\xi &= \boldsymbol{u} \cdot \boldsymbol{i} = \frac{1}{h_\xi}\left(u\frac{dx}{d\xi} + v\frac{dy}{d\xi} + w\frac{dz}{d\xi}\right), \\
u_\eta &= \boldsymbol{u} \cdot \boldsymbol{j} = \frac{1}{h_\eta}\left(u\frac{dx}{d\eta} + v\frac{dy}{d\eta} + w\frac{dz}{d\eta}\right), \\
u_\zeta &= \boldsymbol{u} \cdot \boldsymbol{k} = \frac{1}{h_\zeta}\left(u\frac{dx}{d\zeta} + v\frac{dy}{d\zeta} + w\frac{dz}{d\zeta}\right).
\end{aligned} \tag{2.26}$$

Let us now consider, by way of example, that the normal direction to the wall is η represented by the unit vector $\boldsymbol{j}$, so that u_η is the normal velocity whilst the other two are the tangential components. The condition at j-max is given by

$$\boldsymbol{u} = (u_\xi, 0, u_\zeta)_{j-1}. \tag{2.27}$$

Now this must be reprojected with respect to the directions (x, y, z); if we denote the respective unit vectors by ($\boldsymbol{e_1}$, $\boldsymbol{e_2}$, $\boldsymbol{e_3}$), these will be:

$$\boldsymbol{e_1} = (1, 0, 0), \qquad \boldsymbol{e_2} = (0, 1, 0), \qquad \boldsymbol{e_3} = (0, 0, 1), \tag{2.28}$$

so the final conditions for (u,v,w) can be written as:

$$\begin{aligned}
u &= (u_\xi)_{j-1}(\boldsymbol{e_1} \cdot \boldsymbol{i}) + (u_\zeta)_{j-1}(\boldsymbol{e_1} \cdot \boldsymbol{k}), \\
v &= (u_\xi)_{j-1}(\boldsymbol{e_2} \cdot \boldsymbol{i}) + (u_\zeta)_{j-1}(\boldsymbol{e_2} \cdot \boldsymbol{k}), \\
w &= (u_\xi)_{j-1}(\boldsymbol{e_3} \cdot \boldsymbol{i}) + (u_\zeta)_{j-1}(\boldsymbol{e_3} \cdot \boldsymbol{k}),
\end{aligned} \tag{2.29}$$

As for the other variables, since the non-zero wall velocities imply $E \neq e$, the zero-gradient condition will therefore be imposed directly on the total energy. For ρ, however, the same considerations apply as for the no-slip case.

2.1.4.3 Inflow/Outflow

To impose inflow or outflow conditions in open flows in *dNami*, one needs to solve the equations written in characteristic form. This method, known as NSCBC, was first introduced for hyperbolic systems in [117] - [118] and subsequently extended to the Navier-Stokes equations in [119]. To demonstrate how this method works, let us consider the boundary normal to the direction ξ, for example at $\xi = L$. The characteristic waves will travel in a direction normal to the boundary, so we need only rewrite the hyperbolic part of the equations in the direction ξ in characteristic form. First, we introduce the primitive variable vector $\mathbf{q_p} = (\rho, u, v, w, p)$ and the transformation matrix $\boldsymbol{P}$ and its inverse $\boldsymbol{P}^{-1}$ such that:

$$\boldsymbol{P} = \begin{bmatrix} 1 & 0 & 0 & 0 & 0 \\ u & \rho & 0 & 0 & 0 \\ v & 0 & \rho & 0 & 0 \\ w & 0 & 0 & \rho & 0 \\ \frac{1}{2}(u^2+v^2+w^2) & \rho u & \rho v & \rho w & \frac{1}{\gamma-1} \end{bmatrix}, \tag{2.30}$$

$$\boldsymbol{P}^{-1} = \begin{bmatrix} 1 & 0 & 0 & 0 & 0 \\ -\frac{u}{\rho} & \frac{1}{\rho} & 0 & 0 & 0 \\ -\frac{v}{\rho} & 0 & \frac{1}{\rho} & 0 & 0 \\ -\frac{w}{\rho} & 0 & 0 & \frac{1}{\rho} & 0 \\ \frac{\gamma-1}{2}(u^2+v^2+w^2) & -(\gamma-1)u & -(\gamma-1)v & -(\gamma-1)w & \gamma-1 \end{bmatrix}, \tag{2.31}$$

then we can rewrite 1.25:

$$\frac{\partial \mathbf{q_p}}{\partial t} + \boldsymbol{P}^{-1}\frac{\partial \mathbf{F}}{\partial \xi} + \mathbf{C} = \mathbf{D}, \tag{2.32}$$

where $\mathbf{C}$ contains the transversal convective terms and $\mathbf{D}$ contains all the diffusive terms. The flux in the direction ξ can be expressed by directly showing the dependence on the primitive variables:

$$\frac{\partial \mathbf{q_p}}{\partial t} + \boldsymbol{P}^{-1}\frac{\partial \mathbf{F}}{\partial \mathbf{q_p}}\frac{\partial \mathbf{q_p}}{\partial \xi} + \mathbf{C} = \mathbf{D} \tag{2.33}$$

The matrix to be diagonalised is therefore:

$$\boldsymbol{P}^{-1}\frac{\partial \mathbf{F}}{\partial \mathbf{q_p}} = \begin{bmatrix} U & \rho\xi_x & \rho\xi_y & \rho\xi_z & 0 \\ 0 & U & 0 & 0 & \frac{\xi_x}{\rho} \\ 0 & 0 & U & 0 & \frac{\xi_y}{\rho} \\ 0 & 0 & 0 & U & \frac{\xi_z}{\rho} \\ 0 & \gamma p\xi_x & \gamma p\xi_y & \gamma p\xi_z & U \end{bmatrix}. \tag{2.34}$$

Following the diagonalisation process, finally the system becomes:

$$\frac{\partial \mathbf{q_p}}{\partial t} + \boldsymbol{S_\xi}\boldsymbol{\Lambda_\xi}\boldsymbol{S_\xi}^{-1}\frac{\partial \mathbf{q_p}}{\partial \xi} + \mathbf{C} = \mathbf{D}, \tag{2.35}$$

from which the amplitude of characteristic waves $\mathcal{L}_i$ can be distinguished:

$$\boldsymbol{\Lambda_\xi} \boldsymbol{S_\xi^{-1}} \frac{\partial \mathbf{q_p}}{\partial \xi} = \begin{bmatrix} \mathcal{L}_1 \\ \mathcal{L}_2 \\ \mathcal{L}_3 \\ \mathcal{L}_4 \\ \mathcal{L}_5 \end{bmatrix} = \begin{bmatrix} \left(U - c\sqrt{\xi_x^2+\xi_y^2+\xi_z^2}\right)\left[\frac{\partial p}{\partial \xi} - \frac{\rho c}{\sqrt{\xi_x^2+\xi_y^2+\xi_z^2}}\left(\xi_x \frac{\partial u}{\partial \xi} + \xi_y \frac{\partial v}{\partial \xi} + \xi_z \frac{\partial w}{\partial \xi}\right)\right] \\ U\left[c^2 \frac{\partial \rho}{\partial \xi} - \frac{\partial p}{\partial \xi}\right] \\ U\left[-\xi_y \frac{\partial u}{\partial \xi} + \xi_x \frac{\partial v}{\partial \xi}\right] \\ U\left[-\xi_z \frac{\partial u}{\partial \xi} + \xi_x \frac{\partial w}{\partial \xi}\right] \\ \left(U + c\sqrt{\xi_x^2+\xi_y^2+\xi_z^2}\right)\left[\frac{\partial p}{\partial \xi} + \frac{\rho c}{\sqrt{\xi_x^2+\xi_y^2+\xi_z^2}}\left(\xi_x \frac{\partial u}{\partial \xi} + \xi_y \frac{\partial v}{\partial \xi} + \xi_z \frac{\partial w}{\partial \xi}\right)\right] \end{bmatrix}, \quad (2.36)$$

with associated wave velocities λ_i :

$$\begin{bmatrix} \lambda_1 \\ \lambda_2 \\ \lambda_3 \\ \lambda_4 \\ \lambda_5 \end{bmatrix} = \begin{bmatrix} U - c\sqrt{\xi_x^2+\xi_y^2+\xi_z^2} \\ U \\ U \\ U \\ U + c\sqrt{\xi_x^2+\xi_y^2+\xi_z^2} \end{bmatrix}. \quad (2.37)$$

Finally it is possible to write the flux in the direction ξ by explicitly showing the $\mathcal{L}_i$ as follows:

$$\boldsymbol{S_\xi \Lambda_\xi S_\xi^{-1}} \frac{\partial \mathbf{q_p}}{\partial \xi} = \begin{bmatrix} \frac{1}{c^2}\left[\mathcal{L}_2 + \frac{1}{2}(\mathcal{L}_1 + \mathcal{L}_5)\right] \\ \frac{\xi_x}{\sqrt{\xi_x^2+\xi_y^2+\xi_z^2}}\left(\frac{\mathcal{L}_5 - \mathcal{L}_1}{2\rho c}\right) - \frac{\xi_y \mathcal{L}_3 + \xi_z \mathcal{L}_4}{\xi_x^2+\xi_y^2+\xi_z^2} \\ \frac{\xi_y}{\sqrt{\xi_x^2+\xi_y^2+\xi_z^2}}\left(\frac{\mathcal{L}_5 - \mathcal{L}_1}{2\rho c}\right) + \frac{(\xi_x^2+\xi_z^2)\mathcal{L}_3 - \xi_y \xi_z \mathcal{L}_4}{\xi_x(\xi_x^2+\xi_y^2+\xi_z^2)} \\ \frac{\xi_z}{\sqrt{\xi_x^2+\xi_y^2+\xi_z^2}}\left(\frac{\mathcal{L}_5 - \mathcal{L}_1}{2\rho c}\right) + \frac{(\xi_x^2+\xi_y^2)\mathcal{L}_4 - \xi_y \xi_z \mathcal{L}_3}{\xi_x(\xi_x^2+\xi_y^2+\xi_z^2)} \\ \frac{1}{2}(\mathcal{L}_1 + \mathcal{L}_5) \end{bmatrix}. \quad (2.38)$$

To solve the system (2.35) at the boundary, it will be necessary to calculate the values of each $\mathcal{L}_i$. There is no simple and exact method for calculating the $\mathcal{L}_i$ values of the incoming waves; what is generally done is to use a simplified system, known as the LODI system (Localized One-Dimensional

Inviscid), which reads:

$$\begin{cases} \dfrac{\partial \rho}{\partial t} + \dfrac{1}{c^2}\left[\mathcal{L}_2 + \dfrac{1}{2}(\mathcal{L}_1 + \mathcal{L}_5)\right] = 0, \\ \dfrac{\partial u}{\partial t} + \dfrac{\xi_x}{\sqrt{\xi_x^2+\xi_y^2+\xi_z^2}}\left(\dfrac{\mathcal{L}_5 - \mathcal{L}_1}{2\rho c}\right) - \dfrac{\xi_y\mathcal{L}_3 + \xi_z\mathcal{L}_4}{\xi_x^2+\xi_y^2+\xi_z^2} = 0, \\ \dfrac{\partial v}{\partial t} + \dfrac{\xi_y}{\sqrt{\xi_x^2+\xi_y^2+\xi_z^2}}\left(\dfrac{\mathcal{L}_5 - \mathcal{L}_1}{2\rho c}\right) + \dfrac{(\xi_x^2+\xi_z^2)\mathcal{L}_3 - \xi_y\xi_z\mathcal{L}_4}{\xi_x(\xi_x^2+\xi_y^2+\xi_z^2)} = 0, \\ \dfrac{\partial w}{\partial t} + \dfrac{\xi_z}{\sqrt{\xi_x^2+\xi_y^2+\xi_z^2}}\left(\dfrac{\mathcal{L}_5 - \mathcal{L}_1}{2\rho c}\right) + \dfrac{(\xi_x^2+\xi_y^2)\mathcal{L}_4 - \xi_y\xi_z\mathcal{L}_3}{\xi_x(\xi_x^2+\xi_y^2+\xi_z^2)} = 0, \\ \dfrac{\partial p}{\partial t} + \dfrac{1}{2}(\mathcal{L}_1 + \mathcal{L}_5) = 0, \end{cases} \tag{2.39}$$

where all transverse and viscous terms from (2.35) have been neglected.

Now that the general equations have been derived, let us see how the NSCBC method works for imposing boundary conditions. The method consists of three steps: 1) the physical boundary conditions are imposed, and for each condition set, the corresponding equation is removed from the system (2.35) (for example, if one wishes to impose the pressure value, the energy conservation equation is removed); 2) The LODI relations are used to compute the value of the $\mathcal{L}_i$ for the incoming waves; 3) The remaining equations of the system (2.35) are used in combination with the computed values of the $\mathcal{L}_i$.

When dealing with the full set of equations (2.35), additional conditions for the viscous terms are theoretically required. In *dNami*, this is not done as these conditions are used for open flows where there are no walls, so it is a good approximation to consider only the convective terms. In [120]-[121], it is also shown how to include transverse terms in the characteristic analysis; again, this development is not currently present in *dNami*. Let us now look at the main boundary conditions applied using the NSCBC approach.

-**subsonic inflow**; this type of condition occurs in various flow configurations; the values of the velocity components and the temperature are generally fixed (we consider the plane at $\xi = 0$)

$$\begin{aligned} u(0,\eta,\zeta,t) &= u_0(\eta,\zeta,t), \\ v(0,\eta,\zeta,t) &= v_0(\eta,\zeta,t), \\ w(0,\eta,\zeta,t) &= w_0(\eta,\zeta,t), \\ T(0,\eta,\zeta,t) &= T_0(\eta,\zeta,t). \end{aligned} \tag{2.40}$$

The only wave leaving the domain is $\mathcal{L}_1$, which propagates at a speed of $\lambda_1 = U - c\sqrt{\xi_x^2 + \xi_y^2 + \xi_z^2}$. From the system (2.35), we retain only the continuity equation, as all other variables have been fixed. From the LODI system (2.39), we derive the expressions for the incoming $\mathcal{L}_i$ and then solve the continuity equation. Since we are setting the 3 component of velocity and the temperature, from system 2.39 we get:

$$\begin{aligned} \mathcal{L}_3 &= \mathcal{L}_4 = 0, \\ \mathcal{L}_5 &= \mathcal{L}_1, \\ \mathcal{L}_2 &= \frac{1}{2}(\gamma - 1)(\mathcal{L}_1 + \mathcal{L}_5) \end{aligned} \tag{2.41}$$

It is clear that, from a coding perspective, q-type conditions are always used, except for density, for which an RHS-type condition is used;

supersonic inflow ; this is the simplest case: always considering the plane at $\xi = 0$, all waves enter the domain and therefore all variables must be fixed; nothing can be extrapolated:

$$\begin{aligned} \rho(0, \eta, \zeta, t) &= \rho_0(\eta, \zeta, t), \\ u(0, \eta, \zeta, t) &= u_0(\eta, \zeta, t), \\ v(0, \eta, \zeta, t) &= v_0(\eta, \zeta, t), \\ w(0, \eta, \zeta, t) &= w_0(\eta, \zeta, t), \\ T(0, \eta, \zeta, t) &= T_0(\eta, \zeta, t), \end{aligned} \tag{2.42}$$

in *dNami*, this translates to using all conditions of type q;

subsonic non-reflective outflow; if we consider the boundary at $\xi = L$, use perfectly non-reflective boundary conditions, by setting the amplitude of the incoming wave to zero, would render the problem ill-posed, as there would then be no way to keep the pressure constant at infinity. Similarly, given that there are four outgoing waves and one incoming wave $\mathcal{L}_1$, fixing the pressure value would generate unwanted acoustic waves. For this reason, a slightly modified approach is adopted in this case. Although a specific pressure value p_∞ is desired, all the equations in (2.35) are retained. All the exiting $\mathcal{L}_i$ are extrapolated while the constant pressure condition is used to calculate $\mathcal{L}_1$

$$\mathcal{L}_1 = K(p - p_\infty), \tag{2.43}$$

where $K = \sigma(1 - M_{max}^2)c/L$ with M_{max}^2 is the maximum value of the Mach number, L is the domain size in ξ direction and σ is a constant. This form of K was proposed by [122] and, in general, the value of σ is set to 0.58. Unlike in the previous case, therefore, all RHS-type conditions are used.

2.1.4.4 Riemann invariant inflow/outflow

The inflow/outflow conditions detailed in the previous section are not suitable for confined flows; for this reason, two further type of inflow/outflow conditions [123] have been considered that are better suited to flow within a nozzle or diffuser, which is one of the main cases addressed in this work.

subsonic inflow; in our work, this condition is applied in the specific case where, at the boundary, the velocity components along ξ and along x coincide and are the only non-zero velocity components; it is, of course, possible to generalise the following approach, and the reader may find further details in [123]. We set total pressure p_t and total temperature T_t and we assume that the flow across the boundary is adiabatic and isentropic; in this way, we can exploit the conservation of total enthalpy H_t and the Riemann invariant R^+.

$$\begin{aligned} H_t &= \frac{p}{\rho}\left(\frac{\gamma}{\gamma-1}\right) + \frac{1}{2}(u^2+v^2+w^2), \\ R^+ &= -u - \frac{2c_b}{\gamma-1}. \end{aligned} \tag{2.44}$$

After evaluating previous quantities at the interior points, the two relations can be combined to obtain a quadratic equation for c_b, which is the speed of sound at the boundary:

$$\left[1+\frac{2}{\gamma-1}\right]c_b^2 + 2R^+c_b + \frac{\gamma-1}{2}\left((R^+)^2 - 2H_t\right) = 0. \tag{2.45}$$

The only physically meaningful result is the larger of the two roots; from this, it is possible to calculate the velocity at the boundary and the Mach number:

$$u_b = -\frac{2c_b}{\gamma-1} - R^+, \qquad\qquad M_b = \frac{u_b}{c_b}, \tag{2.46}$$

and then pressure and temperature from the isentropic relations, starting from the total quantities:

$$p_b = \frac{p_t}{\left(1+\frac{\gamma-1}{2}M_b^2\right)^{\frac{\gamma}{\gamma-1}}}, \qquad\qquad T_b = \frac{T_t}{1+\frac{\gamma-1}{2}M_b^2}. \tag{2.47}$$

Within *dNami*, therefore, the values of total enthalpy and the Riemann invariant are calculated using the *varshift*, whilst all the imposed conditions are of type q .

subsonic outflow; if the outflow is subsonic, the outlet pressure p_b is fixed and the other variables are extrapolated, whereas if the flow is supersonic, all variables are extrapolated.

2.2 liNami

liNami is a module of *dNami* that enables the source code generated by *dNami* to be automatically differentiated via TAPENADE [55], creating new differentiated code that retains the syntax, structure and performance of the original source code. Furthermore, coupled with PETSc [124] and SLPEc [125], it contains functions that allow the user to perform the various types of linear analysis described in the previous section.

2.2.1 Automatic differentiation

Suppose we have a program $\mathbf{P}$ which given an input vector $\mathbf{X}$ gives as output a new vector $\mathbf{Y} = \mathbf{P}(\mathbf{X})$, and we want to calculate the derivative of the result $\mathbf{Y}$. The simplest choice is to use finite differences, and so given the normal direction to the input vector $d\mathbf{X}$ and a small positive value ϵ it is possible to approximate the derivative by its incremental ratio:

$$\frac{\mathbf{P}(\mathbf{X} + \epsilon \mathbf{dX}) - \mathbf{P}(\mathbf{X})}{\epsilon} \tag{2.48}$$

or with centred differences:

$$\frac{\mathbf{P}(\mathbf{X} + \epsilon \mathbf{dX}) - \mathbf{P}(\mathbf{X} - \epsilon \mathbf{dX})}{2\epsilon} \tag{2.49}$$

whose limit for ϵ tending to zero coincides with the analytic derivative. The problem is that the computed derivative is just an approximation leading to truncation errors.
A better choice is certainly to use automatic differentiation. It does not require writing a new program, the program $\mathbf{P}$ is sufficient. It builds a new, augmented, program $\mathbf{P'}$, that computes the analytical derivatives along with the original program. Whenever a variable q is defined in $\mathbf{P}$, the programme $\mathbf{P'}$ defines a new variable dq representing the differentiated variable. In addition, each time an operation is performed in the starting program, the new program $\mathbf{P'}$, which we call differentiated program, performs one more operation related to differentials. For example, if we consider that the program $\mathbf{P}$ execute the following operation on variables: $a, b, T(10), c$ with T an array:

$$a = b * T(10) + c \tag{2.50}$$

then the differentiated program must execute additional operations on the variables and their differentials:

$$da = b * dT(10) + T(10) * db + dc \tag{2.51}$$

in this way derivative are computed analytically and there are no more approximation.
TAPENADE uses automatic differentiation but there are two different ways to implement it.

- **Overloading**: consists in telling the compiler that each real number is replaced by a pair of real numbers, the second holding the differential [126]. Each elementary operation on real numbers is overloaded, i.e. internally replaced by a new one, working on pairs of reals, that computes the value and its differential. The advantage is that the original program is virtually unchanged, since everything is done at compile time. The drawback is that the resulting program runs slowly.

- **Source transformation**: consists in adding into the program the new variables, arrays, and data structures that will hold the derivatives, and in adding the new instructions that compute these derivatives. The advantage is that the resulting program can be compiled into an efficient code. The drawback is that this is an enormous transformation, that cannot be done by hand on large programs. Tools are needed to perform this transformation correctly and rapidly.

TAPENADE uses source transformation and *liNami* is the tool used to post-process the differentiated code. Let us now consider a simple example of a function that calculates the square root, to understand the output of TAPENADE and the subsequent output of *liNami* . It can be seen in Figure 2.5 that TAPENADE adds a '_d' suffix to the differentiated variables and then rewrites the operations on the original variables, whereas *liNami* simply changes the names of the differentiated variables, as these will in fact constitute the main terms in the new linear code, whilst an 'fp' is added to the original variables as they will form the fixed point of the linearised code. All operations relating to the fixed-point variables are therefore removed as they have already been carried out in the non-linear code.
Let us therefore return to the case of the 1D Burgers equation initially presented in Fig. 2.1; specifically, we will consider only the convective term and how it is transformed by the successive application of TAPENADE and *liNami* in (2.6). Once again, it can be observed that the term in the non-linear code corresponding to $u^2/2$ is correctly differentiated into $2u_{fp}u/2$, and the differentiated variable has taken the place of the original one, which has instead become a fixed-point variable.

Automatic differentiation therefore appears to be a simple and effective tool for obtaining a linear version of the code without having to perform the differentiation operations manually. However, a

```
subroutine compute_root_square(x, y)
  real ::  x, y
  y = sqrt(x)
end subroutine
```

TAPENADE

```
subroutine compute_root_square_d(x, x_d, y, y_d)
  real ::  x, x_d, y, y_d
  !  TAPENADE write differentiations rules !
  y_d = x_d / (2.0 * sqrt(x))
  !  then recompute original variables
  y = sqrt(x)
end subroutine
```

liNami

```
subroutine compute_root_square_d(xfp, x, y)
  real ::  xfp, x, y
  !  liNami mantain only the new differentiated lines !
  y = x / (2.0 * sqrt(xfp))
  !  no need to recompute original values !
end subroutine
```

Figure 2.5: Source transformation performed by TAPENADE and subsequent post-treatment performed by *liNami*.

programme generally consists of a sequence of instructions that can be expressed as a composite function, and these instructions may be interspersed with control statements (if conditions) that are not differentiable; this is not a problem for TAPENADE as it performs piecewise differentiation.
Another problem arises in URANS equations where turbulence models are present; they are full of non-differentiable functions (min, max for example). How should one proceed in this case? One option is certainly to use regularisation functions to analytically handle the various discontinuities imposed by the model. Nevertheless, this requires further effort on the part of the user, who must modify the initial equations to obtain a result that is 'less accurate'. The second option is to rely on automatic differentiation; in the work by Lee et al. [127], this problem is rigorously addressed.
The authors demonstrate that if a function belongs to the class **PAP** (*Piecewise Analytic under Ana-*

```
!
!
!  ([0.5_wp*u*u]_1x)
!
!

d1_conv_u_dx_0_im1jk = 0.5_wp*q(i-1,j,indvars(1))*q(i-1,j,indvars(1))

d1_conv_u_dx_0_ip1jk = 0.5_wp*q(i+1,j,indvars(1))*q(i+1,j,indvars(1))

d1_conv_u_dx_0_ijk = -0.5_wp*( d1_conv_u_dx_0_im1jk )
                     +0.50000000000000000000_wp*( d1_conv_u_dx_0_ip1jk )

d1_conv_u_dx_0_ijk = d1_conv_u_dx_0_ijk*param_float(1)
```

TAPENADE + liNami

```
!
!
!  ([0.5_wp*2.0_wp*ufp*u]_1x)
!
!

      temp = qst(i-1, j, indvarsfp(1))
      d1_conv_u_dx_0_im1jkd = 0.5_wp*2*temp*q(i-1, j, indvars(1))

      temp = qst(i+1, j, indvarsfp(1))
      d1_conv_u_dx_0_ip1jkd = 0.5_wp*2*temp*q(i+1, j, indvars(1))

      d1_conv_u_dx_0_ijkd = 0.50000000000000000000_wp*d1_conv_u_dx_0_ip1jkd
                          - 0.5_wp*d1_conv_u_dx_0_im1jkd

      d1_conv_u_dx_0_ijkd = param_float(1)*d1_conv_u_dx_0_ijkd
```

Figure 2.6: Source transformation performed by TAPENADE + *liNami* for 1D Burgers convective term.

lytic Partition), then its automatic differentiation will always be robust and well-defined.

But what does it mean for a function to be PAP? Without going into too much heavy mathematical formalism, it means that the domain of the function can be divided into several 'zones' (the *analytic partitions*) separated from one another by geometrically smooth and well-defined boundaries (continuous equations). Within each of these zones, the function must behave in a perfectly smooth and differentiable manner (i.e. it must be an analytic function). In terms of computer programming, this is equivalent to an `if-else` conditional block in which the test conditions have no pathological corners

and the mathematical instructions contained in each branch are standard continuous functions. Consider, for example, the function $f(x) = \max(0, x)$, frequently used in numerical limiters. We can divide the domain into two analytic partitions: the first for strictly positive values (where the test condition is $x > 0$) and the second for negative or zero values (whose complementary condition is $x \leq 0$). The resulting piecewise representation will simply be:

- In the first branch, the function is the identity line $f_1(x) = x$.

- In the second branch, the function is the constant $f_2(x) = 0$.

In this case, automatic differentiation is well-defined. At the critical point $x = 0$, where the classical derivative does not exist, the following occurs: the AD tool does not attempt to evaluate an ambiguous or undefined geometric construct. On the contrary, the logical architecture of the source code (`if-else`) will in any case force the algorithm to branch onto one of the two paths. Since $x = 0$ does not satisfy the strictly greater condition ($0 > 0$ is false), the code will jump to the `else` branch, where the function $f_2(x) = 0$ is defined. The automatic differentiation tool will simply calculate the exact derivative of this latter branch, returning an exact zero. This particular derivative, which depends strictly on the computational execution path taken by the code, is called the *intentional derivative*. Its existence at every point in the domain (including the corners) ensures compliance with the chain rule.
For further information on *liNami* and how the post-processing of linearised code works, please refer to A. Franchini's thesis [53], as he was responsible for developing the *liNami* kernel during his PhD.

2.2.2 Matrix-free methods for stability analysis

Through the use of dNami and liNami, one gains access to a non-linear and a linear source code respectively; both of these codes are matrix-free, meaning that a matrix containing all the information is never created. In this subsection, we will therefore examine time-stepper methods for stability analysis made popular by [128] - [129].

2.2.2.1 Fixed point

For the various stability analyses, the starting point is the computation of the fixed point $\boldsymbol{q}_0$, which for a continuous dynamic system is defined as:

$$\frac{\partial \boldsymbol{q}_0}{\partial t} = \boldsymbol{F}(\boldsymbol{q}_0) = 0 \tag{2.52}$$

There are two main approaches for calculating the fixed point using a matrix-free method: SFD (*Selective Frequency Damping*) or the Newton-Krylov method.

SFD is a technique proposed by Åkervik et al. [130] and based on the work of Pruett et al. [131]. It is based on control theory and uses a low-pass filter to dampen the oscillations of the unstable fixed point; furthermore, it has also proven effective for URANS systems [132] where the more conventional local time stepping has greater difficulty converging. The filtered system reads:

$$\begin{cases} \dfrac{d\boldsymbol{q}}{dt} = \boldsymbol{F}(\boldsymbol{q}) - \chi(\boldsymbol{q} - \tilde{\boldsymbol{Q}}) \\ \dfrac{\partial \tilde{\boldsymbol{Q}}}{\partial t} = \dfrac{1}{\Delta}(\boldsymbol{q} - \tilde{\boldsymbol{Q}}) \end{cases} \tag{2.53}$$

where $\tilde{\mathbf{Q}}$ is the filtered solution, χ is a control coefficient and Δ is inverse of the cut frequency ω_c. One of the reasons why this technique has gained popularity is that it is very simple to implement without having to modify the original code. In fact, as proposed by Jordi et al. [133] , for each time step Δt the system can be solved in two stages: the first is the standard time advancement using the time integration method already available in the code, which yields a provisional solution $\boldsymbol{q}^*$. The second step, instead, consists of solving the second part of the system:

$$\frac{d}{dt}\begin{pmatrix} \boldsymbol{q} \\ \tilde{\boldsymbol{Q}} \end{pmatrix} = \begin{pmatrix} -\chi\boldsymbol{I} & \chi\boldsymbol{I} \\ \frac{1}{\Delta}\boldsymbol{I} & -\frac{1}{\Delta}\boldsymbol{I} \end{pmatrix}\begin{pmatrix} \boldsymbol{q}^* \\ \tilde{\boldsymbol{Q}} \end{pmatrix} \tag{2.54}$$

Which can be done exactly as follows:

$$\begin{pmatrix} \boldsymbol{q}^{j+1} \\ \tilde{\boldsymbol{Q}}^{j+1} \end{pmatrix} = \frac{1}{1+\chi\Delta}\begin{pmatrix} \boldsymbol{I} + \chi\Delta e\boldsymbol{I} & \chi\Delta(\boldsymbol{I} - e\boldsymbol{I}) \\ \boldsymbol{I} - e\boldsymbol{I} & \chi\Delta\boldsymbol{I} + e\boldsymbol{I} \end{pmatrix}\begin{pmatrix} \boldsymbol{q}^* \\ \tilde{\boldsymbol{Q}}^{j} \end{pmatrix} \tag{2.55}$$

where $e = e^{-((\chi+1)/\Delta t)\Delta t}$. One can deduce that the choice of parameters χ and Δ plays a critical role; indeed, convergence is not guaranteed for every value of these parameters, and in any case is generally very slow. An approach proposed in [134] consists of using a field that has partially converged to perform a preliminary stability analysis, and then using the values of the growth rate and frequency

to re-set the values of χ and ω and obtain a fully steady-state solution with a second SFD.
The other method proposed for fixed-point computation is Newton-Krylov. The latter requires a non-linear time-stepping code that returns $\boldsymbol{q}_{k+1} = \boldsymbol{\Phi}_\tau(\boldsymbol{q}_k)$ and a linear one returning $\boldsymbol{q}'_{k+1} = \boldsymbol{M}_\tau \boldsymbol{q}'_k$, where both operators contain information on spatial discretisation and temporal integration. The steps of the Newton-Krylov method are the same as those of the classical Newton method; the difference is that the Jacobian matrix is never formed, let alone its inverse calculated.
Given the non-linear equation , the fixed point $\boldsymbol{q}_0$ will be such that:

$$\boldsymbol{\Phi}_\tau(\boldsymbol{q}) = \boldsymbol{q} \tag{2.56}$$

We can therefore define the function $\boldsymbol{G}$, for which we wish to find the roots, as follows:

$$\boldsymbol{G}(\boldsymbol{q}) = \boldsymbol{\Phi}_\tau(\boldsymbol{q}) - \boldsymbol{q} \tag{2.57}$$

Newton's algorithm for evaluating solutions to $\boldsymbol{G} = 0$ is described in 2.2.2.1. At first glance, it looks like a classic Newton method; the difference lies precisely in step 3, where the system is solved. To solve the system using a matrix-free approach, several methods are available. We use GMRES (Generalised Minimal RESidual), an iterative method based on the creation of a Krylov subspace, but lets proceed step by step.

Algorithm 1: Newton-Krylov

Require : the non-linear time-stepper $\boldsymbol{q}_{k+1} = \Phi_\tau(\boldsymbol{q}_k)$, the linear time-stepper $\boldsymbol{q}'_{k+1} = \boldsymbol{M}_\tau \boldsymbol{q}'_k$, an initial guess $\boldsymbol{q}_0$ for the fixed point.

For $j = 1, 2, \cdots, m$

- Compute the residual $\mathbf{r} = \Phi_\tau(\boldsymbol{q}_j) - \boldsymbol{q}_j$.
- Check for convergence. If $\|\mathbf{r}\| \leq \varepsilon$, return $\boldsymbol{q}_j$ as fixed point solution.
- If not converged, solve the system $\mathbf{J}\boldsymbol{q}' = -\mathbf{r}$ to compute the Newton update.
- Update the solution as $\boldsymbol{q}_{j+1} = \boldsymbol{q}_j + \boldsymbol{q}'$.

Consider a matrix $\boldsymbol{A} \in \mathbb{R}^{n \times n}$ and a vector $\boldsymbol{x} \in \mathbb{R}^n$, a Krylov subspace [135] of dimension m can

be constructed as follows:

$$\mathcal{K}_m(\boldsymbol{A}, \boldsymbol{x}) = \{\boldsymbol{x}, \boldsymbol{A}\boldsymbol{x}, \boldsymbol{A}^2\boldsymbol{x}, \boldsymbol{A}^3\boldsymbol{x}, ..., \boldsymbol{A}^m\boldsymbol{x}\} \tag{2.58}$$

This sequence converges to the eigenvector of $\boldsymbol{A}$ corresponding to the largest eigenvalue; however, it is never used as it stands because the vectors become increasingly parallel. One solution is to construct each Krylov vector so that it is orthogonal to those generated previously, rather than applying a simple power iteration. For this reason, it is preferable to use Arnoldi factorisation [136], which combines power iteration with Gram-Schmidt orthogonalization.

Algorithm 2: Classic Arnoldi

Require : a matrix $\mathbf{A}$, an initial non-zero vector $\boldsymbol{v}$, the target dimension of the Krylov subspace m.

- Initialize: Compute the norm $\beta = \|\boldsymbol{v}\|$ and set the first basis vector $\boldsymbol{v}_1 = \boldsymbol{v}/\beta$.
- For $j = 1, 2, \cdots, m$
  - Compute the new candidate vector: $\mathbf{w} = \mathbf{A}\boldsymbol{v}_j$.
  - For $i = 1, 2, \cdots, j$ *(Gram-Schmidt orthogonalization)*:
    - $h_{i,j} = \boldsymbol{v}_i^T \mathbf{w}$
    - $\mathbf{w} = \mathbf{w} - h_{i,j}\boldsymbol{v}_i$
  - Compute the sub-diagonal element: $h_{j+1,j} = \|\mathbf{w}\|$.
  - Normalize to get the next basis vector: $\boldsymbol{v}_{j+1} = \mathbf{w}/h_{j+1,j}$.

After m-steps the algorithm 2.2.2.1 leads to:

$$\boldsymbol{A}_m\boldsymbol{V}_m = \boldsymbol{V}_m\boldsymbol{H}_m + \boldsymbol{r}_m\boldsymbol{e}_m^T \tag{2.59}$$

where $\boldsymbol{r}_m\boldsymbol{e}_m^T$ is the residual, $\boldsymbol{V}_m$ is a matrix of dimension $n \times m$ while $\boldsymbol{H}_m$ is an upper Hessenberg matrix of dimension $m \times m$. Arnoldi factorisation is used within the GMRES method to solve a linear system such as that mentioned in point 3 of Newton's method. Introduced by Saad & Schultz [137], the GMRES is an iterative method that approximates the solution to the system $\boldsymbol{A}\boldsymbol{x} = \boldsymbol{b}$ by minimising the norm $||\boldsymbol{b} - \boldsymbol{a}\boldsymbol{x}_k||$, where $\boldsymbol{x}_k$ is the vector of the Krylov subspace of dimension k.

Let us now return to point three of Newton's method: the system to be solved is $\boldsymbol{J}\boldsymbol{q}' = -\boldsymbol{r}$, where $\boldsymbol{J}$ is the Jacobian of the function G. If we calculate the latter, it will be given by:

$$\boldsymbol{J} = \boldsymbol{M}_\tau - \boldsymbol{I} \tag{2.60}$$

Therefore, to create the Krylov subspace within the GMRES, it will suffice to advance the linear code in time without ever calculating the Jacobian matrix. In 2.2.2.1 is presented the algorithm to solve the system directly applied to the Newton case, further details can be found in [138].
Two fundamental parameters are undoubtedly the choice of sampling time τ and the dimension of the Krylov subspace m. In [88] a useful range for selecting the values of m and τ was provided, following a parametric study on open-cavity flow, which is as follows:

$$4 < \frac{m\tau}{T} < 20 \tag{2.61}$$

where T corresponds to the period of the leading instability.

Algorithm 3: GMRES

Require : the linear time-stepper $\boldsymbol{q}'_{k+1} = \boldsymbol{M}_\tau \boldsymbol{q}'_k$, an initial guess $\boldsymbol{q}'_0$, restart dimension m, and tolerance ε.

- **Start (Restart Loop):**
  - Compute the Jacobian-vector product for the initial guess: $\mathbf{J}\boldsymbol{q}'_0 = \mathbf{M}_\tau \boldsymbol{q}'_0 - \boldsymbol{q}'_0$.
  - Compute initial residual: $\mathbf{r}_{lin} = \mathbf{b} - \mathbf{J}\boldsymbol{q}'_0$.
  - Compute its norm: $\beta = \|\mathbf{r}_{lin}\|$.
  - Check for convergence: If $\beta \leq \varepsilon$, return $\boldsymbol{q}'_0$ as the solution.
  - Initialize the first Krylov basis vector: $\boldsymbol{v}_1 = \mathbf{r}_{lin}/\beta$.
- **Arnoldi Iteration:** For $j = 1, 2, \cdots, m$
  - Advance linear code (Jacobian action): $\mathbf{w} = \mathbf{M}_\tau \boldsymbol{v}_j - \boldsymbol{v}_j$.
  - For $i = 1, 2, \cdots, j$ *(Modified Gram-Schmidt)*:
    - $h_{i,j} = \boldsymbol{v}_i^T \mathbf{w}$
    - $\mathbf{w} = \mathbf{w} - h_{i,j}\boldsymbol{v}_i$
  - Compute sub-diagonal element: $h_{j+1,j} = \|\mathbf{w}\|$.
  - If $h_{j+1,j} \neq 0$, normalize: $\boldsymbol{v}_{j+1} = \mathbf{w}/h_{j+1,j}$.
- **Least Squares Optimization:**
  - Formulate the minimization problem: $\mathbf{y}_m = \arg\min_{\mathbf{y}} \|\beta \mathbf{e}_1 - \bar{\mathbf{H}}_m \mathbf{y}\|_2$.
  - Compute the analytical solution :

$$\mathbf{y}_m = (\bar{\mathbf{H}}_m^T \bar{\mathbf{H}}_m)^{-1} \bar{\mathbf{H}}_m^T (\beta \mathbf{e}_1)$$

- **Solution Update & Restart Check:**
  - Compute the approximate Newton update: $\boldsymbol{q}'_m = \boldsymbol{q}'_0 + \mathbf{V}_m \mathbf{y}_m$.
  - If the minimization residual is $\leq \varepsilon$, stop and return $\boldsymbol{q}'_m$.
  - Else, set $\boldsymbol{q}'_0 \leftarrow \boldsymbol{q}'_m$ and go back to **Start**.

2.2.2.2 Eigenvalue problem

In the previous section, we saw that the solution to the linear system at time τ can be written as:

$$\boldsymbol{q'}(\tau) = \boldsymbol{q'}(t=0)e^{\tau\mathcal{L}} = \boldsymbol{q'}(t=0)\boldsymbol{M}_\tau \tag{2.62}$$

and the solution to the global stability problem is obtained by calculating the eigenvalues of $\mathcal{L}$. In a matrix-free method, one uses the Arnoldi factorisation described above, advancing the linearised code in time, to approximate $\boldsymbol{M}_\tau$ with the resulting Hessenberg matrix $\boldsymbol{H}_m$ and then calculate its eigenvalues:

$$\boldsymbol{M}_\tau \boldsymbol{V}_m = \boldsymbol{V}_m \boldsymbol{H}_m + \boldsymbol{r}_m \boldsymbol{e}_m^T \tag{2.63}$$

The pairs of eigenvalues and eigenvectors $(\gamma_i, \boldsymbol{y}_i)$ of the matrix $\boldsymbol{H}_m$ are known as Ritz pairs and are related to the eigenpairs $(\mu_i, \boldsymbol{x}_i)$ of the exponential propagator by the following relations:

$$\gamma_i = \mu_i, \qquad\qquad \boldsymbol{x}_i = \boldsymbol{V}_m \boldsymbol{y}_i \tag{2.64}$$

Finally, to calculate the eigenvalues of $\mathcal{L}$ from those of $\boldsymbol{H}$, one simply needs to use the Taylor series expansion of the exponential propagator, which is given by:

$$e^{\mathcal{L}\tau} = \boldsymbol{I} + \mathcal{L}\tau + \frac{(\mathcal{L}\tau)^2}{2} + \frac{(\mathcal{L}\tau)^3}{3!} + ... \tag{2.65}$$

multiplying the series by the eigenvector $\boldsymbol{x}$ of $\mathcal{L}$ gives:

$$e^{\mathcal{L}\tau}\boldsymbol{x} = \left(\boldsymbol{I} + \mathcal{L}\tau + \frac{(\mathcal{L}\tau)^2}{2} + \frac{(\mathcal{L}\tau)^3}{3!} + ...\right)\boldsymbol{x} \tag{2.66}$$

using the definition $\mathcal{L}\boldsymbol{x} = \lambda\boldsymbol{x}$:

$$e^{\mathcal{L}\tau}\boldsymbol{x} = \left(\boldsymbol{I} + \lambda\tau + \frac{(\lambda\tau)^2}{2} + \frac{(\lambda\tau)^3}{3!} + ...\right)\boldsymbol{x} \tag{2.67}$$

and finally noting that the expression in brackets is the expansion of the function $e^{\lambda\tau}$:

$$\boldsymbol{M}_\tau \boldsymbol{x} = e^{\lambda\tau}\boldsymbol{x} \tag{2.68}$$

Therefore, the eigenvectors of $\boldsymbol{M}_\tau$ and $\mathcal{L}$ are the same, whilst the eigenvalues are related by the following equation:

$$\lambda_i = \frac{\log(\mu_i)}{\tau} \tag{2.69}$$

2.2.3 Matrix-forming method

In some cases, the matrix-free approach is the only viable option. When dealing with 3-D configurations involving many degrees of freedom, the RAM available on modern computers is not sufficient to reconstruct the entire Jacobian matrix for stability analysis. However, this is not always the most convenient approach. For 2-D cases, on the other hand, where the aim is to study low-frequency dynamics with strict time-step constraints, using time-stepping methods could be computationally very expensive. For this reason, part of my thesis work involved creating a Python module within liNami to generate the Jacobian matrix in sparse format.

2.2.3.1 Jacobian extraction

The most common approach to extracting the Jacobian matrix is to use its finite-difference approximation, specifically by starting from a non-linear code that calculates:

$$\frac{\partial \boldsymbol{q}}{\partial t} = \boldsymbol{F}(\boldsymbol{q}). \tag{2.70}$$

The approximation of the Jacobian matrix applied to the perturbation can be written as:

$$\mathcal{L}\boldsymbol{q}' \approx \frac{\boldsymbol{F}(\boldsymbol{q}_0 + \epsilon \boldsymbol{q}') - \boldsymbol{F}(\boldsymbol{q}_0)}{\epsilon}, \tag{2.71}$$

where a first-order approximation has been used and it is assumed that the initial point $\boldsymbol{q}_0$ has already been calculated. To correctly extract the entire matrix, the most straightforward approach is to perform N evaluations of the residual, where N is the number of degrees of freedom, substituting the vector $\boldsymbol{q}'$ at each iteration with the corresponding Cartesian basis vector $\boldsymbol{e}$ [139]. In this way, at each ith iteration, the ith column of the matrix is recovered.
If, on the other hand, one has a linear code, obtained via AD, which calculates:

$$\frac{\partial \boldsymbol{q}'}{\partial t} = \mathcal{L}\boldsymbol{q}', \tag{2.72}$$

the basic idea remains the same; the only difference is that one obtains the exact matrix rather than the approximate one.
The problem with the method as described is that for sufficiently large N, the extraction could be quite computationally expensive. First in [140] and then in [56], optimal algorithms have been introduced

to form the matrix in order to perform the minimum number of residual evaluations. The basic idea is that the Jacobian matrix is generally a sparse matrix, whose sparsity depends on the discretisation stencil. It is therefore possible to group the columns of the Jacobian into *partitions*. The columns of each partition are such that they have no non-zero terms in the same row; for this reason, the minimum number n_{min} of RHS evaluations is given by:

$$n_{min} = n_{var} \times (l_{stencil})^D, \tag{2.73}$$

where n_{var} is the number of variables that constitute the state vector, D is the dimension of the problem and $l_{stencil}$ is the stencil length.

Algorithm 4: Jacobian Allocation via Test Vectors

Require : the linear code computing $\mathcal{L}\boldsymbol{q}'$, the number of residual evaluations n_{min}.

- For $k = 1, 2, \cdots, n_{min}$
  - Construct a proper test vector $\boldsymbol{v}_k$.
  - Compute the residual: $\mathbf{r}_k = \mathcal{L}\boldsymbol{v}_k$.
  - Allocate Jacobian elements *(Compute global indices)*.

At first glance, the extraction algorithm 2.2.3.1 may appear equivalent to that proposed in [141], but the difference lies in the third point, namely the reconstruction of the matrix from the residual. In fact, assigning a pair of global indices $(\tilde{i}, \tilde{j})$, referring to the rows and columns of the matrix, to the i-th element of the residual depends not only on the discretisation stencil but also on how the code operates. In the specific case of *dNami*, for example, where the stencil is reduced near the boundary, special measures must be taken. Furthermore, the presence of RHS-type and q-type boundary conditions necessitates constructing a separate part of the matrix linked to the q-type conditions, as these cannot be obtained through the calculation of the residual. Moreover, the null elements in the residual are discarded in step three rather than *a posteriori*; consequently, at the end of the loop there will be three lists of non-null elements containing, respectively, the entries of $\mathcal{L}$ and their corresponding indices $\tilde{i}$ and $\tilde{j}$

To gain a better understanding of how the extraction works, let us return to the case of the 1-D

Burgers equation, which has a single variable and a single dimension. We will then see how to extend this to cases with multiple dimensions and multiple variables.
The 1-D Burgers equation can be written as:

$$\frac{\partial u}{\partial t} + \frac{\partial}{\partial x}\left(\frac{u^2}{2}\right) = \nu \frac{\partial^2 u}{\partial x^2}. \tag{2.74}$$

We want to write the Jacobian matrix by hand, to see how it is structured so that we can figure out how to reconstruct it from the linearised code. Within our framework, to obtain the linearised source code, we first discretise the equation and then differentiate it. Let us therefore consider a 1-D domain consisting of N_x points, where we denote the boundaries by i_{min} and i_{max}. Applying a fourth-order centred scheme for the convective term and a second-order scheme for the diffusive term, we obtain:

- $\frac{\partial}{\partial x}\left(\frac{u^2}{2}\right) = \frac{1}{12\Delta x}\left(\left(\frac{u^2}{2}\right)_{i+2} - 8\left(\frac{u^2}{2}\right)_{i+1} + 8\left(\frac{u^2}{2}\right)_{i-1} - \left(\frac{u^2}{2}\right)_{i-2}\right)$,
- $\frac{\partial}{\partial x}\left(\frac{\partial u}{\partial x}\right) = \frac{\partial}{\partial x}\left(\frac{u_{i+1} - u_{i-1}}{2\Delta x}\right) = \left(\frac{u_{i+2} - 2u_i + u_{i-2}}{4\Delta x^2}\right)$.

In *dNami*, the stencil reduction is applied near the edges, so we discretise differently at the points $i_{min} + 1$:

- $\frac{\partial}{\partial x}\left(\frac{u^2}{2}\right) = \frac{1}{2\Delta x}\left(\left(\frac{u^2}{2}\right)_{i+1} - \left(\frac{u^2}{2}\right)_{i-1}\right)$,
- $\frac{\partial}{\partial x}\left(\frac{\partial u}{\partial x}\right) = \frac{\partial}{\partial x}\left(\frac{u_{i+1} - u_{i-1}}{2\Delta x}\right) = \left(\frac{u_{i+2} - u_i}{4\Delta x^2}\right) - \left(\frac{-3u_{i+1} + 4u_i - u_{i-1}}{4\Delta x^2}\right)$,

and at $i_{max} - 1$:

- $\frac{\partial}{\partial x}\left(\frac{u^2}{2}\right) = \frac{1}{2\Delta x}\left(\left(\frac{u^2}{2}\right)_{i+1} - \left(\frac{u^2}{2}\right)_{i-1}\right)$,
- $\frac{\partial}{\partial x}\left(\frac{\partial u}{\partial x}\right) = \frac{\partial}{\partial x}\left(\frac{u_{i+1} - u_{i-1}}{2\Delta x}\right) = \left(\frac{3u_{i+1} - 4u_i + u_{i-1}}{4\Delta x^2}\right) - \left(\frac{u_i - u_{i-2}}{4\Delta x^2}\right)$,

while at boundary we consider q-type boundary conditions, for example at $i_{min} \rightarrow u_i = 0$ and at $i_{max} \rightarrow \frac{\partial u}{\partial x} = 0$ corresponding to $u_i = -\frac{4}{3}u_{i-1} + \frac{1}{3}u_{i-2}$ with 2^{nd} order decentered representation.
Now we are ready to perform the differentiation. The only term that needs to be treated is $d(u^2/2)$ who becomes udu and using previous notation we rewrite as $u_0 u'$ where u_0 is the steady solution. For the sake of simplicity, all the coefficients just calculated have been grouped in the table 2.1 . Finally

	i + 2	**i + 1**	**i**	**i − 1**	**i − 2**
bulk	$A = -\frac{u_0}{12\Delta x} + \frac{\nu}{4\Delta x^2}$	$B = \frac{8u_0}{12\Delta x}$	$C = -\nu\Delta x^2$	$D = -B$	$E = \frac{u_0}{12\Delta x} + \frac{\nu}{4\Delta x^2}$
imin+1	$F = \frac{\nu}{4\Delta x^2}$	$G = -\frac{u_0}{2\Delta x} + \frac{\nu}{4\Delta x^2}$	$H = -\frac{5\nu}{4\Delta x^2}$	$I = \frac{u_0}{2\Delta x} + \frac{3\nu}{4\Delta x^2}$	
imax-1		$L = -\frac{u_0}{2\Delta x} + \frac{3\nu}{4\Delta x^2}$	$M = H$	$N = \frac{u_0}{2\Delta x} + \frac{\nu}{4\Delta x^2}$	$\frac{\nu}{4\Delta x^2}$
imin			1		
imax			1	$P = -\frac{4}{3}$	$Q = \frac{1}{3}$

Table 2.1: Stencil coefficients for 1D Burgers equation

we are ready to have a representation of the final matrix corresponding to a state vector of type $[u'_1, u'_2, ..., u'_{N_x}]$. On the left-hand side of Figure (2.7), the columns belonging to the first *partition* – and thus recovered at iteration $k = 1$ – are highlighted in red. To obtain the coefficients corresponding to the columns within the residual, the test vector must be filled with 1s alternating with $l_{stencil}$ 0s. At the next iteration, $k = 2$, to recover the second partition, the non-zero entries of the test vector must shift forward by one position, as can be seen on the right-hand side of the figure. It is clear that in this case the minimum number of evaluations of the residual is precisely $n_{min} = l_{stencil}$.

Now, however, we need to understand how to rearrange the coefficients within the matrix. If we

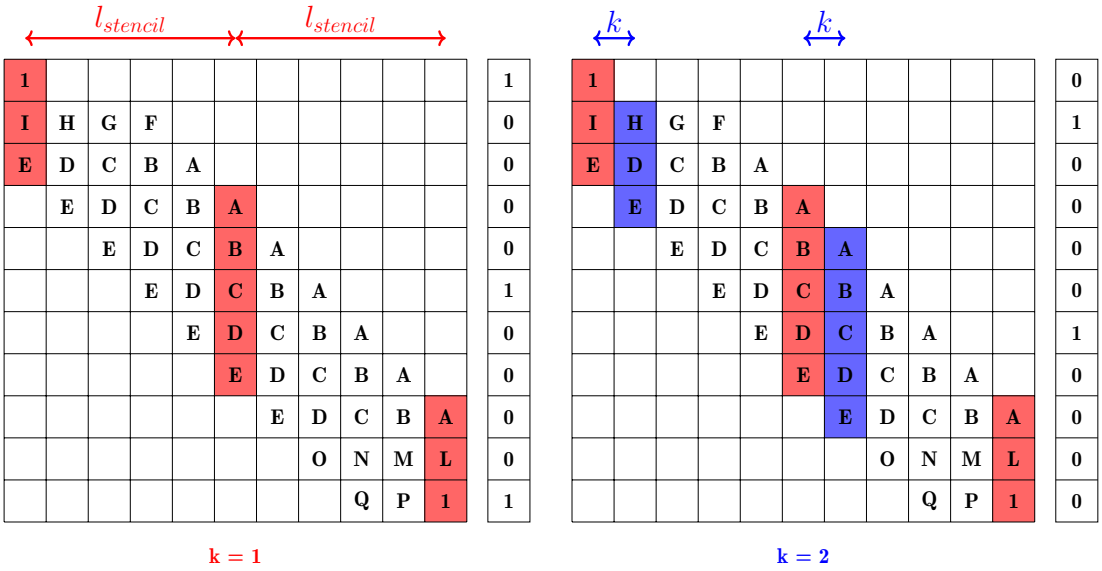


Figure 2.7: Matrix coloring at two different iterations.

denote by $(\tilde{i}, \tilde{j})$ the rows and columns of the Jacobian to be reconstructed, respectively, and by i the

rows of the state vector and hence also of the residual, we can immediately see that $\tilde{i} = i$ whilst $\tilde{j}$ will be given by a multiple of $l_{stencil} + k$, since at each iteration we move one column to the right:

$$\tilde{i} = i, \qquad \tilde{j} = M l_{stencil} + k, \tag{2.75}$$

where M is an incremental coefficient that starts at 0 and increases within a loop over the elements of the residual, before being reset when moving on to the next iteration k. Within the *bulk* region, where the same discretisation is always used, each time $l_{stencil}$ non-zero elements are filled in a column, the process moves to the next column of the same partition and M increases by 1. However, this does not apply to the first columns where a stencil reduction is used, so special precautions must be taken for the first columns processed.

Another point to bear in mind is that only the coefficients relating to an application of the matrix to the vector $\boldsymbol{\mathcal{L}v}_k$ can be obtained, and all boundary conditions of type q yield a residual that is actually equal to 0 at those points. In our example, this corresponds to the first and last rows actually being filled with zero elements at the end of the extraction process. For this reason, a second matrix is created, which we call $\mathcal{L}_{BC}$, whose rows $\tilde{i}$ are related to the state vector by the following mapping function (in the more general 2D case with multiple variables):

$$\tilde{i} = i + jN_x + eN_xN_y. \tag{2.76}$$

Consequently, given prior knowledge of the boundary conditions imposed on the perturbation vector $\boldsymbol{q}'$ and the mapping function, the matrix $\mathcal{L}_{BC}$ can easily be populated with the necessary coefficients. If we denote the extracted matrix by $\mathcal{L}_{RHS}$, the final Jacobian will be given by:

$$\mathcal{L} = \mathcal{L}_{RHS} + \mathcal{L}_{BC}. \tag{2.77}$$

Now let's move on to the case involving multiple dimensions and variables, such as the 2-D Burgers equations. We will now confine ourselves to evaluating certain characteristics that are important for the extraction, without calculating the matrix coefficient by coefficient. The equations read:

$$\begin{cases} \dfrac{\partial u}{\partial t} + u\dfrac{\partial u}{\partial x} + v\dfrac{\partial u}{\partial y} = \nu\left(\dfrac{\partial^2 u}{\partial x^2} + \dfrac{\partial^2 u}{\partial y^2}\right), \\ \dfrac{\partial v}{\partial t} + u\dfrac{\partial v}{\partial x} + v\dfrac{\partial v}{\partial y} = \nu\left(\dfrac{\partial^2 v}{\partial x^2} + \dfrac{\partial^2 v}{\partial y^2}\right). \end{cases} \tag{2.78}$$

The system is discretised in the x-direction with N_x points and in the y-direction with N_y points, whilst the number of variables to be solved is $n_{var} = 2$. In *dNami*, the state vector will therefore consist of

two matrices of N_x by N_y points. To understand the overall structure of the Jacobian matrix, one must decide how to reorganise the two matrices into vector form; several options are possible. What is done in *liNami* is to concatenate the columns one variable at a time, as shown in the figure (2.8): In this way, the state vector will be ordered as follows:

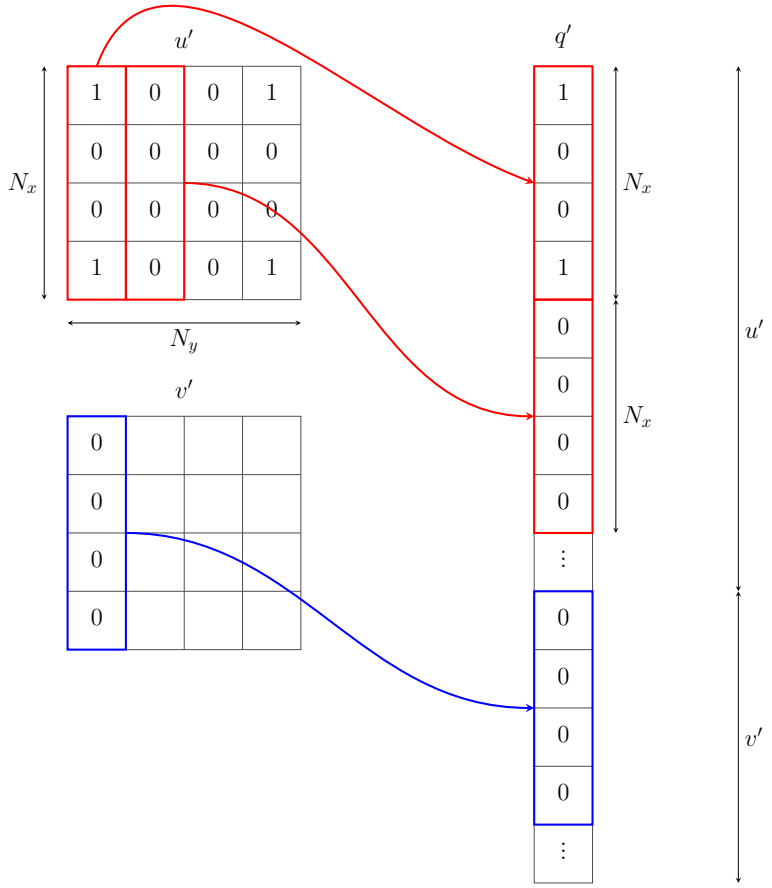


Figure 2.8: Test vector construction st first iteration.

$$\boldsymbol{q'} = [u'_{1,1}, u'_{1,2}, ..., u'_{N_x,1}, u'_{1,2}, u'_{2,2}, ..., u'_{Nx,2}, ..., u'_{1,N_y}, u'_{N_x,N_y}, v'_{1,1}, v'_{1,2}, ..., v'_{N_x,1}, v'_{1,2}, v'_{2,2}, ..., v'_{N_x,N_y}]. \tag{2.79}$$

In the same figure, the state vector has already been filled with non-zero entries for the first iteration, assuming $l_{stencil} = 3$. It is important to note that variables are evaluated one at a time and that the 1s are spaced by a distance of $l_{stencil}$ in both directions. In order to reconstruct the entire matrix, this translates to a total number of evaluations equal to n_{min}, as mentioned earlier, but which essen-

tially constitute 3 concatenated cycles, namely `m in nvar`, `l in lstencil`, `k in lstencil`, where m moves to the next variable, l to the next row and k to the next column.
Starting from the vector $\boldsymbol{q}'$, it can be seen that the matrix to be extracted will consist of n_{var}^2 submatrices of size $(N_x \times N_y) \times (N_x \times N_y)$, as shown in the figure (2.10), where:

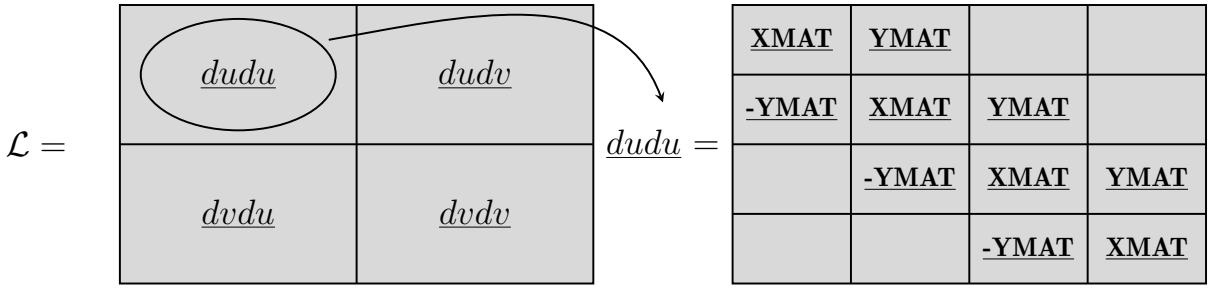


Figure 2.9: Full Jacobian matrix structure.

- $\underline{dudu}$: is the matrix related to $\partial u'/\partial t$ equation and multiplies u' part of the state vector;
- $\underline{dudv}$: is the matrix related to $\partial u'/\partial t$ equation and multiplies v' part of the state vector;
- $\underline{dudv}$: is the matrix related to $\partial v'/\partial t$ equation and multiplies u' part of the state vector;
- $\underline{dvdv}$: is the matrix related to $\partial v'/\partial t$ equation and multiplies v' part of the state vector.

Each of these matrices will consist of the matrices relating to the discretisation in the x-direction on the main diagonal, which we denote by **XMAT** of dimension N_x, and other off-diagonal matrices relating to the discretisation in the y-direction, which we denote by **YMAT** and which are diagonal matrices, also of dimension N_x.
For simplicity, let us consider only the matrix $\underline{dudu}$, shown in Figure (2.10) with the corresponding portion of the text vector u'. At the first iteration ($k = 1$, $l = 1$), the columns retrieved are not only those at a distance of $l_{stencil}$ but also those at a distance of $N_x l_{stencil}$ due to the construction of the test vector. At the next k-th iteration, the next column of the vector is filled, corresponding to a shift of $(k-1)N_x$ in the index $\tilde{j}$, as shown in Figure (2.11), whilst at the next l-th iteration , the next row of the state vector is filled, corresponding to a shift of l in $\tilde{j}$. As for the index $\tilde{i}$, it follows the mapping function defined previously. For index $\tilde{j}$, we can write:

$$\tilde{j} = M_i l_{stencil} + M_j l_{stencil} N_x + k N_x + l, \tag{2.80}$$

where M_i and M_j are two incremental coefficients as described in the 1-D case.

When we then consider the entire matrix, and thus move on to the next m^{th}variable, it is clear that there will be another term to add to $\tilde{j}$, which will be mN_xN_y Once again, care must be taken

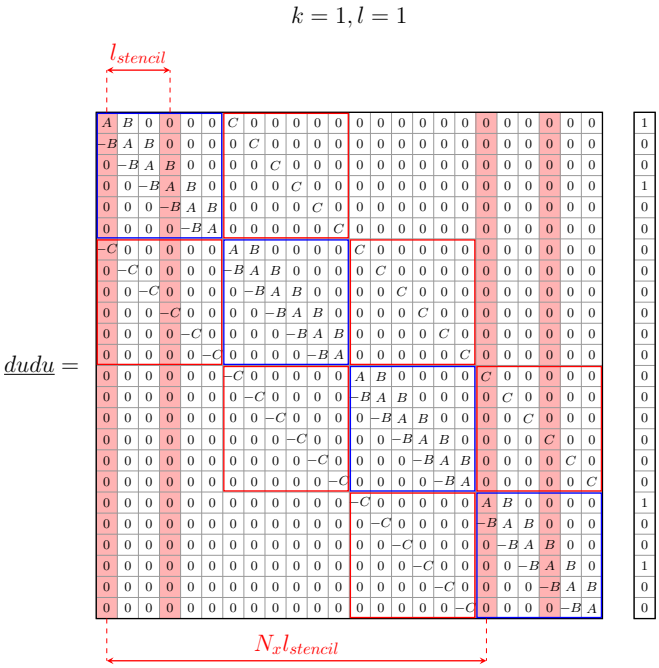


Figure 2.10: $\underline{dudu}$ matrix extraction at iteration k=1,l=1.

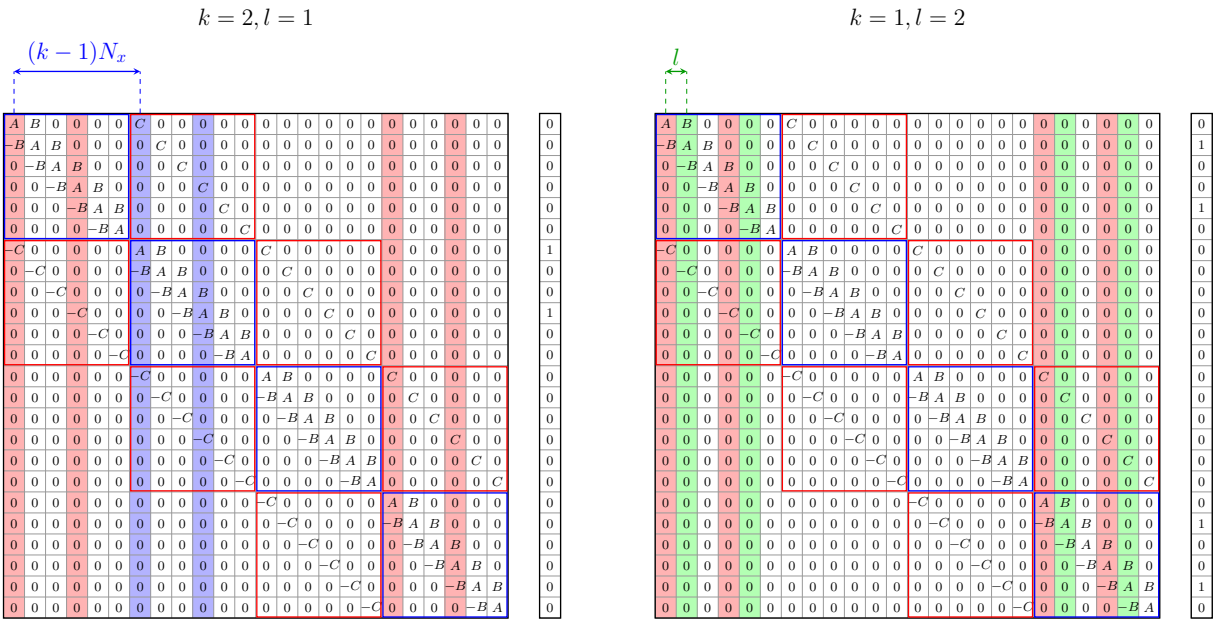


Figure 2.11: $\underline{dudu}$ matrix extraction at iteration k=2,l=1 (left) and k=1,l=2 (right).

with regions where there is a reduction in the stencil near the boundaries; for this reason, specific *if conditions* are used.

We have therefore seen how to perform matrix extraction for the most general case possible, but there are still a few points to note. When dealing with the Navier-Stokes equations in *dNami*, the problem being solved, to be precise, is:

$$\frac{\partial \boldsymbol{q}'_c}{\partial t} = \boldsymbol{\mathcal{L}} \boldsymbol{q}'_p, \tag{2.81}$$

for 2-D case, with $\boldsymbol{q}'_c = [(\rho)', (\rho u)', (\rho v)', (\rho E)']$ and $\boldsymbol{q}'_p = [(\rho)', (u)', (v)', (E)']$, because the equations are written in conservative form, but the primitive variables are allocated in memory. For this reason, the extracted matrix requires further processing.

When $\boldsymbol{\mathcal{L}}_{RHS}$ is extracted via the residual evaluations, (2.81) is solved; whereas when the coefficients are imposed on the matrix $\boldsymbol{\mathcal{L}}_{BC}$, the boundary conditions are applied directly to the primitive variables, so in that case the system to be solved is:

$$\frac{\partial \boldsymbol{q}'_p}{\partial t} = \boldsymbol{\mathcal{L}}_{BC} \boldsymbol{q}'_p = 0. \tag{2.82}$$

For this reason, before adding the two matrices, $\boldsymbol{\mathcal{L}}_{BC}$ must be made compatible with the system solved by the linearised code. If we denote by $\boldsymbol{A}$ the transformation matrix such that $\boldsymbol{q}_c = \boldsymbol{A}\boldsymbol{q}_p$, the latter will be given by:

$$\boldsymbol{A} = \begin{bmatrix} 1 & 0 & 0 & 0 \\ u_0 & \rho_0 & 0 & 0 \\ v_0 & 0 & \rho_0 & 0 \\ E_0 & 0 & 0 & \rho_0 \end{bmatrix}. \tag{2.83}$$

Now the system (2.82) can be rewritten as:

$$\frac{\partial \boldsymbol{q}'_c}{\partial t} = \boldsymbol{A}\boldsymbol{\mathcal{L}}_{BC} \boldsymbol{q}'_p = 0, \tag{2.84}$$

and consequently the full system (2.81):

$$\frac{\partial \boldsymbol{q}'_c}{\partial t} = (\boldsymbol{\mathcal{L}}_{RHS} + \boldsymbol{A}\boldsymbol{\mathcal{L}}_{BC}) \boldsymbol{q}'_p, \tag{2.85}$$

Finally, the user can choose for which variable to solve the stability problem: whether for $\boldsymbol{q}'_c$ or $\boldsymbol{q}'_p$, or whether they wish to use temperature instead of total energy (in which case, another transformation matrix must be added). For the first two cases, the final systems will be:

$$\frac{\partial \boldsymbol{q}'_c}{\partial t} = (\boldsymbol{\mathcal{L}}_{RHS} + \boldsymbol{A}\boldsymbol{\mathcal{L}}_{BC}) \boldsymbol{A}^{-1} \boldsymbol{q}'_c, \qquad \frac{\partial \boldsymbol{q}'_p}{\partial t} = \boldsymbol{A}^{-1} (\boldsymbol{\mathcal{L}}_{RHS} + \boldsymbol{A}\boldsymbol{\mathcal{L}}_{BC})\ \boldsymbol{q}'_p. \tag{2.86}$$

With this matrix-forming method, it is also possible to perform a 2-D stability analysis, i.e. with a base flow that is always 2.5-D (i.e. $w_0 = 0$ and $\partial/\partial z = 0$) but with a perturbation that is 3-D, using the following ansatz.

$$\boldsymbol{q}'(x, y, z, t) = \hat{\boldsymbol{q}}(x, y)e^{i\beta z+\lambda t} + \ c.c.. \tag{2.87}$$

This approach to stability analysis had already been introduced by Barkley in [142] and subsequently formalised by Theofilis [29], but starting from the extraction of the matrix, the first work on this subject was that of Bugeat et al. [143] . By using a code linearised via finite differences as in [144], they carried out a resolvent-type analysis of a supersonic boundary layer.
In our case, we start with a linearised code as in [141], and to extract the full matrix with respect to a 3-D perturbation, it is necessary to perform three sub-extractions.
The starting point is the 3-D NS/URANS equations. In compact form, they can be written as:

$$\frac{\partial \boldsymbol{q}}{\partial t} = \left(\boldsymbol{\mathcal{N}}_q + \boldsymbol{\mathcal{N}}_{\frac{\partial q}{\partial z}} + \boldsymbol{\mathcal{N}}_{\frac{\partial^2 q}{\partial z^2}}\right), \tag{2.88}$$

where $\boldsymbol{\mathcal{N}}_q$ is the part of the 3D operator problem without any derivative in z, $\boldsymbol{\mathcal{N}}_{\frac{\partial q}{\partial z}}$ contains first order z-derivatives , including mixed derivatives present in viscous terms, and $\boldsymbol{\mathcal{N}}_{\frac{\partial^2 q}{\partial z^2}}$ contains second order z-derivatives.
Before differentiating the nonlinear code with respect to $\boldsymbol{q}$, the gradients in z are replaced with new variables that lose their dependence on $\boldsymbol{q}$: $\partial \boldsymbol{q}/\partial z = dqdz$ and $\partial^2 \boldsymbol{q}/\partial z^2 = d2qdz2$. In this way, they will be ignored during the first differentiation process. The matrix extracted from the linearized code will be $\boldsymbol{\mathcal{L}}_q$, which does not contain any terms in z. The code is then differentiated for $dqdz$ and $d2qd2z$, and the matrix is extracted after each differentiation, thus obtaining the Jacobians of $\boldsymbol{\mathcal{N}}_{\frac{\partial q}{\partial z}}$ and $\boldsymbol{\mathcal{N}}_{\frac{\partial^2 q}{\partial z^2}}$.
At this point, it is possible to reconstruct the total matrix of 2-D stability problem:

$$\boldsymbol{\mathcal{L}}_{2.5D} = \boldsymbol{\mathcal{L}}_q + i\beta\boldsymbol{\mathcal{L}}_{\frac{\partial q}{\partial z}} - \beta^2\boldsymbol{\mathcal{L}}_{\frac{\partial^2 q}{\partial z^2}}, \tag{2.89}$$

where the subscript 2.5D refers to a 3-D perturbation superposed to a 2-D baseflow. Since z is treated as the Fourier direction, there is no need to discretise the equations along the latter, this means that the total size of the problem increases only by the additional variable considered, i.e. the velocity component along z.

2.2.3.2 Eigenvalue problem

Whether it is global stability or resolvent analysis, once the matrix has been extracted, we will still be dealing with solving an eigenvalue problem. To do this, we always use PETSc and SLPEc. Within the PETSc environment, we reconstruct the matrix in CSR (Compressed Sparse Row) format; together with the Jacobian matrix, we construct a second matrix $\boldsymbol{B}$ which allows us to solve the generalised problem $\mathcal{L}\boldsymbol{x} - \lambda\boldsymbol{B}\boldsymbol{x} = 0$ to impose boundary conditions of type q. In fact, $\boldsymbol{B}$ is nothing more than an identity matrix such that, for every ith row of $\mathcal{L}$ containing q-type conditions, a 0 is added to the ith element of the diagonal of $\boldsymbol{B}$. Due to the matrix-forming approach, we can use the shift-and-invert method to solve the eigenvalue problem. The latter involves solving the following modified problem:

$$\mathcal{L}\boldsymbol{x} - s\boldsymbol{B}\boldsymbol{x} = \lambda\boldsymbol{B}\boldsymbol{x} - s\boldsymbol{B}\boldsymbol{x}, \tag{2.90}$$

where s is called *shift*. After few manipulations one get a new eigenvalue problem:

$$\frac{1}{\lambda - s}\boldsymbol{x} = (\mathcal{L} - s\boldsymbol{B})^{-1}\boldsymbol{B}\boldsymbol{x}. \tag{2.91}$$

By applying a Krylov or Krylov-Schur method [145] for the solution, the highest eigenvalues are obtained. In the new problem, this corresponds to finding the eigenvalues λ closest to s, allowing the user to choose which region of the spectrum to compute. The trade-off for this approach is the inversion of a matrix; however, in PETSc it is possible to perform LU factorisation via MUMPS (Multifrontal Massively Parallel Solver) [146]-[147], so that the inversion is carried out only at the start without significantly increasing computational costs.
2.2.3.2 provides a detailed explanation of how various steps are carried out using PETSc and SLPEc.

Algorithm Shift-and-Invert Krylov-Schur for Generalised Eigenvalue Problems

Require : the non-zero elements of Jacobian $\mathcal{L}$, the target shift s, the number of wanted eigenvalues k, the maximum Krylov subspace dimension m, and tolerance ε.

- **Step 1: Matrix Setup**
  - Assemble matrices $\mathbf{A}$ and $\mathbf{B}$ from coordinate lists (COO) into Compressed Sparse Row (CSR).
- **Step 2: Shift-and-Invert Initialization**
  - Form the shifted matrix: $\mathbf{M} = \mathcal{L} - s\mathbf{B}$.
  - Compute the exact $\mathbf{LU}$ factorization of $\mathbf{M}$.
  - Set $p = 1$.
- **Step 3: Krylov-Schur Loop** *(Repeat until convergence or max restarts)*
  - **Arnoldi Expansion:** For $n = p, \ldots, m$, expand the Krylov subspace to obtain $\mathbf{V}_m$ and $\mathbf{H}_m$.
  - **Convergence Check:** Compute the Ritz pairs from $\mathbf{H}_m$ and evaluate their residuals. If the k wanted eigenvalues have converged ($\leq \varepsilon$), **break** .
  - **Subspace Truncation** If convergence is not reached, compute the Schur decomposition of $\mathbf{H}_m$ and truncate it to a $k \times k$ matrix . Set $p = k + 1$ and return to **Arnoldi Expansion**.
- **Step 4: Physical Eigenvalues Extraction**
  - Back-transform the computed mathematical eigenvalues μ_i to the physical eigenvalues λ_i using the shift relation: $\lambda_i = s_i + \frac{1}{\mu_i}$ for $i = 1, \ldots, k$.

Once the Jacobian matrix has been reconstructed in CSR format, we can proceed to perform the resolvent analysis. In this case, the problem to be solved is as follows

$$\begin{cases} \boldsymbol{\mathcal{R}}^{\dagger} \boldsymbol{W}_{Chu} \boldsymbol{\mathcal{R}} = \sigma_{\omega}^{2} \boldsymbol{W} \hat{\mathbf{f}}, \\ \hat{\boldsymbol{q}} = \dfrac{1}{\sigma_{\omega}} \boldsymbol{\mathcal{R}} \hat{\mathbf{f}}, \end{cases} \tag{2.92}$$

where $\boldsymbol{R}$ is, as mentioned, the resolvent operator. So, first of all, set to the value of ω specified by the

user, the inverse of resolvent operator and its adjoint must be constructed:

$$\boldsymbol{R}^{-1} = i\omega\boldsymbol{I} - \boldsymbol{\mathcal{L}}, \qquad (\boldsymbol{R}^{\dagger})^{-1} = -i\omega\boldsymbol{I} - \boldsymbol{\mathcal{L}}^{\dagger} \tag{2.93}$$

then the weight matrix is built using the mapping function 2.76 such that $\boldsymbol{W}_{\tilde{i}\tilde{i}} = J_{ij}$ and the matrix $\boldsymbol{W}_{Chu}$ is defined ,for 2-D N-S equations, as:

$$\boldsymbol{W}_{Chu} = \begin{bmatrix} \frac{(C_p - C_v)T_0}{J\rho_0} & 0 & 0 & 0 \\ 0 & \frac{\rho_0}{J} & 0 & 0 \\ 0 & 0 & \frac{\rho_0}{J} & 0 \\ 0 & 0 & 0 & \frac{C_v\rho_0}{JT_0} \end{bmatrix} \tag{2.94}$$

where in the state vector $\boldsymbol{q}'$ is used T' instead of E' in order to directly adopt relation 1.98.
The solution algorithm is very similar to the previous one; this time, to create the Krylov basis at each iteration m, the vector $\boldsymbol{v} = (-i\omega\boldsymbol{I} - \boldsymbol{\mathcal{L}}^{\dagger})^{-1}\boldsymbol{W}_{Chu}(i\omega\boldsymbol{I} - \boldsymbol{\mathcal{L}})^{-1}\boldsymbol{x}$ is generated. Therefore, at the start, the LU factorisation of the inverses of the resolvent and the adjoint resolvent is performed. The other difference is that there is no need to perform the shift and invert operation, as the method converges towards the eigenvalue with the highest value, which is the one we wish to calculate. Finally, the gain σ_ω will be given by the square root of the calculated eigenvalue, and the optimal response can be reconstructed using the relation $\hat{\boldsymbol{q}} = 1/\sigma_\omega \boldsymbol{R}\hat{\boldsymbol{f}}$ where $\hat{\boldsymbol{f}}$ is the eigenvector of the eigenvalue problem just solved.

Chapter 3

Validation test cases

3.1 Turbulent boundary layer

The first test case considered is the 2-D zero-pressure-gradient flat plate. This case is one of many benchmark cases proposed by the TMBWG (Turbulence Model Benchmarking Working Group) to provide the CFD community with reference tests [148]-[149]. The absence of a pressure gradient and a curved wall means that the flow is governed solely by wall turbulence, thereby highlighting the ability of the model employed to reproduce the physics of the turbulent boundary layer under steady-state conditions.

The configuration under investigation consists of a two-dimensional flat plate whose leading edge is located at $x = 0$. The flow regime is incompressible; however, since the numerical framework relies on an explicit time-marching compressible solver, a non-zero freestream Mach number must be prescribed. A value of $M_\infty = 0.2$ is adopted as a practical compromise: at this Mach number, compressibility effects on the mean velocity field and on the skin friction coefficient are negligible. The Reynolds number, based on the half-plate length $L_x/2$, the freestream streamwise velocity U_∞ , and the freestream kinematic viscosity ν_∞, is $Re_\infty = U_\infty(L_x/2)/\nu_\infty = 5 \times 10^6$.

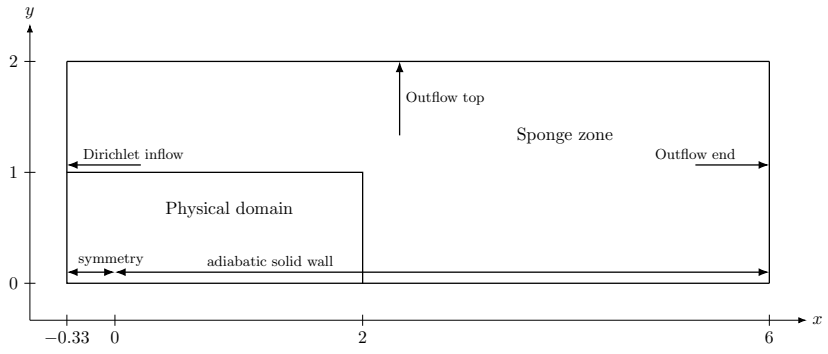


Figure 3.1: Sketch of 2D zero pressure gradient flat plate with sponge zones.

A schematic of the computational setup is shown in Figure (3.1). Dirichlet boundary conditions are prescribed at the inlet, imposing the freestream thermodynamic and kinematic state. Adiabatic no-slip conditions are enforced on the plate surface. At outflow and far-field boundaries, non-reflecting conditions are applied through the Locally One-Dimensional Inviscid (LODI) formulation, with the far-field pressure p_∞ prescribed. Symmetry conditions are imposed on the lower boundary upstream of the plate leading edge. Finally, sponge-layer regions are added near the domain boundaries to absorb undesired perturbations and prevent spurious reflections from contaminating the interior solution. The

approach used for sponge zones follows the same philosophy as that proposed by Colonius *et al.* [150], who refer to 'exit zones'. In these regions of the domain that lie ahead of the boundaries, coarser cells are used and a filter is added to improve the non-reflection of the imposed conditions.

A structured mesh of $(n_x \times n_y) = (174 \times 104)$ is used with stretching in the wall normal direction $(\Delta y = 2 \times 10^{-6})$ to ensure a value of $y^+ < 1$ where $y^+ = y/\delta^+$ with $\delta^+ = \nu/u_\tau$ and $u_\tau = \sqrt{\tau_w/\rho_w}$ and in the streamwise direction near the discontinuity. The turbulence model used is the negative Spalart-Allmaras model. An initial attempt was made using the standard version, but this resulted in negative values for the viscosity ν_{SA}; it was therefore necessary to switch to the negative version . Regarding the Spalart-Allmaras viscosity a value of $\nu_{SA} = 3/Re_\infty$ is set both to impose the condition on the inflow and to initialize the simulation, as it is the prescribed value to ensure a turbulent behaviour [78]. In the following comparison, a 6th order is used for the convective terms, a 4th order for the diffusive terms and a 5th order for the Jameson-type scheme. The results were compared

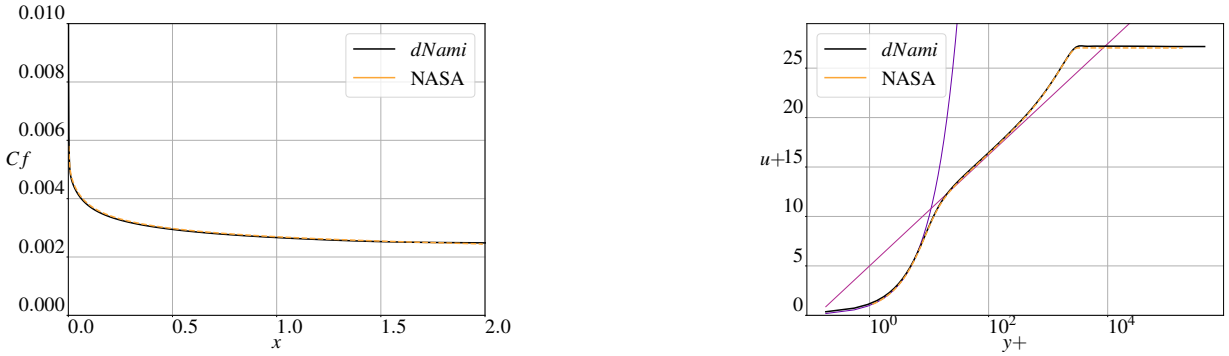


Figure 3.2: Friction coefficient C_f (left), and inner streamwise velocity u^+ (right) at $x = 0.97$.

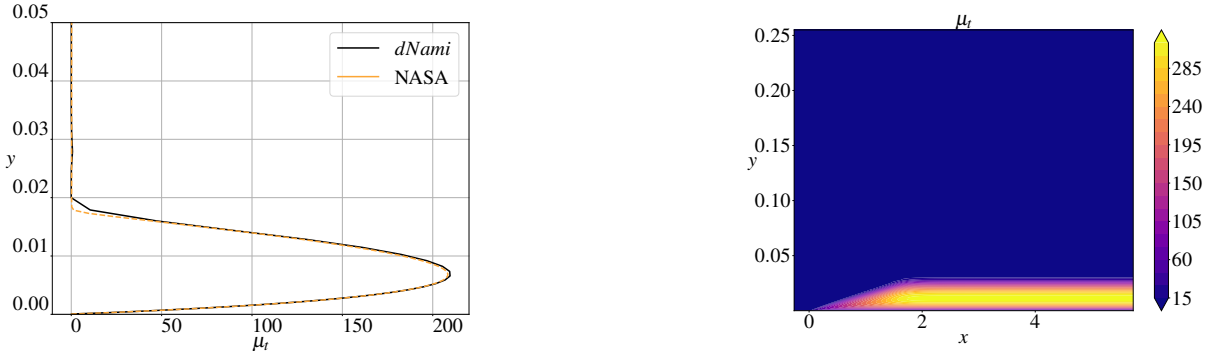


Figure 3.3: Turbulent viscosity μ_t/μ_∞. Profile at $x = 0.97$ (left) and contours (right).

with the database provided by NASA [151], specifically with the results obtained using a mesh of size

$(n_x \times n_y) = (545 \times 385)$ with $y^+ \approx 0.1$. Figures (3.2) show the friction coefficient $C_f = 2\tau_w/\rho_\infty U_\infty^2$ where τ_w is the wall shear stress and the inner scale streamwise velocity $u^+ = \tilde{u}/u_\tau$ with $u_\tau = \sqrt{\tau_w/\rho_w}$. The plot of the inner velocity also includes a comparison with the analytical expressions. Specifically, the linear law:

$$u^+ = y^+ \tag{3.1}$$

is shown in violet, while the logarithmic law:

$$u^+ = \frac{1}{\kappa}\log(y^+) + B \tag{3.2}$$

is shown in purple, with $\kappa = 0.41$ and $B \approx 5$. Figures (3.3) instead show the ratio between turbulent and molecular viscosity both profile at $x = 0.97$ and the entire contours. Although the mesh used is coarser and has a higher y^+ value than the reference one, the results show good agreement, thereby validating the implementation of the turbulence model.

To investigate the effect of the value of y^+ at the wall, two further grids were considered, each with the same number of points and with wall Δy values of $\Delta y = 6 \times 10^{-6}$, $\Delta y = 3 \times 10^{-6}$ and $\Delta y = 2 \times 10^{-6}$ respectively. These values correspond to $y^+ = 0.54$, $y^+ = 0.27$ and $y^+ = 0.18$ in the section located at $x = 0.97$. Figure (3.4) compares the results; while each grid yields satisfactory agreement, it is clear that reducing Δy brings the numerical solution ever closer to the reference curves.

The order of spatial discretisation is then briefly assessed. Two cases are compared: the first uses 6th order for the convective terms, 4th order for the diffusive terms and 5th order for the Jameson-type scheme, whilst the second uses 4th order for the convective terms, 2nd order for the diffusive terms and 3rd order for the Jameson-type scheme. In both cases, the low order dissipation term is set to zero and the calculations are carried out on a mesh with $\Delta y = 2. \times 10^{-6}$. The results are shown in Figure (3.5). The curves are almost superimposed as the discretisation order varies; for this reason, the lower order numerical strategy has been adopted in the following chapter.

3.2 Flow around a cylinder

Under certain conditions, flows around bluff bodies may exhibit the onset of an intrinsic dynamic as a result of strong separation. Among the various possible configurations, the flow past an infinitely long circular cylinder is of particular interest for validating a stability code, as it is a well-known case in the literature and exhibits the onset of global instability at relatively low Re values.

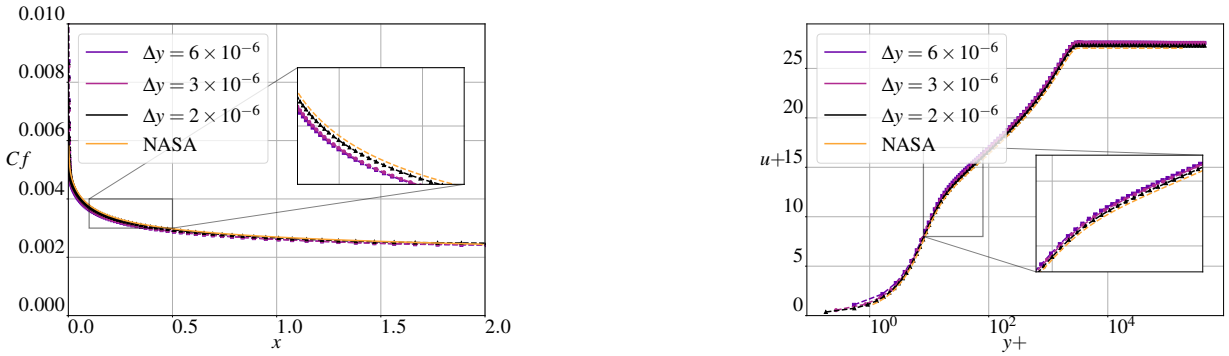


Figure 3.4: Comparison of friction coefficient (left) and inner velocity (right) profiles for different Δy values

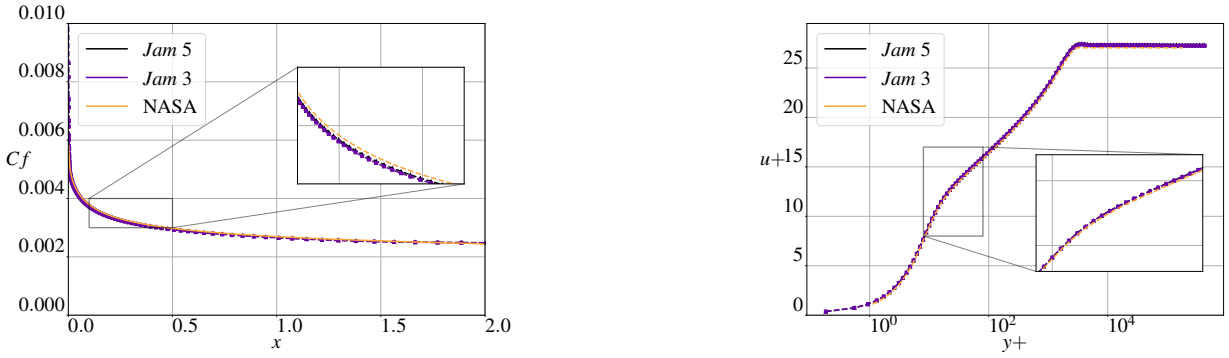


Figure 3.5: Comparison of friction coefficient (left) and inner velocity (right) profiles for different spatial discretisation order

One of the best-known experimental studies is that of Coutanceau and Bouard [152], in which Re values ranging from 5 to 40 were examined. In their work, a separation zone is observed at $Re = 9.6$ for a cylinder-to-tank diameter ratio $\lambda = 0.12$, and unsteadiness is encountered at $Re = 39.5$ for $\lambda = 0.7$. Subsequently, Williamson [153] presented a more detailed explanation of the various flow regimes as the Reynolds number varies. For $Re < 5$ there is no wake. For $5 < Re < 49$, with a symmetric and stationary recirculation region, the regime is laminar and steady. From $Re = 49$ to $140 \rightarrow 200$, instability begins to be observed, leading to a break in symmetry. The length of the recirculation zone increases with Re. This regime is defined by Williamson as 'laminar vortex shedding'. Subsequently, the regime ceases to be 2-D (higher Re regimes are then explained in the review).

Jackson [34] was one of the first to study the stability of flow around a cylinder (both circular and non-circular in cross-section) using a finite element approach. In the circular cross-section configuration, the Re_c at which bifurcation to an oscillatory regime occurs is $Re_c = 46.14$ with a frequency $St = 0.138$. During the same period, Zebib [33] obtained similar results using a spectral method, finding an unstable flow at $Re > 50$.

Subsequently, the work of Giannetti and Luchini [154] went beyond the analysis of global stability to attempt to understand why instability occurs. To this end, the adjoint mode is analysed, the maximum amplitude of which is close to the separation points. The spatial structures of the direct mode and its adjoint are different; therefore, to identify the source of global instability, the wave maker is introduced, namely the structural sensitivity defined as $||\hat{\boldsymbol{q}}||\,||\boldsymbol{q}^\dagger||/ < \hat{\boldsymbol{q}}, \boldsymbol{q}^\dagger >$. However, sensitivity to base flow is not taken into account. Marquet et al. [155] explored this aspect by proposing a general approach for assessing the sensitivity of an eigenvalue to changes in base flow, and applied it to the case of the flow past a cylinder.

In this thesis, this flow configuration is used to compare the results of the stability analysis using the two methods described above (time stepper and matrix forming). In his thesis, Franchini [53] has already validated the global stability results in *dNami* by comparing them with [154]-[156] for different Reynolds numbers. For this reason, only two cases, $Re = 40$ and $Re = 50$, will be considered. The first will also be used to test the calculation of adjoint modes and the resolvent analysis using the matrix forming method.

The case is analysed using the 2-D compressible Navier-Stokes equations, with the Mach number set to $M_\infty = 0.1$. Adiabatic no-slip conditions are imposed on the cylinder, whilst subsonic inflow and

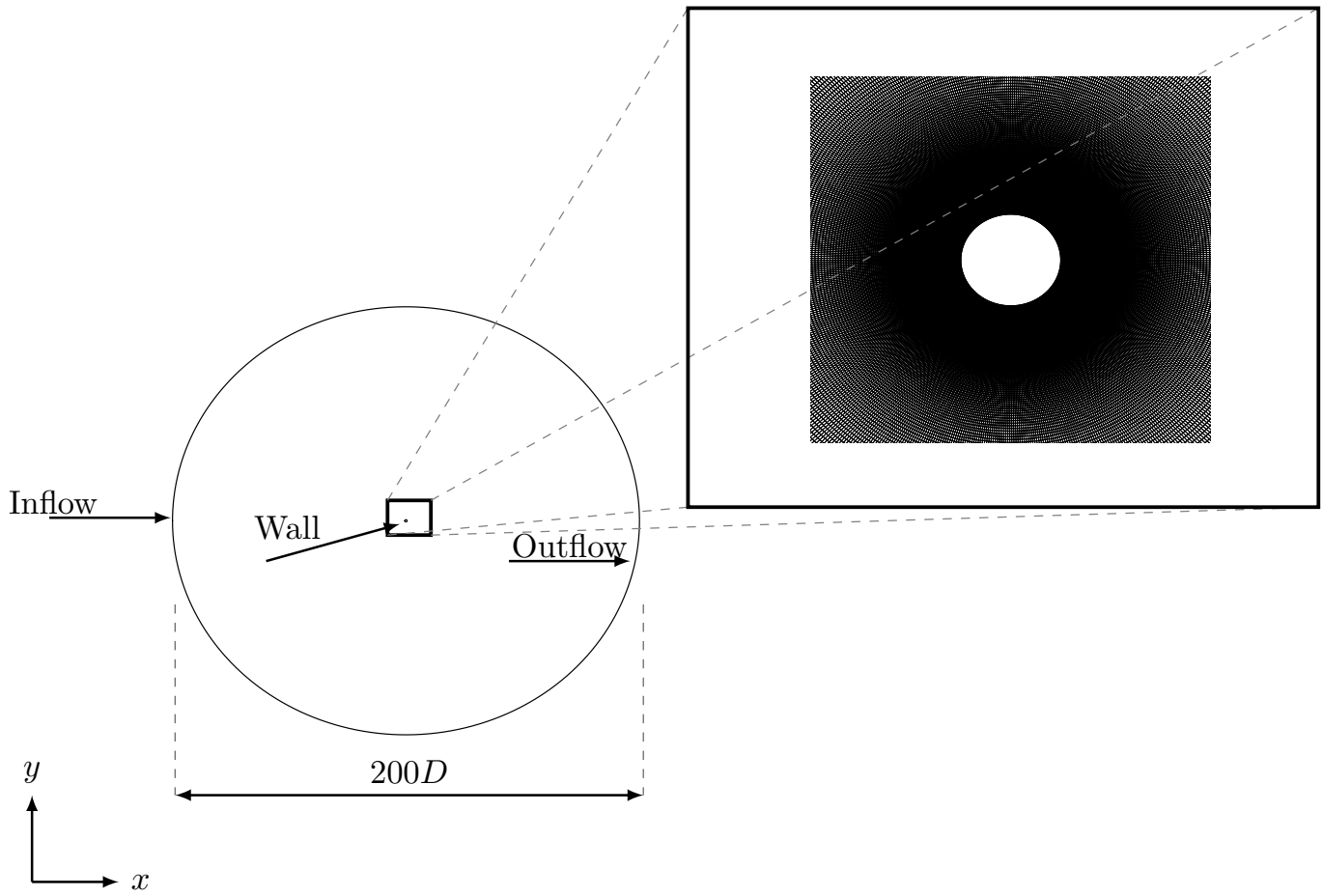


Figure 3.6: Sketch of 2D flow past circular cylinder

subsonic non-reflective outflow conditions are imposed in the far field. The computational domain ranges from $-100D$ to $100D$, where D is the cylinder diameter set to 1; as can be seen in the figure 3.6, an O-grid is used to employ a single block later in the Jacobian extraction phase.

For the mesh, 300 points are used in the radial direction and 600 in the tangential direction. In terms of spatial discretisation, a 4th-order scheme is used for the convective terms, a 2nd-order scheme for the diffusive terms, and a 3rd-order Jameson scheme is employed.

To calculate the fixed point, we use the Newton-Krylov method. The sampling time τ has been set to approximately $(1/10f_c)$, where f_c is the dimensionless critical frequency, i.e. the St calculated in the previous analyses. In [154], for $Re = 50$ we have $St \approx 0.1$, therefore $\tau = 1$ has been adopted. Figure 3.7 shows the streamwise velocity contours at $Re = 50$; as can be seen, the profile is perfectly symmetrical with a significant recirculation zone behind the cylinder. It is important to evaluate the length of the

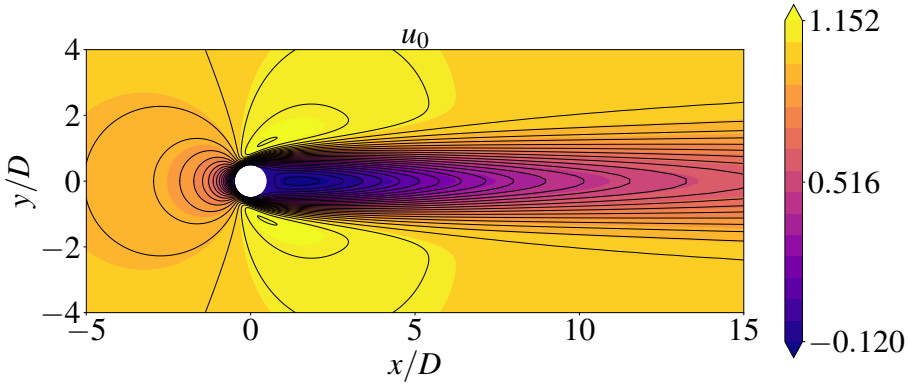


Figure 3.7: Fixed point streamwise velocity contours u_0 for $Re = 50$.

recirculation bubble. It has been shown that this varies linearly with the Reynolds number Re [154] . For this reason, Figure 3.8 shows the streamlines with the respective bubble length. For $Re = 40$, the length is approximately $L = 2.2D$, whilst for the case at $Re = 50$, the length increases to $L = 2.9D$, in accordance with previous studies. A global stability analysis has been carried out for both cases, using

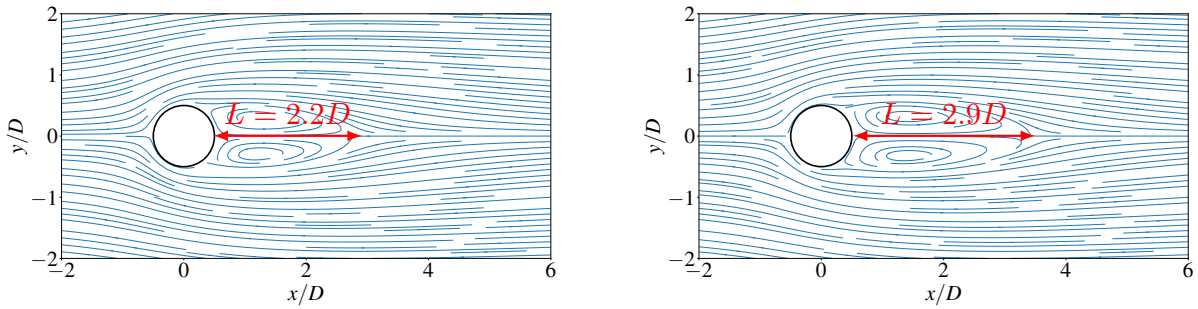


Figure 3.8: Streamlines for the case $Re = 40$ (left) and $Re = 50$ (right)

both the time-stepping method and the extraction of the Jacobian operator, in order to validate the latter. For the first approach, a Krylov basis of size $m = 400$ was used, whilst for the matrix-forming approach, the shift-and-invert method was used with a complex shift of $s = 0.001+0.8j$, corresponding to an unstable mode at the frequency identified in previous work.

Figure (3.9) shows the results of the stability analysis as Re varies, compared with [154]. In terms of growth rate, the modes align well with the reference; however, the frequency is slightly underestimated. This behaviour is consistent with previous work in [156] and [53], likely due to the different approach used (compressible NS in [156] and [53] and this work, and incompressible NS in [154]). It

is also important to note that the results of the two approaches perfectly overlap.

The growth rate at $Re = 40$ is $\sigma = -0.0317$, whilst at $Re = 50$ it is $\sigma = 0.0118$. By means of linear interpolation, we can estimate the Re_c at which the Hopf bifurcation occurs, that is $Re_c \approx 47$. Figure

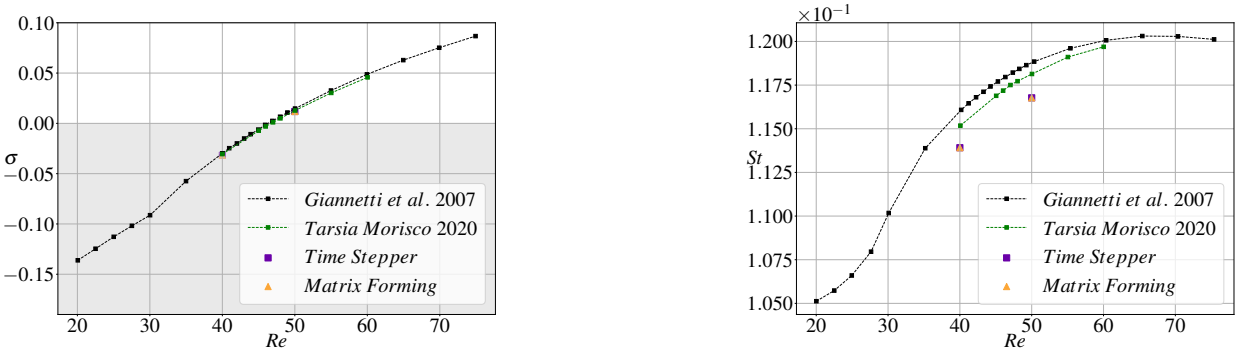


Figure 3.9: Evolution of growth rate σ (left) and St (right) in function of Re.

(3.10) shows the mode at $Re = 40$, specifically the real part of the two velocity components. The peak activity occurs far out in the wake, beyond the recirculation zone shown by a black contour line. The streamwise velocity is antisymmetric about the x-axis, whilst the cross-stream velocity is symmetric, as is typical of von Karman vortices.

Unlike the time-stepping approach, in *dNami*, the matrix-forming approach also gives us access to the adjoint and the resolvent. For this reason, the eigenvalues of the transposed-conjugate operator (discrete adjoint) have been calculated. The eigenspectrum obtained is compared with the direct one in Figure (3.11). The modes are well superimposed, and the spatial structure of the mode at $St = 0.114$ is shown in Figure 3.12 As Giannetti has already noted, the adjoint mode has a different spatial structure from the direct mode, as it is located in the near wake of the cylinder, with its maximum occurring near the point where the recirculation bubble originates.

To continue the validation phase for the stability tools, we have also calculated the structural sensitivity. This has been done for the case where $Re = 40$, and the result is shown in Figure (3.13). The spatial structure is symmetric, with maxima at $x/D \approx 2$, and shows where the direct-adjoint feedback is strongest. The contours shown are consistent with those of the reference [154].

Finally, a resolvent analysis has been conducted for a few values of ω corresponding to $0.079 < St < 0.143$, still considering $Re = 40$. The optimal gain trend is shown in Figure (3.14) . The peak occurs at $St = 0.114$, corresponding to the mode identified by the global stability analysis. At $Re = 40$, the

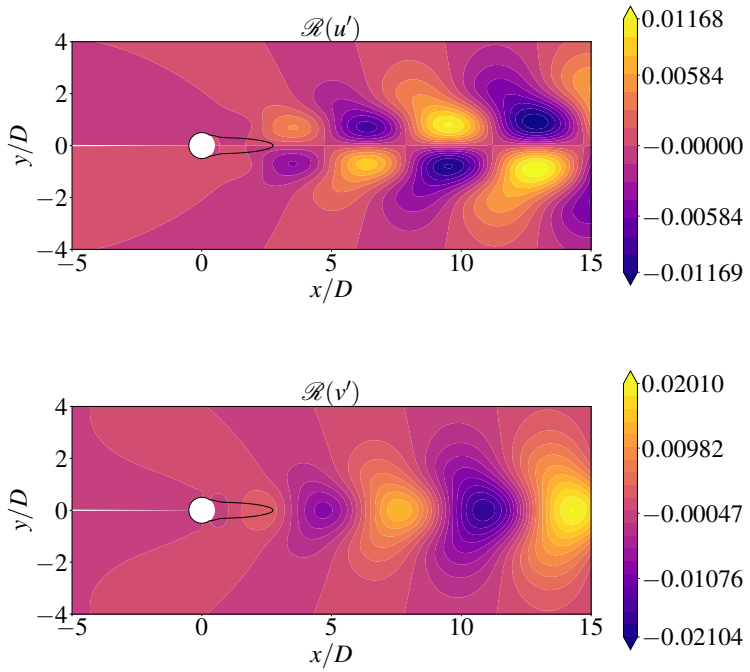


Figure 3.10: Real part of streamwise velocity perturbation $\mathcal{R}(u')$ and cross-stream velocity perturbation $\mathcal{R}(v')$for $Re = 40$

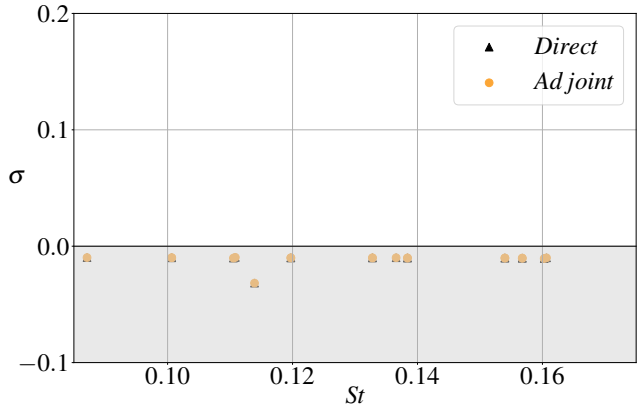


Figure 3.11: Direct and adjoint eigenspectra comparison for $Re = 40$

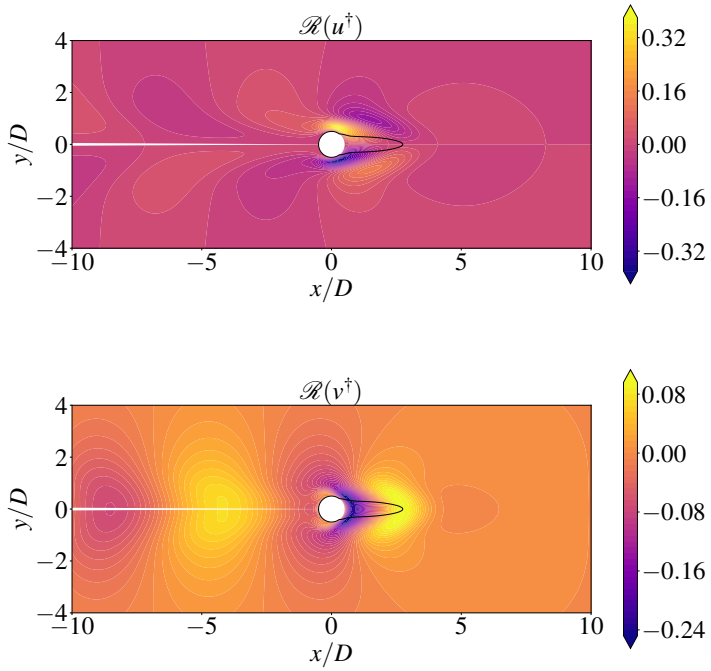


Figure 3.12: Real part of adjoint streamwise velocity $\mathcal{R}(u^\dagger)$ and adjoint cross-stream velocity $\mathcal{R}(v^\dagger)$ for $Re = 40$

system is still linearly stable but prone to pseudo-resonance when subjected to a forcing.

Figures (3.15)-(3.16) show the optimal excitations and responses for the streamwise and cross-stream velocity components, respectively. It can be seen that, for both components, the optimal excitation is equal to the adjoint mode, whilst the optimal response is equal to the direct mode; in fact, we are close to resonance for the case at $Re = 40$ and $St = 0.114$, and the forcing collapses onto the adjoint vector, whilst the optimal response collapses onto the direct vector.

3.3 Lid driven cavity

Flow in an open cavity is a pattern found in numerous aerospace and aeronautical applications such as landing gears, weapon bays, and cavity flame holders in scramjet engines. For this reason, it is a phenomenon that has been extensively investigated in the literature in recent years, together with its simplification, the lid driven cavity. In this case, it is not shear that drives the flow, but the lid moving along its axis, moreover this last case is of particular interest due to its simplicity and it is, therefore, widely used in the literature for code and algorithm validation.

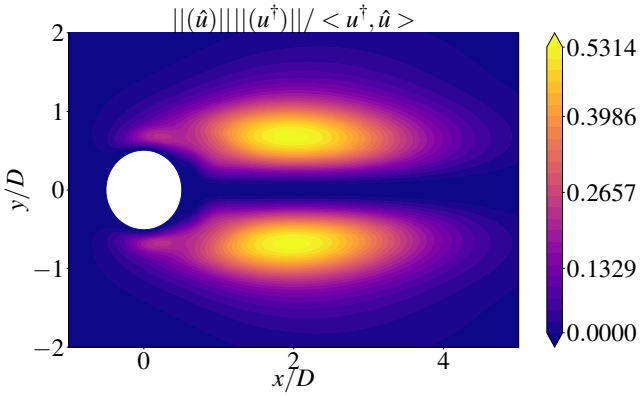


Figure 3.13: Structural sensitivity for $Re = 40$.

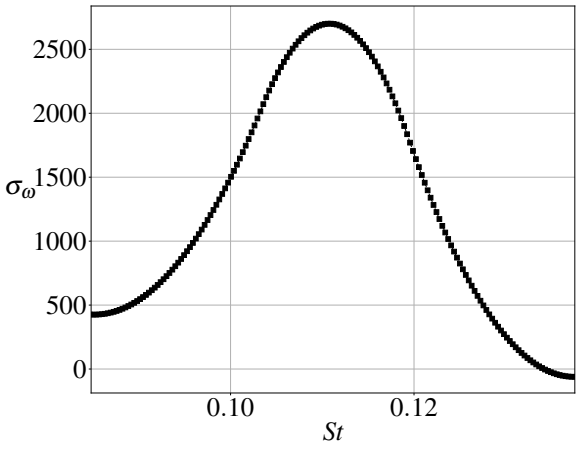


Figure 3.14: Evolution of the gain σ_ω in function of St at $Re = 40$



Figure 3.15: Optimal forcing (left) and optimal response (right) of the streamwise velocity component for $Re = 40$ and $St = 0.114$



Figure 3.16: Optimal forcing (left) and optimal response (right) of the cross stream velocity component for $Re = 40$ and $St = 0.114$

An initial approach to the study of 2-D lid-driven cavities that can be found in the literature is that of Burggraf in 1966 [157], who studied this flow configuration for values of Re up to 400. For lower values of Re, the center of the core vortex is located near the moving boundary, whereas for higher values, the latter moves towards the center, giving rise to an increasingly symmetrical primary vortex. In the same years, Pan & Acrivos [158] conducted the first experiments for $Re \in [20, 4000]$, where the flow patterns were obtained using photographic techniques for finite cavities. For the first numerical two-dimensional simulations, at higher Re, we had to wait for the work of Ghia *et al* (1982) [35], in which multigrid methods were used to solve incompressible Navier-Stokes up to $Re = 10000$, while the following year Schreiber & Keller [159] managed to obtain high-resolution stationary solutions using an adaptive Newton method.

Goodrich *et al.* (1990) [160] considered the case with an aspect ratio $A_{yx} = L_y/L_x = 2$ (where x is the direction in which the lid moves and y is the perpendicular direction) and stated that a Hopf bifurcation occurs for $2500 < Re < 5000$ because in their numerical simulations they find asymptotic periodic behavior for $Re = 5000$. Shen (1991) [161] also mentions the Hopf bifurcation, but for slightly different conditions. In fact, the case considered is that of a square cavity ($A_{yx} = 1$) with a regularization function for the velocity of the lid: $u(x, y = y_{max}) = 16x^2(1 - x)^2$. This therefore

implies a loss of singularity at the two upper vertices, since the velocity is zero. The results obtained by Shen are therefore different; in fact, he observed periodic behavior for $Re \in [10000, 10500]$, while for lower values, the flow converges towards a steady state.

The first studies using a stability analysis approach were carried out by Poliashenko & Aidun 1995 [162] and Fortin 1997 [4]. In our validation study, we will refer to Fortin's analysis of the 2-D lid-driven cavity. Although we will focus only on the case of a uniform lid velocity, Fortin also examined the case of a regularization function in his work. In the first case, the value of Re_{cr} found is around 8000 with a dimensionless critical frequency $f_{cr} = 0.45166$, while in the second case, the addition of the regularization function increases the value of Re_{cr} up to 10255 and gives a frequency $f_{cr} = 0.331063$, different from that found by Shen [161]. The reason why the value of Re_{cr} changes lies in the fact that the first unstable mode originates in the upper right corner (i.e., the corner of the lid at x=x_{max} and y =y_{max}) and is then advected and amplified along the streamline that divides the core vortex from the secondary vortices up to the top left corner. Therefore, different velocities near the corners of the lid lead to different results .

Although the numerical studies seen so far are interesting, based on two-dimensional simulations, they are not sufficient to describe reality. The first attempts to approach reality therefore involved taking into account the third dimension but considering periodic conditions in the spanwise direction. This means that the base flow remains two-dimensional, given the absence of side walls, but the perturbations are 3-D. In 1994, Ramanan & Homsy [163] investigated this configuration using the global stability tool. They found that the first unstable mode is 3-D at $Re = 594$ and spanwise wavenumber $\beta = 2.12$. This instability is of the Taylor-Görtler type, i.e. it corresponds to equidistant vortices in the boundary layer whose axes are parallel to the main direction of flow [164] (in the cavity , where walls are perpendicular straight line, the role of the concave walls is played by the external streamlines of the primary vortex). This type of vortex was also observed by Koseff and Street [165] in their experiments and by Kim and Moin [166] in their DNS simulations, but for higher values of Re (≈ 1000). A few years later, Ding and Kawahara [167]-[168] approached the same problem, namely the square lid driven by two-dimensional base flow perturbed in three directions. They also found an unstable mode of Taylor-Görtler, but with a critical Reynolds number closer to that of the experiments and numerical simulations ($Re_{cr} = 920$, $\beta_{cr} = 7.4$,$f_{cr} = 0.08$). In order to address this uncertainty in the literature of the time, Theofilis [169] conducted a global stability study for $Re \in [775 - 1100]$ and

$\beta \in [0 - 30]$, which will be used in our study to validate the 3-D extraction. He found four unstable modes: one stationary mode S1 and three travelling modes T1, T2 and T3, for which he plotted the neutral curves. All four instabilities are centrifugal, with peaks of activity in the right corners ($x = x_{max}$). The first instability found is the zero-frequency one at $Re_{cr} = 782.61$, $\beta_{cr} = 15.37$, followed by modes T1, T2 and T3 at $Re_{cr} = 844.57$, 922.10 , 960.54 and $\beta_{cr} = 15.77$, 7.4, 14.31 respectively. It can therefore be seen that the same mode obtained by Ding and Kawahara is found. As mentioned earlier, the 2-D lid-drivend cavity case is used as a test to validate the matrix-forming approach in comparison with the reference, whilst Theofilis's extension allows the 2.5D approach to be assessed, again using matrix forming.

3.3.1 LDC 2D

The square cavity is the case under consideration, the x direction coincides with the direction in which the lid moves, while the y direction coincides with the direction perpendicular to the latter. The lid moves at a constant speed u_0 and the length of the walls is $L_x = L_y = L$.
Since in dNami we cannot solve the Navier-Stokes equations written in incompressible form, complete equations are considered by imposing a $M = u_0/c = 0.1$ to remain within the incompressible range. Regarding $Re = u_0 L/\nu$, a supercritical value of $Re = 8050$ compared to Fortin ($Re_{cr} \approx 8000$) is imposed to immediately find the unstable mode.
For all walls adiabatic-no slip boundary conditions are imposed, with the exception for the top wall (lid) where a streamwise velocity $u = u_0 = 1$ is used.
The domain is discretized with $n_x = n_y = 150$ points, stretched near the boundaries in order to better compute velocity gradients. For convective terms a fourth-order discretisation is adopted, while for diffusive terms a second-order one. 3rd-order Jameson scheme is also employed with a high-order dissipation coefficient $k_{2(P+2)}$ lower w.r.t. the one proposed in literature. In figure 3.18 is shown our fixed point compared to the one of Fortin *et al.* [4]. It consists of a core vortex, then secondary vortices in the bottom right, bottom left and top left corners, and also a tertiary vortex in the bottom right corner. The latter is important for stability calculations. In fact, when the reference coefficient $k_{2(P+2)}$ was used in a first attempt, this vortex was dissipated in the fixed point and all modes were stable in the stability calculation. Then the contours of streamwise velocity u_0 and wall-normal velocity v_0 of the fixed point are presented in Figure (3.19). Both methodologies, time-stepper and matrix forming,

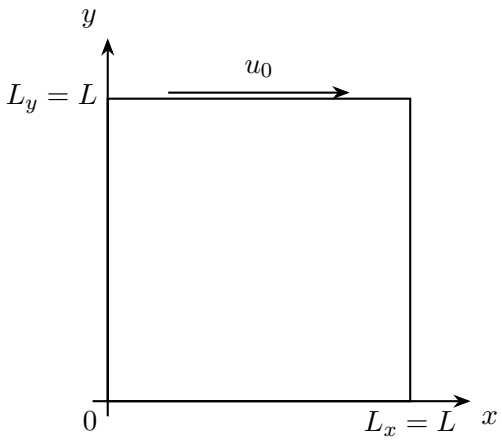


Figure 3.17: Schematic representation of the 2D lid-driven cavity.

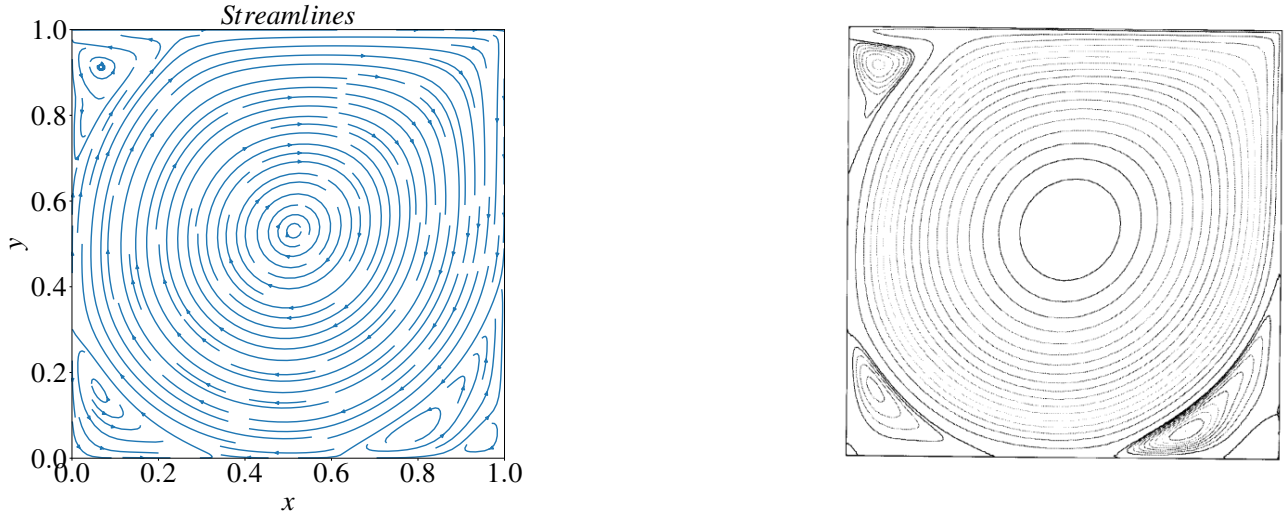


Figure 3.18: Fixed points comparisons between *dNami* computed (left) and Fortin computed [4] (right).

are used to calculate the eigenvalue spectrum. The same fixed point is used for both approaches. In the case of the time-stepper, a Krylov basis of size $m = 500$ is selected with a sampling time $\tau_s = 0.2214$ in order to capture the unstable mode which has an adimensional frequency $f = 0.45166$ corresponding to a period of $T = 2.214$. For the Jacobian extraction method instead, a shift and invert method is used by imposing a shift of $s = 0.01 + 2.8j$ to directly capture the unstable mode.

The eigenspectra obtained are shown in figure 3.20. There is a perfect overlap between the two spectra, and a straight line at the unstable St found by Fortin *et al.* for $Re = 8000$ has been plotted.

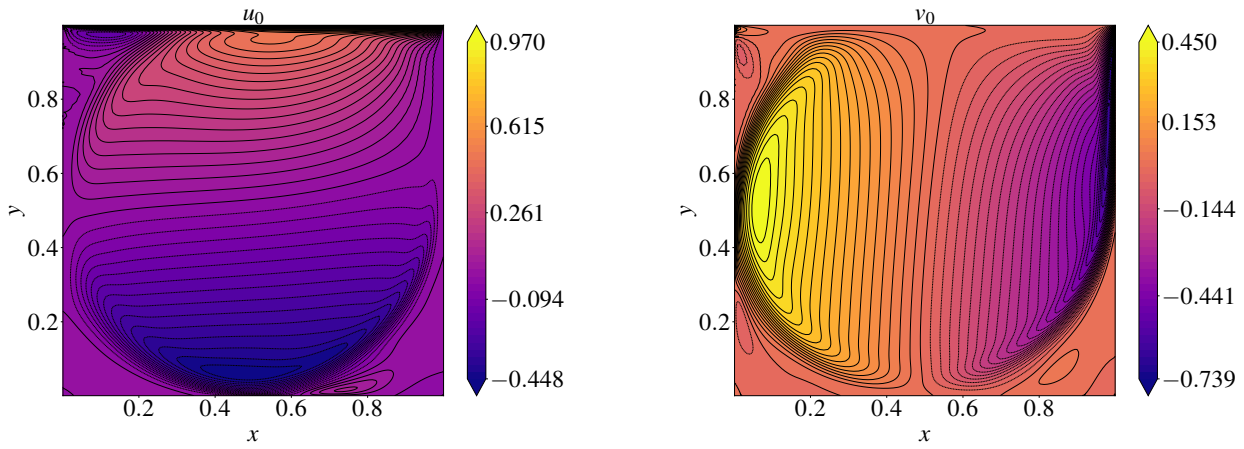


Figure 3.19: Streamwise velocity u_0 and wall-normal velocity v_0 contours of the fixed point for $Re = 8050$.

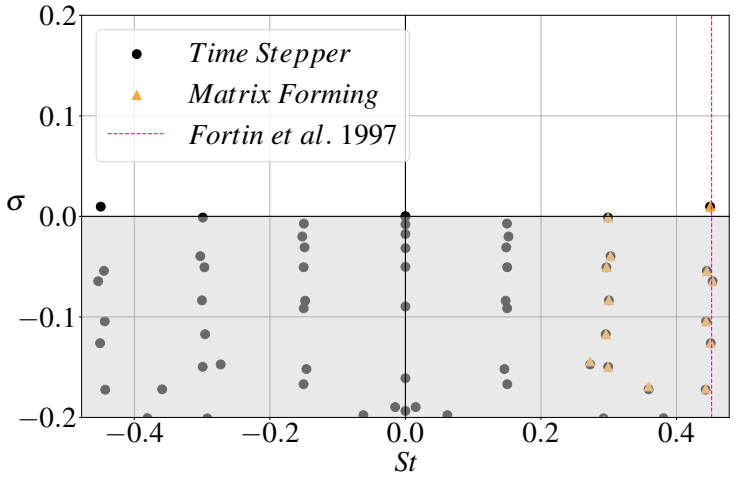


Figure 3.20: Eigenspectra comparison between time stepper and Jacobian extraction methods.

The straight line hits the unstable mode at $St = 0.45$; in fact, for small variations in Re, we do not expect an appreciable variation in frequency.

Observing the unstable mode, it can be seen that it originates in the upper right corner and is then transported and amplified along the shear flow, along the streamline that separates the main vortex from the vortices in the corner.

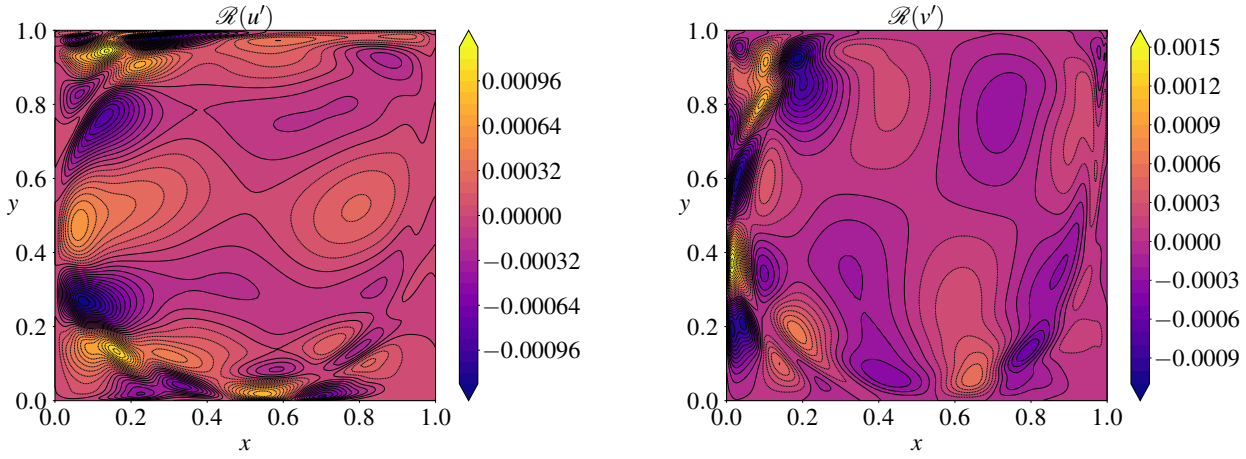


Figure 3.21: Real part of streamwise velocity perturbation (left) and wall-normal perturbation (right)

3.3.2 LDC 3-D

For the 2.5D case, the flow at $Re = 1000$ has been considered ; this is because, in his work, Theofilis presented the neutral curve for the four unstable modes identified, and the straight line at $Re = 1000$ intercepts all four neutral curves for $\beta \in [5, 25]$. The grid is discretized with $n_x = n_y = 128$, always stretched near the walls. Otherwise, the numerical configuration is the same as in the previous case. Figure 3.22 shows a schematic representation of the case under investigation. The spanwise length is

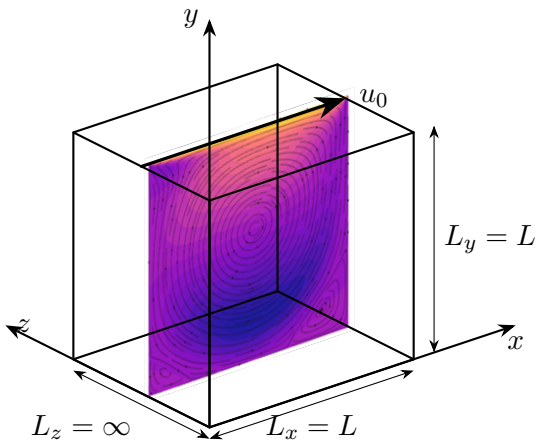


Figure 3.22: Schematic representation of th 2.5D lid-driven cavity.

marked as ∞ because we are considering a base flow that is always 2D. Furthermore, the cross-section

of the cavity is always square. The figure also shows the streamlines of the fixed point calculated as in the previous case. As one can see at $Re = 1000$, the vortex in the top corner disappears and only two vortices remain in the bottom corners. In this case, the global stability analysis is performed solely using the matrix-forming approach. By varying β, four unstable modes have been identified, the same as in [169]. These consist of one steady-state mode, S1, and three unsteady-state modes, T1, T2 and T3.

The first to become unstable is the steady mode at $Re < 800$, followed by the T1, T2 and T3 modes respectively. However, the T2 mode at $Re = 1000$ becomes unstable for lower values of β than the other three modes, making it more difficult to observe experimentally. Whilst the $T2$ mode reaches its maximum growth rate at $\beta \approx 7.5$, the other three modes reach their maximum at $\beta \approx 15$.

The evolution of the growth rate σ as a function of β is shown in Figure (3.23). The results obtained are compared with the straight line that intersects Theofilis's neutral curve at $Re = 1000$ and closely match the beginning and end points of the instability for each mode. Furthermore, the right-hand frame of the figure also shows the evolution of St as β varies. Mode T2 is the one with the lowest frequency, $St \approx 0.077$, followed by mode $T1$ at $St \approx 0.11$ and mode T3 at $St \approx 0.22$.

Figure (3.24) shows only the T2 mode at $\beta = 7.5$; specifically, the real component of the spanwise velocity in the right-hand frame and the 3-D reconstruction in the left-hand frame. This is because all modes have the same spatial structure; as stated earlier, this is a centrifugal instability caused by the curvature imposed by the streamlines.

3.4 Buffet over OAT15 profile

The final case discussed in this validation chapter is the buffet over OAT15 profile. The latter allows the turbulence model to be validated both in terms of URANS simulations and stability analysis, by testing the automatic differentiation of more complex equations. Due to the geometry under consideration (truncated profile), this case must be handled in a multi-block configuration, and therefore only the time-stepper method will be used for the global stability analysis.

This phenomenon consists in the occurrence of a low-frequency oscillation of the shock wave along the airfoil profile once a certain critical angle of attack is reached at transonic regime. If these oscillations couple with a structural mode, structural vibrations may occur, leading to wing failure. This is the reason why buffet was studied intensively following the Second World War.

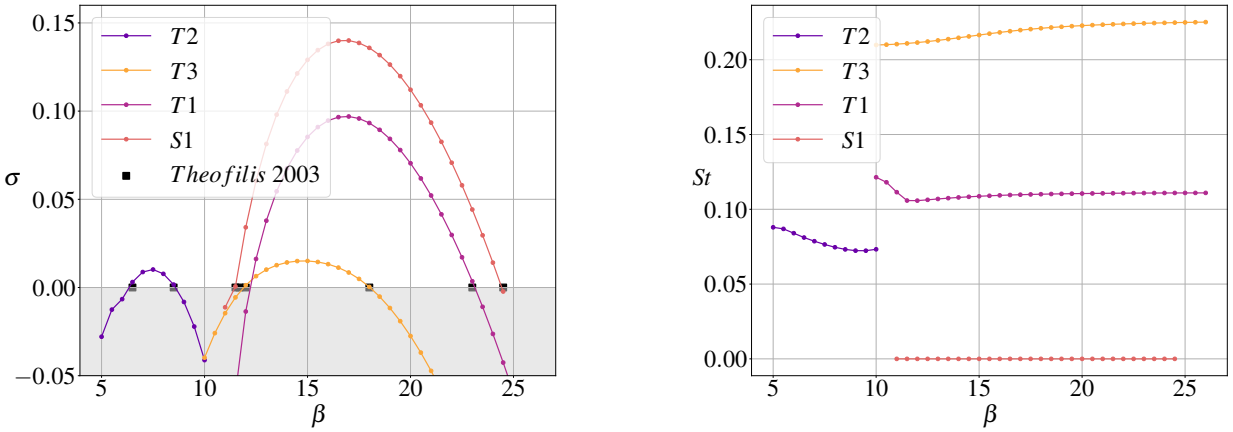


Figure 3.23: Evolution of growth rate (left) and frequency (right) in function of β for modes S1, T1, T2, T3 at $Re = 1000$.

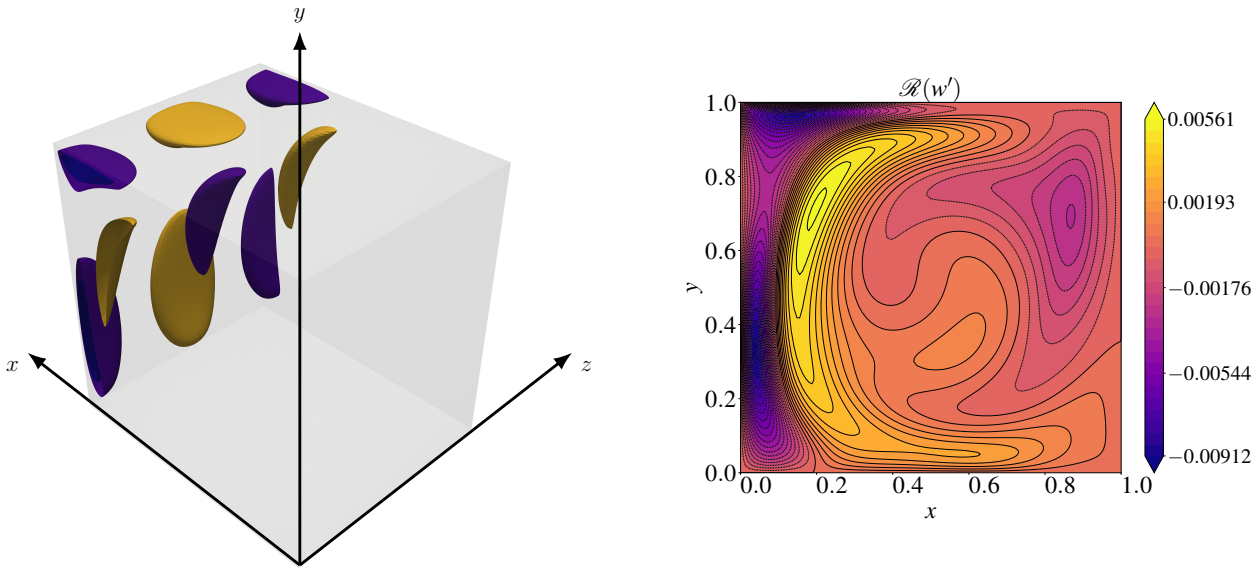


Figure 3.24: Real part of spanwise velocity perturbation $\mathcal{R}(w')$ and 3-D reconstruction of the mode $\mathcal{R}\left(\hat{w}(x,y)e^{i\beta z}\right)$

Hilton & Fowler were the first to conduct experiments in which they characterised the oscillations as aperiodic [28]. Among the subsequent experimental studies carried out, the work by McDevitt & Okuno [42] certainly stands out. The authors examined the flow behaviour around the NACA0012

profile by increasing the angle of attack whilst keeping the Mach number constant. As the flow velocity increased, the critical angle at which buffeting occurred decreased. Subsequently, Jacquin et al. [45] conducted an experimental study on the supercritical profile discussed in this section, namely the OAT15. The study revealed that, for a flow at $M = 0.73$, buffet onset occurs at an angle of attack of $\theta \approx 3.1°$. Furthermore they detected the modal nature of the buffet through a phase average approach.

From a numerical point of view, the low frequency unsteadiness allows the use of a URANS method. In [170] the various turbulence models employed overshoot the critical angle of attack for the NACA0012 profile. Subsequent work by Brunet [171] and Deck [172]-[44] has shown that, even in the case of the OAT15 supercritical profile, regardless of the turbulence model, the average position of the shock differs from the experimental result, and that a higher angle of attack is required for buffet to occur. A ZDES-type approach, on the other hand, has enabled a better match with the experimental results. There have been several attempts to explain this phenomenon over the years [27], but Crouch's work [40] is of particular interest. This study has explained the onset of buffet on a NACA0012 profile through a global stability approach. Noteworthly, Crouch [40] was the first to extend this kind of analysis to a compressible and turbulent case. Using a base flow obtained by RANS, and perturbing all state variables including the modified Spalart-Allmaras viscosity, an unstable mode was obtained starting from a critical angle of attack of $\theta = 3.03°$. Afterwards, the same methodology was used by Sartor [5], who found the range of non-stationary angles of attack for the OAT15 profile. He detected the onset of buffet for $\theta = 3.5°$ and then the offset for $\theta > 6°$ with a frequency around $77Hz$, then through a resolvent analysis a second peak in frequency was found ($\approx 2kHz$-$3kHz$) related to KH instability arising from the mixing layer.

It is easy to understand how the study of this case is crucial for validating all the analyses reported in the next chapter.

To simulate the flow around the OAT15 airfoil the same configuration employed by Sartor [5] has been adopted. The equations are normalized with respect to the chord length c and the quantities at infinity, with $Re_\infty = 3.2 \times 10^6$ and $M_\infty = 0.73$. Only one angle of attack is considered, $\theta = 4.5°$, as it is one of the most unstable.

A type C mesh is used, extending up to $40c$ in each direction to limit the effects of boundary conditions. In the semi-circular section of the mesh, 407 points are used along the contour of the airfoil and

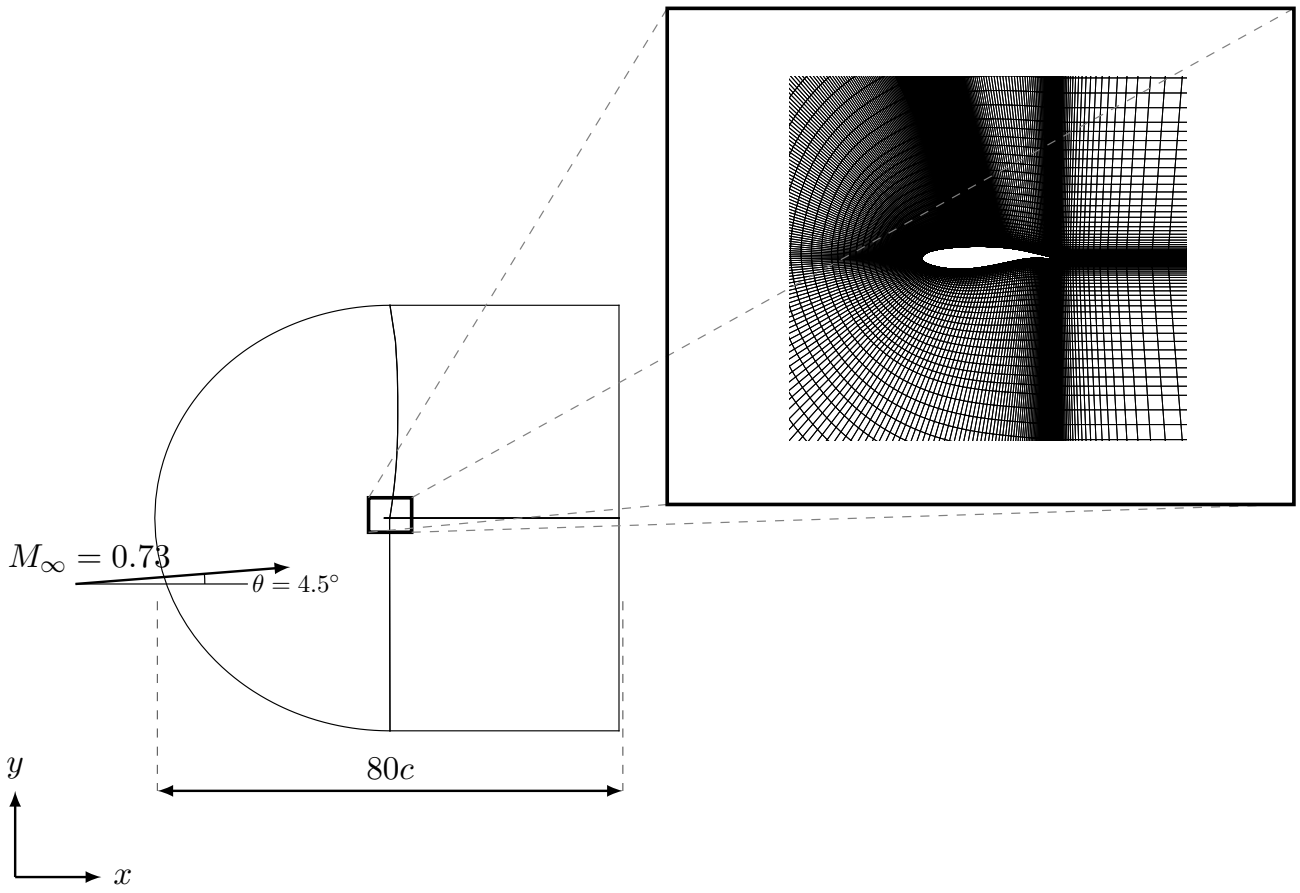


Figure 3.25: Geometry and computational mesh for the buffet on OAT15 profile.

124 perpendicular to the wall, whilst for the rectangular section, 90 points are used in the x direction and 286 in the y direction relative to the reference in the figure 3.25. The first wall point is located at $\Delta = 6 \times 10^{-6}$ to ensure that $y^+ < 1$,furthermore, a refinement up to $\Delta x = 0.003c$ is used in the area where the shock oscillates (see figure (3.25)). For the convective term a 4-th order discretisation is used and a second-order one for diffusive terms. This flow configuration is also the first one faced that presents shocks wave, and in this regard, the Jameson scheme with active low-order dissipation is employed with 3rd-order.

For this case, the Spalart–Allmaras model has been used, as in references [40]-[5]. The boundary conditions imposed are the same as for the flow around a cylinder case, with the addition of the modified viscosity term ν_{SA}. In the far field, a value of $\nu_{SA} = 3\nu_\infty$ is imposed, whilst at the wall $\nu_{SA} = 0$. It has been observed that the time step used is severely limited by the Fourier condition, due to the fact that the peak in turbulent viscosity occurs in the near wake region (see right frame of Figure (3.27)),

an area where the mesh is significantly refined. For this reason, it was necessary to apply a mesh enlargement treatment near the trailing edge.

The fixed point of URANS equation is computed as described in the previous chapter, using a Newton-Krylov time-stepper method.

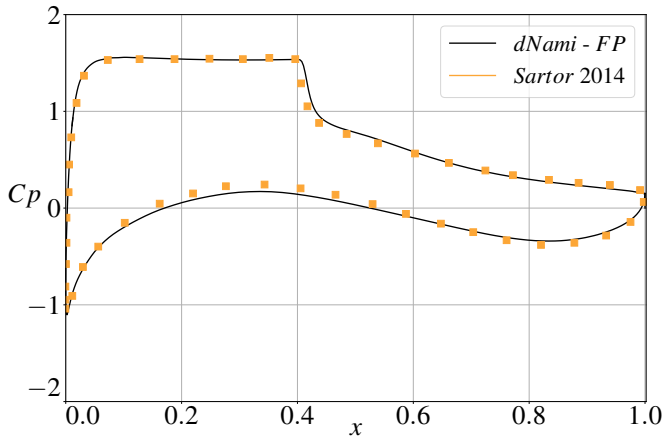


Figure 3.26: Pressure coefficient distribution compared with [5]

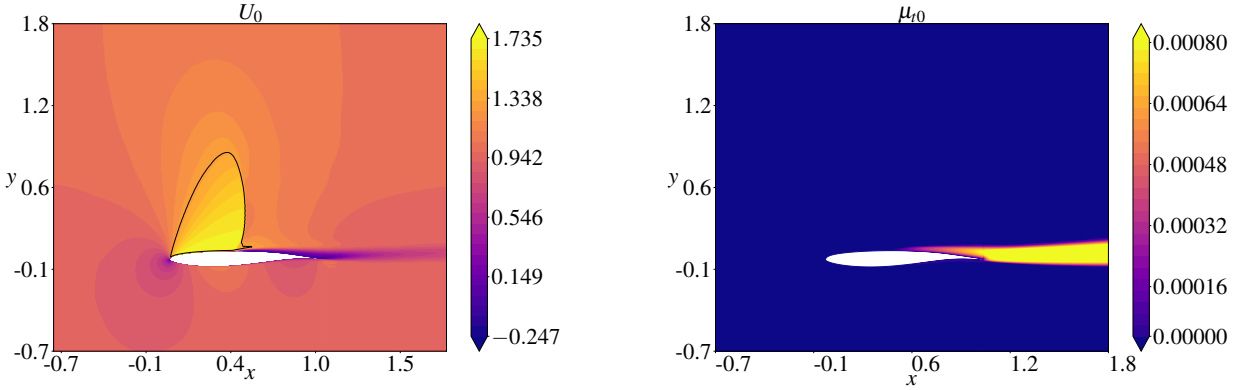


Figure 3.27: Streamwise velocity contours (left) and turbulent viscosity contours (right) of the fixed point

Figure (3.26) shows the distribution of the fixed-point pressure coefficient obtained, compared with the baseflow used by Sartor [5]. The results are reasonably consistent, with the shock shifted slightly to the right to $x = 0.41c$. Figure (3.27) shows the streamwise velocity (left frame) and turbulent viscosity (right frame) contours. To better highlight the supersonic zone, the isoline at $M = 1$ has

been superimposed in black on streamwise contours. One can appreciate how, at this angle of attack, the shock wave exhibits the classic lambda shape with the formation of a recirculation zone at its base. For the stability analysis, a Krylov basis was constructed with 350 snapshots taken with a sampling time $\tau = 1/(10 f_c)$, where f_c is the critical oscillation frequency known from previous studies. The

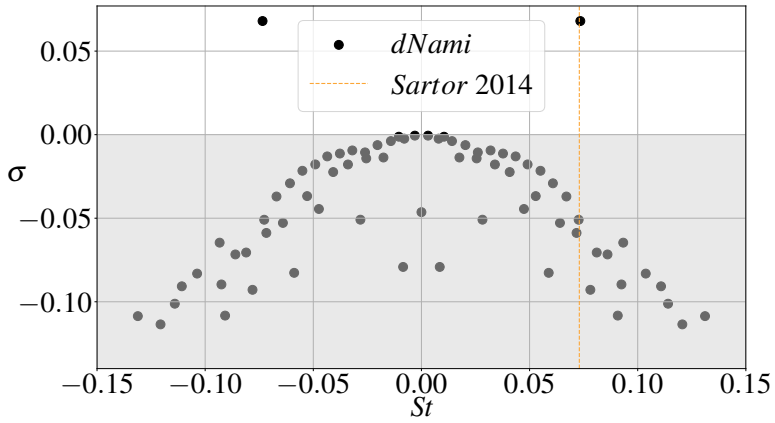


Figure 3.28: Eigenspectrum for buffet configuration at $\theta = 4.5°$

eigenvalue spectrum in Figure (3.28) clearly shows a single unstable mode at $\sigma = 0.066$ and $St = 0.0725$, which corresponds to a frequency of 79 Hz, the same as that found by Sartor but slightly higher than the frequency of 69 Hz found by Jacquin [45] in his experimental studies.

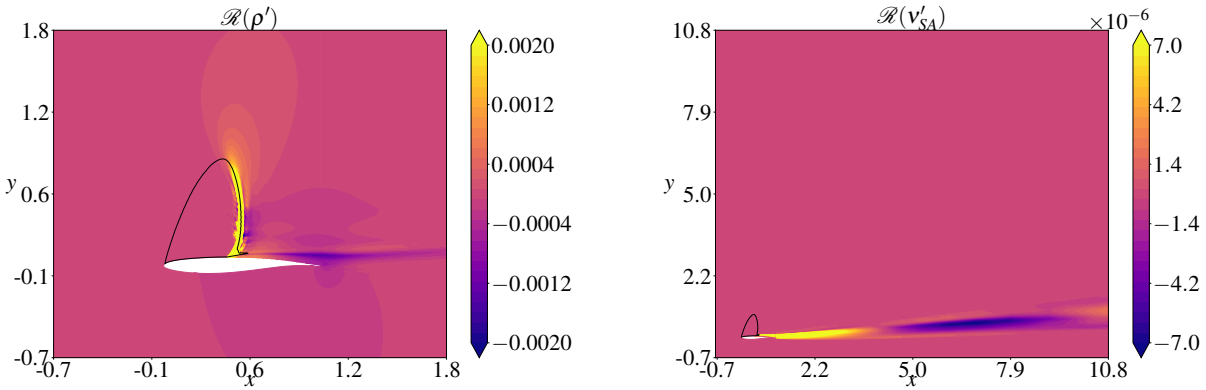


Figure 3.29: Real part of density ρ' (left) and modified viscosity ν'_{SA} (right) of the unstable mode at $St = 0.0725$

Figure (3.29) shows the unstable mode, specifically the real part of the density perturbation ρ' and modified viscosity ν'_{SA}. It can be noticed that most of the activity is located in the shock region

(visible through the isoline at $M = 1$) and in the recirculation zone with opposite sign. This phase opposition is typical of the interaction configuration between shock and boundary layer. Furthermore, the turbulent viscosity fluctuations are located in the wake, probably due to the contractions and expansions of the recirculation bubble following the movement of the shock.

A second stability calculation is then carried out, significantly reducing the sampling time in order to observe the higher-frequency modes. Figure (3.30) shows the calculated spectrum and the mode at $St > 1$ (corresponding to $f > 1kHz$). The frequency of the mode corresponds to that seen in the second peak of Sartor's resolvent analysis; the mode is of the KH type and is stable, as it requires triggering by an external force.

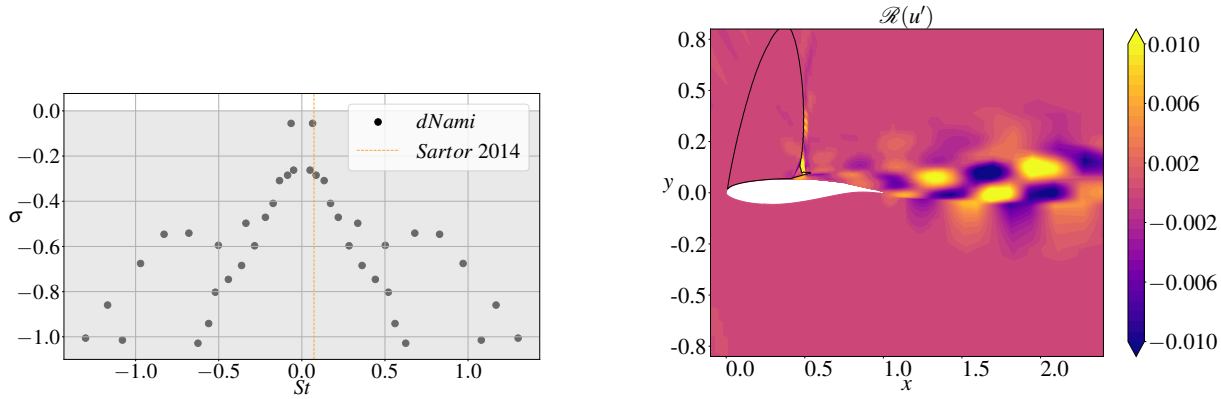


Figure 3.30: Eigenspectrum computed with $\tau = 0.0625$ (left) and real part of streamwise component of the mode at higher frequency ($St > 1$) (right).

Chapter 4

Sajben Diffuser

Contenu

4.1 Geometric configuration 124
4.2 2D Global stability and resolvent analysis 128
4.3 Parametric study on Sajben diffuser 140
4.3.1 Diffuser length variation 140
4.3.2 Pressure ratio variation 145
4.4 Physical discussion 148

4.1 Geometric configuration

This chapter is devoted entirely to the study of the Sajben diffuser, which was briefly mentioned in the introduction and which was the subject of an extensive programme of experimental and numerical research in the 1980s. This research sought to shed light on the mechanism responsible for the low-frequency dynamics observed in ramjet intakes. The two main geometric models considered are known in the literature as Model B and Model G, respectively. The former has a ratio of outlet cross-sectional area to throat cross-sectional area of 2.37, whilst the latter has a ratio of 1.52. Both diffusers feature a square cross-section and several suction slots along the bottom wall to make the flow as two-dimensional as possible. In 1977, using Schlieren high-speed photography, Sajben et al.[13] analysed Model B for a maximum Reynolds number of $Re = 10^6$ based on throat quantities and different ratios ν between inlet isentropic stagnation pressure p_t and outlet static pressure p_u. The first shock appears from $\nu = 1.1$ onwards, but for lower values the shape of a separation region due to the adverse pressure gradient is still evident. For $\nu = 1.28$, the onset of the separation bubble coincides with the shock foot, and as ν value is further increased, it assumes the characteristic lambda shape; for $\nu = 1.34$, the vortex sheet is clearly visible.

In subsequent experiments, the influence of boundary layer thickening [14] and non-stationary dynamics [22] was investigated. Specifically, by analysing the pressure signal collected by the various sensors, it is evident that in cases where separation is not linked to shock formation ($\nu < 1.13$), four peaks are present, the first at 110 Hz and the subsequent ones can be considered its harmonics. In regimes of strong shock, however, the spectrum appears to be broader but with a single low-frequency peak.

During the same period, the first numerical simulations were also carried out on Model B to test turbulence models on complex compressible configurations. Specifically, the work of Coakley *et al.* [173] and Liou *et al.* [174] showed that by using a slightly modified $k - \omega$ model [175], results can be obtained that compare well with the experimental mean flow.

Building on the work of Bogar *et al.* in 1981 [18] , there have been two further experimental studies [15] - [16] on G-model geometry. In this case, the reference parameter is $M_{\sigma u}$, which corresponds to the Mach number upstream of the shock at the edge of the top wall boundary layer. Two regimes can be distinguished: the weak shock regime $M_{\sigma u} < 1.27$, where there is no boundary layer separation, and $M_{\sigma u} > 1.27$, where there is shock-induced separation. What has emerged is that, in the case of a weak shock, an increase in the length of the downstream region with constant cross section near

the outlet leads to a reduction in the shock oscillation frequency, whilst for the strong shock regime this dependence disappears, showing a constant frequency of approximately 210 Hz. This suggests according to Bogar, that in the case of attached flow, the non-stationary dynamics are due to the propagation of acoustic waves, whilst in the case of detached flow, a convective mechanism appears to come into play due to the formation of vortices, and the new characteristic scale appears to be the length of the core flow, which remains constant. Through experiments conducted using the Laser Doppler Velocimeter technique by Bogar *et al.* in 1986 [18], a further step forward was taken in understanding the strong shock regime. It was observed that the vortex structure detaches from the region where the recirculation zone forms, is carried along, and grows in strength and size, causing the core flow to flutter.

Many studies have been carried out on the G-model using numerical simulations, particularly by Hsieh *et al.* [19]-[20]-[21]-[176]-[177], but also with a more numerical focus by Liou and Coakley [178] - [23]. Considering only the case of a strong shock, corresponding to $p_e/p_t = 0.72$, and focusing on the non-stationary dynamics, it can be seen that the shock oscillation frequency is approximately 300 Hz, regardless of the mesh refinement; furthermore, when the length of the exit section is varied, the frequency changes, in contrast to what has been observed experimentally. A DES was also recently carried out by Martelli *et al.* [179], in which they varied the pressure ratio to intensify the shock, starting from the experimental case of $R_p = 0.72$; in their study, no resonance was observed via wavelet analysis.

Finally, the nature of the loop is still not entirely clear, and although this configuration is now mostly used to test different turbulence models [180], it is worth investigating further to try to gain a better understanding of the physics involved.

With the aim of studying shock-boundary layer interaction in 2D channel flow, the experimental campaign conducted by Bur *et al.* [181]-[182]-[183]-[184] in the late 1990s and early 2000s is of equal interest. Specifically, initially, the effects of active and passive control were studied by maintaining a stationary shock via a second throat positioned in the outlet section, which isolates the flow field from pressure perturbations. Subsequently, the response to a forced oscillation created by a rotating shaft positioned near the second throat was evaluated. In this case, whether or not flow separation occurs, the shock oscillates at a frequency twice that of the rotating shaft. During the same period, and using the same 'double-throat' geometry, Reijasse *et al.* [185]-[186] investigated shock-induced

separation configurations that were more intense than those of their colleagues, noting not only the onset of instability from a certain aspect ratio, but also the loss of flow symmetry, which evolves into a symmetric divergent channel, unlike Sajben's diffuser.

Despite the extensive literature on the subject, the phenomenology underlying self-sustained oscillation in the presence of strong shocks is not entirely clear; it is therefore of interest to employ other strategies to investigate it. In this context, the use of linear stability analysis of dynamical systems is a valid option.

Throughout their experimental campaign, Sajben and colleagues used boundary layer suction systems. This made it possible to minimise the effect of the side walls, allowing them to focus on the two-dimensional characteristics. For this reason, this diffuser can be studied using a 2D approach. As mentioned previously, the diffuser models analysed are various, with most studies focusing on models B and G. In this work, only the latter is examined. The geometry consists of a converging-diverging duct with a square cross-section, preceded and followed by sections with a constant cross-section. The analytical profiles of the duct are given in [17] and follow the subsequent laws:

$$h(x/h_{th}) = \frac{\alpha \cosh \zeta}{(\alpha - 1) + \cosh \zeta}, \tag{4.1}$$

with:

$$\zeta = \frac{C_1(x/L_{cd})[1 + C_2(x/L_{cd})]^{C_3}}{(1 - x/L_{cd})^{C_4}}, \tag{4.2}$$

where the original values of coefficients have been reported in 4.1. In this chapter, the first case to be

Table 4.1: Constant for convergent and divergent profile computation.

Constant	**Converging**	**Diverging**
α	1.4114	1.5
L_{cd}	-2.598	7.216
C_1	0.81	2.25
C_2	1.0	0
C_3	0.5	-
C_4	0.6	0.6

analysed is the configuration known in the literature as a 'strong shock', corresponding to $R_p = 0.72$. For this pressure ratio, global stability analyses (in 2D and 2.5D) and the resolvent analysis will be

conducted, followed by an examination of the case known as the 'weak shock' at $R_p = 0.813$, and then various parametric studies. For the main case, the influence of the y^+ of the first cell and the number of grid points considered has been briefly evaluated; both studies are presented in the appendix. All the main cases are summarized in Table 4.2. Both the geometric configuration with the

Table 4.2: Summary of computational cases and parameters.

CASE	R_p	L/h_{in}	**Mesh** $(n_x \times n_y)$	β
STRONG SHOCK	0.72	9.05	126×100	0 to 17
WEAK SHOCK	0.813	9.05	126×100	0 to 5
PARAM L1	0.72	9.75	131×100	/
PARAM L2	0.72	10.45	136×100	/
PARAM L3	0.72	11.15	141×100	/
PARAM RP1	0.68	9.05	126×100	/
PARAM RP2	0.64	9.05	126×100	/
PARAM RP3	0.60	9.05	126×100	/

various dimensions and the final mesh used are shown in Figure (4.1). The mesh consists of $n_x = 126$ points in the streamwise direction of the flow and $n_y = 100$ points in the wall-normal direction. The grid presents two refinements: the first in the streamwise direction in the region $1 < x/h_{in} < 3$ to accurately resolve the shock with $\Delta x = 0.03 h_{in}$, and the second in the direction normal to the wall to satisfy the condition $y^+ < 1$ everywhere with $\Delta y = 2 \times 10^{-5}$. For all configurations in Table 4.2

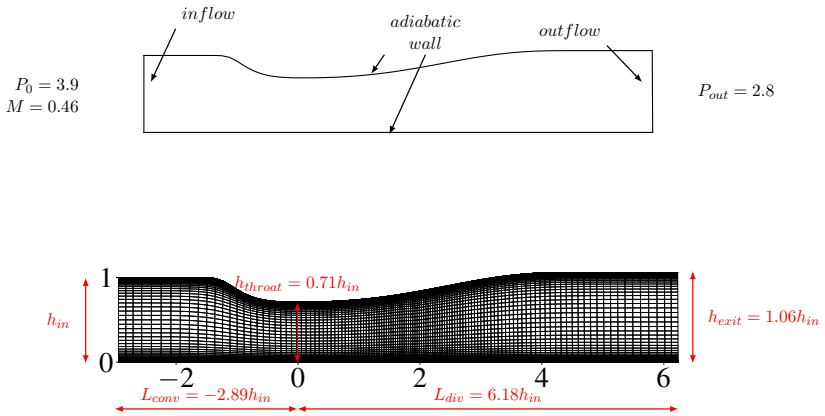


Figure 4.1: Compu.

two different initializations are employed in the convergent and divergent to ensure supersonic flow in

the divergent section and thus ensure proper operating conditions. Specifically, the entire convergent is initialized with the inlet conditions ($M_{in} = 0.46$), while the entire divergent is initialized with the outlet conditions ($M_{out} = 0.65$). To clarify the initialization of the strong shock case, the inlet conditions are known and fixed, namely $M_{in} = 0.46$ with $p_0 = 3.9$, corresponding to $p_0 = 135000Pa$. The streamwise velocity, temperature and density are set to 1, as we are normalising with respect to the inlet conditions. However, in terms of outlet conditions, only the pressure $p_{out} = 2.8$ is known, which corresponds to $p_{out} = 97200Pa$. For this reason, to initialize the calculation, a value of $M_{out} = 0.65$ is set, which is an average value in the outlet section derived from previous studies. Regarding boundary conditions employed, no-slip adiabatic boundary conditions are imposed on the two walls. At the inlet, the conditions are imposed through Riemann invariants [123], while at the outlet, an extrapolation is applied for all state variables except for energy, which takes into account a set pressure such that $R_p = p_{exit}/p_0 = 0.72$, where p_0 is the isentropic stagnation pressure. Since we are dealing with a confined flow, these inlet/outlet conditions are more suitable than the conditions imposed by classical LODI based BC [119], which are more appropriate for external aerodynamics.

4.2 2D Global stability and resolvent analysis

The first step in the stability analysis is to determine the fixed point; this is calculated using the same procedure outlined for the validation tests, namely a Newton-Krylov method, taking into account a sampling time relative to the principal frequency observed in the experiments. The frequency of the strong shock case corresponds to $210Hz$, which, for our dimensionless system, is equivalent to $St = 0.087$; therefore, a sampling time of $\tau_c = 1/(10 \times 0.087) = 1.153$ is used.

Figure (4.2) shows the fixed point obtained. From the density contours, a shock wave can be seen in the divergent region. At the foot of the shock, due to the high intensity, a recirculation zone is formed, where the maximum turbulent viscosity is therefore found. Figures (4.3) and (4.4) show the wall pressure distribution and the streamwise velocity profile u_0 in two different sections, respectively. The results were compared with both the experiments and the NASA database [187]. The pressure distribution shows the exact position of the shock at $x/h_{in} = 1.35$ on the upper wall and $x/h_{in} = 1.55$ on the lower wall, in agreement with the experiments. Furthermore, there is a good overlap between the velocity profiles in the different sections located downstream of the shock, validating the turbulence

model implementation.

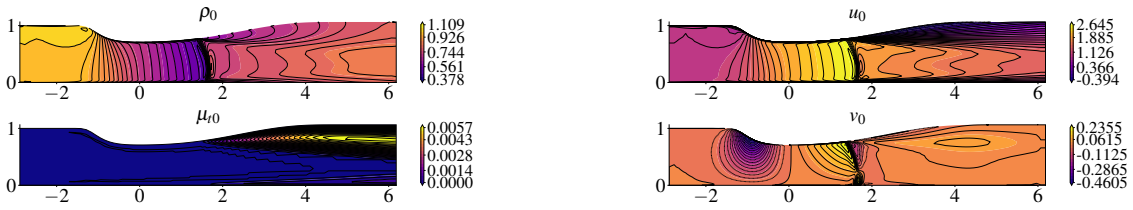


Figure 4.2: Fixed point contours. Density ρ_0 and turbulent viscosity μ_{t0} (left), streamwise velocity u_0 and wall normal velocity v_0 (right).

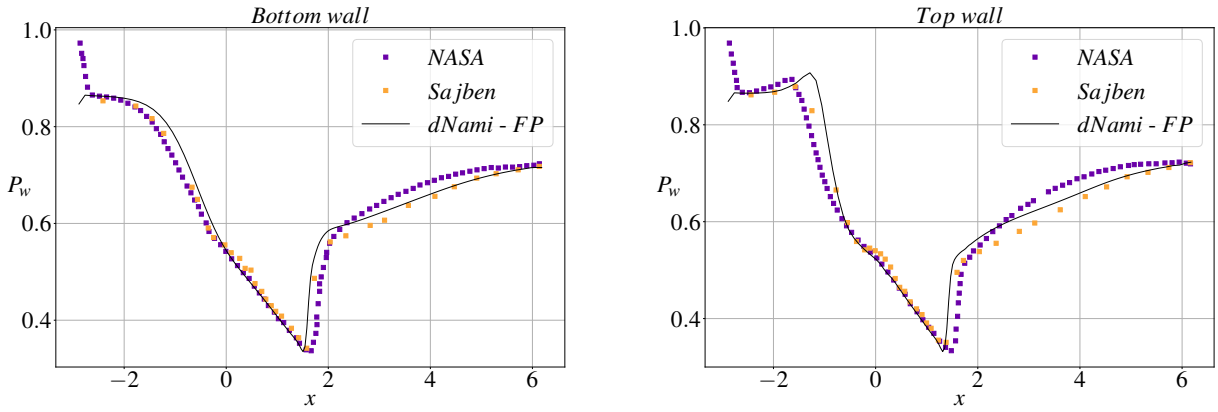


Figure 4.3: Wall pressure distribution. Bottom wall (left) , top wall (right)

The global stability study is carried out using the fixed point shown as the base flow. Given the small size of the problem, it is possible to extract the Jacobian matrix and calculate its eigenvalues in a matter of seconds, compared to a time stepper approach which, due to the tool available that relies on explicit time marching, would take several days. Therefore, the first method is preferred in order to then carry out a parametric study.

After extracting the matrix, the shift and invert method is used to compute the eigenspectrum shown in Figure (4.5). The frequency found experimentally by Bogar [18] and the frequency found with URANS numerical simulations by Hsieh [20] have been superimposed on the spectrum. The results obtained using matrix forming are also compared with those from the time-stepper, which is used solely for this base case. No unstable modes are present; however, the *least stable* mode is found between the experimental and numerical frequencies. This mode has $St = 0.11$, which corresponds to a dimensional frequency of $f = 270$ Hz. The corresponding eigenvector can be seen in Figure (4.6),

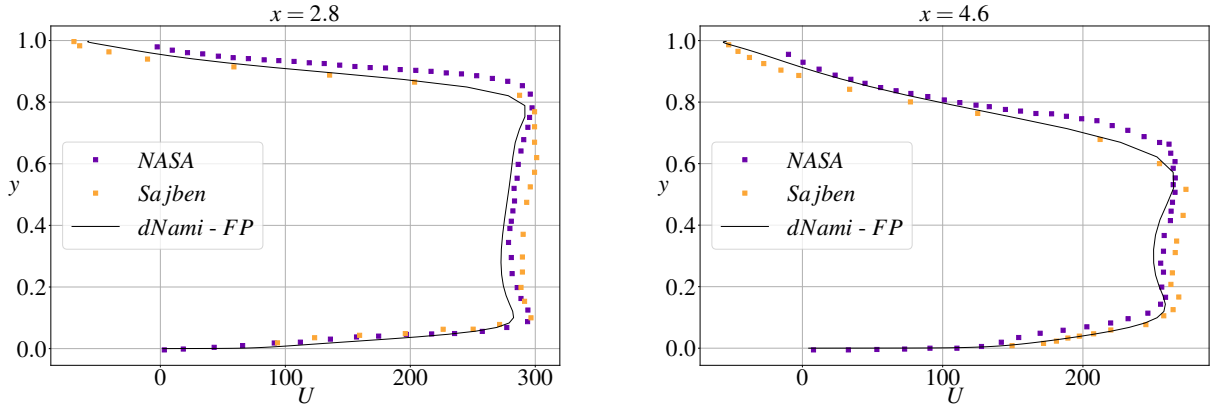


Figure 4.4: Streamwise velocity profile at two different sections. $x/h_{in} = 2.8$ (left) , $x/h_{in} = 4.6$ (right).

which shows the contours of its real part superimposed on the streamwise velocity isolines of the fixed point u_0. Large values of the u', v' and ρ' components of the mode are present in the shock zone and in the recirculation zone with opposite signs. This behaviour has already been reported in the validation section for the unstable buffet mode, as it is typical of strong interactions between shock and boundary layer. The modified viscosity ν_{SA} also behaves similarly to that of the buffet, as it fluctuates in the recirculation zone where turbulent viscosity is highest.

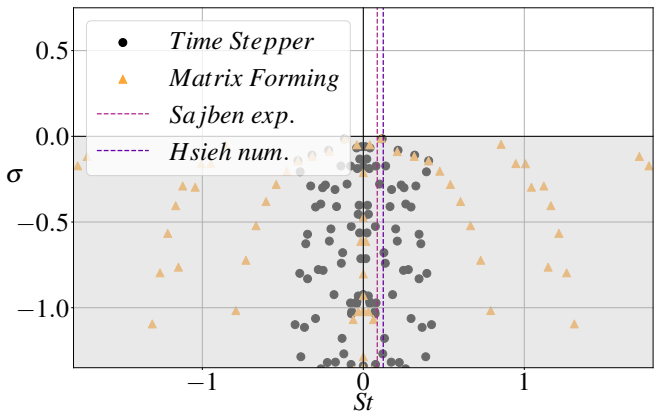


Figure 4.5: Eigenspectra compared with experimental frequency and numerical frequency of reference.

Since the stability analysis shows that no mode is globally unstable, it is certainly worth computing

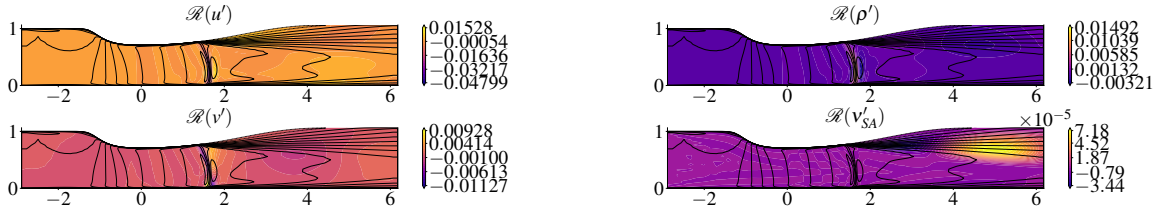


Figure 4.6: Real part of the mode at $St = 0.11$ (270 Hz). Streamwise and wall-normal velocity (left), density and turbulent eddy viscosity (right).

the pseudospectrum. The latter is defined as follows:

$$\mathbf{\Lambda}_\epsilon(\boldsymbol{\mathcal{L}}) = \{\lambda \in \mathbb{C} : ||(\lambda \boldsymbol{I} - \boldsymbol{\mathcal{L}})^{-1}|| > \epsilon^{-1}\}. \tag{4.3}$$

where $\mathbf{\Lambda}_\epsilon(\boldsymbol{\mathcal{L}})$ is the pseudospectrum of the operator $\boldsymbol{\mathcal{L}}$ [38]. It allows us to assess how sensitive the less stable modes are to an external perturbation. The pseudospectrum has been computed in the frequency range of the three less stable modes, mapping the spectral space for $-0.1 < \sigma < 0.1$ and $0.03 < St < 0.3$, computing the SVD of the operator $(\mathcal{L} - \lambda \boldsymbol{I})^{-1}$ and considering only the largest singular value. Figure (4.7) shows that a noise level of $\epsilon = 10^{-5}$ is sufficient to destabilise the mode at $St = 0.11$, triggering non-stationary dynamics. This noise may be related to the background turbulence, or to the acoustic noise or else, to disturbances of another nature. Due to the non-normality of the operator, the system enters a state of pseudo-resonance, that is, it responds with strong amplification (proportional to $1/\epsilon$) at given mode's frequencies, despite these modes being asymptotically stable in the absence of any noise.

Global stability analysis alone is therefore not sufficient to describe this flow configuration; it is necessary to investigate the receptivity mechanism that drives the dynamics, using a resolvent analysis. In order to perform this analysis (see equation 1.100), one should first validate the adjoint operator $\boldsymbol{\mathcal{L}}^\dagger$. In the present case it is convenient to use a discrete adjoint [188]. Figure (4.8) shows the spectrum of the adjoint operator, which overlaps perfectly with the direct spectrum, ensuring its consistency. The same figure also shows the adjoint modes superimposed on the isolines of the fixed point velocity u_0. It is very interesting to note how the adjoint modes originate from the foot of the shock, where there is maximum activity, and rise towards the neck. The direct and adjoint mode computations allow us to investigate the structural sensitivity of the flow before performing the resolvent analysis. The latter is obtained by dividing the product between the norms of the direct and adjoint vectors

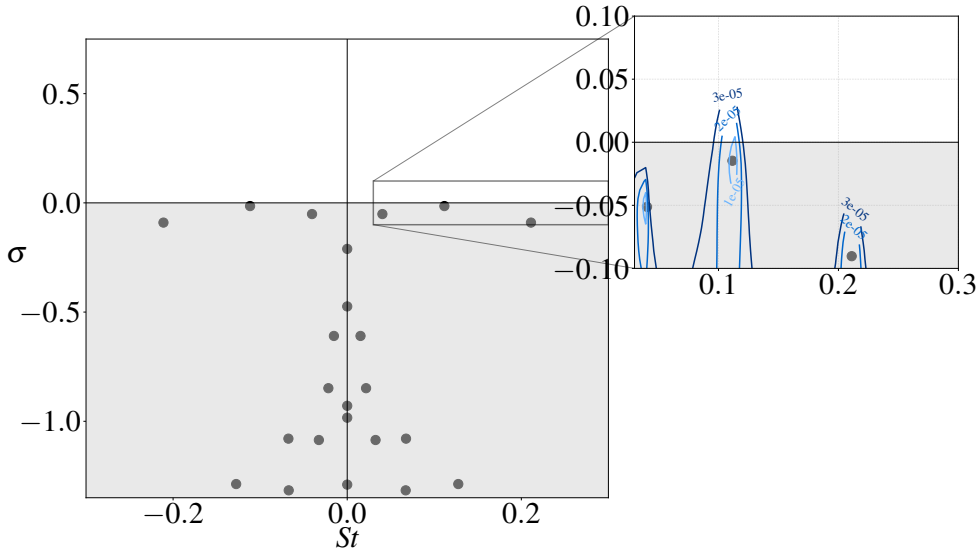


Figure 4.7: Spectrum and pseudospectrum.

by their scalar product $||(\hat{\boldsymbol{q}})||\ ||(\boldsymbol{q}^{\dagger})||/ < \boldsymbol{q}^{\dagger}, \hat{\boldsymbol{q}} >$ [154]. Although generally used to show where global instability arises, computation of the structural sensitivity of the stable mode at $St = 0.11$ can also be interesting as it indicates the region of the flow that is most sensitive to disturbance. Figure (4.9) shows the wavemaker for the mode at $St = 0.11$. As expected, the maximum is found in the region where the shock is located and at the foot of the shock where there is interaction with the boundary layer. This means that a change at the base of the shock would lead to a profound change in the mode, so this is the appropriate area to act for controlling the instability. However, the downstream region also shows peaks, which could indicate that the mechanism underlying the observed oscillation is related to acoustic waves that are reflected at the outlet. To clarify this aspect, a parametric analysis will be presented in the following section.

The resolvent analysis is performed by solving the eigenvalue problem reported in equation (1.100) and imposing Chu's norm for energy. Since this is a completely turbulent case, it is natural to think of an extension of the latter, but due to the turbulence model used, there is no way, to our knowledge, to calculate the turbulent kinetic energy from the modified viscosity and thus extend the norm. The analysis is performed for 100 values of St between 0.06 and 0.16. The energy gain σ, shown in Figure (4.10), suggests that there is a single receptivity mechanism determining the physics and, given the high peak value at $St = 0.11$, even a small disturbance can trigger the oscillatory dynamics, even

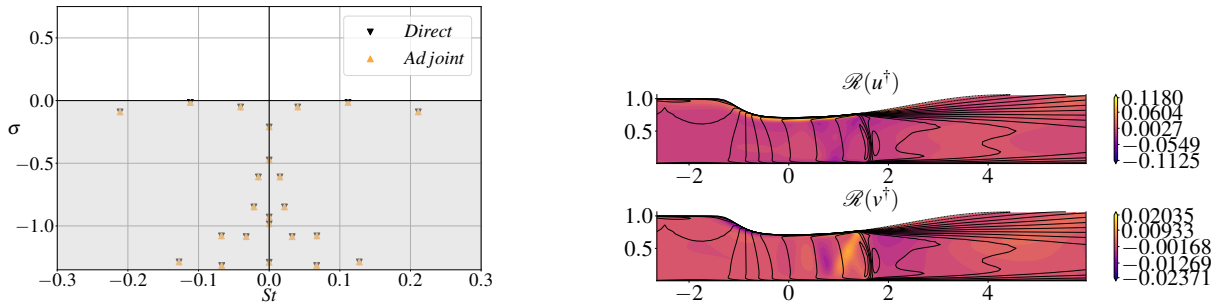


Figure 4.8: Direct and adjoint eigenspectra comparison (left) and real part of streamwise $u^\dagger$ and wall-normal $v^\dagger$ adjoint mode at St = 0.11.

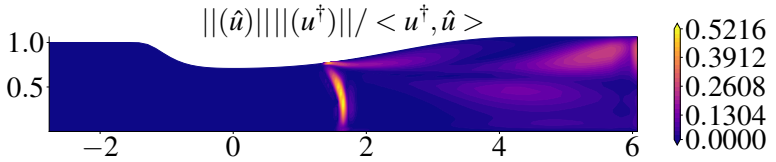


Figure 4.9: Structural sensitivity or wavemaker for the mode at $St = 0.11$. Streamwise velocity component $\|(\hat{u})\|\ \|(u^\dagger)\|/ < u^\dagger, \hat{u} >$.

if not self-sustained. On the right-hand side of the same figure, it is also possible to observe the optimal forcing and the corresponding optimal response of the streamwise velocity at $St = 0.11$. It is immediately clear that the optimal forcing has the same pattern as the adjoint mode, while the optimal response has the same shape as the direct mode. This is also an expected result, as the adjoint mode can be seen as the best way to force the direct mode.

After completing the 2D linear analysis, we move on to the case of spanwise-dependent perturbations, in order to evaluate the influence of the spanwise direction on the flow instability. Once the operator $\boldsymbol{\mathcal{L}}_{2.5D}$ was extracted, we first studied its global stability for small values of β ($\beta < 1$) to follow the two-dimensional mode. Figure (4.11) shows the eigenspectra for two different values of the spanwise wavenumber. At $\beta = 0$ we obtained the same eigenspectrum of the 2D case, but with some additional modes. This is due to the fact that the system at $\beta = 0$ is decoupled and the extra modes have a non-zero spanwise component. Furthermore, the mode previously observed at $St = 0.11$ becomes increasingly stable when β increases. This behavior is best observed in Figure (4.12), where the growth rate σ and the pulsation ω of the 2D mode are tracked as β varies. The fact that β is non-zero adds a term to the dispersion relation, leading to higher values of ω, and also adds an additional dissipative

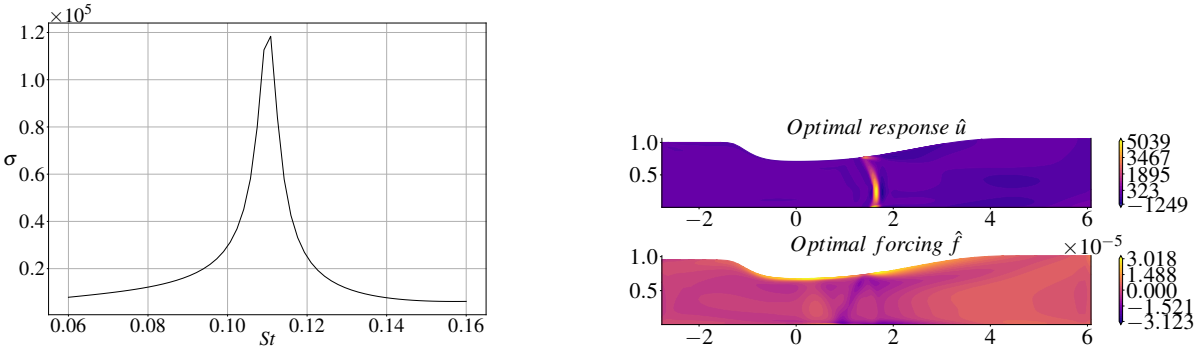


Figure 4.10: Optimal gain in function of St (left) and optimal response and forcing of the streamwise velocity component at $St = 0.11$ (right).

term to the energy balance relation, leading to lower values of σ.

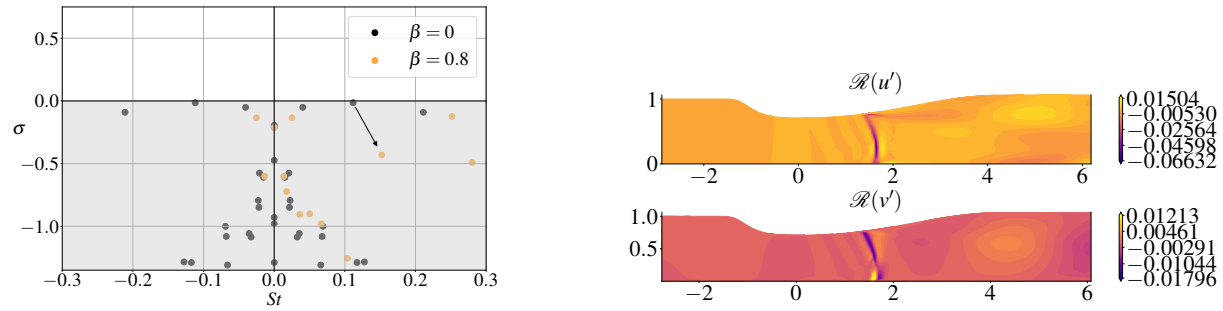


Figure 4.11: Eigenspectra comparison at $\beta = 0$ and $\beta = 0.8$ (left) and real part of streamwise velocity and wall normal velocity perturbation at low β (right).

For higher β values, starting from $\beta = 1$, the dominant mechanism is no longer the interaction between shock and boundary layer but a stationary mode ($\omega = 0$). Figure (4.13) displays the eigenspectrum at $\beta = 8$ directly. It clearly reveals that there is only one dominant unstable mode, while the 2D mode of shock/boundary layer interaction is no longer detectable. On the right side of the same figure, we have evaluated the trend of σ as β varies. This mode quickly becomes unstable, reaching a peak growth rate at $\beta \approx 8$.

This stationary mode with $\sigma > 0$ corresponds to a centrifugal instability also known as Taylor-Görtler instability. Due to the higher values of β, the wavelength is reduced, making the centrifugal effect due to the concave walls predominant. The mode consists of counter-rotating longitudinal vortices aligned

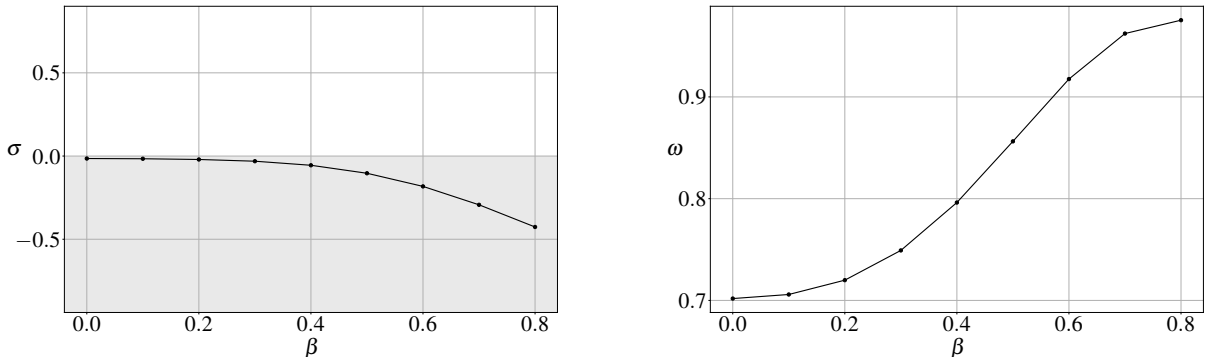


Figure 4.12: Evolution of growth rate σ and pulsation ω at different β values for 2D mode.

with the main direction of flow along the curved wall. Being a zero-frequency instability, it directly modifies the baseflow creating a 3D flow with transverse periodicity. The longitudinal vortices can be clearly seen in Figures (4.14 - 4.15 - 4.16) where the 3D perturbations have been reconstructed using the ansatz. They are located on the upper wall where there is the greatest curvature. For a value of $\beta = 8$, which corresponds to the maximum growth rate, the wavelength of the mode is $\lambda_z = 0.785 h_{in}$. Considering the width s of the diffuser used in the experiments, which corresponds to $s = 2.8254 h_{in}$, one may conclude that a factor of $s/\lambda_z \approx 4$ could be sufficient for the instability to set in. Furthermore, as shown by the black curve in Figure (4.13), the mode remains unstable for even higher values of β, further reducing the possible influence of the side-walls, which are not taken into account in the $2.5D$ analysis. This means that it would be possible to observe the mode experimentally. With the

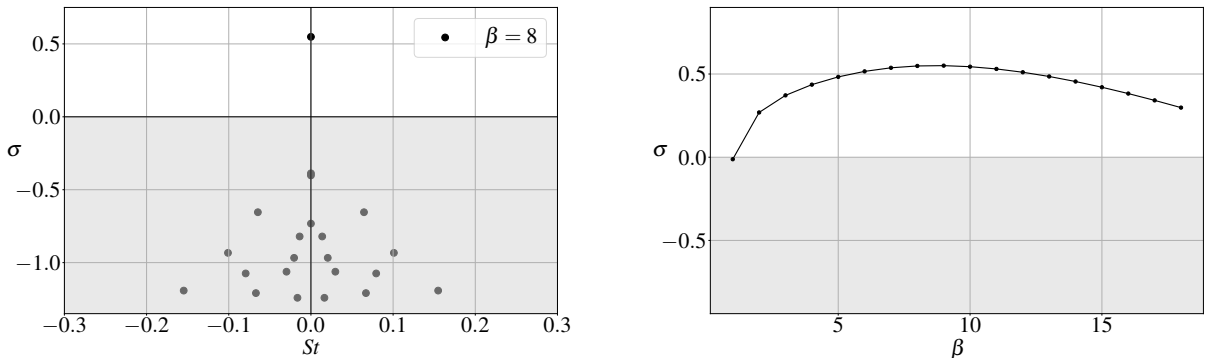


Figure 4.13: Eigenspectrum at $\beta = 8$ (left) and evolution of growth rate σ at different β values for 3D mode (right).

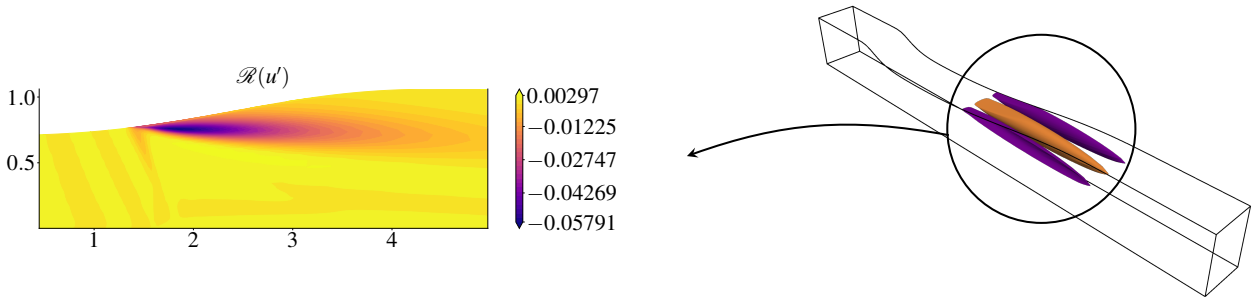


Figure 4.14: Real part of streamwise velocity u' of the stationary mode at $\beta = 8$. 2D contours (left) and 3D contours reconstruction $\hat{u}e^{(i\beta z)}$ (right).

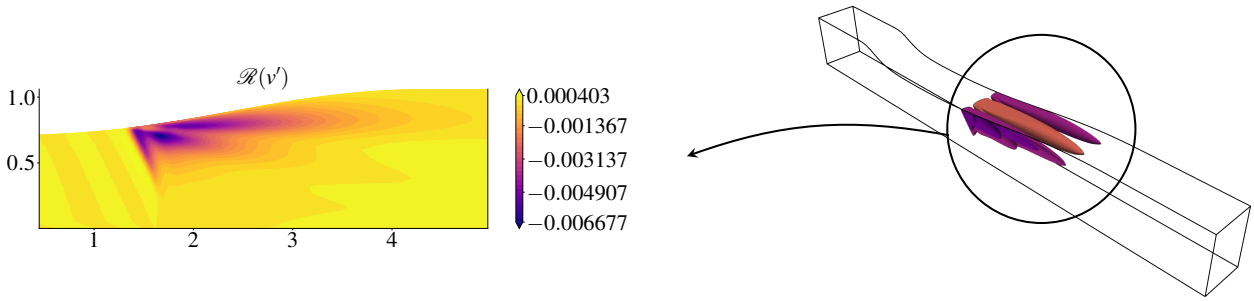


Figure 4.15: Real part of wall-normal velocity v' of the stationary mode at $\beta = 8$. 2D contours (left) and 3D contours reconstruction $\hat{v}e^{(i\beta z)}$ (right).

aim of determining, at least qualitatively, the pressure ratio at which this 3D instability occurs, two further pressure ratios were considered: $R_p = 0.785$ and $R_p = 0.813$. In particular, in accordance with [18], $R_p = 0.813$ corresponds to the value at which there is no boundary layer separation on the upper wall. Figure (4.17) shows the evolution of the growth rate of the 3D mode for the new pressure ratios considered as β varies. Whilst for $R_p = 0.785$ the instability is still present, albeit within a limited range of β, in the case of $R_p = 0.813$ it disappears completely, thus demonstrating a clear link between the formation of longitudinal vortices and the presence of a recirculation zone. The concave surface of the divergent is not sufficient to trigger the instability; the flow must undergo a further deflection for the centrifugal phenomenon to occur, and this deflection is due to the recirculation bubble. To obtain an initial estimate of the critical pressure ratio, a simple linear interpolation is performed between the

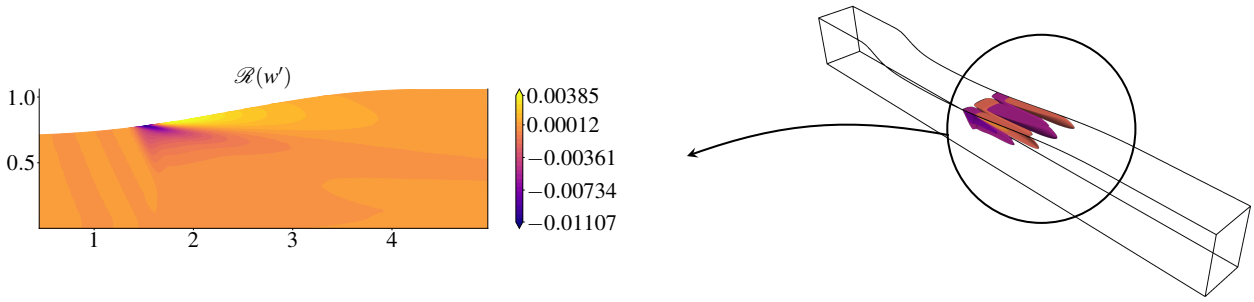


Figure 4.16: Real part of spanwise velocity w' of the stationary mode at $\beta = 8$. 2D contours (left) and 3D contours reconstruction $\hat{w}e^{(i\beta z)}$ (right).

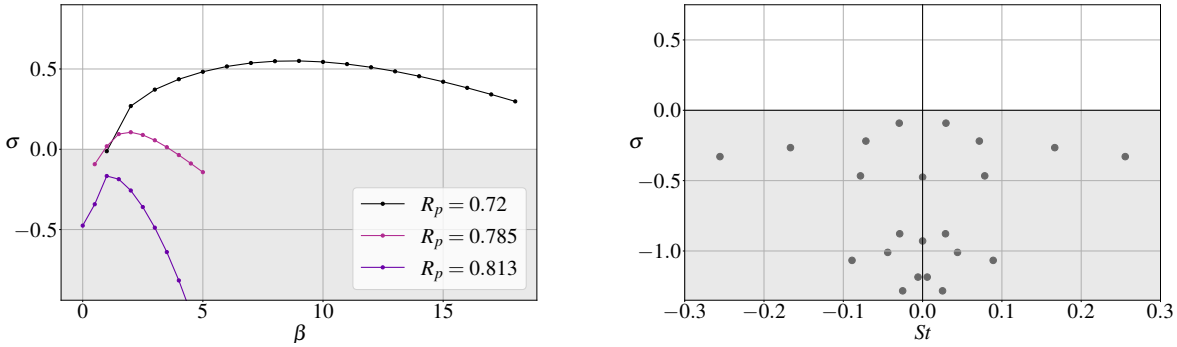


Figure 4.17: Evolution of growth rate σ at different β values and different pressure ratios (left); 2D eigenspectrum for the case at $R_p = 0.813$ (right).

two peaks of the curves at $R_p = 0.785$ and $R_p = 0.813$, yielding $R_p^c \simeq 0.796$ and $\beta^c \simeq 1.76$.

The Görtler number has also been calculated in order to compare it with the results obtained from the stability analysis. For turbulent flows, Tani [189] proposes a new definition of the Görtler number in which molecular viscosity is replaced by turbulent viscosity. Previously, Clauser's relation [190] was used to calculate the latter, but since we have access to its local value via the turbulence model, we use the approach proposed by Zhang in his recent work [191], which consists of selecting the maximum value within the section under consideration. Therefore, for turbulent flows, the Görtler number at each section can be calculated as:

$$Gr = \frac{\rho_e U_e \theta}{\max(\mu_t)} \sqrt{\frac{\theta}{R}} \tag{4.4}$$

where θ is the momentum thickness for compressible flows, U_e and ρ_e are the streamwise velocity and

density computed at the distance from the upper wall where the streamwise velocity reaches a local maximum and R is the radius of curvature. However, in the case of separation, it is not possible to calculate the analytical radius of curvature; instead, one must calculate the radius of curvature of the curve that separates the recirculation bubble from the rest of the flow. For the weak shock case, as there is no recirculation zone, the curvature can be calculated analytically based on the analytical profile of the diffuser presented in 4.1 as:

$$R = \left(\frac{|h''(x)|}{[1 + (h'(x))^2]^{3/2}} \right)^{-1}, \tag{4.5}$$

where the absolute value has been used to disregard the sign. In the case of a strong shock, however, the flow does not follow the curvature of the wall due to the recirculation zone. To calculate the curvature imposed on the flow, we used the same approach as that employed in multiphase flows [192]. First, let us denote by $u(\xi)$ the velocity component along the ξ direction of the computational grid:

$$u(\xi) = \tilde{u} \frac{x_\xi}{\sqrt{x_\xi^2 + y_\xi^2}} + \tilde{v} \frac{y_\xi}{\sqrt{x_\xi^2 + y_\xi^2}}, \tag{4.6}$$

we can define a Heaviside function as follows:

$$H(\xi, \eta) = \begin{cases} 1 & u(\xi) < 0, \\ 0 & u(\xi) \geq 0, \end{cases} \tag{4.7}$$

At this point, the radius of curvature is given by:

$$R = \frac{1}{\boldsymbol{\nabla} \cdot \left(\frac{\boldsymbol{\nabla} H}{||\boldsymbol{\nabla} H||} \right)} \tag{4.8}$$

By definition, it is a local quantity; however, it takes on non-zero values only at the boundary between the recirculation zone and the rest of the flow. As can be seen in Figure (4.18), in the case of a weak shock, the value of Gr always remains below the limit proposed by [191], passing through the instability trigger region between $Gr = 1.8$ and $Gr = 2.4$ only for values where the curvature is slightly stronger, whereas in the case of a strong shock, it is always above the threshold for every section. Because a discontinuous function such as H has been used and the calculation of R is not analytical, the value of the radius of curvature fluctuates considerably. This explains the behaviour of Gr in the strong-shock case.

To take this further, a resolvent analysis is carried out for the case of weak shock without separation bubble by varying β and ω. Specifically, we have considered $0 < \beta < 10$ and $0 < \omega < 1$ and we

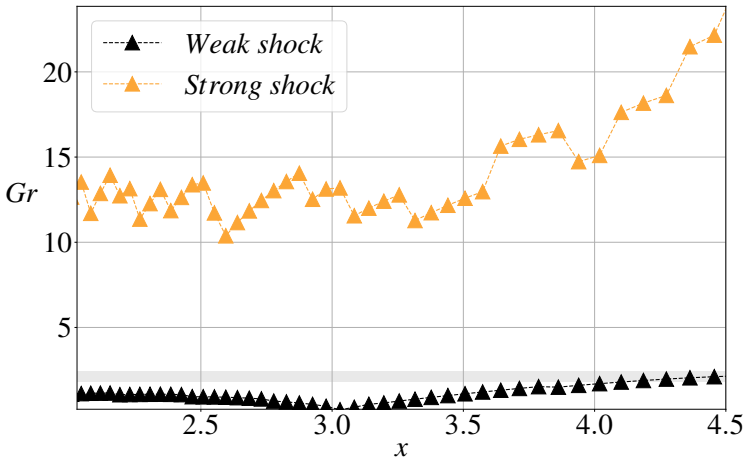


Figure 4.18: Gr number evolution in divergent part of the diffuser for $R_p = 0.813$ (weak shock) and $R_p = 0.72$ (strong shock). The are shown in shaded gray is the instability trigger region.

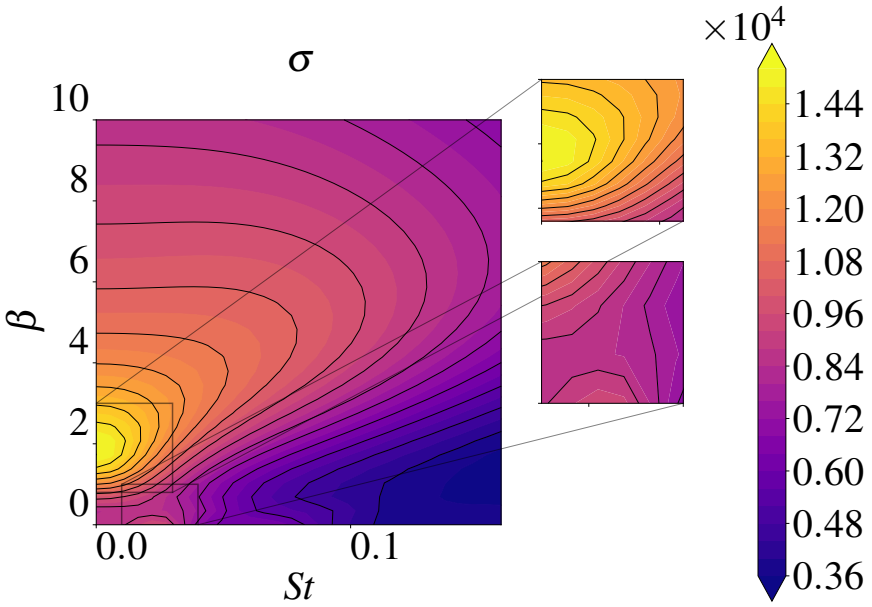


Figure 4.19: Contours of optimal gain for $R_p = 0.813$ for different ω and β values.

have extended the Chu norm using the spanwise velocity component. This enabled us to plot the map showing the isovalues of the optimal gain, as illustrated in Figure 4.19. Two peaks are visible: the first, which is less pronounced, at $St = 0.023$, corresponds to the same frequency as the less stable

mode observable in the right-hand of Figures (4.17) -(4.20). The second; however, is a zero-frequency peak at $\beta = 2$. Figure 4.20 shows the optimal excitation and the optimal response corresponding to this second peak.

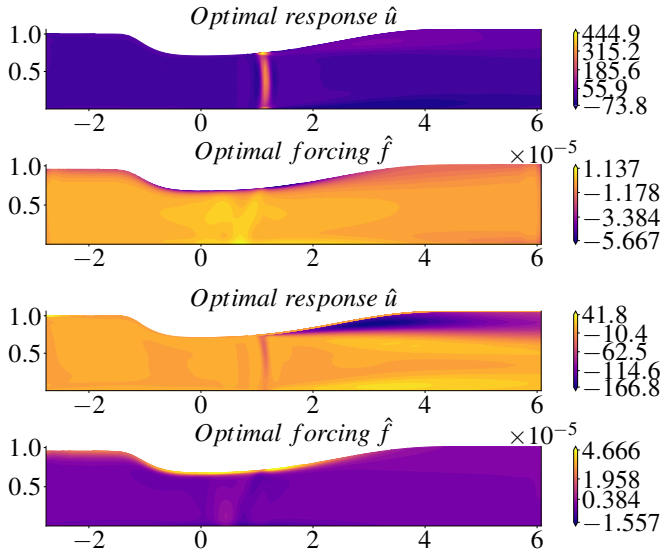


Figure 4.20: Streamwise velocity optimal response (top) and forcing (bottom) at $(St, \beta) = (0.023, 0)$ (left) and $(St, \beta) = (0, 2)$ (right) for $R_p = 0.813$.

As can be seen, the optimal forcing is located on the upper wall, at the base of the shock, meanwhile, the optimal response consists of the formation of longitudinal streaks.

4.3 Parametric study on Sajben diffuser

To better understand the receptivity mechanism that drives the non-stationary dynamics within this type of diffuser, a parametric analysis is performed. Specifically, the length of the region with a constant cross-section and the pressure imposed in the outlet section are varied in the strong shock regime.

4.3.1 Diffuser length variation

In order to carry out a parametric study on the length of the region with constant cross-section, three additional lengths were considered: $L_1/h_{in} = 6.8$, $L_2/h_{in} = 7.5$, $L_3/h_{in} = 8.2$. For each new length, the downstream region with constant cross section near the outlet has been elongated by an amount

of $\Delta L = 0.7h_{in}$, discretised using five evenly spaced points in the streamwise direction (see Table 4.2). The fixed point is calculated, as was done in the previous section for each new case. Figure (4.21) shows the contour plots of the fixed point for the streamwise velocity, whilst Figures (4.22) and (4.23) compare, respectively, the pressure profiles on both walls and the streamwise velocity in two different sections. As the length increases, the position of the shock tends to shift slightly further towards the outlet, despite the pressure ratio remaining unchanged. This is probably due to the fact that, as the length increases, the thickness of the boundary layer and the pressure losses also increase; however, since the pressure is fixed at the outlet, the flow must adapt in order to satisfy the outlet conditions. Figure (4.25) shows the least stable mode for the case with the longest length $L = L_3$ at the new frequency $St \approx 0.09$. The streamwise velocity contour lines at the fixed point have been superimposed on the figure to confirm that this mode is of the same nature as that in the reference case, namely a mode located in the shock zone and in the separation region .

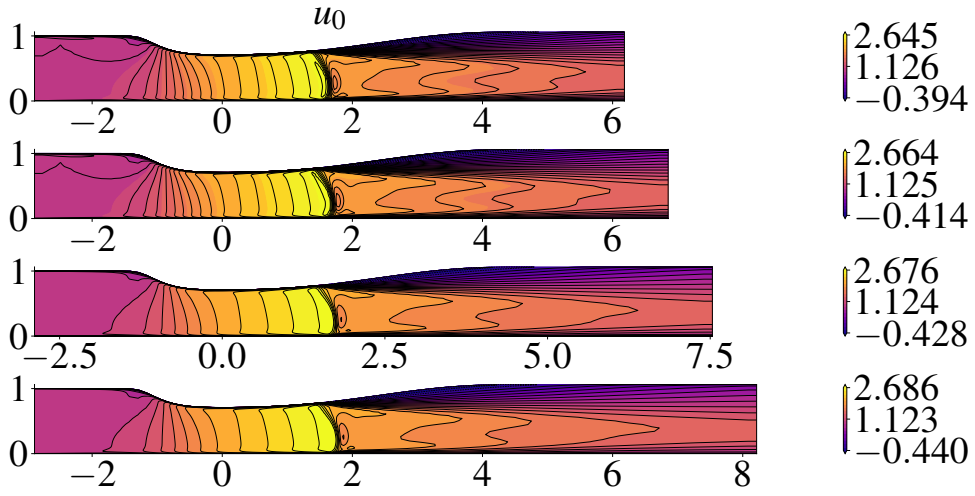


Figure 4.21: Streamwise velocity contours of the fixed point at different diffuser length. From top to bottom: $L/h_{in} = 6.1$, $L_1/h_{in} = 6.8$, $L_2/h_{in} = 7.5$, $L_3/h_{in} = 8.2$

.

The most interesting result emerges from the stability analysis. Looking at Figure (4.24) and focusing on the least stable mode ($St = 0.11$), we can see that as the length increases, the mode becomes more stable and its frequency decreases in line with all the numerical simulations carried out in the past, but not with the experiments. Let us therefore try to use two simple models to better understand this result. The first one is employed by Bogar [17] to describe a 1D wave travelling through a flow at a

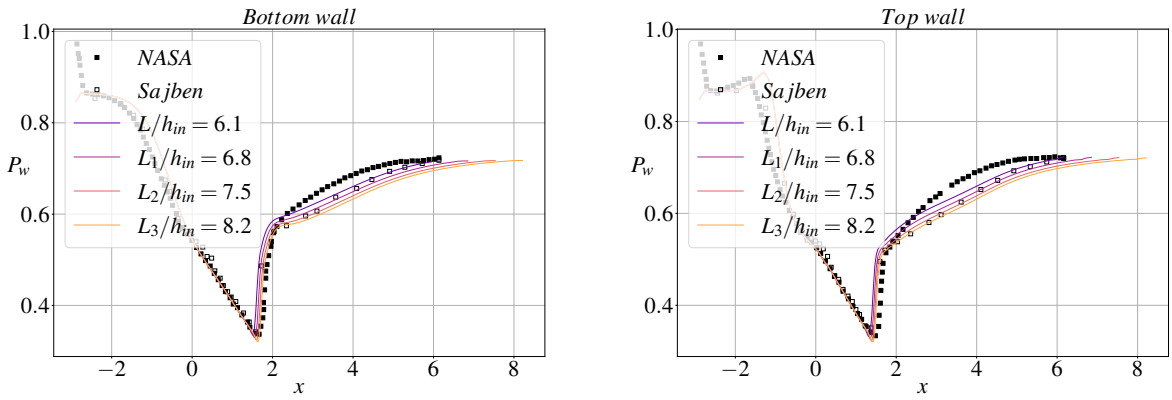


Figure 4.22: Pressure wall distribution for different lengths. Bottom wall (left) and top wall (right).

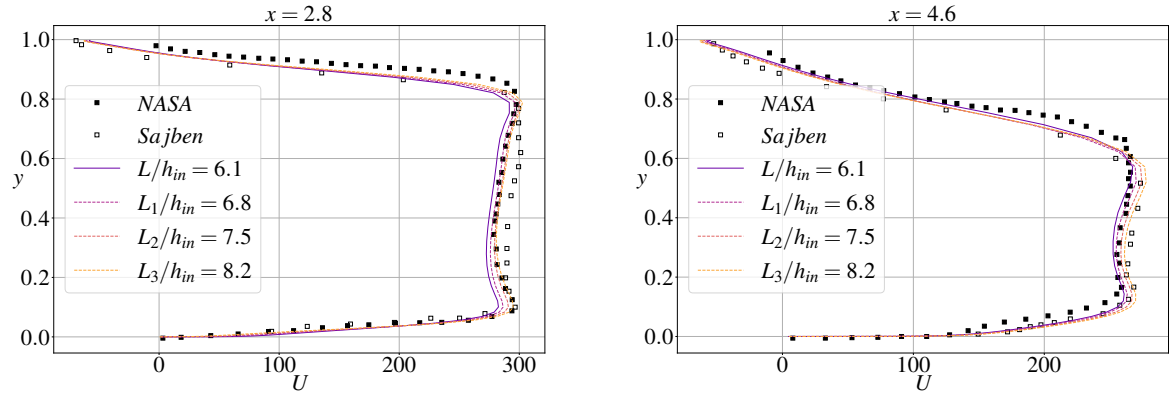


Figure 4.23: Streamwise velocity profile at two different sections for different lengths. $x/h_{in} = 2.8$ (left) and $x/h_{in} = 4.6$ (right).

velocity u. For a channel of length L, the characteristic frequencies are given by:

$$f_n = \frac{c}{L}(2n-1)\left(\frac{1-M^2}{4}\right) \tag{4.9}$$

In our case L is the distance between the section after the shock at half of the height L_s and the outlet section L_e, while the Mach number M and the speed of sound c are computed by doing the integral on the centerline between L_e and L_s:

$$M = \frac{1}{L}\int_{L_e}^{L_s} M(\xi)d\xi, \qquad c = \frac{1}{L}\int_{L_e}^{L_s} c(\xi)d\xi \tag{4.10}$$

The other model is the one proposed by Rossiter [193] to describe the convective-acoustic loop in open cavities and reads:

$$f_m = \frac{U}{L}\left(\frac{m-\gamma}{\frac{1}{k}+M}\right) \tag{4.11}$$

where γ is a phase lag, kU is the convection velocity of the vortices. We have set $k = 0.5$ and considered the two cases with and without phase delay. The average streamwise velocity and the speed of sound were again calculated using an integral, as shown previously; this time the characteristic length considered is the length of the recirculation bubble projected onto the nozzle axis.
Results are reported in Table 4.3. As can be seen, the acoustic model is able to provide frequency

CASE	**Mode (St)**	**A-A** ($n = 2$)	**C-A** ($m = 1$,$\gamma = 0$)	**C-A** ($m = 1$,$\gamma = 0.25$)
STRONG SHOCK	0.111	0.108	0.1428	0.1071
PARAM L1	0.102	0.0983	0.1458	0.1094
PARAM L2	0.093	0.0892	0.1425	0.1069
PARAM L3	0.085	0.0844	0.1447	0.1085

Table 4.3: Comparison between frequency of least stable mode , 1D acoustic model **A-A** and 1D convective-acoustic model **C-A**.

values that are very similar to those of the global stability, with the results varying as the length of the diffuser changes. In contrast, the model describing acoustic convective feedback almost always maintains a constant frequency. The latter is consistent with previous experimental work, as the characteristic length varies only slightly with changes in duct length, as do other thermodynamic and kinematic quantities, but not with the numerical studies found in the literature, including the present one.

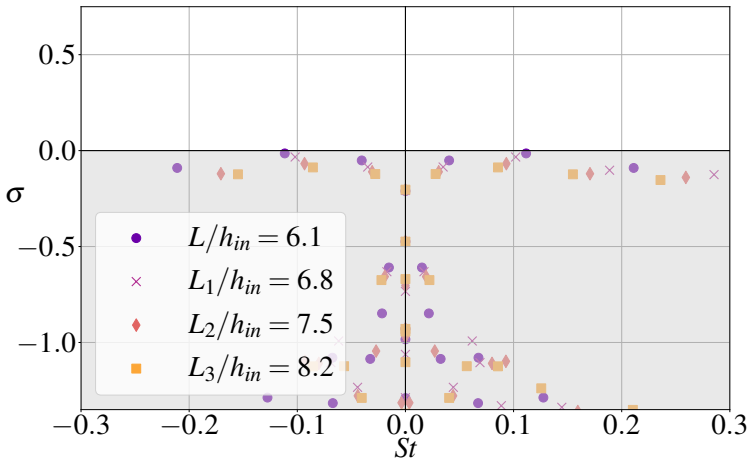


Figure 4.24: Eigenspectra comparison for different diffuser length.

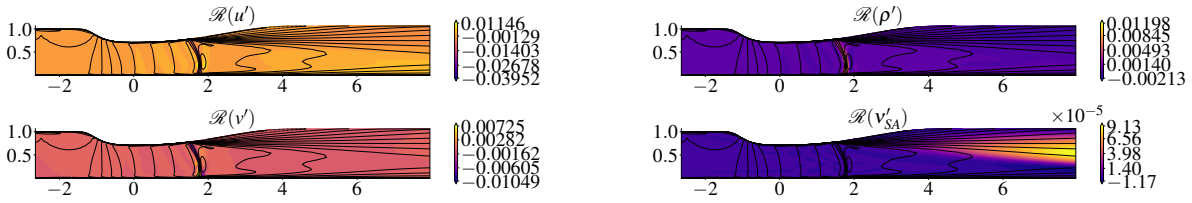


Figure 4.25: Real part of the mode at $St = 0.09$ for the case at $L = L_3$. Streamwise and wall-normal velocity (left), density and modified viscosity (right)

4.3.2 Pressure ratio variation

As in the previous case, three new scenarios are considered, this time keeping the nozzle length constant and varying the pressure ratio R_p by reducing it. The new pressure ratios considered are $R_{p1} = 0.68$, $R_{p2} = 0.64$, $R_{p3} = 0.6$ where $R_p = p_{exit}/p_0$. When the outlet pressure is varied, the fixed point changes significantly compared to the previous parametric case; in fact, the shock front shifts from a position of $x/h_{in} = 1.55$ in the base case to $x/h_{in} = 2.35$ in the R_{P3} case, due to the significant acceleration caused by the reduction in p_{exit} (Figures 4.26 - 4.27). As the flow accelerates, the intensity of the shock increases progressively, taking on a distinct λ-shaped form in the two cases with the lower R_p, where the recirculation zone is therefore wider. Figure (4.28) represents streamwise velocity profiles at the same sections as before. It is noteworthy to observe that, for the lowest pressure ratio, at $x/h_{in} = 2.8$ the velocity profiles are completely different from the reference ones, being in the proximity of the shock. Using the fixed points presented here as the base flow, a global stability analysis is carried out for each pressure ratio.

Figures (4.29 – 4.30) show, respectively, the eigenvalue spectrum for each R_p and the mode at $St = 0.17$ for $R_p = R_{p3}$. In the spectrum, starting again from the reference mode at $St = 0.11$, it can be observed that reducing the pressure ratio increases the frequency of the mode and stabilises it (although non-monotonically). The former effect is in line with the fact that the acoustics determines the frequency of the unsteady dynamics. In fact, by reducing the pressure ratio, the shock moves further downstream, reducing the distance travelled by the acoustic waves travelling back from the outlet, thereby increasing the frequency. However, the stabilising effect of the pressure reduction is counterintuitive. Nevertheless, one can consider that a shock of greater intensity might be more resistant to pressure perturbations arriving from the outlet and therefore more stable. However, a clarification is needed regarding the case at R_{p3}. In fact, this case appears to have a higher growth rate than the case at R_{p2}, resulting in a non-monotonic trend in the evolution. This is due to the fact that, in the case at R_{p3}, the baseflow fails to reattach to the upper wall, thereby intensifying the reflection at the outlet.

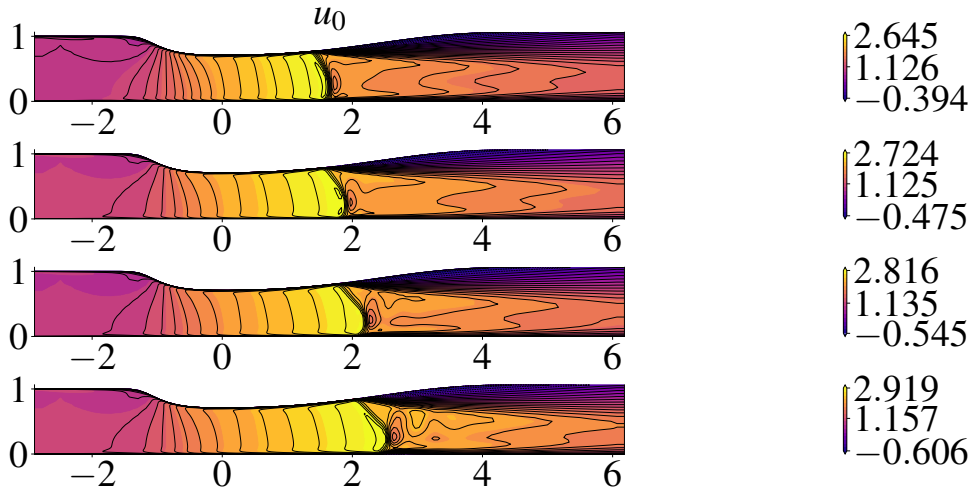


Figure 4.26: Streamwise velocity contours of the fixed point at different pressure ratios. From top to the bottom: $R_p = 0.72$, $R_{p1} = 0.68$, $R_{p2} = 0.64$, $R_{p3} = 0.60$.

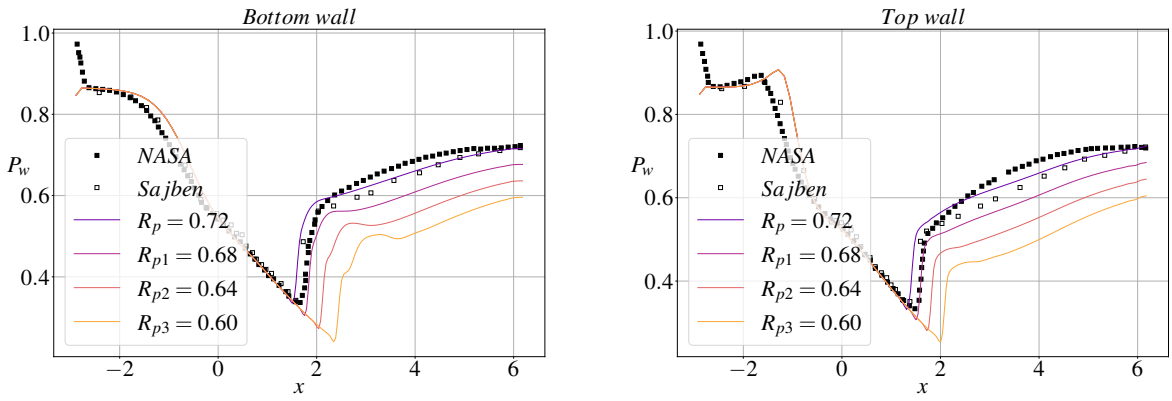


Figure 4.27: Pressure wall distribution for different pressure ratios. Bottom wall (left) and top wall (right).

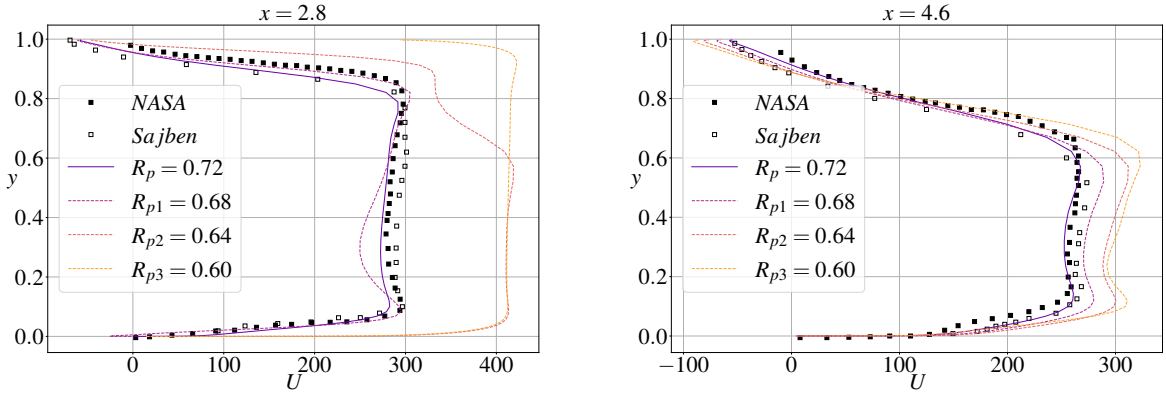


Figure 4.28: Streamwise velocity profile at two different sections for different pressure ratios. $x/h_{in} = 2.8$ (left) and $x/h_{in} = 4.6$ (right).

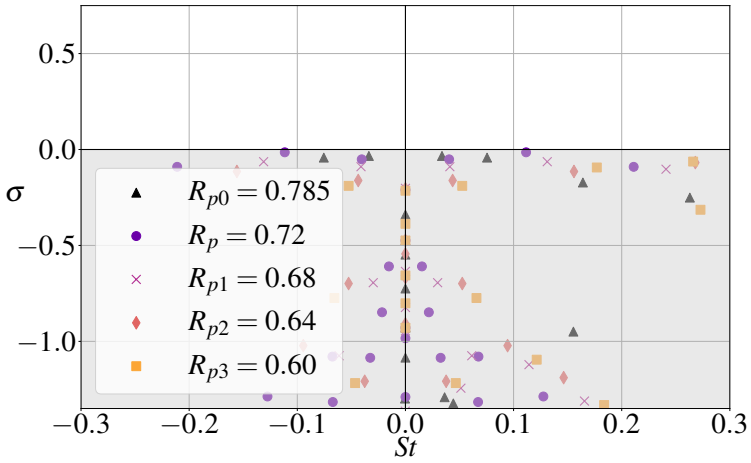


Figure 4.29: Eigenspectra comparison for different pressure ratios.

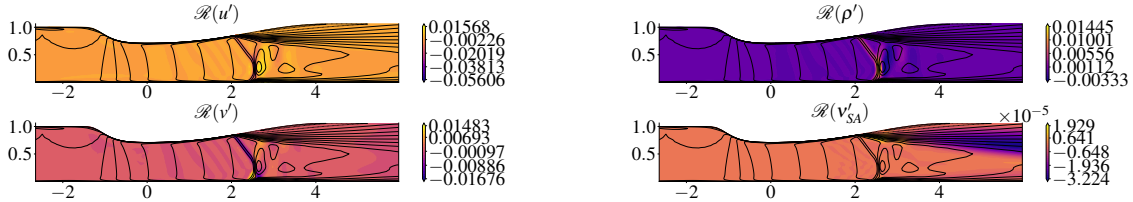


Figure 4.30: Real part of the mode at $St = 0.17$ for the case at $R_p = R_{p3}$. Streamwise and wall-normal velocity (left), density and modified viscosity (right)

4.4 Physical discussion

The aim of this section is to summarise the results obtained through linear analysis and to provide a physical interpretation of them. Let us begin by noting that the case of a strong shock ($R_p = 0.72$) does not have self-sustaining dynamics, as no unstable mode has been found. The underlying mechanism is likely a selective noise amplifier, as already observed in the flow configuration over a bump [51]; however, the analysis of the pseudo-spectrum reveals that an uncertainty of magnitude $\varepsilon = 10^{-5}$ is sufficient to render the mode unstable. Such a phenomenon consists of a receptivity mechanism with strong selectivity and a quasi-resonance around the least-stable mode, as shown by the resolvent analysis. The Sajben strong shock case can be viewed as an intermediate case between the corresponding Sajben weak shock case, where the mechanism is entirely acoustic, and the even stronger shock regime studied by Reijasse [185], where it is likely to be a self-sustaining mechanism. The experimental setup adopted by Sajben is, in fact, less isolated, with no second sonic throat, than that of Bur and Reijasse, allowing disturbances from outside to travel upstream in the flow.

Regarding the nature of the mechanism, it is certainly not purely acoustic, as is the case with a weak shock at $R_p = 0.813$ or in the case of a straight pipe or duct. When the intensity of the shock is intermediate, the self-sustaining oscillations arise from a feedback loop coupling several physical mechanisms:

(i) the shock wave generates and disturbs the detached boundary-layer, which in turn produces Kelvin-Helmholtz shear waves and eventually impinges on or interacts with the downstream duct geometry (e.g. throat, diffuser exit, or reattachment region);

(ii) this interaction radiates an upstream-propagating pressure disturbance (acoustic wave) back through the subsonic portion of the flow (i.e. the boundary layer or the subsonic outer flow surrounding the supersonic core);

(iii) the upstream wave reaches the shock and perturbs its position and/or strength — the shock is highly receptive to upstream acoustic forcing at specific frequencies;

(iv) the perturbation is convected downstream by the separated shear layer, which acts as a selective noise amplifier (convective instability). The shear layer amplifies disturbances over a band of Strouhal numbers, closing the loop with the right phase for constructive interference.

If this feedback loop is sufficiently intense, these oscillations become self-sustaining. The difference between experiments and numerical simulations lies precisely in the nature of the nozzle exit and the

ability to generate vortices intense enough to power the feedback loop. It is important to emphasise that in RANS numerical simulations, if the separation between the wall turbulence scales modelled by the turbulence model and the Kelvin-Helmholtz instabilities produced by the separation zone is insufficient, the turbulence model cannot adequately generate enough vortex-driven unsteadiness to trigger the feedback loop observed in experiments. A configuration that could be intrinsically self-sustaining remains subcritical (i.e. it does not reach the instability threshold); therefore, it is necessary to force the flow to exhibit unsteadiness. Furthermore, one potential limitation of the adopted approach is that imposing boundary conditions at the outlet, without accounting for the external exiting jet flow dynamics, can lead to discrepancies between experiments and numerical simulations in their ability to generate sufficient fluctuations to trigger the feedback loop that sustains the oscillations. In this context, it would be interesting in future work to perform simulations that account for the output external flow to test this hypothesis. High-fidelity simulations, such as LES, would also be valuable. To that end, it is worth noting that more recently, Martelli *et al.* [179] carried out a DES on the same Model G geometry, starting from a pressure ratio corresponding to the severe-shock case. The analysis of the wall pressure signal revealed that it is broader than in previous URANS simulations, with a low-frequency peak at 278 Hz, comparable to the result obtained in the present thesis work.

Chapter 5

3-D Counter current jet

Contenu

5.1 Geometric configuration 152
5.2 No incidence angle 158
5.3 Incidence angle $\theta = 10°$ 160
5.3.1 URANS simulation 160
5.3.2 Global stability analysis 162
5.4 Physical discussion 168

5.1 Geometric configuration

Following the successful landing of SpaceX's Falcon 9, the aerospace industry has taken a keen interest in RVLs (reusable launch vehicles). Although the initial aim was to reduce the cost of space access, there are other advantages, including, of course, sustainability, the possibility of storing rockets in advance, and versatility (a rocket can be used for different missions) [194]. There are two main recovery methods currently under study: VTVL (Vertical Take-off Vertical Landing), as used for SpaceX's Falcon 9, and VTHL (Vertical Take-off Horizontal Landing), which was used for the Space Shuttle. This work focuses solely on VTVL, but a comprehensive comparison can be found in [195]. With the VTVL approach, there are two possible trajectories: the Return To Launch Site (RTLS), in which the stage must perform a boostback manoeuvre to alter its trajectory and return to the launch site, or the downrange landing (DRL), which requires less propellant as the stage continues along its trajectory before landing on a platform at sea. However, unlike VTHL, both systems use retropropulsion to slow the rocket down.

The term retropropulsion refers to the technique of directing the thrust produced by the engine in the opposite direction to the vehicle's direction of movement. The earliest studies on this subject date back the 1950s, when the main focus was on investigating a counter-flow jet emitted from a stubby body struck by a supersonic flow, in order to assess its effects in terms of bow-shock distance and drag reduction [196]-[197]. From a practical point of view, retropropulsion had already been used in the Vostok and Mercury missions to carry out manoeuvres to exit orbit, but it was with the Apollo missions that we saw it used to carry out the lunar landing phase [198]. In this case, due to the almost complete absence of an atmosphere, the interaction between the jets and the external environment is virtually null (a simpler aerothermodynamic configuration), but the lack of aerodynamic drag must be compensated for by firing the main engine throughout the entire landing phase [199]. On the other hand, landing on Mars is more complex than a lunar landing; the atmospheric density is insufficient to rely on a parachute alone. In past Viking missions, a combination of parachutes and subsonic retropropulsion was used, however, in the future, for more important payloads, it will be necessary to apply retropropulsion whilst still travelling at supersonic speeds [200].

It was only following the success of SpaceX that retropropulsion emerged as a technique for landing reusable vehicles. The European space community has therefore begun to move in the same direction; much of the literature can be found in the ENTRAIN (European Next Reusable Ariane) project, the

aim of which was to compare the two landing philosophies (VTVL and VTHL) in order to assess their impact on performance, mass, structure and launch costs [201]. Shortly afterwards, we come to the RETALT (Retropropulsion Assisted Launch Technologies) project, in which numerous wind tunnel experiments and numerical simulations were carried out to study the assisted descent and landing phases. The stage under consideration is similar to SpaceX's Falcon 9 and involves a supersonic re-entry boost that slows the vehicle down before it enters the region where the atmosphere is denser, followed by a landing boost in which only a central engine is fired to enable landing [202] - [203]. Marwege *et al.* carried out experiments on the landing burn phase, considering a counterflow at M_∞ = 0.8 and a M_{jet} = 3.275. The flow field exhibits strongly unsteady behaviour with a dominant frequency $St = 0.2$ [204]. A recent study by Anoop & Kumar [205] involves both numerical simulations and experiments on a supersonic jet in opposition to a subsonic flow, varying the NPR and switching between over-expanded and under-expanded configurations. The interaction between the jet and the counterflow leads to the formation of large, symmetrical recirculation zones surrounding the jet core. From a non-stationary perspective, the introduction of the counterflow suppresses the growth of the Kelvin–Helmholtz instability, thereby weakening the jet oscillations.

The study presented in this chapter fits into this context, examining the landing phase during which the vehicle is in a state of subsonic retropropulsion using a global stability approach. The configuration under consideration is an academic simplification of a geometry proposed by CNES; specifically, the aim is to study a supersonic jet opposed to a subsonic flow as the angle of attack varies. Indeed, during the descent phase, the jet is not always at zero angle of attack, and it has been observed that the presence of an angle of attack contributes to the jet's unsteadiness.

The geometry shown in Figure 5.1 is greatly simplified compared to that of a practical application; it considers only the divergent portion of the nozzle. The forebody consists of a cylinder with an outer diameter of 13 mm, terminating upstream in a hemispherical nose. Proceeding downstream, the outer geometry presents a 1 mm backward-facing step, which reduces the outer diameter to 11 mm. This section forms a thin cylindrical collar of 12 mm in length. At the exit plane, the internal nozzle diameter is D = 10 mm, leaving a final nozzle lip thickness of 0.5 mm. Some dimensions are not shown in the sketch for reasons of confidentiality. The use of simplified geometry allows the creation of an accessible mesh using a structured approach; in this study, a geometry of the type shown in Figure 5.2 is sufficient, as the main focus of the study is the interaction between the jet and the counter-flow.

The nozzle profile under consideration is isentropic, thus making it unnecessary to solve the boundary layer. This is essential for reducing computation time; indeed, for a diameter of D = 10 mm, the jet's Reynolds number is approximately 2×10^6, which would require the height of the first wall cell to be very, very low in order to ensure $y^+ \approx 1$.

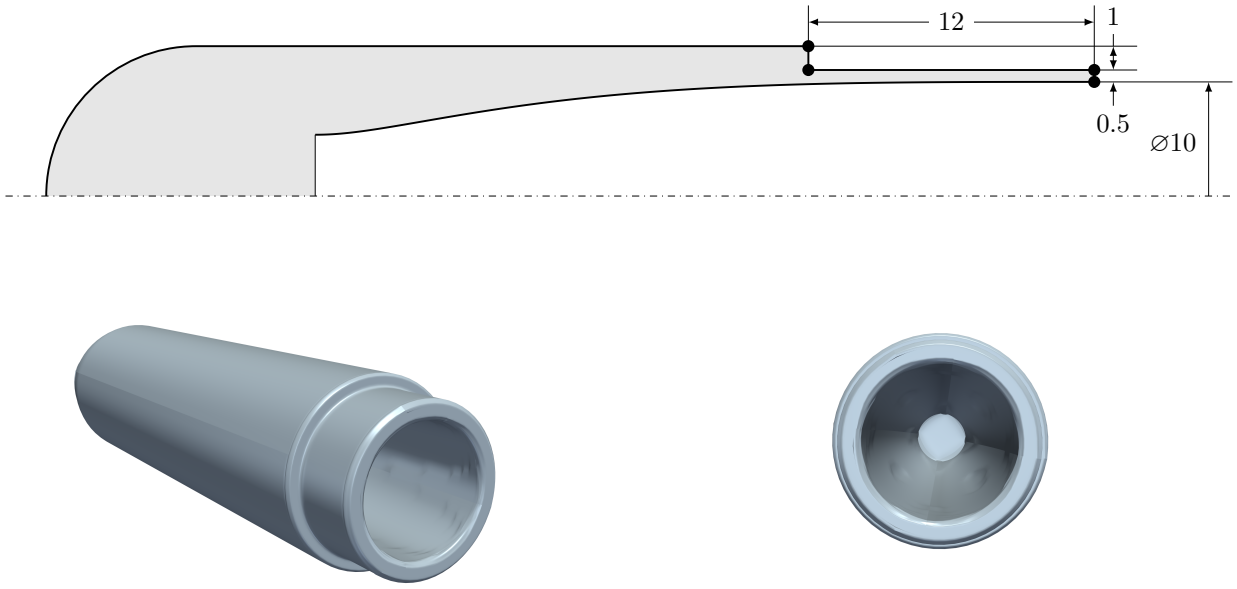


Figure 5.1: Academic simplified vehicle geometry.

Figure 5.2 shows the $x - y$ plane of the computational grid. The grid consists of several blocks, for a total of $N \approx 2.8$ million points, of which $n_\theta = 60$ are in the tangential direction. The mesh is constructed by a 360° revolution, which results in a pole on the axis that would lead to constrained numerics; for this reason, a topology known as *butterfly* is used, which allows the hexahedral cells to be retained, as can be seen in the close-up of Figure 5.2. The domain origin is located at the nozzle outlet on the axis of symmetry. The grid extends up to $x/D = 50$ and $r/D = 33$ in the axial and radial directions, respectively.

Regarding the simulation parameters, we consider only the case with counterflows at $M_\infty = 0.8$ and variable angles of incidence such that $\theta \in [0°, 10°]$. Furthermore, adaptation conditions are imposed; this means that the jet pressure p_{jet} corresponds to the external pressure, i.e. that of the counterflow

p_∞. Regarding the thermodynamic and kinematic parameters of the jet and the counter-flow, these are summarised in Table 5.1. They are presented in both dimensional and dimensionless terms, as the equations to be solved are made dimensionless with respect to the jet quantities. Concerning the

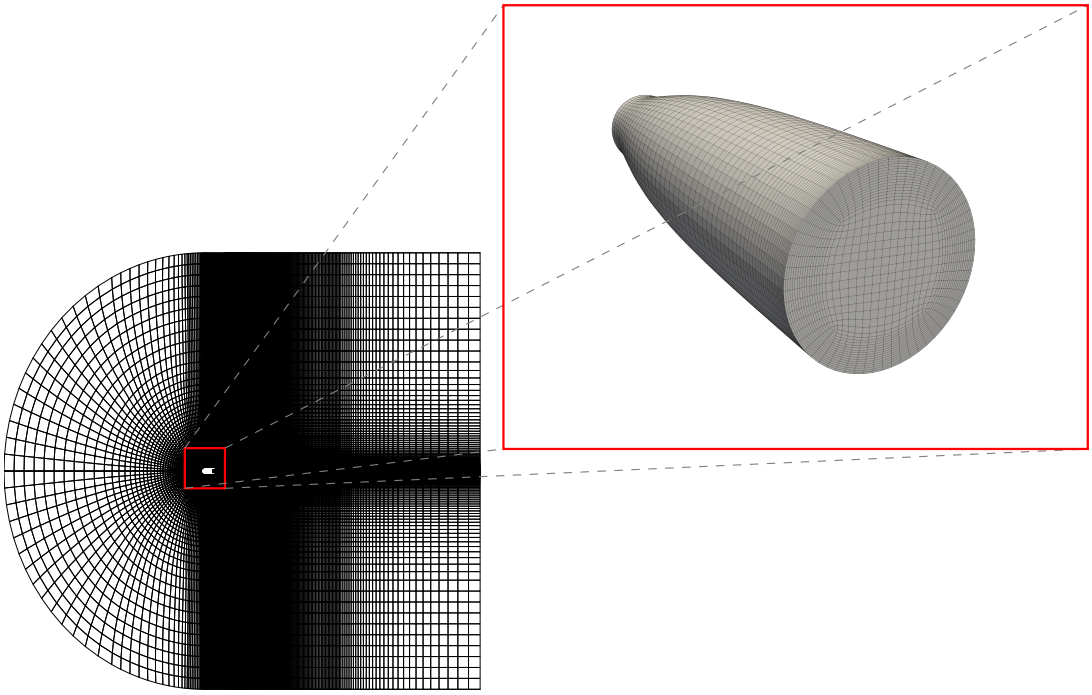


Figure 5.2: 2D representation of the computational grid in $x-y$ plane with a close-up on the 3D nozzle.

initialisation of the divergent duct, the quasi-1D isentropic steady-flow relations are employed, which express the ratio of the generic cross-section to the critical cross-section A/A^* with the Mach number of the cross section M:

$$\frac{A}{A^*} = \frac{1}{M}\left[\frac{2}{\gamma+1}\left(1+\frac{\gamma-1}{2}M^2\right)\right]^{\frac{\gamma+1}{2(\gamma-1)}}. \tag{5.1}$$

Equation (5.1) has two possible solutions, but we consider only the supersonic one ($M > 1$), which gives us an exit Mach number of $M_{jet} = 2.79$. Given the total quantities and the local Mach number, it is possible to compute the other components of the state vector using the isentropic relations (5.2), the ideal gas equation (5.3), and the definitions of the speed of sound (5.4) and the Mach number (5.5).

$$\frac{T}{T_0} = \left(1+\frac{\gamma-1}{2}M^2\right)^{-1}, \qquad \frac{p}{p_0} = \left(1+\frac{\gamma-1}{2}M^2\right)^{-\frac{\gamma}{\gamma-1}}. \tag{5.2}$$

Table 5.1: Summary of thermodynamic and kinematic parameters .

Variable	**Jet (DIM)**	**Jet (ADIM)**	**Counter-Flow (DIM)**	**Counter-Flow (ADIM)**
Total Temperature T_0	300.0 $[K]$	2.56	300.0 $[K]$	2.56
Total Pressure p_0	26.72 $[bar]$	2.45	1.52 $[bar]$	0.14
Static Temperature T	117.34 $[K]$	1.0	265.9 $[K]$	2.266
Static Pressure p	1.0 $[bar]$	0.0918	1.0 $[bar]$	0.0918
Density ρ	2.968 $[kg/m^3]$	1.0	1.31 $[kg/m^3]$	0.44
Speed of sound c	217.17 $[m/s]$	0.358	326.95 $[m/s]$	0.54
Velocity module $\|\boldsymbol{u}\|$	605.87 $[m/s]$	1.0	261.56 $[m/s]$	0.43

$$\rho = \frac{p}{RT} \tag{5.3}$$

$$c = \sqrt{\frac{\gamma p}{\rho}} \tag{5.4}$$

$$|\boldsymbol{u}| = cM \tag{5.5}$$

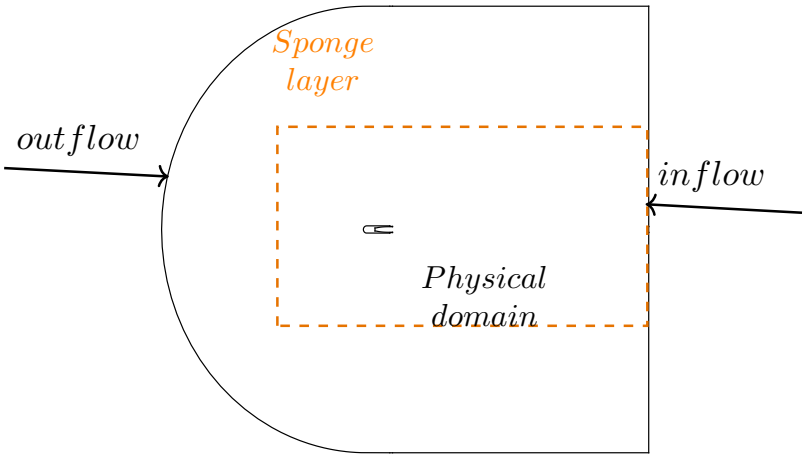


Figure 5.3: A simplified overview of the case under investigation with boundary conditions

The case under investigation has a $Re_{jet} \approx 2 \times 10^6$, so a URANS approach must be used. On this

occasion, we adopt the $k - \log(\omega)$ SST model with compressibility correction described in Chapter 2, as it best depicts the jet dynamics [206]. To initialize the turbulent variables, free-stream values are applied to the counter-flow, as suggested in Chapter 1. However, it is not possible to do the same within the nozzle. Using a single value to initialise k_t and $\tilde{\omega}$ would lead to numerical instability during the transitory phase; for this reason, a turbulent intensity $I_t = 0.01$ and a ratio R_t between the turbulent viscosity μ_t and the molecular viscosity μ within the nozzle of $R_t = \mu_t/\mu = 5$ have been employed. Subsequently the turbulent kinetic energy and dissipation rate can be calculated as:

$$\begin{aligned} k_t^{Noz} &= 1.5(U_{jet} I_t)^2 \\ \tilde{\omega}^{Noz} &= \log\left(\rho_{jet} k_t^{Noz} \frac{1}{\mu_{jet}} \frac{1}{R_t}\right) \end{aligned} \quad , \tag{5.6}$$

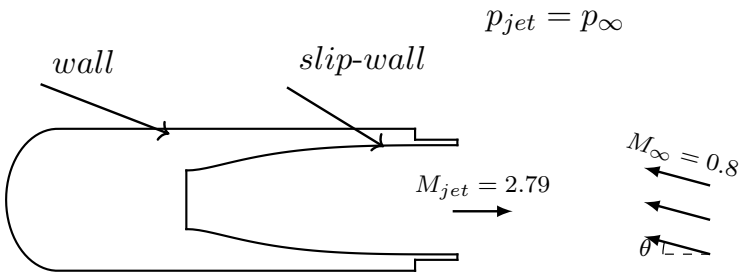


Figure 5.4: A simplified overview of the case under investigation with boundary conditions (close up on the nozzle)

Figure 5.3 shows the physical domain and the sponge zones required to reduce oscillations. To be more precise, the physical domain extends axially across the entire region downstream of the jet up to $x/D = 50$, whilst radially it ends at $r/D = 33$. The remainder of the domain consists of sponge zones. Subsonic inflow conditions are imposed on the face normal to x at the end of the domain, whilst non-reflective outflow conditions are imposed on all remaining external faces. Figure 5.4 shows a close-up of the configuration under examination. Adiabatic no-slip conditions are used for the outer walls, whilst slip-wall conditions are used for the inner walls of the nozzle. The Mach number of the jet will always be held constant at $M_{jet} = 2.79$ and that of the counterflow at $M_\infty = 0.8$, whilst the angle

θ will be varied. From a numerical point of view, the same approach as in the Sajben case has been adopted: fourth-order spatial discretisation for convective terms, second-order spatial discretisation for diffusive terms, and a third-order Jameson-type scheme. In all the simulations that follow, the initial transient is very severe, so it is necessary to adapt the time step to the CFL, which is set at 0.5. In the following sections, URANS simulations will first be presented, followed by the results of the global stability analysis.

5.2 No incidence angle

The first case considered is that with a zero angle of incidence, $\theta = 0°$. To assess whether the jet is steady or not, two pressure sensors were installed along the nozzle axis positioned at $x/D = 10$ and $x/D = 15$ respectively. Figure 5.5 shows the time history of the two sensors, after a sharp transient, both sensors stabilise . Figure 5.6 shows the contours of the streamwise velocity component $\tilde{u}$ with the

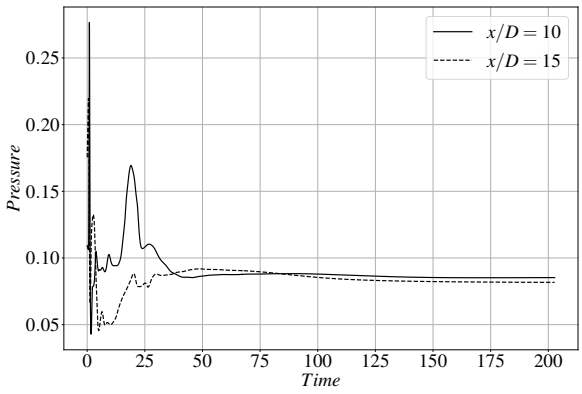


Figure 5.5: Pressure sensors at three different location.

streamlines superimposed whilst Figure 5.7 still displays streamwise velocity contours, but in the $z-y$ plane at $x = 15D$ (left frame) and in the $x - z$ plane (right frame) respectively. The jet is perfectly axially symmetric; indeed, the $x - y$ and $x - z$ planes are indistinguishable, whilst in the $y - z$ plane the isolines of $\tilde{u}$ form concentric circles.

The outgoing jet is adapted; its total pressure is much higher than that of the counterflow. For this reason, the jet extends as far as the region $x/D \approx 25$, where the stagnation point is located. Subsequently, the flow is forced to be ejected in the radial direction, where it encounters the counterflow in the opposite direction, which carries it back towards the nozzle inlet, where it is once again propelled

forwards. A recirculation zone is thus formed, which can be observed via the streamlines shown in Figure 5.6.

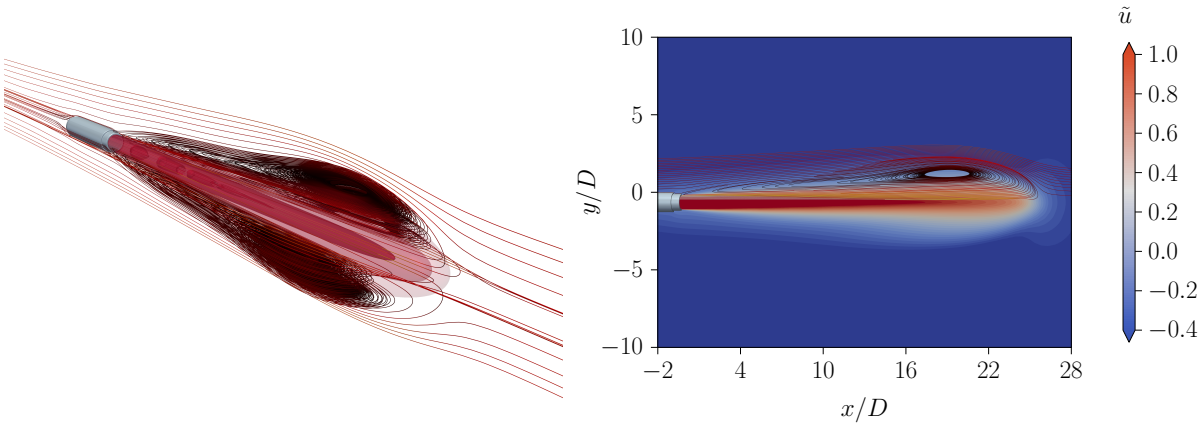


Figure 5.6: Contours of streamwise velocity $\tilde{u}$ with streamlines in 3-D (left) and $x-y$ plane (right).

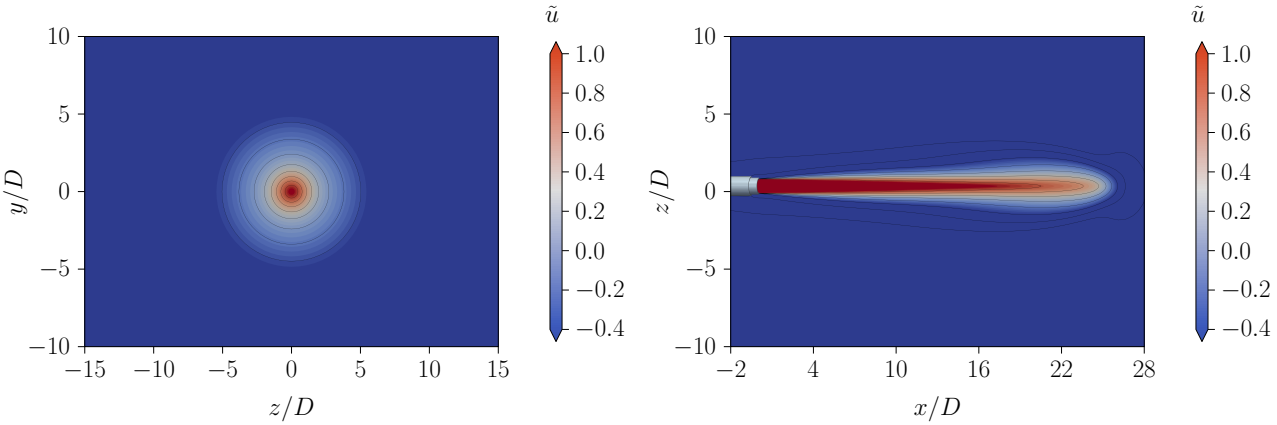


Figure 5.7: Contours of streamwise velocity $\tilde{u}$ with streamlines in $z-y$ plane at $x = 15D$ (left) and $x-z$ plane (right).

Figure 5.8, on the other hand, reports the turbulent kinetic energy k_t (left frame) and the logarithm of the turbulent dissipation rate $\tilde{\omega}$. It can be seen that the flow inside the nozzle satisfies the slip-wall condition; due to the absence of gradients, there is no turbulent production, and the inviscid core flow at the outlet maintains the dimensions of the nozzle diameter. Following interaction with the counterflow, the size of the core gradually decreases, assuming the classic conical shape. The maximum turbulent kinetic energy is found, as expected, in the mixing layer where production is highest, but also near the stagnation point. The maximum value of $\tilde{\omega}$ is found near the nozzle lips; unlike k_t, it

has a shorter spatial scale. Furthermore, from the $\tilde{\omega}$ contours, one can observe to some extent the phenomenon known as turbulence decay in the free-stream, which is well described in [207]. Due to the absence of gradients, the turbulent variables tend to decay; therefore, it may be necessary to impose minimum values. Given that the URANS simulation converges to a steady-state RANS solution, for

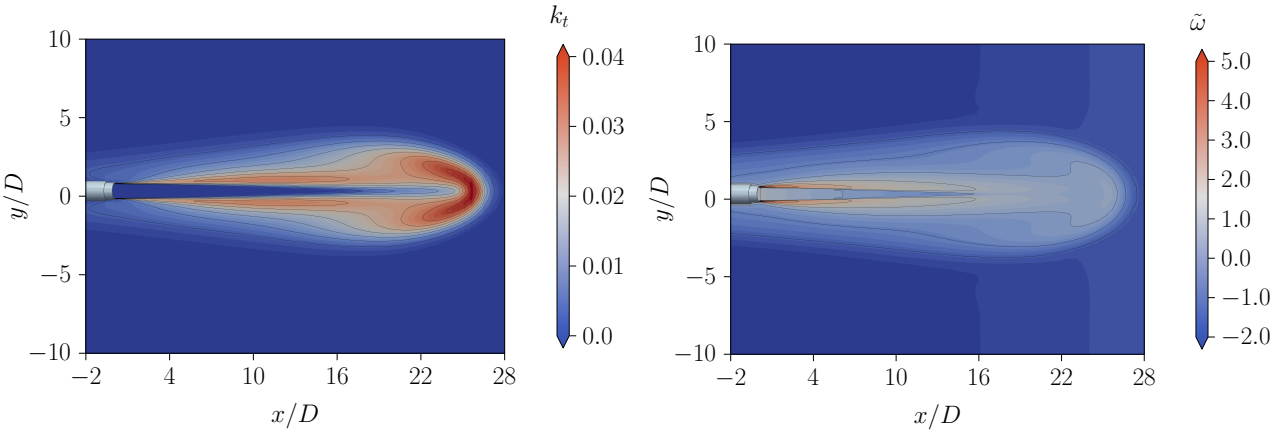


Figure 5.8: Contours of turbulent kinetic energy k_t (left) and logarithm of turbulent dissipation rate $\tilde{\omega}$ (right) in $x - y$ plane.

this case, at $\theta = 0°$, the global stability analysis is not performed.

5.3 Incidence angle $\theta = 10°$

5.3.1 URANS simulation

In order to identify an unstable configuration straight away, the next step was to consider an angle of attack $\theta = 10°$ in the $x - y$ plane; for the other parameters, however, the same values as for the case where $\theta = 0°$ are retained, meaning that the only change is that:

$$\tilde{u}_\infty = |\tilde{\boldsymbol{u}}| \cos\theta, \qquad \tilde{v}_\infty = |\tilde{\boldsymbol{u}}| \sin\theta. \tag{5.7}$$

are now imposed at the inflow and at initialization. The same pressure sensors located on the axis at $x/D = 10$ and $x/D = 15$ have been considered. Figure 5.9 therefore shows the pressure trend over time; as can be clearly seen, compared with the previous case, the signal is highly unsteady even after the initial transient. In order to try to understand which frequencies are the most energetic, the PSD (Power Spectral Density) of the two signals is calculated; this can be observed in the right-hand frame

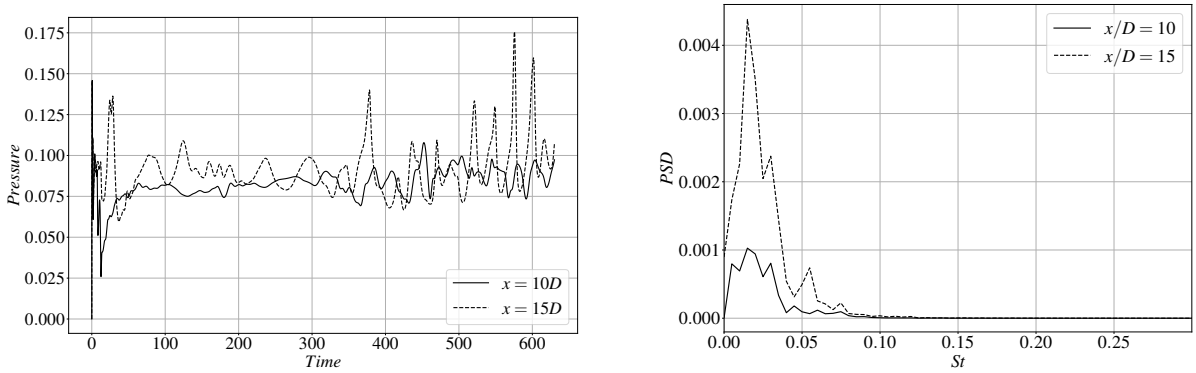


Figure 5.9: Pressure sensors at three different location.

of Figure 5.9. The PSD is obtained by considering only the signals following the transient, which ends at an advection time $t = 34$; thereafter, the time step stabilises at a constant value of $\Delta t = 7.14 \times 10^{-4}$. Furthermore, for each signal, the mean value computed over the useful range (excluding the transient) has been removed in order to evaluate the PSD of the pressure fluctuation. Both signals exhibit maximum energy at low frequencies, and the two main peaks occur at $St = 0.014$ and $St = 0.03$.

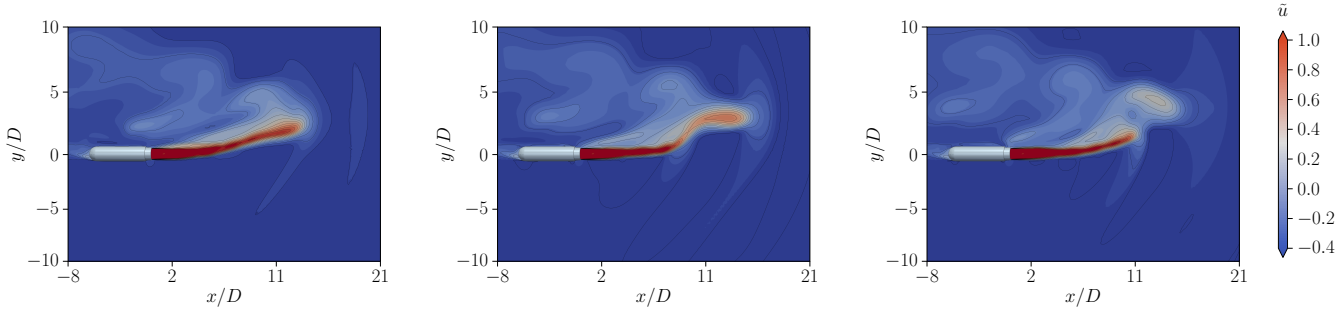


Figure 5.10: Contours of streamwise velocity $\tilde{u}$ at three different time instances in $x - y$ plane.

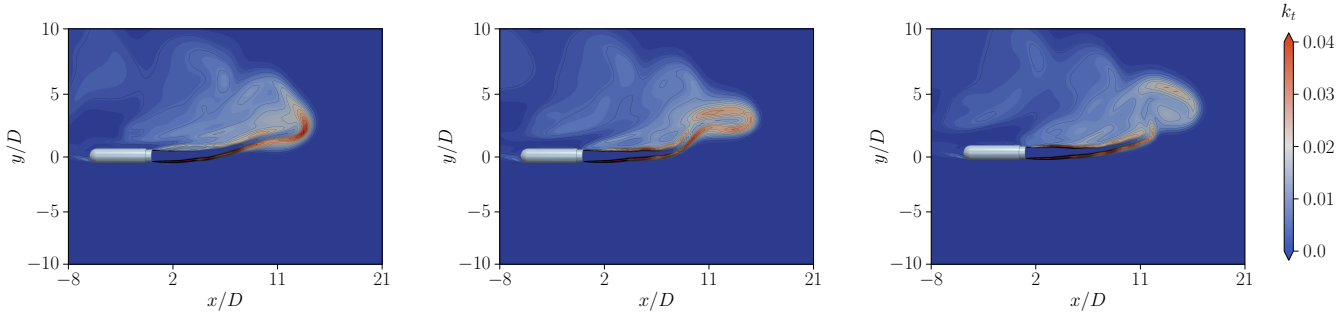


Figure 5.11: Contours of turbulent kinetic energy k_t at three different time instances in $x - y$ plane.

Given that the URANS simulation is highly non-stationary, we have reported in Figures 5.10 and 5.11 three snapshots at the advective times $t = 590$, $t = 600$ and $t = 610$ respectively. It can be seen that the jet leaves the nozzle at a high axial velocity, but the incoming counter-flow imposes an asymmetric pressure gradient on the contact surface, so that the jet is forced to deviate in the direction of least aerodynamic resistance, as evident from the curvature of the plume. In the first frame, large-scale vortical structures (light blue isocontours) can also be observed. The momentum in the axial direction along the plume weakens due to the continuous energy exchange with the counterflow along the shear layer; a pinch-off region forms, clearly visible in the central frame of the figure, where the jet head is almost topologically separated from the main body and begins to roll up. In the final frame at $t = 610$, the head has definitively detached; the jet core is shorter and is ready to bend again, whilst the head is advected upstream by the counterflow.

5.3.2 Global stability analysis

To perform the stability analysis, a base flow must first be identified. As already explained in Chapter 2, the approach adopted in this thesis involves using the RANS solution as the base flow. An initial attempt to calculate the fixed point was conducted using the Newton-Krylov method. This method involves advancing both the URANS and LURANS systems in time, starting from a given initial solution. What we observed was that, regardless of the initial solution used (various time snapshots), the Newton method converged to non-physical solutions (for example, negative k_t in some areas of the domain or negative ρ) or, at times, the linear code itself had difficulty advancing in time (localised areas where the perturbation of $\tilde{\omega}$ diverged). For this reason, an SFD-type approach was used, as described in [133]. Considering the lack of information regarding previous studies on the configuration under investigation, we based our setting of the cut-off frequency ω_c on the results obtained from the URANS simulation. The cut-off frequency must be set to half the instability frequency; based on the PSD of the pressure signal, this corresponds to 0.014, so the final value used was $\omega_c = 0.007$. It is, however, more difficult to determine the damping coefficient χ; this must be twice the growth rate, a value for which no data is available. For this reason, we started with a tentative value of $\chi = 0.014$. This value was then increased through a trial-and-error approach up to three times its original value; any further increase results in a rise in the residual.

The residual error computed using this approach, $||r||_2$, is:

$$||r||_2 = \frac{||\boldsymbol{F}(\boldsymbol{q}(t+\tau)) - \boldsymbol{F}(\boldsymbol{q}(t))||_2}{\sqrt{N}} < 5 \times 10^{-4} \tag{5.8}$$

Methods for achieving a more convergent result are currently under investigation; the aim is to determine whether it is possible to perform the Newton iteration starting from the SFD result, or to use an approach such as that described in [134] to improve the convergence of the solution.

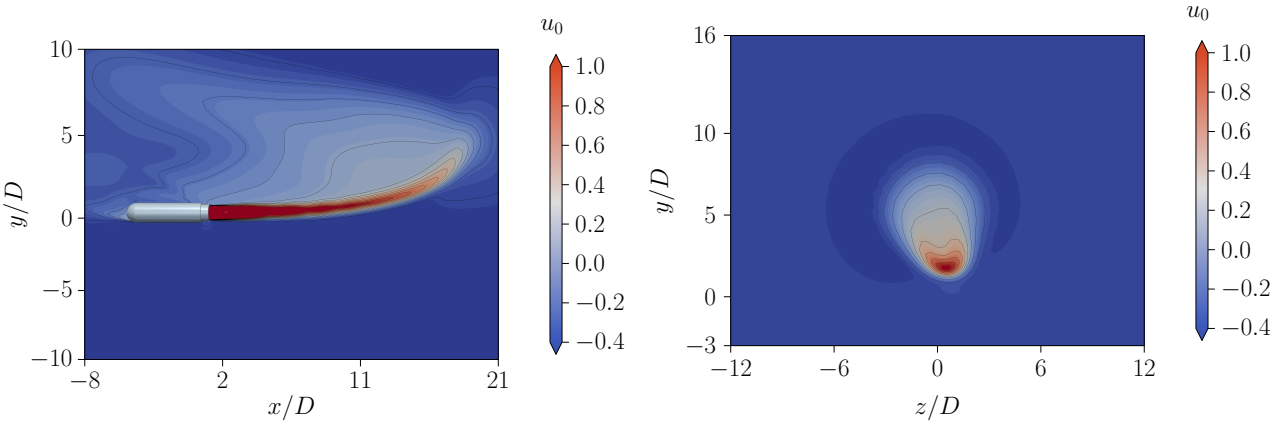


Figure 5.12: Contours of streamwise velocity u_0 of the base flow at $\theta = 10°$ in $x - y$ plane (left) and $z - y$ plane at $x = 15D$ (right).

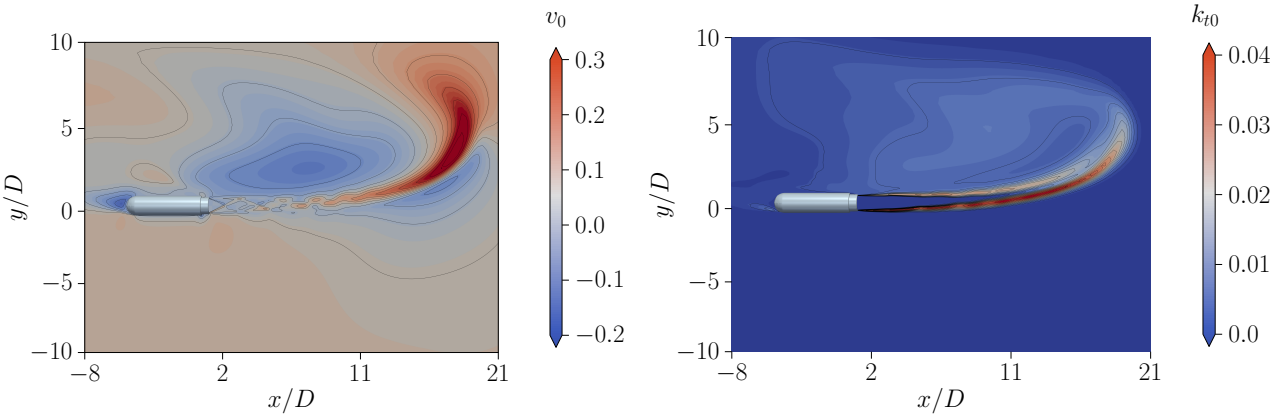


Figure 5.13: Contours of the transversal velocity v_0 of the base flow at $\theta = 10°$ (left) and turbulent kinetic energy k_{t0} (right) in $x - y$ plane .

Figures 5.12–5.13 show the velocity component contours for u_0 and v_0, and the turbulent kinetic energy k_{t0}, of the RANS solution obtained. The first noticeable effect introduced by the angle of

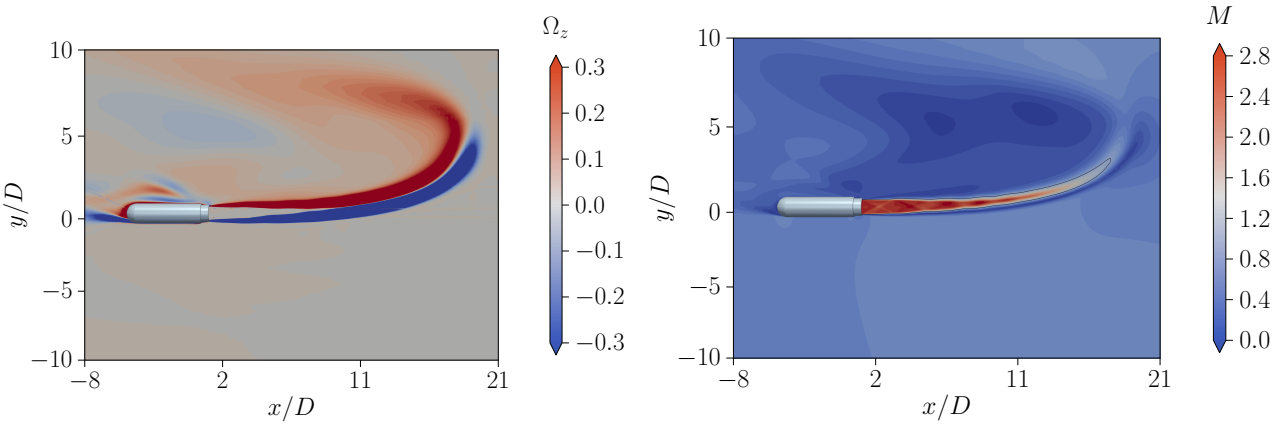


Figure 5.14: Contours of the vorticity component Ω_z of the base flow at $\theta = 10°$ (left) and Mach number M (right)in $x - y$ plane.

attack is the loss of axial symmetry; the plume appears visibly tilted compared to the configuration at $\theta = 0°$. The supersonic jet is deflected by the new transverse component of the counter-flow, bending towards the leeward region and causing the stagnation point to shift off-axis. Focusing on the right-hand frame in Figure 5.12, which shows the $z - y$ plane, it can be seen that, in addition to losing axial symmetry, the base field also loses the planar symmetry imposed by the geometry; the flow is completely three-dimensional (this point will be discussed later in the perspectives). Compared again to the case at $\theta = 0°$, the recirculation zone is more extensive in the leeward zone and appears compressed/suppressed in the windward one. As in the axially symmetric case, the highest levels of turbulent kinetic energy are found along the mixing layer and in the stagnation region, particularly in the windward portion. Furthermore, the length of the core flow is greatly reduced compared to the case where $\theta = 0°$.

Figure 5.14 depicts the contours of the z-component of the vorticity $\Omega_z = \partial v/\partial x - \partial u/\partial y$ and of the local Mach number M. The Mach number contours clearly show the supersonic core; furthermore, the sonic isoline at $M = 1$ is shown in black to divide the plane into two regions, whilst the contours of Ω_z reveal the existence of two vortical regions originating from the nozzle lips with opposite signs. The region originating from the upper lip has positive values; as one moves from the nozzle axis in the positive y direction, the streamwise component u_0 undergoes a drastic reduction until it reverses sign, so that $\partial u/\partial y$ is strongly negative, resulting in $\Omega_z > 0$. This leads to a counter-clockwise rotation of the fluid particles. In contrast, the region originating from the lower lip exhibits $\partial u/\partial y > 0$, thus

leading to clockwise rotation. Between these two high-shear zones, the central irrotational core is evident due to the slip condition imposed within the nozzle.

To better observe the overall pattern of the base flow under consideration, it is useful to visualise the behaviour of the streamlines. These are shown in Figure 5.15 alongside the 3D streamwise velocity contours. The streamlines surround the recirculation zone, which acts as an obstacle to the counterflow. In the section on physical discussion at the end of this chapter, further aspects of the base flow will be presented in relation to the global instabilities observed. Regarding global stability analysis, this is

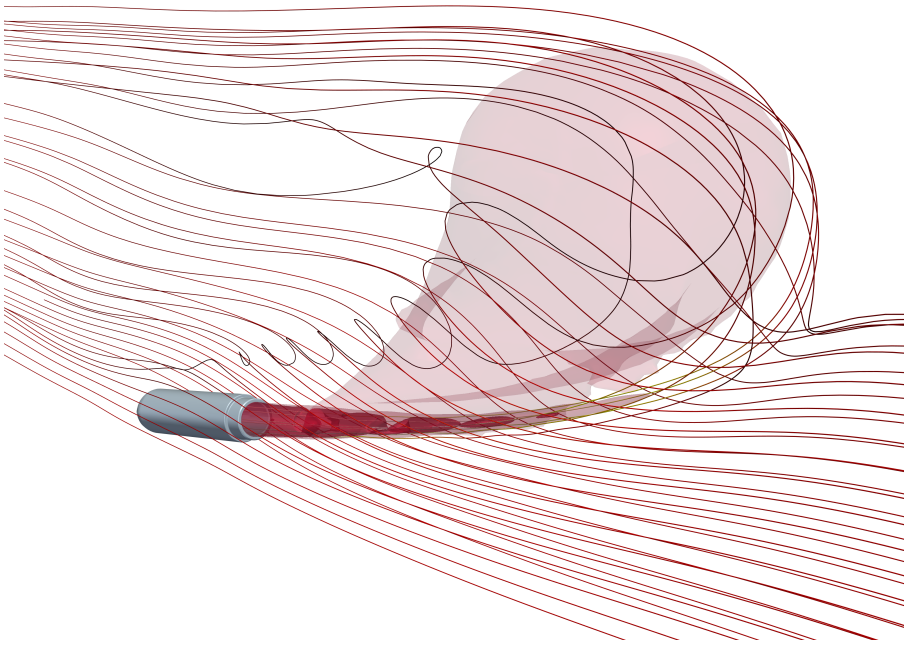


Figure 5.15: Contours of streamwise velocity with streamlines superposed in plane $(x - y)$ 3-D of the base flow at $\theta = 10°$

carried out exclusively using the time-stepper approach due to the high number of degrees of freedom in the problem. For the Krylov-Schur approach, a Krylov space dimension of $m = 250$ and a sampling time of $\tau = 2.2$ have been used. The chosen dimension m is lower than in the cases discussed previously in order to speed up the calculation; however, it remains above the lower limit suggested in [88].

The spectrum obtained using the parameters specified above is shown in Figure 5.16. Two vertical lines have been added to the same figure, corresponding to the frequencies derived from the PSD of the pressure signal from the URANS simulation at $St = 0.014$ and $St = 0.03$ respectively.

Several unstable modes have been identified, two of which coincide with the frequencies extracted

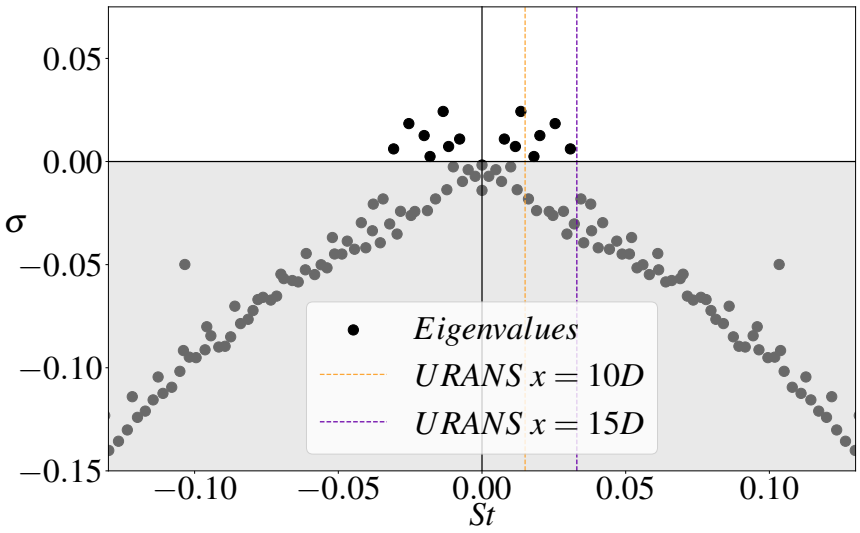


Figure 5.16: Eigenspectrum compared with main URANS frequencies.

by URANS; the fact that there are multiple unstable modes may be linked to the large distance from the threshold at which instability arises. Figures 5.17-5.18-5.19-5.20 show the contours of the unstable mode at the highest frequency $(\sigma, St) = (0.006, 0.03)$; to be more precise, they depict, respectively, the real part of the streamwise velocity component $\mathcal{R}(u')$, the density $\mathcal{R}(\rho')$, the transversal velocity components $\mathcal{R}(v')$ and $\mathcal{R}(w')$, and finally the turbulent kinetic energy $\mathcal{R}(k_t')$ and the z-component of the vorticity $\mathcal{R}(\Omega_z')$. The contour plots in the $(x - y)$ plane reveal that the spatial support is confined to the terminal region of the jet and to the region associated with the separation of vortices observed from the fixed point. Due to the angle of attack of 10°, the jet loses its axial symmetry and is deflected; consequently, the instability does not develop along the geometric horizontal axis, but rather follows the curvilinear trajectory of the vorticity sheets identified in the base flow, before being convected downstream into the wake. In other words, the jet appears to be warped, breaking the geometry's natural planar symmetry. The perturbation $\mathcal{R}(v')$ appears to be symmetric with respect to the curvilinear trajectory; this results in a transverse oscillation of the jet. Whilst in the $(x-y)$ plane the symmetry is broken by the angle of attack, as can be seen from the velocity component $\mathcal{R}(w')$ of the mode, which is organised into a wave-packet structure that is antisymmetric with respect to the x-axis, we might consider the mode to be a distorted version of the sinuous mode of axially symmetric jets. Indeed, it is evident from observing the perturbations in the $(z-y)$ planes of density and velocity

that the mode is strongly three-dimensional; the structure does not appear in rings but rather takes on a much more irregular shape. The contours of turbulent kinetic energy also exhibit antisymmetric behaviour with respect to the curvilinear trajectory; the onset of the instability imposes a modulation on $\mathcal{R}(k_t')$. The most unstable mode is the one with the lowest frequency at $(\sigma, St) = (0.024, 0.014)$;

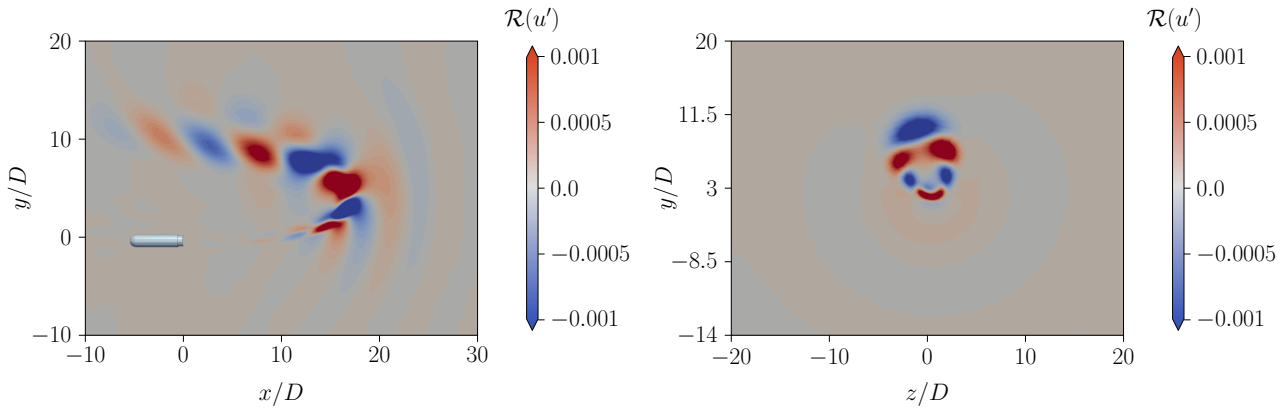


Figure 5.17: Contours of the real part of streamwise velocity $\mathcal{R}(u')$ of the mode at $St = 0.03$ in $x - y$ plane (left) and $z - y$ plane at $x = 15D$ (right).

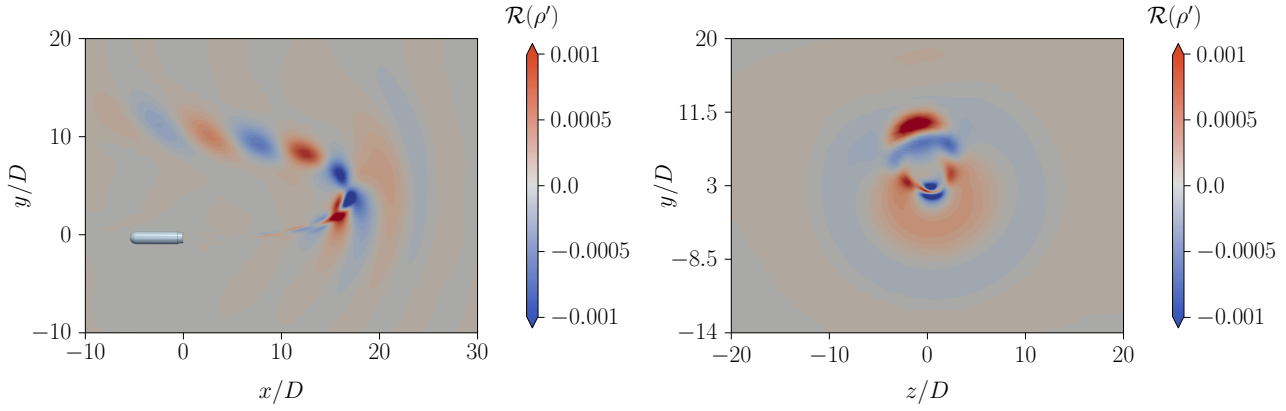


Figure 5.18: Contours of the real part of density $\mathcal{R}(\rho')$ of the mode at $St = 0.03$ in $x - y$ plane (left) and $z - y$ plane (right).

Figures 5.21,5.22, 5.23 and 5.24 are the same as in the previous case but adapted to the new mode under examination. Overall, from the activity peaks of the contours visible in the figures, one might discern a different nature to the mode; the spatial structure is more thin with a longer wavelength and is located in the mixing layer closest to the nozzle lips and in the stagnation point region. The

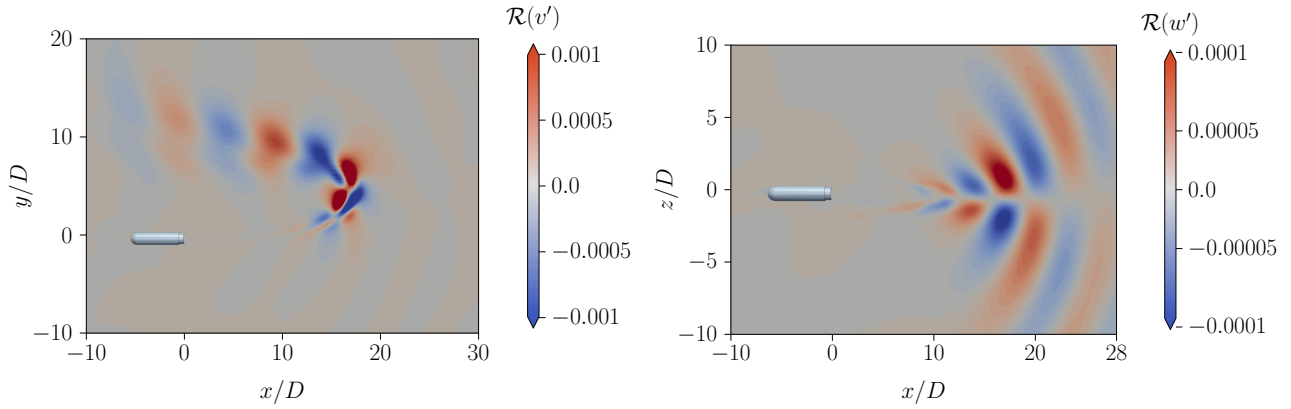


Figure 5.19: Contours of the real part of transversal velocity mode $\mathcal{R}(v')$ at $St = 0.03$ in $x - y$ plane (left) and real part of spanwise velocity $\mathcal{R}(w')$ in $x - z$ plane (right).

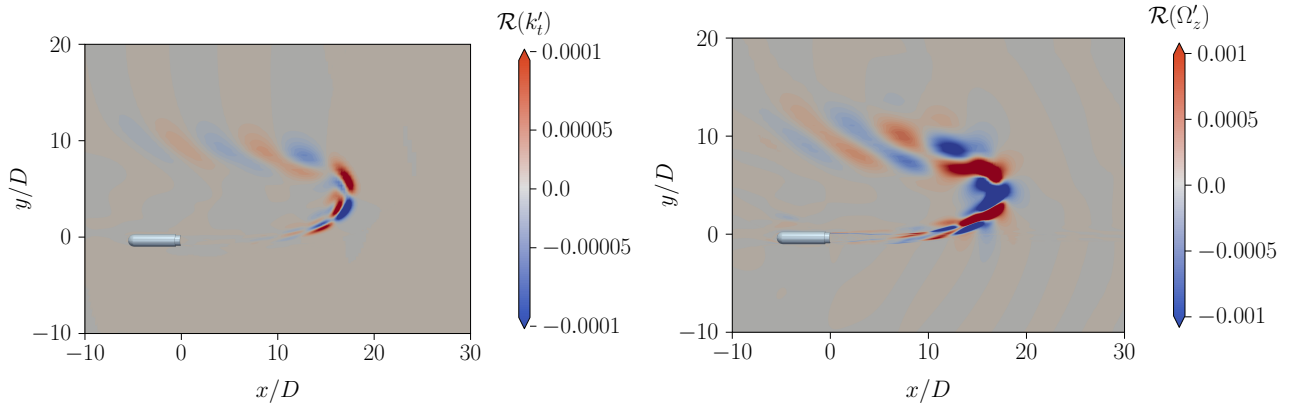


Figure 5.20: Contours of the real part of turbulent kinetic energy $\mathcal{R}(k_t')$ (left) and $z-$ component of vorticity vector $\mathcal{R}(\Omega_z')$ (right) of the mode at $St = 0.03$ in $x - y$ plane .

component $\mathcal{R}(w')$ remains globally antisymmetric with respect to the x-axis in the downstream part of the jet, but also for this component, the peaks of activity are now found close to the nozzle. Looking at the streamwise component in Fig. 5.21 in the $z - y$ plane, we see that, compared to before, it peaks in the region closest to the jet axis. For this mechanism no peaks are observed in the wake region.

5.4 Physical discussion

The aim of this section is to go beyond a mere description of the unstable modes in order to try to understand their nature and assess whether they actually constitute two distinct families. First,

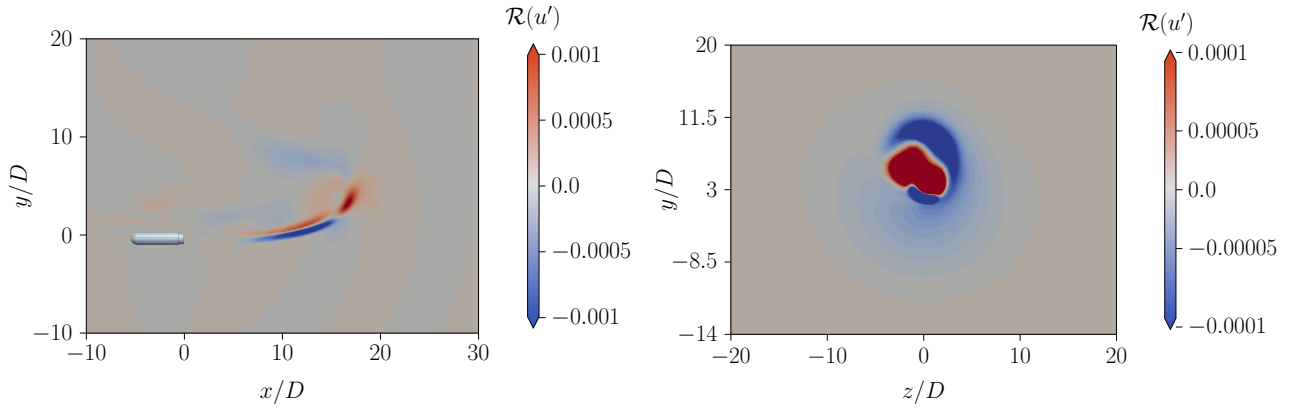


Figure 5.21: Contours of the real part of streamwise velocity $\mathcal{R}(u')$ of the mode at $St = 0.014$ in $x - y$ plane (left) and $z - y$ plane (right).

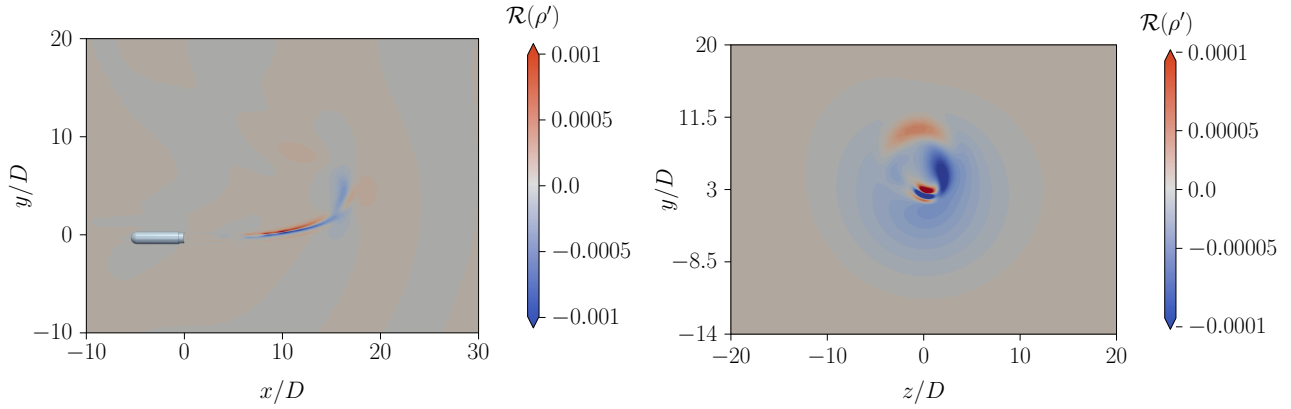


Figure 5.22: Contours of the real part of density $\mathcal{R}(\rho')$ of the mode at $St = 0.014$ in $x - y$ plane (left) and $z - y$ plane (right).

therefore, let us consider the possibility that there is a K-H-type instability, given the presence of the mixing layer. As shown in Figure 5.14, the mixing layer extends to the tip of the jet and is then dissipated in the recirculation zone. Following the streamline of the fixed point originating from the centre of the nozzle's exit section, we draw perpendicular planes (see Figure 5.25). Let $\boldsymbol{e_t}$ denote the normal to each plane (and t the axis), which thus corresponds to the tangent to the streamline. From the intersection of the planes obtained and the plane with normal z that bisects them, we obtain the direction $\boldsymbol{e_n}$ (and the axis n) perpendicular to the streamline. We thus project the velocity vector along the direction $\boldsymbol{e_t}$ and examine its evolution with respect to n.

This is shown in Figures 5.26, 5.27 and 5.28, where, for planes located at $s/L_S = 0.16, 0.5, 0.83$

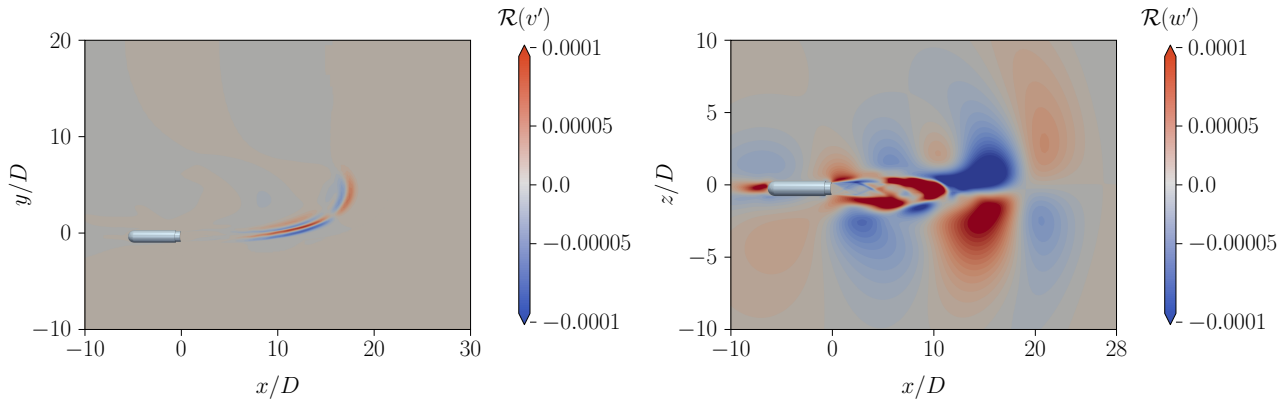


Figure 5.23: Contours of the real part of transversal velocity mode $\mathcal{R}(v')$ at $St = 0.014$ in $x - y$ plane (left) and real part of spanwise velocity $\mathcal{R}(w')$ in $x - z$ plane (right).

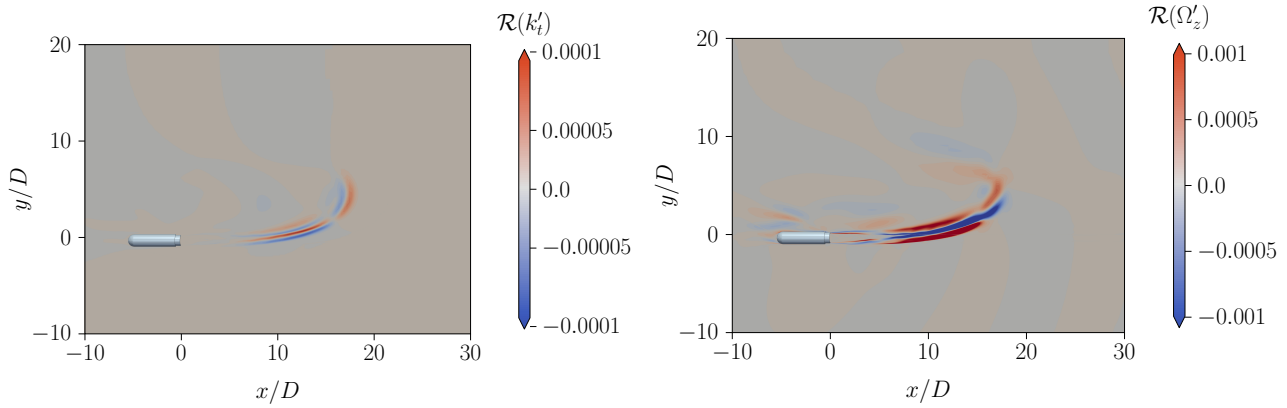


Figure 5.24: Contours of the real part of turbulent kinetic energy $\mathcal{R}(k_t')$ (left) and $z-$ component of vorticity vector $\mathcal{R}(\Omega_z')$ (right) of the mode at $St = 0.014$ in $x - y$ plane .

respectively, both the tangential velocity contours and their evolution with respect to the perpendicular direction are illustrated. It can be seen that, as one moves along the streamline, the jet deforms and loses velocity. Furthermore, the leeward region ($n > 0$) no longer exhibits the counterflow velocity; instead, the velocity is almost zero due to the presence of the large recirculation bubble.

Rayleigh's criterion states that a necessary condition for instability to occur for an inviscid layer is the presence of an inflection point in the velocity profile; the generalised criterion for compressible cases, when applied to our flow, becomes:

$$\frac{\partial}{\partial n}\left(\rho_0 \frac{\partial u_t}{\partial n}\right) = D_2(u_t) = 0 \tag{5.9}$$

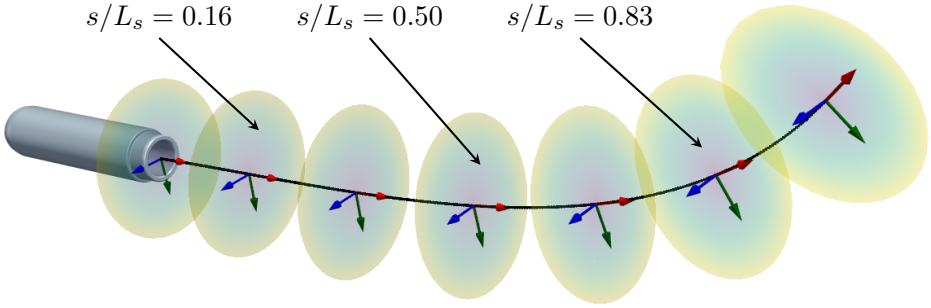


Figure 5.25: A streamline of length L_s originating at $(0, 0, 0)$ with its respective normal planes. The opaque contours in the planes represent the distance from the streamline.

For this reason, we check whether the fixed point presents an inflection point calculated as in 5.9, and we also plot the module of the pressure perturbation $|p'| = \sqrt{(\mathcal{R}(p')^2 + \mathcal{I}(p')^2}$. Figures 5.29-5.30 therefore display the profiles of $D_2(u_t)$ and $|p'|$ in the same three cross-sections examined previously for the modes at $St = 0.03$ and $St = 0.014$, respectively. As might be expected from a jet configuration, two inflection points are observed; for both modes, the magnitude of the pressure perturbation exhibits similar behaviour, with peaks at the inflection points, thus suggesting that both modes arise as K-H-type instabilities. However, in the last plane considered, the mode at $St = 0.03$ no longer exhibits the same pattern, suggesting a possible change in mechanism.

To try to describe both modes more clearly, we have also plotted the profiles of the tangential velocity perturbation $\mathcal{R}(u'_t)$ shown in Figures 5.31-5.32. Both modes in the planes perpendicular to the streamline exhibit an almost antisymmetric behaviour, making it difficult to distinguish between them on the basis of this criterion. In the region along the mixing layer formed by the jet, the two modes

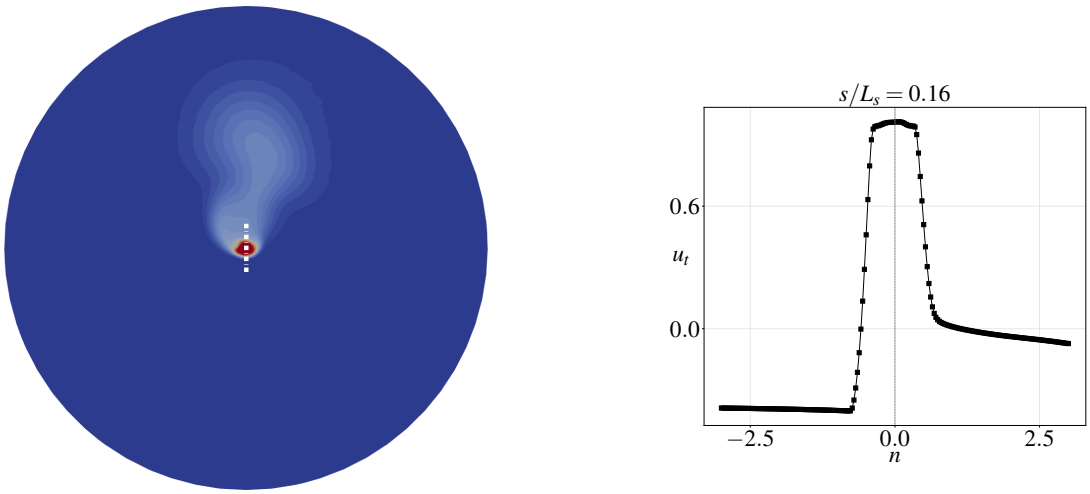


Figure 5.26: In the left frame tangential velocity contours u_t on the plane at $s/L_s = 0.16$. The portion of the curve n that is perpendicular to the current line is shown in white with a dotted line. In the frame on the right, a plot of the tangential velocity relative to this curve is shown.

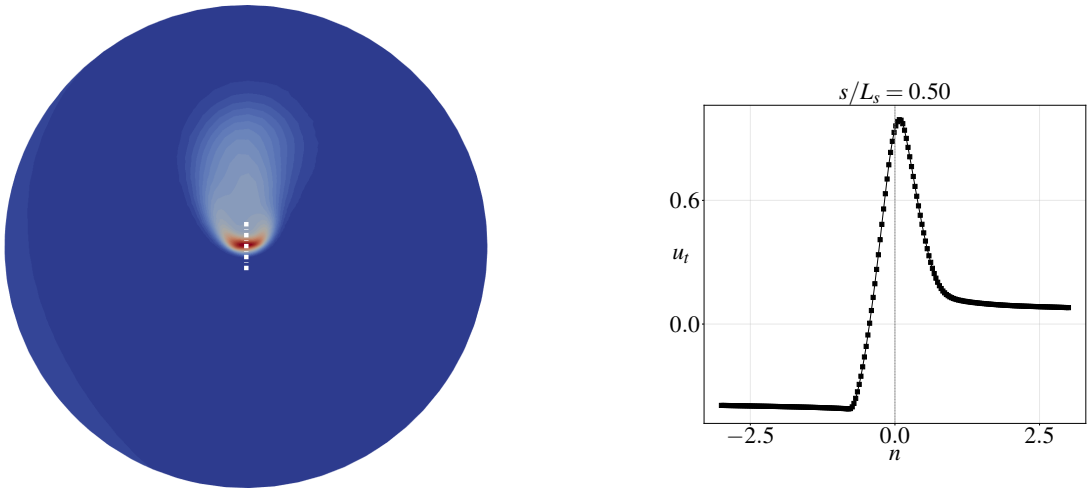


Figure 5.27: In the left frame tangential velocity contours u_t on the plane at $s/L_s = 0.50$. The portion of the curve n that is perpendicular to the current line is shown in white with a dotted line. In the frame on the right, a plot of the tangential velocity relative to this curve is shown.

have a similar spatial distribution, although the mode at $St = 0.014$ has a much longer wavelength in the region where it exhibits its peak activity. Therefore, to distinguish between the two modes, one must examine the region near the recirculation bubble. In this regard, we continued to trace the streamline, not stopping where the jet ends, but following it backwards as shown in Figure 5.33, where the normal planes are also depicted; here, the contours of the vorticity component $\boldsymbol{\Omega}_0 \cdot \boldsymbol{e_t}$ are also

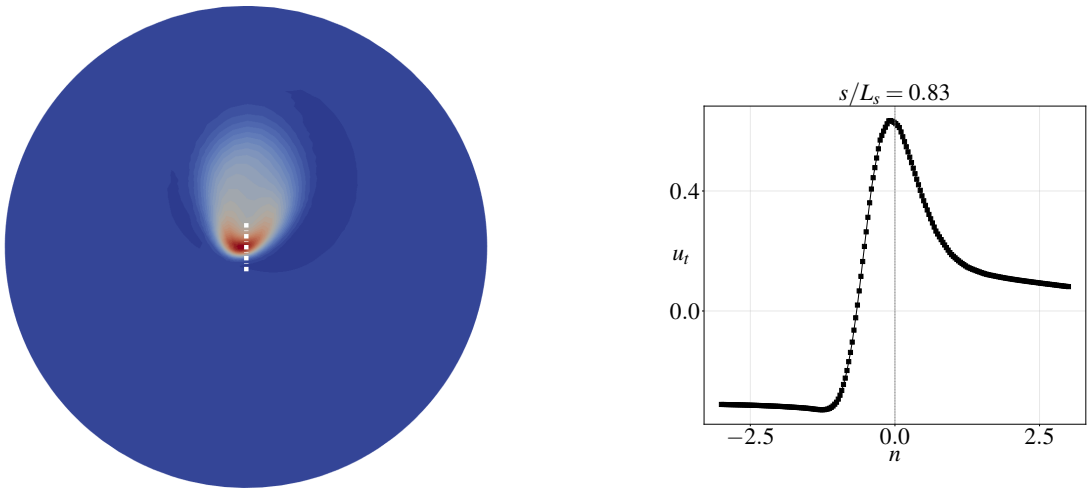


Figure 5.28: In the left frame tangential velocity contours u_t on the plane at $s/L_s = 0.83$. The portion of the curve n that is perpendicular to the current line is shown in white with a dotted line. In the frame on the right, a plot of the tangential velocity relative to this curve is shown.

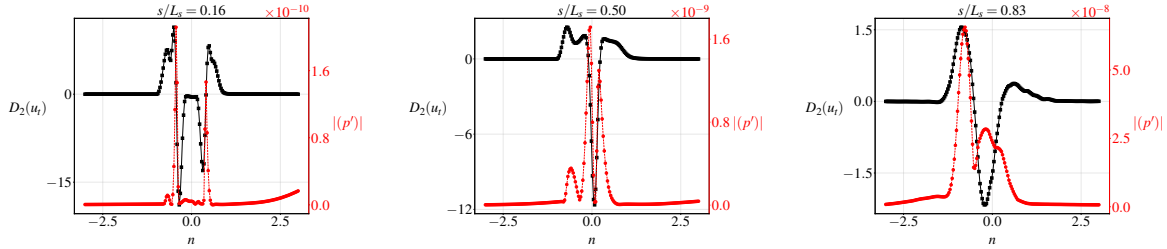


Figure 5.29: Profile of second derivative $D_2(u_t)$ and module of pressure perturbation $|p'|$ for the mode at $St = 0.03$ in planes $s/L_s = 0.16$ (left), $s/L_s = 0.5$ (center) and $s/L_s = 0.83$ (right).

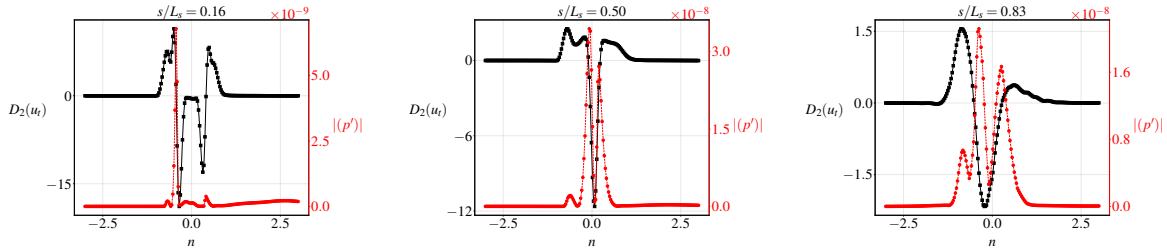


Figure 5.30: Profile of second derivative $D_2(u_t)$ and module of pressure perturbation $|p'|$ for the mode at $St = 0.014$ in planes $s/L_s = 0.16$ (left), $s/L_s = 0.5$ (center) and $s/L_s = 0.83$ (right).

shown. In K-H-type instability, the mode overlaps along the mixing layer; for this reason, Figure 5.34 shows the contours for both modes of the perturbation to the vorticity component $\boldsymbol{\Omega}' \cdot \boldsymbol{e_t}$. In the lower region, both modes have a spatial support that overlaps with the vorticity of the base flow; however,

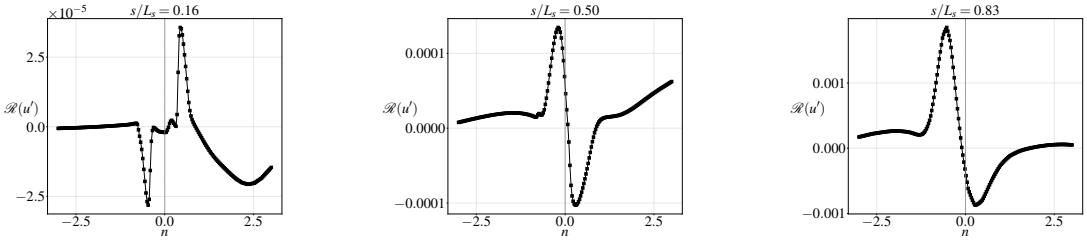


Figure 5.31: Profile of real part of tangential velocity perturbation $\mathcal{R}(u'_t)$ for the mode ad $St = 0.03$ in planes $s/L_s = 0.16$ (left), $s/L_s = 0.5$ (center) and $s/L_s = 0.83$ (right).

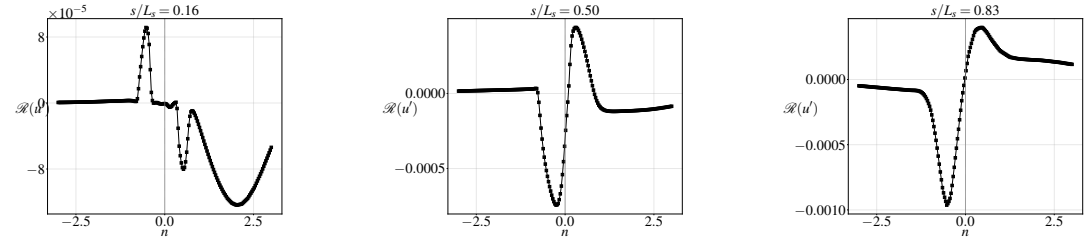


Figure 5.32: Profile of real part of tangential velocity perturbation $\mathcal{R}(u'_t)$ for the mode ad $St = 0.014$ in planes $s/L_s = 0.16$ (left), $s/L_s = 0.5$ (center) and $s/L_s = 0.83$ (right).

in the upper region, the vorticity in the base flow is dissipated. The mode at $St = 0.014$ is also no longer visible in the recirculation zone, whilst the mode at $St = 0.03$ reaches a peak of activity in this zone, thus suggesting a change in nature. If we look again at the contours of the real part of the velocity perturbation for the mode at $St = 0.03$ and superimpose on them the streamlines forming the recirculation zone and those passing beyond it (see Figure 5.35), it seems as though a wake-type instability forms in the direction of the counter-flow, since the recirculation zone behaves like a bluff body, downstream of which we see the mode lobes with alternating signs. Another feature that is partially visible in the figure is the presence of acoustic waves. In this regard, let us therefore plot the contours of the divergence perturbation in the right-hand frame of Figure 5.35. We can see that there are acoustic waves emitted following the impact of the jet with the counterflow, which both continue in the direction of the jet and propagate upstream in the direction of the counterflow. It is difficult to say whether, and to what extent, they have an impact on the observed instability. Indeed, whilst in the screech phenomenon upstream waves (acoustic or k^- wave) are necessary to re-trigger the K-H-type instability, here the perturbations can be transported back to the nozzle directly by the counterflow.

Furthermore, Figure 5.36 shows, together, both the Mach contours of the fixed point and the mode

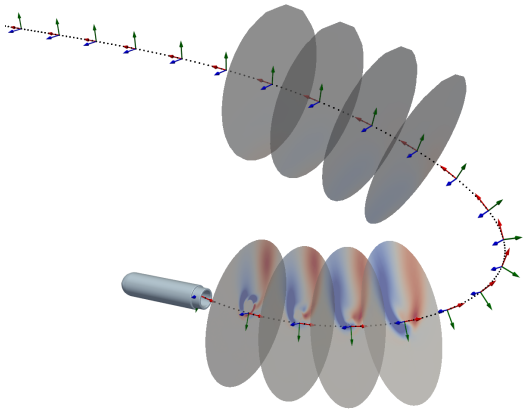


Figure 5.33: A streamline originating at $(0, 0, 0)$ with multiple normal planes superposed. Each plane depicts the contours of the tangential component of vorticity of the fixed point.

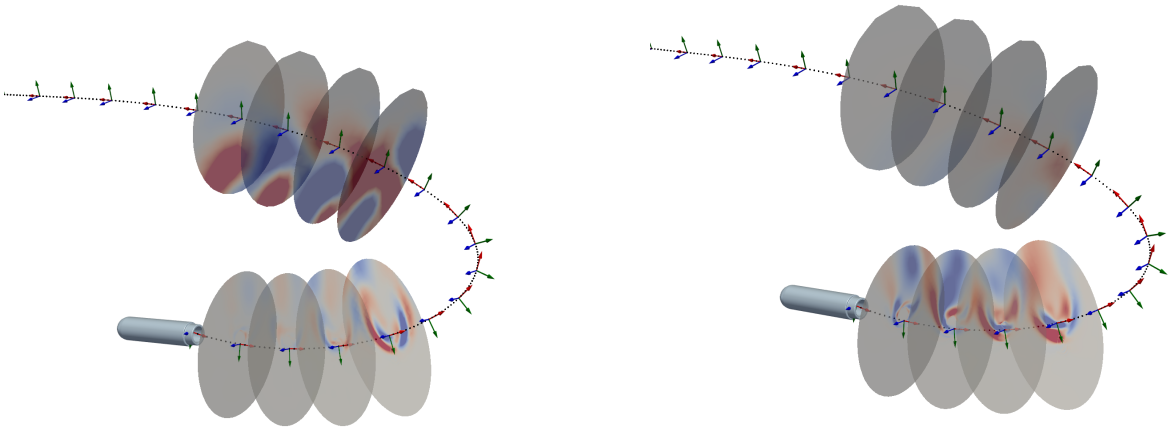


Figure 5.34: A streamline originating at $(0, 0, 0)$ with multiple normal planes superposed. Each plane depicts the contours of the tangential component of vorticity of the perturbation. Mode at $St = 0.03$ (left), mode at $St = 0.014$ (right).

isolines, as well as the streamline passing through them, which acts as an axis of antisymmetry. The tangential velocity profile u_t in the region of the plane where the perturbation is highlighted (dotted line) is similar to half of the velocity profiles of the wakes (left frame of Figure 5.36) It is also interesting to determine whether the curvature imposed on the flow by the incidence angle might play a role in the instability. With this aim we calculated an equivalent Görtler number for each of the stations

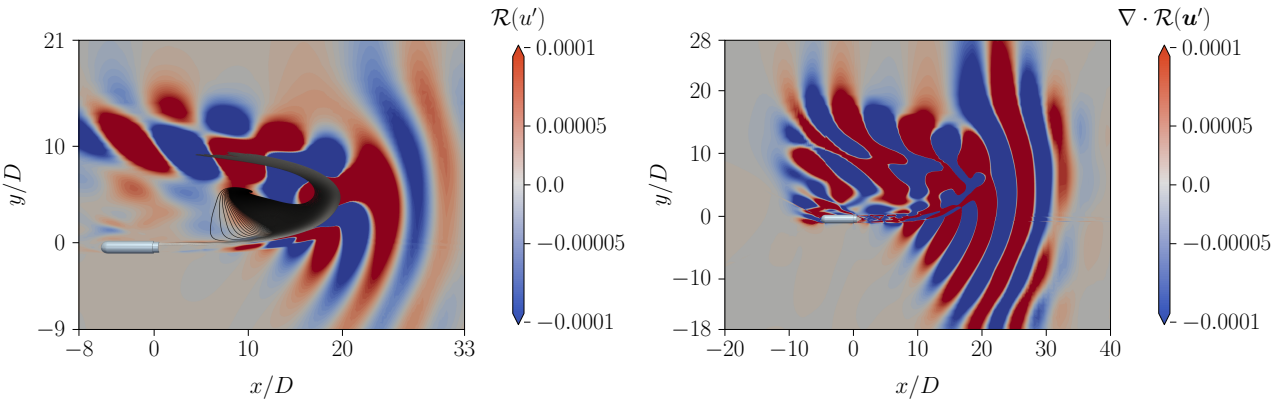


Figure 5.35: Contours of the real part of streamwise velocity $\mathcal{R}(u')$ (left) and of the divergence $\nabla \cdot \mathcal{R}(u')$ of the mode at $St = 0.03$ in $x - y$ plane with streamlines superimposed .

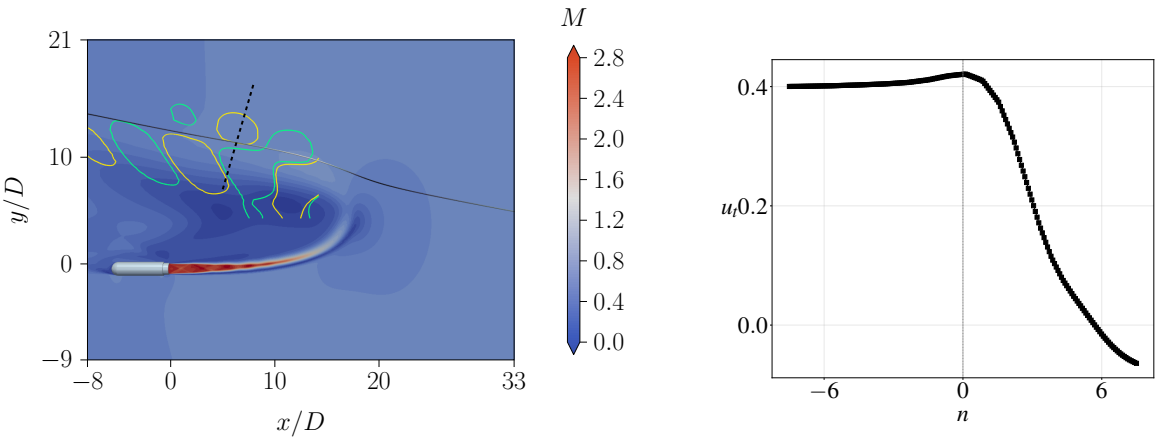


Figure 5.36: Left: Mach number contours with isolines of the real part of the streamwise velocity for the mode at $St = 0.03$ (green for positive and yellow for negative), with the streamline passing through the perturbation superimposed and the normal axis n shown as a dashed line . Right: Profile of the tangential velocity u_t relative to the dashed axis in the figure on the left .

shown in Figure 5.37 as follows:

$$Gr = \frac{\max(\rho)\max(u_t)\delta_\omega}{\max(\mu_t)}\sqrt{\frac{\delta_\omega}{R}} \tag{5.10}$$

where the thickness of the mixing layer δ_ω replaces the momentum thickness used in Chapter 4. The radius of curvature R considered is also the radius of curvature of the streamline, whilst the thickness of the mixing layer is calculated as:

$$\delta_\omega = \frac{\Delta u_t}{\max\left(\partial u_t/\partial n\right)} \tag{5.11}$$

It can be seen that the value of Gr exceeds the threshold value indicated in the previous chapter across almost the entire curved region; furthermore, an interesting detail is that it reaches its maximum at

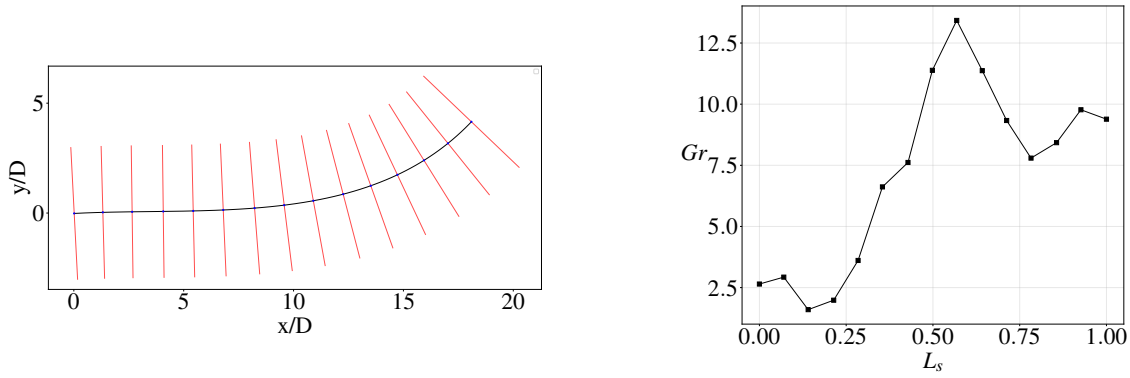


Figure 5.37: Different planes normal to the central streamline (left) and Görtler number computed for each plane.

the station corresponding to the coordinate $x/D \approx 10$, the same coordinate at which the perturbation of the mode at $St = 0.014$ reaches its peak activity (see left frame of Figures 5.21, 5.22 and 5.23). This could indicate that the effect of curvature influences the spatial amplification of the mode.

Finally, we will try to describe how the entire feedback loop works for both modes. A schematic representation is presented in figure 5.38. From the previous analyses, we have seen that in both cases the instability originates as a mixing-layer instability at the nozzle lips and is then amplified spatially along the curvilinear trajectory; in this process of spatial amplification, the curvature imposed by the streamlines of the base flow may play a role, as evidenced by the peak in the Görtler number. The interaction with the counterflow in the terminal region of the jet leads to the formation of acoustic waves that propagate coherently, particularly in the forward direction; however, it is difficult to say whether they play a role in the self-sustaining mechanism. At this point, the two modes exhibit different behaviour. The mode at $St = 0.014$ appears to dissipate in the recirculation zone, where the structures are weaker and more disorganised and could feed back into the K-H-type instability. The mode at $St = 0.03$, instead, reaches new peaks beyond the recirculation zone, where it arranges itself in an almost orderly, antisymmetric manner with respect to the counter-flow streamline, exhibiting wake-type instability behaviour. However, this organised perturbation is not directed towards the nozzle to re-feed the instability. The closure of the loop at this stage could be driven by either hydrodynamic or acoustic fluctuations.

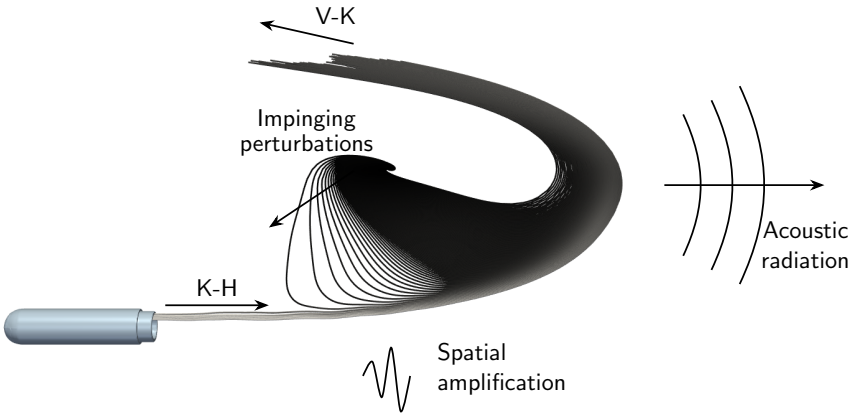


Figure 5.38: Representation of the self-sustaining mechanism.

Conclusions and perspectives

Conclusion

Turbulent compressible flows in the aerospace sector are often characterized by low-frequency unsteady configurations; this characteristic allows them to be investigated with a certain degree of accuracy using a URANS approach, as the time scales of the turbulence are decoupled from those of the low-frequency unsteadiness. In this context, a global stability approach – involving perturbation of the entire URANS state vector – can be a powerful tool for analysing the linear mechanisms at play in more depth. Two distinct strategies can be employed for global stability analysis: a classical matrix-forming approach, which relies on explicitly constructing the Jacobian matrix of the linearised system and performing a spectral decomposition to examine the signs of the eigenvalues; and a matrix-free time-stepper approach, which is necessary when the number of degrees of freedom in the system is too high. In this second approach, the matrix is never explicitly built; instead, the linearised code is advanced in time, and a Krylov-Schur factorization is applied to solve the eigenvalue problem.

A primary objective of this thesis was to develop a unified framework capable of performing both stability approaches, alongside solving standard NS/URANS equations. The tool in question is dNami, a multi-language framework that enables the solution of systems of balance equations through the automatic generation of Fortran routines from simple Python strings. Following previous work by A. Franchini, who coupled dNami with the TAPENADE (automatic differentiation tool developed by INRIA) to enable time-stepper stability analysis, the present work focused on extending this capability to matrix-forming methods. Specifically, I was personally responsible for implementing the modules relating to URANS turbulence modelling in dNami and for developing the routines needed to extract the Jacobian matrix from the linearised code; indeed, rather than writing the Jacobian matrix by hand, it is possible to extract it from the differentiated code using a 'colouring' technique, meaning that the user does not have to linearise the equations or construct the matrix.

To validate the newly implemented features in dNami (turbulence modelling and matrix extraction), several well-documented tests in the literature have been considered. The Jacobian extraction modules were verified against literature data and cross-checked against the time-stepper method using the flow past a circular cylinder and the 2D lid-driven cavity. The cylinder case was additionally used to validate the resolvent analysis via the matrix-forming method, whilst the lid-driven cavity also allowed the $2.5D$ extraction (three-dimensional perturbation superimposed on a two-dimensional base flow) to be validated. The case of the turbulent flat plate with zero pressure gradient served to test

the turbulence model alongside a suitable numerical scheme, which was subsequently adopted for engineering relevant cases. Finally, the study of buffet stability on the OAT15 airfoil enabled the linearisation of the turbulence model to be assessed, a more delicate task as it has been carried out using automatic differentiation.

Following validation, the framework was applied to two complex aerospace configurations. The first is flow through a supersonic diffuser, whose transient dynamics can cause side loads and are not yet fully understood. Specifically, a 2-D geometry known in the literature as 'Model G' has been taken into account; this was adopted by Sajben and colleagues for an extensive experimental and numerical study demonstrating low-frequency dynamics due to shock oscillation in the divergent section. For this case, a global stability analysis and a resolvent analysis have been performed in both 2-D and 2.5D, and in strong-shock configuration (with flow separation) and a weak-shock configuration (without flow separation). The 2-D stability analysis revealed that the experimentally observed unsteadiness is not driven by a global instability, but the flow acts as a selective noise amplifier; The dynamics are governed by receptivity mechanisms, with the shock-foot region being the most sensitive to external forcing. To understand the influence of three-dimensionality, a quasi-3-D analysis has been carried out by superimposing a sinusoidal perturbation $\hat{\boldsymbol{q}}(x,y)e^{i\beta z+\lambda t}$, where β is the spanwise wave number, which is varied. For the strong shock configuration, the flow becomes globally unstable for $\beta \geq 1$. The mode has zero frequency and reaches its maximum growth rate at $\beta = 8$; this is a centrifugal instability caused by the curvature imposed on the flow by the recirculation zone. Conversely, the weak-shock configuration remains stable to 3-D perturbations due to the insufficient curvature of the duct itself. Finally, two parametric studies have been conducted. In the first, we start from the strong shock case and vary the length of the constant-cross-section region at the outlet. The stability analysis revealed that the frequency of the 2-D mode changes as the length varies, as already shown in previous numerical simulations; furthermore, when comparing the results with the 1-D model of an acoustic wave travelling in a channel, the results match quite well. In the second study, instead, the pressure ratio p_{out}/p_0 is reduced to intensify the shock and assess its influence on the global instability. The 2D mode remains stable throughout; indeed, the intensification of the shock appears to have a stabilising effect.

The second case of engineering interest focused on a supersonic jet interacting with a subsonic counter-flow at a variable angle of attack; this configuration corresponds to the landing phases of reusable

launch vehicles, where the flow is already subsonic and engine ignition is used to complete the landing. While recent European projects (e.g., ENTRAIN, REALT) have provided experimental and numerical data on similar configurations, global stability analyses on these flows remain absent in the literature. As this is a full 3-D case, it has been addressed using a time-stepping method; furthermore, unlike previous simulations or experiments, we consider the case where the jet is in a state of adaptation. The geometry under examination is a simplified version of a real-world case of engineering interest; The computational domain includes only the divergent profile of the nozzle and an external cylindrical surface with a step near the nozzle lips. Two cases have been analysed: the zero angle of attack ($\theta = 0°$) and the case at $\theta = 10°$.

The URANS simulation at $\theta = 0°$ turns out to be steady, so no stability analysis has been performed. As regards the URANS simulation at $\theta = 10°$, however, this is highly unsteady, and the PSD analysis of the signal highlighted that the maximum energy lies in the low-frequency range $0.01 < St < 0.07$, with two peaks at $St = 0.014$ and $St = 0.03$. The spectrum obtained from the global stability analysis shows several unstable modes at the same frequencies observed by the PSD. Examining them one by one, they can be divided into two categories: lower-frequency modes at $St \approx 0.014$, whose peak activity lies in the mixing layer and which constitute a KH-type instability, and higher-frequency modes at $St \approx 0.03$, that arise as K-H type instabilities but whose peak activity lies in the wake region suggesting a change of nature towards a wake-like instability.

Perspectives

The objective of this thesis was to demonstrate how global stability analysis is a powerful tool, not only for studying flow transitions at low Re, but also for examining complex flows in applications of real engineering interest; and to develop a tool capable of adapting to as many cases as possible, thereby reducing user effort. Nevertheless, several avenues for future development remain. Firstly, the matrix-forming approach needs to be extended to cases where a multi-block decomposition is required for topological reasons (such as for airfoils with a trailing edge of non-zero thickness); furthermore, the matrix-forming concept can be used to carry out sensitivity analysis; in this regard, it would be useful to develop routines within dNami for extracting the Hessian operator. From a time-stepping stability perspective, however, TAPENADE can be used to generate code that advances the adjoint system in time; this also provides access to transient growth analyses.

A wall-law approach should also be implemented. Indeed, whilst low-frequency unsteady dynamics allow stability analysis to be carried out using the URANS approach, they also impose long periods and therefore long computation times for the time-stepping approach, which can only be reduced by using a wall-law in a code that explicitly integrates the equations in time. In this regard, preliminary results on the implementation of the wall-law approach are presented in Appendix B.

Concerning the physical applications, future studies on the Sajben diffuser should investigate the influence of the imposed boundary conditions by adding a chamber to simulate the external space. We then wish to assess the impact of the turbulence model; in this regard, preliminary results from non-linear simulations carried out using the $k - \log(\omega)$ model are presented in Appendix A.

Finally, the global stability analysis of the retropropulsion configuration must be regarded as a foundational first step, paving the way for more detailed investigations. A mesh sensitivity study needs to be carried out to solidify the spectral results. Subsequently, we need to understand the cause of the loss of plane symmetry for the case $\theta = 10°$; it is not yet clear whether this is linked to a numerical problem or perhaps to a pitchfork bifurcation. This type of bifurcation, in fact, has zero frequency; therefore, it cannot be filtered out using an SFD method. For this reason, we are currently working on a half-domain, specifically by enforcing symmetry conditions on the $x - y$ plane. The convergence of the fixed point also needs to be improved; currently, we have limited ourselves to a classical SFD method, but there are several options in the literature for improving convergence where possible. Finally, the main objective is to carry out a comprehensive parametric study of θ in order to identify a critical value at which instability sets in.

Bibliography

[1] O. Reynolds, "Xxix. an experimental investigation of the circumstances which determine whether the motion of water shall be direct or sinuous, and of the law of resistance in parallel channels," *Philosophical Transactions of the Royal society of London*, n°. 174, p. 935–982, 1883.

[2] G. L. Brown et A. Roshko, "On density effects and large structure in turbulent mixing layers," *Journal of Fluid Mechanics*, vol. 64, n°. 4, p. 775–816, 1974.

[3] D. C. Wilcox *et al.*, *Turbulence modeling for CFD*. DCW industries La Canada, CA, 1998, vol. 2.

[4] A. Fortin, M. Jardak, J. Gervais et R. Pierre, "Localization of hopf bifurcations in fluid flow problems," *International Journal for Numerical Methods in Fluids*, vol. 24, n°. 11, p. 1185–1210, 1997.

[5] F. Sartor, C. Mettot et D. Sipp, "Stability, receptivity, and sensitivity analyses of buffeting transonic flow over a profile," *Aiaa Journal*, vol. 53, n°. 7, p. 1980–1993, 2015.

[6] L. Nave et G. Coffey, "Sea level side loads in high-area-ratio rocket engines," dans *9th propulsion conference*, 1973, p. 1284.

[7] R. Schmucker, "Flow processes in overexpanded chemical rocket nozzles. part 2: Side loads due to asymmetric separation," Rapport technique, 1984.

[8] M. Frey et G. Hagemann, "Restricted shock separation in rocket nozzles," *Journal of Propulsion and Power*, vol. 16, n°. 3, p. 478–484, 2000.

[9] V. Jaunet, S. Arbos, G. Lehnasch et S. Girard, "Wall pressure and external velocity field relation in overexpanded supersonic jets," *AIAA Journal*, vol. 55, n°. 12, p. 4245–4257, 2017.

[10] J. Östlund, T. Damgaard et M. Frey, "Side-load phenomena in highly overexpanded rocket nozzles," *Journal of Propulsion and Power*, vol. 20, n°. 4, p. 695–704, 2004.

[11] A. Ferri et L. M. Nucci, "The origin of aerodynamic instability of supersonic inlets at subcritical conditions," Rapport technique, 1951.

[12] C. L. Dailey, "Supersonic diffuser instability," *Journal of the Aeronautical Sciences*, vol. 22, n°. 11, p. 733–749, 1955.

[13] M. Sajben, J. Kroutil et C. Chen, "A high-speed schlieren investigation of diffuser flows with dynamic distortion," dans *13th Propulsion Conference*, 1977, p. 875.

[14] M. Sajben et J. Kroutil, "Effects of initial boundary-layer thickness on transonic diffuser flows," *AIAA Journal*, vol. 19, n°. 11, p. 1386–1393, 1981.

[15] M. Sajben, T. Bogar et J. Kroutil, "Forced oscillation experiments in supercritical diffuser flows," *AIAA journal*, vol. 22, n°. 4, p. 465–474, 1984.

[16] J. Salmon, T. Bogar et M. Sajben, "Laser doppler velocimeter measurements in unsteady, separated, transonic diffuser flows," *AIAA journal*, vol. 21, n°. 12, p. 1690–1697, 1983.

[17] T. Bogar, M. Sajben et J. Kroutil, "Characteristic frequency and length scales in transonic diffuser flow oscillations," dans *14th Fluid and Plasma Dynamics Conference*, 1981, p. 1291.

[18] T. Bogar, "Structure of self-excited oscillations in transonic diffuser flows," *AIAA journal*, vol. 24, n°. 1, p. 54–61, 1986.

[19] T. Hsieh, A. Wardlaw, JR et T. Coakley, "Numerical simulation of a ramjet inlet flowfield in response to large amplitude combustor pressure oscillation," dans *20th Joint Propulsion Conference*, 1984, p. 1363.

[20] T. Hsieh et T. Coakley, "Unsteady separated boundary layer in a transonic diffuser flow with self-excited oscillations," dans *4th Joint Fluid Mechanics, Plasma Dynamics and Lasers Conference*, 1986, p. 1037.

[21] ——, "Downstream boundary effects on the frequency of self-excited oscillations in transonic diffuser flows," dans *25th AIAA Aerospace Sciences Meeting*, 1987, p. 161.

[22] C. Chen, M. Sajben et J. Kroutil, "Shock-wave oscillations in a transonic diffuser flow," *AIAA journal*, vol. 17, n°. 10, p. 1076–1083, 1979.

[23] T. Coakley et T. Hsieh, "A comparison between implicit and hybrid methods for the calculationof steady and unsteady inlet flows," dans *21st Joint Propulsion Conference*, 1985, p. 1125.

[24] C. K. Tam, "Supersonic jet noise," *Annual review of fluid mechanics*, vol. 27, n°. 1, p. 17–43, 1995.

[25] A. Powell, "The noise of choked jets," *The Journal of the Acoustical Society of America*, vol. 25, n°. 3, p. 385–389, 1953.

[26] J. Seiner, J. Manning et M. Ponton, "Model and full scale study of twin supersonic plume resonance," dans *25th AIAA Aerospace Sciences Meeting*, 1987, p. 244.

[27] B. Lee, "Self-sustained shock oscillations on airfoils at transonic speeds," *Progress in Aerospace Sciences*, vol. 37, n°. 2, p. 147–196, 2001.

[28] W. F. Hilton et R. Fowler, "Photographs of shock wave movement," 1947.

[29] V. Theofilis, "Advances in global linear instability analysis of nonparallel and three-dimensional flows," *Progress in aerospace sciences*, vol. 39, n°. 4, p. 249–315, 2003.

[30] W. M. Orr, "The stability or instability of the steady motions of a perfect liquid and of a viscous liquid. part ii: A viscous liquid," dans *Proceedings of the Royal Irish Academy. Section A: Mathematical and Physical Sciences*, vol. 27. JSTOR, 1907, p. 69–138.

[31] A. Sommerfeld, *Ein beitrag zur hydrodynamischen erklaerung der turbulenten fluessigkeitsbewegungen*, 1908.

[32] S. A. Orszag, "Accurate solution of the orr–sommerfeld stability equation," *Journal of Fluid Mechanics*, vol. 50, n°. 4, p. 689–703, 1971.

[33] A. Zebib, "Stability of viscous flow past a circular cylinder," *Journal of Engineering Mathematics*, vol. 21, n°. 2, p. 155–165, 1987.

[34] C. Jackson, "A finite-element study of the onset of vortex shedding in flow past variously shaped bodies," *Journal of fluid Mechanics*, vol. 182, p. 23–45, 1987.

[35] U. Ghia, K. N. Ghia et C. Shin, "High-re solutions for incompressible flow using the navier-stokes equations and a multigrid method," *Journal of computational physics*, vol. 48, n°. 3, p. 387–411, 1982.

[36] P. M. Gresho, D. K. Gartling, J. Torczynski, K. Cliffe, K. Winters, T. Garratt, A. Spence et J. W. Goodrich, "Is the steady viscous incompressible two-dimensional flow over a backward-facing step at re= 800 stable?" *International Journal for Numerical Methods in Fluids*, vol. 17, n°. 6, p. 501–541, 1993.

[37] P. Huerre et P. Monkewitz, "Local and global instabilities in spatially developing flows," *Annual review of fluid mechanics*, vol. 22, n°. 1, p. 473–537, 1990.

[38] L. N. Trefethen, "Pseudospectra of linear operators," *SIAM review*, vol. 39, n°. 3, p. 383–406, 1997.

[39] W. Reynolds et A. Hussain, "The mechanics of an organized wave in turbulent shear flow. part 3. theoretical models and comparisons with experiments," *Journal of Fluid Mechanics*, vol. 54, n°. 2, p. 263–288, 1972.

[40] J. D. Crouch, A. Garbaruk et D. Magidov, "Predicting the onset of flow unsteadiness based on global instability," *Journal of Computational Physics*, vol. 224, n°. 2, p. 924–940, 2007.

[41] J. D. Crouch, A. Garbaruk, D. Magidov et A. Travin, "Origin of transonic buffet on aerofoils," *Journal of fluid mechanics*, vol. 628, p. 357–369, 2009.

[42] J. B. McDevitt et A. F. Okuno, "Static and dynamic pressure measurements on a naca 0012 airfoil in the ames high reynolds number facility," Rapport technique, 1985.

[43] M. C. Iorio, L. M. Gonzalez et E. Ferrer, "Direct and adjoint global stability analysis of turbulent transonic flows over a naca0012 profile," *International Journal for Numerical Methods in Fluids*, vol. 76, n°. 3, p. 147–168, 2014.

[44] S. Deck, "Numerical simulation of transonic buffet over a supercritical airfoil," *AIAA journal*, vol. 43, n°. 7, p. 1556–1566, 2005.

[45] L. Jacquin, P. Molton, S. Deck, B. Maury et D. Soulevant, "Experimental study of shock oscillation over a transonic supercritical profile," *AIAA journal*, vol. 47, n°. 9, p. 1985–1994, 2009.

[46] S. Timme et R. Thormann, "Towards three-dimensional global stability analysis of transonic shock buffet," dans *AIAA Atmospheric Flight Mechanics Conference*, 2016, p. 3848.

[47] S. Timme, "Global instability of wing shock buffet," *arXiv preprint arXiv:1806.07299*, 2018.

[48] J. Crouch, A. Garbaruk et M. Strelets, "Global instability in the onset of transonic-wing buffet," *Journal of Fluid Mechanics*, vol. 881, p. 3–22, 2019.

[49] E. PALADINI, S. Beneddine, J. Dandois, D. Sipp et J.-C. Robinet, "Transonic buffet instability: from two-dimensional airfoils to three-dimensional swept wings," 2019.

[50] C. Mettot, F. Renac et D. Sipp, "Computation of eigenvalue sensitivity to base flow modifications in a discrete framework: Application to open-loop control," *Journal of Computational Physics*, vol. 269, p. 234–258, 2014.

[51] F. Sartor, C. Mettot, R. Bur et D. Sipp, "Unsteadiness in transonic shock-wave/boundary-layer interactions: experimental investigation and global stability analysis," *Journal of Fluid Mechanics*, vol. 781, p. 550–577, 2015.

[52] J. Hao, "On the low-frequency unsteadiness in shock wave–turbulent boundary layer interactions," *Journal of Fluid Mechanics*, vol. 971, p. A28, 2023.

[53] A. Franchini, "Global stability analysis via automatic differentiation: application on turbulent jets," Thèse de doctorat, École Nationale Supérieure des Arts et Métiers, 2025.

[54] N. Alferez, E. Touber, S. Winn et Y. Ali, "dnami: a framework for solving systems of balance laws using explicit numerical schemes on structured meshes," *Zenodo*.

[55] L. Hascoet et V. Pascual, "The tapenade automatic differentiation tool: principles, model, and specification," *ACM Transactions on Mathematical Software (TOMS)*, vol. 39, n°. 3, p. 1–43, 2013.

[56] T. F. Coleman et J. J. Moré, "Estimation of sparse jacobian matrices and graph coloring problems," *SIAM journal on Numerical Analysis*, vol. 20, n°. 1, p. 187–209, 1983.

[57] A. Poulain, C. Content, D. Sipp, G. Rigas et E. Garnier, "Broadcast: A high-order compressible cfd toolbox for stability and sensitivity using algorithmic differentiation," *Computer Physics Communications*, vol. 283, p. 108557, 2023.

[58] W. Sutherland, "Lii. the viscosity of gases and molecular force," *The London, Edinburgh, and Dublin Philosophical Magazine and Journal of Science*, vol. 36, nº. 223, p. 507–531, 1893.

[59] J. D. Anderson Jr, *Hypersonic and High-Temperature Gas Dynamics*. American Institute of Aeronautics and Astronautics, 2006.

[60] M. Vinokur, "Conservation equations of gasdynamics in curvilinear coordinate systems," *Journal of Computational Physics*, vol. 14, nº. 2, p. 105–125, 1974.

[61] T. H. Pulliam, "Implicit solution methods in computational fluid dynamics," *Applied numerical mathematics*, vol. 2, nº. 6, p. 441–474, 1986.

[62] M. R. Visbal et D. V. Gaitonde, "On the use of higher-order finite-difference schemes on curvilinear and deforming meshes," *Journal of Computational Physics*, vol. 181, nº. 1, p. 155–185, 2002.

[63] P. D. Thomas et C. K. Lombard, "Geometric conservation law and its application to flow computations on moving grids," *AIAA journal*, vol. 17, nº. 10, p. 1030–1037, 1979.

[64] G. Hagen, "Ueber die bewegung des wassers in engen cylindrischen röhren," *Annalen der Physik*, vol. 122, nº. 3, p. 423–442, 1839.

[65] J. L. Poiseuille, *Recherches expérimentales sur le mouvement des liquides dans les tubes de très-petits diamètres*. Imprimerie Royale, 1844.

[66] L. Prandtl, "Uber flussigkeitsbewegung bei sehr kleiner reibung," *Verhandl. 3rd Int. Math. Kongr. Heidelberg (1904), Leipzig*, 1905.

[67] T. Von Karman, "Über den mechanismus des widerstandes, den ein bewegter körper in einer flüssigkeit erfährt," *Nachrichten von der Gesellschaft der Wissenschaften zu Göttingen, Mathematisch-Physikalische Klasse*, vol. 1911, p. 509–517, 1911.

[68] G. I. Taylor, "Viii. stability of a viscous liquid contained between two rotating cylinders," *Philosophical Transactions of the Royal Society of London. Series A, Containing Papers of a Mathematical or Physical Character*, vol. 223, nº. 605-615, p. 289–343, 1923.

[69] J. O. Hinze, *Turbulence*. McGraw-Hill, New York, NY, 1975.

[70] E. N. Lorenz, "Deterministic nonperiodic flow 1," dans *Universality in Chaos, 2nd edition.* Routledge, 2017, p. 367–378.

[71] L. F. Richardson, *Weather prediction by numerical process.* Franklin Classics, 1922.

[72] H. Tennekes et J. L. Lumley, *A first course in turbulence.* MIT press, 1972.

[73] A. N. Kolmogorov, "The local structure of turbulence in incompressible viscous fluid for very large reynolds number," *Cr Acad. Sci. USSR*, vol. 30, p. 301, 1941.

[74] O. Reynolds, "Iv. on the dynamical theory of incompressible viscous fluids and the determination of the criterion," *Philosophical transactions of the royal society of london.(a.)*, n°. 186, p. 123–164, 1895.

[75] A. Favre, "Equations des gaz turbulents compressibles," *J. de Mecanique*, vol. 4, n°. 3, 1965.

[76] J. Boussinesq, "Theorie de l'ecoulement tourbillant," *Mem. Acad. Sci.*, vol. 23, p. 46, 1877.

[77] P. Spalart et S. Allmaras, "A one-equation turbulence model for aerodynamic flows," dans *30th aerospace sciences meeting and exhibit*, 1992, p. 439.

[78] S. R. Allmaras et F. T. Johnson, "Modifications and clarifications for the implementation of the spalart-allmaras turbulence model," dans *Seventh international conference on computational fluid dynamics (ICCFD7)*, vol. 1902. Big Island, HI, 2012, p. 1–11.

[79] A. Kolmgorov, "Equations of turbulent motion of an incompressible fluid," *Izv Akad. Nauk SSR, Seria Fiz. VI*, vol. 1, p. 56–58, 1942.

[80] F. Menter, "Zonal two equation kw turbulence models for aerodynamic flows," dans *23rd fluid dynamics, plasmadynamics, and lasers conference*, 1993, p. 2906.

[81] F. R. Menter, "Two-equation eddy-viscosity turbulence models for engineering applications," *AIAA journal*, vol. 32, n°. 8, p. 1598–1605, 1994.

[82] F. R. Menter, M. Kuntz, R. Langtry *et al.*, "Ten years of industrial experience with the sst turbulence model," *Turbulence, heat and mass transfer*, vol. 4, n°. 1, p. 625–632, 2003.

[83] D. C. Wilcox, "Reassessment of the scale-determining equation for advanced turbulence models," *AIAA journal*, vol. 26, n°. 11, p. 1299–1310, 1988.

[84] F. R. Menter, "Influence of freestream values on k-omega turbulence model predictions," *AIAA journal*, vol. 30, n°. 6, p. 1657–1659, 1992.

[85] S. Sarkar, G. Erlebacher, M. Y. Hussaini et H. O. Kreiss, "The analysis and modelling of dilatational terms in compressible turbulence," *Journal of Fluid Mechanics*, vol. 227, p. 473–493, 1991.

[86] O. Zeman, "Dilatation dissipation: the concept and application in modeling compressible mixing layers," *Physics of Fluids A: Fluid Dynamics*, vol. 2, n°. 2, p. 178–188, 1990.

[87] D. C. Wilcox, "Dilatation-dissipation corrections for advanced turbulence models," *AIAA journal*, vol. 30, n°. 11, p. 2639–2646, 1992.

[88] R. A. Frantz, J.-C. Loiseau et J.-C. Robinet, "Krylov methods for large-scale dynamical systems: Application in fluid dynamics," *Applied Mechanics Reviews*, vol. 75, n°. 3, p. 030802, 2023.

[89] H. P. Chomaz, J.M. et L. Redekopp, "Bifurcations to local and global modes in spatially developping flows," *Phsycal review letters*, vol. 60, n°. 1, p. 25, 1988.

[90] P. J. Schmid et L. Brandt, "Analysis of fluid systems: stability, receptivity, sensitivity: lecture notes from the flow-nordita summer school on advanced instability methods for complex flows, stockholm, sweden, 2013," *Applied Mechanics Reviews*, vol. 66, n°. 2, p. 024803, 2014.

[91] J.-C. Loiseau, M. A. Bucci, S. Cherubini et J.-C. Robinet, "Time-stepping and krylov methods for large-scale instability problems," *Computational modelling of bifurcations and instabilities in fluid dynamics*, p. 33–73, 2019.

[92] L. N. Trefethen, A. E. Trefethen, S. C. Reddy et T. A. Driscoll, "Hydrodynamic stability without eigenvalues," *Science*, vol. 261, n°. 5121, p. 578–584, 1993.

[93] B.-T. Chu, "On the energy transfer to small disturbances in fluid flow (part i)," *Acta Mechanica*, vol. 1, n°. 3, p. 215–234, 1965.

[94] D. Barkley, "Linear analysis of the cylinder wake mean flow," *EPL (Europhysics Letters)*, vol. 75, n°. 5, p. 750–756, 2006.

[95] D. Sipp et A. Lebedev, "Global stability of base and mean flows: a general approach and its applications to cylinder and open cavity flows," *Journal of Fluid Mechanics*, vol. 593, p. 333–358, 2007.

[96] V. Mantič-Lugo, C. Arratia et F. Gallaire, "Self-consistent mean flow description of the nonlinear saturation of the vortex shedding in the cylinder wake," *Physical review letters*, vol. 113, n°. 8, p. 084501, 2014.

[97] K. Gudmundsson et T. Colonius, "Instability wave models for the near-field fluctuations of turbulent jets," *Journal of Fluid Mechanics*, vol. 689, p. 97–128, 2011.

[98] B. J. McKeon et A. S. Sharma, "A critical-layer framework for turbulent pipe flow," *Journal of Fluid Mechanics*, vol. 658, p. 336–382, 2010.

[99] S. Beneddine, D. Sipp, A. Arnault, J. Dandois et L. Lesshafft, "Conditions for validity of mean flow stability analysis," *Journal of Fluid Mechanics*, vol. 798, p. 485–504, 2016.

[100] C. Mettot, D. Sipp et H. Bézard, "Quasi-laminar stability and sensitivity analyses for turbulent flows: prediction of low-frequency unsteadiness and passive control," *Physics of Fluids*, vol. 26, n°. 4, 2014.

[101] W. Reynolds et W. Tiederman, "Stability of turbulent channel flow, with application to malkus's theory," *Journal of Fluid Mechanics*, vol. 27, n°. 2, p. 253–272, 1967.

[102] C. Cossu, G. Pujals et S. Depardon, "Optimal transient growth and very large–scale structures in turbulent boundary layers," *Journal of Fluid Mechanics*, vol. 619, p. 79–94, 2009.

[103] G. Pujals, M. García-Villalba, C. Cossu et S. Depardon, "A note on optimal transient growth in turbulent channel flows," *Physics of fluids*, vol. 21, n°. 1, 2009.

[104] P. Morra, O. Semeraro, D. S. Henningson et C. Cossu, "On the relevance of reynolds stresses in resolvent analyses of turbulent wall-bounded flows," *Journal of Fluid Mechanics*, vol. 867, p. 969–984, 2019.

[105] R. Cess, "A survey of the literature on heat transfer in turbulent tube flow," *Res. Rep*, vol. 8, p. 0529, 1958.

[106] C. Benoit, S. Péron et S. Landier, "Cassiopee: a cfd pre-and post-processing tool," *Aerospace Science and Technology*, vol. 45, p. 272–283, 2015.

[107] C. Hirsch, *Numerical computation of internal and external flows: The fundamentals of computational fluid dynamics*. Elsevier, 2007.

[108] S. K. Lele, "Compact finite difference schemes with spectral-like resolution," *Journal of computational physics*, vol. 103, n°. 1, p. 16–42, 1992.

[109] R. F. Warming et B. J. Hyett, "The modified equation approach to the stability and accuracy analysis of finite-difference methods," *Journal of computational physics*, vol. 14, n°. 2, p. 159–179, 1974.

[110] C. Bogey et C. Bailly, "A family of low dispersive and low dissipative explicit schemes for flow and noise computations," *Journal of Computational physics*, vol. 194, n°. 1, p. 194–214, 2004.

[111] S. Gottlieb et C.-W. Shu, "Total variation diminishing runge-kutta schemes," *Mathematics of computation*, vol. 67, n°. 221, p. 73–85, 1998.

[112] C.-W. Shu et S. Osher, "Efficient implementation of essentially non-oscillatory shock-capturing schemes," *Journal of computational physics*, vol. 77, n°. 2, p. 439–471, 1988.

[113] A. Jameson, W. Schmidt et E. Turkel, "Numerical solution of the euler equations by finite volume methods using runge kutta time stepping schemes," dans *14th fluid and plasma dynamics conference*, 1981, p. 1259.

[114] L. Sciacovelli, D. Passiatore, P. Cinnella et G. Pascazio, "Assessment of a high-order shock-capturing central-difference scheme for hypersonic turbulent flow simulations," *Computers & Fluids*, vol. 230, p. 105134, 2021.

[115] F. Ducros, V. Ferrand, F. Nicoud, C. Weber, D. Darracq, C. Gacherieu et T. Poinsot, "Large-eddy simulation of the shock/turbulence interaction," *Journal of Computational Physics*, vol. 152, n°. 2, p. 517–549, 1999.

[116] A. Bhagatwala et S. K. Lele, "A modified artificial viscosity approach for compressible turbulence simulations," *Journal of computational physics*, vol. 228, n°. 14, p. 4965–4969, 2009.

[117] K. W. Thompson, "Time dependent boundary conditions for hyperbolic systems," *Journal of computational physics*, vol. 68, n°. 1, p. 1–24, 1987.

[118] ——, "Time-dependent boundary conditions for hyperbolic systems, ii," *Journal of computational physics*, vol. 89, n°. 2, p. 439–461, 1990.

[119] T. J. Poinsot et S. Lelef, "Boundary conditions for direct simulations of compressible viscous flows," *Journal of computational physics*, vol. 101, n°. 1, p. 104–129, 1992.

[120] G. Lodato, P. Domingo et L. Vervisch, "Three-dimensional boundary conditions for direct and large-eddy simulation of compressible viscous flows," *Journal of computational physics*, vol. 227, n°. 10, p. 5105–5143, 2008.

[121] G. Lodato, "Tridimensional boundary conditions for direct and large-eddy simulation of turbulent flows. sub-grid scale modeling for near-wall region turbulence," Thèse de doctorat, INSA de Rouen, 2008.

[122] D. H. Rudy et J. C. Strikwerda, "A nonreflecting outflow boundary condition for subsonic navier-stokes calculations," *Journal of Computational Physics*, vol. 36, n°. 1, p. 55–70, 1980.

[123] J.-R. Carlson, "Inflow/outflow boundary conditions with application to fun3d," Rapport technique, 2011.

[124] L. D. Dalcin, R. R. Paz, P. A. Kler et A. Cosimo, "Parallel distributed computing using python," *Advances in Water Resources*, vol. 34, n°. 9, p. 1124–1139, 2011.

[125] V. Hernandez, J. E. Roman et V. Vidal, "Slepc: A scalable and flexible toolkit for the solution of eigenvalue problems," *ACM Transactions on Mathematical Software (TOMS)*, vol. 31, n°. 3, p. 351–362, 2005.

[126] T. A. Albring, M. Sagebaum et N. R. Gauger, "Efficient aerodynamic design using the discrete adjoint method in su2," dans *17th AIAA/ISSMO multidisciplinary analysis and optimization conference*, 2016, p. 3518.

[127] W. Lee, H. Yu, X. Rival et H. Yang, "On correctness of automatic differentiation for non-differentiable functions," *Advances in neural information processing systems*, vol. 33, p. 6719–6730, 2020.

[128] S. Bagheri, E. Åkervik, L. Brandt et D. S. Henningson, "Matrix-free methods for the stability and control of boundary layers," *AIAA journal*, vol. 47, n°. 5, p. 1057–1068, 2009.

[129] W. Edwards, L. S. Tuckerman, R. A. Friesner et D. Sorensen, "Krylov methods for the incompressible navier-stokes equations," *Journal of computational physics*, vol. 110, n°. 1, p. 82–102, 1994.

[130] E. Åkervik, L. Brandt, D. S. Henningson, J. Hœpffner, O. Marxen et P. Schlatter, "Steady solutions of the navier-stokes equations by selective frequency damping," *Physics of fluids*, vol. 18, n°. 6, 2006.

[131] C. Pruett, T. Gatski, C. E. Grosch et W. Thacker, "The temporally filtered navier–stokes equations: properties of the residual stress," *Physics of Fluids*, vol. 15, n°. 8, p. 2127–2140, 2003.

[132] F. Richez, M. Leguille et O. Marquet, "Selective frequency damping method for steady rans solutions of turbulent separated flows around an airfoil at stall," *Computers & Fluids*, vol. 132, p. 51–61, 2016.

[133] B. E. Jordi, C. J. Cotter et S. J. Sherwin, "Encapsulated formulation of the selective frequency damping method," *Physics of Fluids*, vol. 26, n°. 3, 2014.

[134] ——, "An adaptive selective frequency damping method," *Physics of Fluids*, vol. 27, n°. 9, 2015.

[135] A. Krylov, "On the numerical solution of equation by which are determined in technical problems the frequencies of small vibrations of material systems," *News Acad. Sci. USSR*, vol. 7, p. 491–539, 1931.

[136] W. E. Arnoldi, "The principle of minimized iterations in the solution of the matrix eigenvalue problem," *Quarterly of applied mathematics*, vol. 9, n°. 1, p. 17–29, 1951.

[137] Y. Saad et M. H. Schultz, "Gmres: A generalized minimal residual algorithm for solving non-symmetric linear systems," *SIAM Journal on scientific and statistical computing*, vol. 7, n°. 3, p. 856–869, 1986.

[138] Y. Saad, *Iterative methods for sparse linear systems*. SIAM, 2003.

[139] B. M. Averick, J. J. Moré, C. H. Bischof, A. Carle et A. Griewank, "Computing large sparse jacobian matrices using automatic differentiation," *SIAM Journal on Scientific Computing*, vol. 15, n°. 2, p. 285–294, 1994.

[140] A. R. Curtis, M. J. Powell et J. K. Reid, "On the estimation of sparse jacobian matrices," *IMA Journal of Applied Mathematics*, vol. 13, n°. 1, p. 117–119, 1974.

[141] A. Poulain, "Solutions optimales linéaires et non-linéaires dans une couche limite hypersonique: stabilité et contrôle en boucle ouverte," Thèse de doctorat, Institut Polytechnique de Paris, 2023.

[142] D. Barkley et R. D. Henderson, "Three-dimensional floquet stability analysis of the wake of a circular cylinder," *Journal of Fluid Mechanics*, vol. 322, p. 215–241, 1996.

[143] B. Bugeat, J.-C. Chassaing, J.-C. Robinet et P. Sagaut, "3d global optimal forcing and response of the supersonic boundary layer," *Journal of Computational Physics*, vol. 398, p. 108888, 2019.

[144] C. Mettot, "Stabilité linéaire, sensibilité et contrôle passif d'écoulements turbulents par différences finies," Thèse de doctorat, Ecole Polytechnique X, 2013.

[145] G. W. Stewart, "A krylov–schur algorithm for large eigenproblems," *SIAM Journal on Matrix Analysis and Applications*, vol. 23, n°. 3, p. 601–614, 2002.

[146] P. Amestoy, I. S. Duff, J. Koster et J.-Y. L'Excellent, "A fully asynchronous multifrontal solver using distributed dynamic scheduling," *SIAM Journal on Matrix Analysis and Applications*, vol. 23, n°. 1, p. 15–41, 2001.

[147] P. Amestoy, A. Buttari, J.-Y. L'Excellent et T. Mary, "Performance and Scalability of the Block Low-Rank Multifrontal Factorization on Multicore Architectures," *ACM Transactions on Mathematical Software*, vol. 45, p. 2:1–2:26, 2019.

[148] C. Rumsey, B. Smith et G. Huang, "Description of a website resource for turbulence modeling verification and validation," dans *40th fluid dynamics conference and exhibit*, 2010, p. 4742.

[149] C. L. Rumsey, "Recent developments on the turbulence modeling resource website," dans *22nd AIAA Computational Fluid Dynamics Conference*, 2015, p. 2927.

[150] T. Colonius, S. K. Lele et P. Moin, "Boundary conditions for direct computation of aerodynamic sound generation," *AIAA journal*, vol. 31, n°. 9, p. 1574–1582, 1993.

[151] NASA Langley Research Center, "Turbulence Modeling Resource: 2D Zero Pressure Gradient Flat Plate," https://tmbwg.github.io/turbmodels/flatplate.html.

[152] M. Coutanceau et R. Bouard, "Experimental determination of the main features of the viscous flow in the wake of a circular cylinder in uniform translation. part 1. steady flow," *Journal of Fluid Mechanics*, vol. 79, n°. 2, p. 231–256, 1977.

[153] C. Wiliamson, "Vortex dynamics in the cylinder wake," 1996.

[154] F. Giannetti et P. Luchini, "Structural sensitivity of the first instability of the cylinder wake," *Journal of Fluid Mechanics*, vol. 581, p. 167–197, 2007.

[155] O. Marquet, D. Sipp et L. Jacquin, "Sensitivity analysis and passive control of cylinder flow," *Journal of Fluid Mechanics*, vol. 615, p. 221–252, 2008.

[156] C. T. Morisco, "Nonlinear dynamics and linear stability analysis of over-expanded nozzle flows," Thèse de doctorat, HESAM Université, 2020.

[157] O. R. Burggraf, "Analytical and numerical studies of the structure of steady separated flows," *Journal of Fluid Mechanics*, vol. 24, n°. 1, p. 113–151, 1966.

[158] F. Pan et A. Acrivos, "Steady flows in rectangular cavities," *Journal of Fluid Mechanics*, vol. 28, n°. 4, p. 643–655, 1967.

[159] R. Schreiber et H. B. Keller, "Driven cavity flows by efficient numerical techniques," *Journal of Computational Physics*, vol. 49, n°. 2, p. 310–333, 1983.

[160] J. W. Goodrich, K. Gustafson et K. Halasi, "Hopf bifurcation in the driven cavity," *Journal of Computational Physics*, vol. 90, n°. 1, p. 219–261, 1990.

[161] J. Shen, "Hopf bifurcation of the unsteady regularized driven cavity flow," *Journal of Computational Physics*, vol. 95, n°. 1, p. 228–245, 1991.

[162] M. Poliashenko et C. K. Aidun, "A direct method for computation of simple bifurcations," *Journal of Computational Physics*, vol. 121, n°. 2, p. 246–260, 1995.

[163] N. Ramanan et G. M. Homsy, "Linear stability of lid-driven cavity flow," *Physics of Fluids*, vol. 6, n°. 8, p. 2690–2701, 1994.

[164] H. Görtler, *On the three-dimensional instability of laminar boundary layers on concave walls*. National Advisory Commitee for Aeronautics, 1954, vol. 1375.

[165] J. Koseff et R. Street, "Visualization studies of a shear driven three-dimensional recirculating flow," 1984.

[166] J. Kim et P. Moin, "Application of a fractional-step method to incompressible navier-stokes equations," *Journal of computational physics*, vol. 59, n°. 2, p. 308–323, 1985.

[167] Y. Ding et M. Kawahara, "Three-dimensional linear stability analysis of incompressible viscous flows using the finite element method," *International journal for numerical methods in fluids*, vol. 31, n°. 2, p. 451–479, 1999.

[168] ——, "Linear stability of incompressible flow using a mixed finite element method," *Journal of Computational Physics*, vol. 139, n°. 2, p. 243–273, 1998.

[169] V. Theofilis, P. Duck et J. Owen, "Viscous linear stability analysis of rectangular duct and cavity flows," *Journal of Fluid Mechanics*, vol. 505, p. 249–286, 2004.

[170] G. Barakos et D. Drikakis, "Numerical simulation of transonic buffet flows using various turbulence closures," *International Journal of Heat and Fluid Flow*, vol. 21, n°. 5, p. 620–626, 2000.

[171] V. Brunet, "Computational study of buffet phenomenon with unsteady rans equations," dans *21st AIAA Applied Aerodynamics Conference*, 2003, p. 3679.

[172] S. Deck, "Detached-eddy simulation of transonic buffet over a supercritical airfoil," dans *22nd Applied Aerodynamics Conference and Exhibit*, 2004, p. 5378.

[173] T. Coakley et M. Bergmann, "Effects of turbulence model selection on the prediction of complex aerodynamic flows," dans *17th Aerospace Sciences Meeting*, 1979, p. 70.

[174] M.-S. Liou, T. Coakley et M. Bergmann, "Numerical simulation of transonic flows in diffusers," dans *14th Fluid and Plasma Dynamics Conference*, 1981, p. 1240.

[175] D. C. Wilcox et M. W. Rubesin, "Progress in turbulence modeling for complex flow fields including effects of compressibility," Rapport technique, 1980.

[176] T. Hsieh, A. Wardlaw Jr, P. Collins et T. Coakley, "Numerical investigation of unsteady inlet flowfields," *AIAA journal*, vol. 25, n°. 1, p. 75–81, 1987.

[177] T. Hsieh, T. Bogar et T. Coakley, "Numerical simulation and comparison with experiment for self-excitedoscillations in a diffuser flow," *AIAA journal*, vol. 25, n°. 7, p. 936–943, 1987.

[178] M.-S. Liou et T. J. Coakley, "Numerical simulations of unsteady transonic flow in diffusers," *AIAA journal*, vol. 22, n°. 8, p. 1139–1145, 1984.

[179] E. Martelli, P. P. Ciottoli, M. Bernardini, F. Nasuti et M. Valorani, "Detached-eddy simulation of shock unsteadiness in an overexpanded planar nozzle," *AIAA Journal*, vol. 55, n°. 6, p. 2016–2028, 2017.

[180] X. Qian et R. K. Agarwal, "High fidelity cfd verification workshop 2024 test case: Transonic turbulent flow in sajben diffuser," dans *AIAA SCITECH 2025 Forum*, 2025, p. 2403.

[181] R. Bur, B. Corbel et J. Delery, "Study of passive control in a transonic shock wave/boundary-layer interaction," *AIAA journal*, vol. 36, n°. 3, p. 394–400, 1998.

[182] R. Bur, R. Benay, B. Corbel et J. Delery, "Physical study of shock-wave/boundary-layer interaction control in transonic flow," dans *38th Aerospace Sciences Meeting and Exhibit*, 2000, p. 933.

[183] A. Galli, B. Corbel et R. Bur, "Control of forced shock-wave oscillations and separated boundary layer interaction," *Aerospace science and technology*, vol. 9, n°. 8, p. 653–660, 2005.

[184] R. Bur, R. Benay, A. Galli et P. Berthouze, "Experimental and numerical study of forced shock-wave oscillations in a transonic channel," *Aerospace science and technology*, vol. 10, n°. 4, p. 265–278, 2006.

[185] P. Reijasse, B. Corbel et D. Soulevant, "Unsteadiness and asymmetry of shock-induced separation in a planar two-dimensional nozzle-a flow description," dans *30th Fluid Dynamics Conference*, 1999, p. 3694.

[186] A. Bourgoing et P. Reijasse, "Experimental analysis of unsteady separated flows in a supersonic planar nozzle," *Shock Waves*, vol. 14, n°. 4, p. 251–258, 2005.

[187] NASA Glenn Research Center, "NPARC Alliance Validation Archive: Sajben Transonic Diffuser," https://www.grc.nasa.gov/WWW/wind/valid/transdif/transdif.html.

[188] P. Luchini et A. Bottaro, "Adjoint equations in stability analysis," *Annual Review of Fluid Mechanics*, vol. 46, n°. Volume 46, 2014, p. 493–517, 2014. [En ligne]. Disponible: https://www.annualreviews.org/content/journals/10.1146/annurev-fluid-010313-141253

[189] I. Tani, "Production of longitudinal vortices in the boundary layer along a concave wall," *Journal of Geophysical Research*, vol. 67, n°. 8, p. 3075–3080, 1962.

[190] F. H. Clauser, "The turbulent boundary layer," *Advances in applied mechanics*, vol. 4, p. 1–51, 1956.

[191] Z. Zhang, J. Hao et K. C. K. Uy, "Characterising görtler vortices in supersonic turbulent flows over concave surfaces," *Journal of Fluid Mechanics*, vol. 1012, p. A29, 2025.

[192] S. Shin, "Computation of the curvature field in numerical simulation of multiphase flow," *Journal of Computational Physics*, vol. 222, n°. 2, p. 872–878, 2007. [En ligne]. Disponible: https://www.sciencedirect.com/science/article/pii/S0021999106004190

[193] J. Rossiter, "Wind-tunnel experiments on the flow over rectangular cavities at subsonic and transonic speeds," 1964.

[194] P. Rickmers, E. Dumont, S. Krummen, J. L. R. Gutierrez, L. Bussler, S. Kottmeier, G. Wübbels, H. Martens, S. Woicke, M. Sagliano *et al.*, "The callisto and refex flight experiments at dlr-challenges and opportunities of a wholistic approach," *Acta Astronautica*, vol. 225, p. 417–433, 2024.

[195] S. Stappert, J. Wilken, L. Bussler et M. Sippel, "A systematic assessment and comparison of reusable first stage return options," dans *Proceedings of the International Astronautical Congress, IAC*, 2019.

[196] E. S. Love, *The effects of a small jet of air exhausting from the nose of a body of revolution in supersonic flow.* National Advisory Committee for Aeronautics, 1952.

[197] P. Finley, "The flow of a jet from a body opposing a supersonic free stream," *Journal of Fluid Mechanics*, vol. 26, n°. 2, p. 337–368, 1966.

[198] T. Bykerk, S. Karl, M. Laureti, M. Ertl et T. Ecker, "Retro-propulsion in rocket systems: Recent advancements and challenges for the prediction of aerodynamic characteristics and thermal loads," *Progress in Aerospace Sciences*, vol. 151, p. 101044, 2024.

[199] W. R. Hammock Jr, E. C. Currie et A. E. Fisher, "Apollo experience report: Descent propulsion system," Rapport technique, 1973.

[200] A. M. Korzun, R. D. Braun et J. R. Cruz, "Survey of supersonic retropropulsion technology for mars entry, descent, and landing," *Journal of Spacecraft and Rockets*, vol. 46, n°. 5, p. 929–937, 2009.

[201] S. Stappert, J. Wilken et M. Sippel, "Evaluation of european reusable vtvl booster stages," dans *2018 AIAA SPACE and Astronautics Forum and Exposition*, 2018, p. 5239.

[202] T. Ecker, S. Karl, E. Dumont, S. Stappert et D. Krause, "Numerical study on the thermal loads during a supersonic rocket retropropulsion maneuver," *Journal of Spacecraft and Rockets*, vol. 57, n°. 1, p. 131–146, 2020.

[203] D. Charbonnier, J. Vos, A. Marwege et C. Hantz, "Computational fluid dynamics investigations of aerodynamic control surfaces of a vertical landing configuration," *CEAS Space Journal*, vol. 14, n°. 3, p. 517–532, 2022.

[204] A. Marwege et A. Guelhan, "Aerodynamic characteristics of the retro propulsion landing burn of vertically landing launchers," *Experiments in Fluids*, vol. 65, n°. 8, p. 115, 2024.

[205] S. Anoop et A. Kumar, "Flow dynamics of a supersonic retropropulsion jet interacting with a low-speed opposing stream," *Aerospace Science and Technology*, p. 112610, 2026.

[206] T. Bykerk et S. Karl, "Preparatory cfd studies for subsonic analyses of a reusable first stage launcher during landing within the retpro project," dans *10th EUCASS–9th CEAS Conference 2023*, 2023, p. 1–10.

[207] P. R. Spalart et C. L. Rumsey, "Effective inflow conditions for turbulence models in aerodynamic calculations," *AIAA journal*, vol. 45, n°. 10, p. 2544–2553, 2007.

[208] É. Goncalves, "Implantation et validation de lois de paroi dans un code navier-stokes," Thèse de doctorat, Toulouse, ENSAE, 2001.

[209] E. R. Van Driest, "Turbulent boundary layer in compressible fluids," *Journal of the Aeronautical Sciences*, vol. 18, n°. 3, p. 145–160, 1951.

Appendix A

More on Sajben diffuser

In addition to the mesh described in Chapter 4, a coarser mesh has also been used, with dimensions more similar to those in the database; indeed, the reference uses $(n_x \times n_y) = (91 \times 59)$ points, whilst our coarser mesh uses $(n_x \times n_y) = (82 \times 58)$.The meshes shown in this appendix all have the same $\Delta y = 2 \times 10^{-5}$ at the wall. Figures A.1 and A.2 show the wall pressure distributions and velocity profiles in two different cross-sections respectively, again in comparison with experiments and databases. Although the coarse mesh also yields good results, the finer mesh produces a less dissipated shock and was therefore preferred for the analyses carried out in Chapter 4.

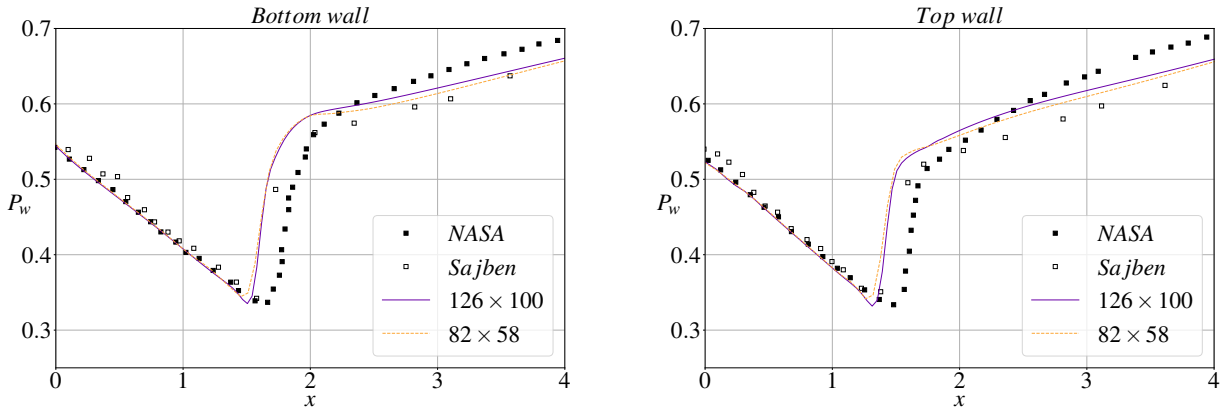


Figure A.1: Comparison of wall pressure distribution. Bottom wall (left) , top wall (right)

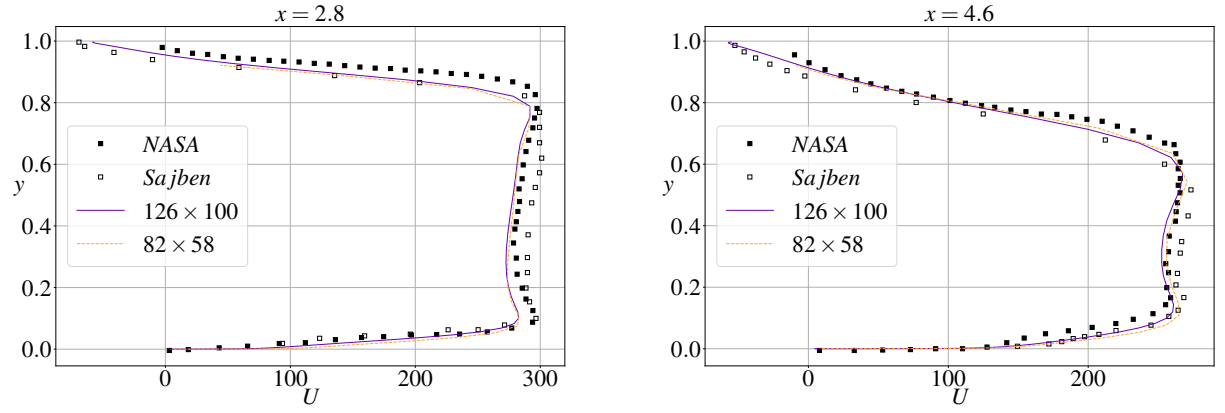


Figure A.2: Comparison of Streamwise velocity profile at two different sections. $x/h_{in} = 2.8$ (left) , $x/h_{in} = 4.6$ (right)

The $k - \log(\omega)$ model was validated in dNami by Franchini in his thesis [53]; in the present study, however, it was used only for the counter-current jet case because it allows for less dissipation of the

spreading rate and yields a correct jet length. However, in the final section, we have partially revisited the Sajben nozzle case to test the $k-\log(\omega)$ SST model. This appendix therefore presents the results obtained using the SA model. From Figure $A.3$, it can be seen that the $k-\log(\omega)$ SST model comes closer to the numerical reference, yielding a shock position slightly further downstream compared with the experimental results. As regards the stability analysis, however, the results are still preliminary, but it would be interesting to continue this work, particularly from the perspective of the energy norm in the resolvent analysis. With the Spalart-Allmaras method, in fact, there is no access to turbulent kinetic energy, whereas with the $k-\log(\omega)$ SST method there is, so it would be possible to extend Chu's energy norm.

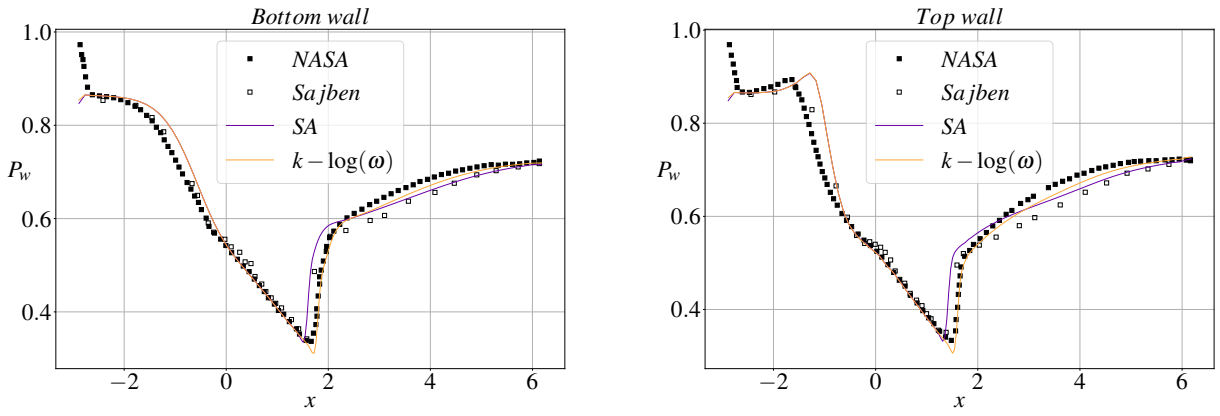


Figure A.3: Turbulence model comparison of wall pressure distribution. Bottom wall (left) , top wall (right)

A.1 Strong shock case: acoustic mode

In the eigenvalue spectrum for the strong shock case ($R_p = 0.72$), calculated using the matrix-forming method, there are also two further branches at higher frequencies which could not be computed using the time-stepper method, as can be seen in Figure A.5. For this reason, it may be of interest to take a look at the least stable mode for each branch. The mode of the second branch in Figure (A.6) appears to be a coupled mode, the main activity occurs both close to the shock and in the divergent region and has a wavelength that is half that of the main mode; by contrast, the mode of the third branch in Figure A.7 appears to be a purely acoustic mode, due to its high frequency, and is very similar to that found by Sartor in [51]

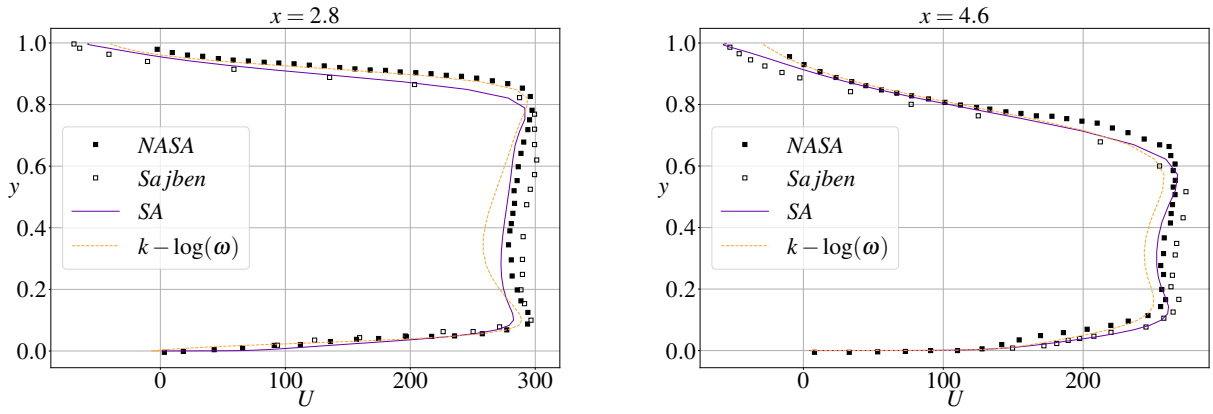


Figure A.4: Turbulence model comparison of streamwise velocity profile at two different sections. $x/h_{in} = 2.8$ (left) , $x/h_{in} = 4.6$ (right)

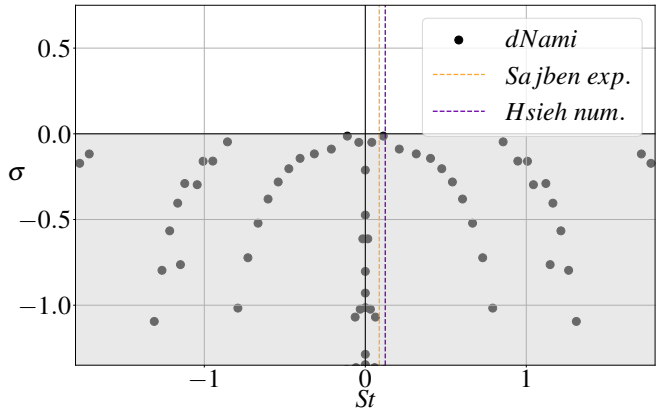


Figure A.5: Eigenspectrum compared with experimental frequency and numerical frequency of reference



Figure A.6: Real part of the mode at $St = 0.86$ for the case at $R_p = 0.72$. Streamwise and wall-normal velocity (left), density and modified viscosity (right)

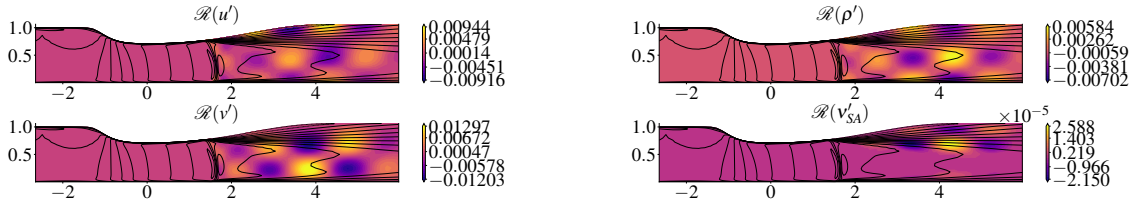


Figure A.7: Real part of the mode at $St = 1.7$ for the case at $R_p = 0.72$. Streamwise and wall-normal velocity (left), density and turbulent eddy viscosity (right)

Appendix B

Wall Law in dNami

When dealing with RANS methods, wall laws are often employed. The latter allows reducing the number of mesh points and increasing the time step, particularly in the case of codes using explicit time integration such as dNami.

Using a wall-law approach involves imposing different boundary conditions at the wall. These conditions are based on the existence of an analytical relationship for turbulent boundary layers that links velocity to the distance from the wall via the wall shear stress [208]. Exploiting this relationship allows us to relax the constraint of imposing the first fluid point at $y^+ \approx 1$ near a wall.

There are a number of analytical laws that describe the velocity profile in the turbulent boundary layer; in our case, we have considered the following law:

$$\begin{aligned} U^+ &= y^+ && \text{if} \quad y^+ < 11.13 \\ U^+ &= \frac{1}{\kappa}\log y^+ + C && \text{if} \quad y^+ > 11.13 \end{aligned} \tag{B.1}$$

with $\kappa = 0.41$ the von Karman constant and $C \approx 5.25$. So far, only the case of an adiabatic wall has been examined. To apply the boundary condition, we refer both to the wall quantities denoted by the subscript 'w' and to the quantities at the first fluid point, denoted by the subscript '1' .

Starting from the energy equation, and neglecting the convective terms, the integral between the wall and the first point in the fluid gives us the following relationship to determine the wall temperature:

$$T_w = T_1 + \left[\frac{\mu_1 + \mu_{t1}}{C_p\left(\frac{\mu_1}{Pr} + \frac{\mu_t}{Pr_t}\right)}\right]\frac{1}{2}U_{t1}^2 \tag{B.2}$$

where U_t refers to the component of velocity vector tangential to the wall. The wall viscosity μ_w can be calculated using Sutherland's formula, whilst the density can be determined by imposing the condition of a zero pressure gradient:

$$\rho_w = \rho_1\frac{T_1}{T_w} \tag{B.3}$$

To take account of the effects of compressibility, the tangential velocity must be corrected using the Van Driest equation [209]:

$$\overline{U}_t = \int_0^{U_t}\sqrt{\frac{\rho}{\rho_w}}dU_t \tag{B.4}$$

whose solution is given by:

$$\overline{U}_t = \frac{1}{\sqrt{B}}\left[\arcsin\left(U_t\right)\right] \tag{B.5}$$

with

$$B = \frac{A}{2T_w}, \qquad A = \frac{\mu_1 + \mu_{t1}}{C_p\left(\frac{\mu_1}{Pr} + \frac{\mu_t}{Pr_t}\right)} \tag{B.6}$$

Given the values for velocity, temperature and density, the wall law can be solved to compute the friction velocity u_τ using Newton's method. Subsequently, as we are using the URANS approach, the modified viscosity ν_{SA} must be recalculated using the following fourth-order relationship (more details in [208]):

$$(\rho\nu)^4 - \mu_t(\rho\nu_{SA})^3 = \mu\mu_t C_v^3 \tag{B.7}$$

Finally, given u_τ, it is possible to recompute the correct wall shear stress and, consequently, the wall-normal velocity gradient.

The first test involved restarting a simulation that had already converged, applying the wall law within the same computational mesh. In order to obtain a result unaffected by the presence of the discontinuity, the domain was cut starting from the coordinate $x = 1$ and the previously developed profiles of the state vector were imposed at the inlet. The results are shown in Figure B.1. As can be seen, the original profiles are correctly preserved, so we can move on to the next test.

In this second test, we take a step further, starting from the same previous reference solution, which is, however, interpolated onto a new mesh. In this case, the first point of the new mesh is located at $y = 2 \times 10^{-4}$, corresponding to $y^+ \approx 35$. In this second test too, the results are satisfactory, although the turbulent viscosity is slightly overestimated compared with the reference case, as can be seen in Figure B.2. In the third test, the entire domain is considered, including the discontinuity, always

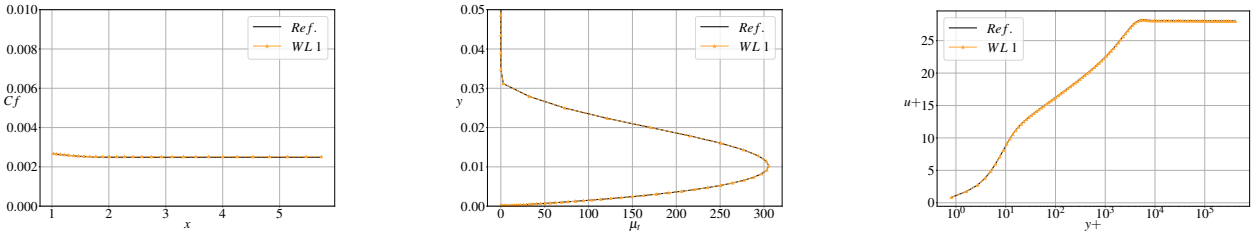


Figure B.1: Comparison between reference solution and wall law results (test 1) of friction coefficient (left), turbulent viscosity (center) and inner velocity (right) profiles.

starting from a previously interpolated solution. Homogeneous profiles are therefore imposed at the inflow. The C_f is calculated correctly, whilst the overestimation of the turbulent viscosity persists (see Figure B.3). The next step is to have the solution developed directly using wall laws, but the appropriate strategy has not yet been identified.

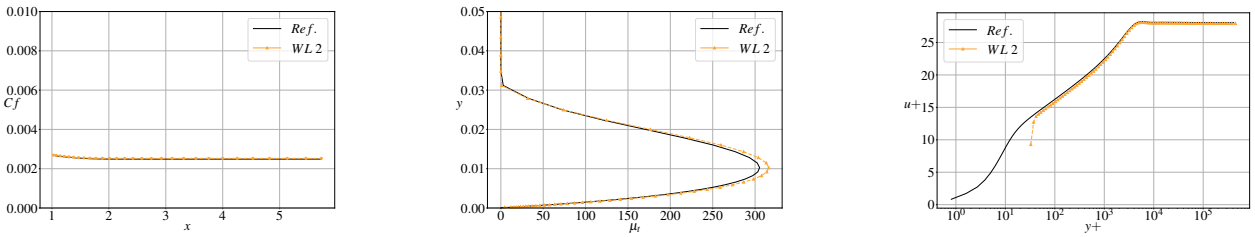


Figure B.2: Comparison between reference solution and wall law results (test 2) of friction coefficient (left), turbulent viscosity (center) and inner velocity (right) profiles.

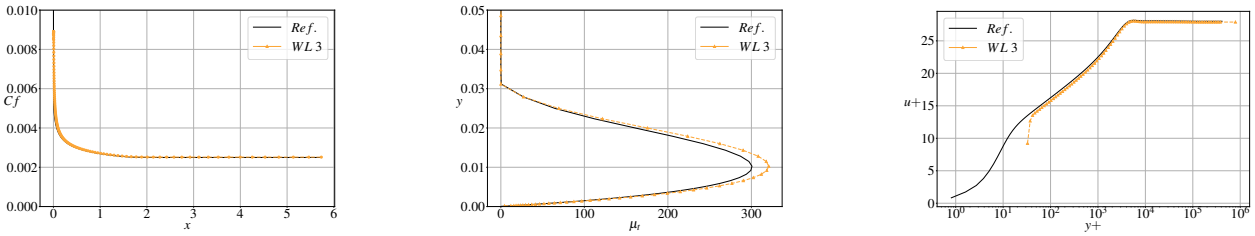


Figure B.3: Comparison between reference solution and wall law results (test 3) of friction coefficient (left), turbulent viscosity (center) and inner velocity (right) profiles.